

**TECHNISCHE
UNIVERSITÄT
DRESDEN**

Integrable Approximations
for
Dynamical Tunneling

Dissertation
zur Erlangung des wissenschaftlichen Grades
Doctor rerum naturalium

vorgelegt von

Clemens Löbner
geboren am 05.08.1985 in Dresden

Institut für Theoretische Physik
Fachrichtung Physik
Fakultät für Mathematik und Naturwissenschaften
Technische Universität Dresden
2015

Eingereicht am 22.05.2015

1. Gutachter: Prof. Dr. Roland Ketzmerick
2. Gutachter: Prof. Dr. Peter Schlagheck

Abstract

Generic Hamiltonian systems have a mixed phase space, where classically disjoint regions of regular and chaotic motion coexist. For many applications it is useful to approximate the regular dynamics of such a mixed system H by an integrable approximation H_{reg} . We present a new, iterative method to construct such integrable approximations. The method is based on the construction of an integrable approximation in action representation which is then improved in phase space by iterative applications of canonical transformations. In contrast to other known approaches, our method remains applicable to strongly non-integrable systems H . We present its application to 2D maps and 2D billiards. Based on the obtained integrable approximations we finally discuss the theoretical description of dynamical tunneling in mixed systems.

Zusammenfassung

Typische Hamiltonsche Systeme haben einen gemischten Phasenraum, in dem disjunkte Bereiche klassisch regulärer und chaotischer Dynamik koexistieren. Für viele Anwendungen ist es zweckmäßig, die reguläre Dynamik eines solchen gemischten Systems H durch eine integrable Näherung H_{reg} zu beschreiben. Wir stellen eine neue, iterative Methode vor, um solche integrablen Näherungen zu konstruieren. Diese Methode basiert auf der Konstruktion einer integrablen Näherung in Winkel-Wirkungs-Variablen, die im Phasenraum durch iterative Anwendungen kanonischer Transformationen verbessert wird. Im Gegensatz zu bisher bekannten Verfahren bleibt unsere Methode auch auf stark nichtintegrable Systeme H anwendbar. Wir demonstrieren sie anhand von 2D-Abbildungen und 2D-Billiards. Mit den gewonnenen integrablen Näherungen diskutieren wir schließlich die theoretische Beschreibung von dynamischem Tunneln in gemischten Systemen.

Contents

Contents	v
1. Introduction	1
2. Fundamentals	3
2.1. Hamiltonian dynamical systems	3
2.1.1. Time-continuous Hamiltonian systems	3
2.1.2. Canonical transformations	4
2.1.3. Time-discrete Hamiltonian systems	6
2.2. Integrable systems and action–angle coordinates	8
2.3. Non-integrable systems	14
2.4. Integrable approximations	17
3. Iterative canonical transformation method	19
3.1. Basic idea	19
3.2. Frequency approximation	19
3.3. Shape approximation	21
3.3.1. Initial integrable approximation	21
3.3.2. Family of canonical transformations	21
3.3.3. Iterative improvement	22
3.4. Overview	24
4. Integrable approximation of symplectic 2D maps	27
4.1. Example system	27
4.2. Application of the iterative canonical transformation method	28
4.2.1. Frequency approximation	28
4.2.2. Shape approximation	29
4.3. Damping mechanism	32
4.3.1. Invertibility	32
4.3.2. Existence of damped solutions	34
4.3.3. Illustration for 2D maps	35
4.3.4. Adapted damping	38
4.4. Choice of the orders \mathcal{N} and convergence	40

4.5.	Comparison to other methods	43
4.5.1.	Method of normal forms	43
4.5.2.	Comparison to the method of normal forms	45
4.5.3.	Method of Lie transforms	48
4.5.4.	Comparison to the method of Lie transforms	49
4.5.5.	Conclusion	51
4.6.	Integrable approximations including a separatrix	53
4.7.	Integrable approximations including a nonlinear resonance chain	55
4.7.1.	Basic idea	55
4.7.2.	Frequency approximation	57
4.7.3.	Application to the standard map	59
5.	Integrable approximation of 2D billiards	61
5.1.	Billiards	61
5.2.	Boundary simplification	63
5.3.	Scaling systems	67
5.4.	Application of the iterative canonical transformation method	70
5.4.1.	Frequency approximation	70
5.4.2.	Shape approximation	71
6.	Dynamical tunneling	75
6.1.	Dynamical tunneling and the fictitious integrable system approach	75
6.2.	Tunneling predictions in 2D maps using integrable approximations	77
6.3.	Influence of the quantization rule	79
6.4.	Tunneling predictions in 2D billiards using integrable approximations	83
6.4.1.	Fictitious integrable system approach for 2D billiards	83
6.4.2.	Numerical computation of eigenstates in 2D confined systems	84
6.4.3.	Application	92
7.	Summary and outlook	99
	Appendix	103
A.	Approximation of the cost function \mathcal{L}	103
B.	Closed form for H_{reg}^N	104
C.	Properness of the implicit function ϕ	105
D.	Inversion of the pendulum transformation T_{pend}	105
E.	Implementation of the normal-form transformation T^*	107
F.	Scaling property	108
G.	Stability of the cosine billiard	109
G.1.	Stability condition	109
G.2.	Derivation of the parameter δ for the cosine billiard	110

H.	Derivation of the boundary transformation \mathcal{T}_1	111
H.1.	Conditions	111
H.2.	Nonexistence of a solution	117
H.3.	Solution for the relaxed problem	117
H.4.	Invertibility for the cosine billiard	118
H.5.	Boundary transformation for smooth billiards	119
I.	Generalized quantizations \mathcal{Q}	122
I.1.	Monomial formulae	122
I.2.	Conditions for the integral kernel $w(\theta, \tau)$	123
I.3.	Matrix element formulae	125
J.	Optimized algorithm for the Weyl matrix elements $A_{\mathbf{nm}}$	126

List of figures	130
------------------------	------------

1. Introduction

When Newton introduced the concept of force to describe the planetary motion, he marked the genesis of classical mechanics. Among many equivalent versions of classical mechanics, which have been developed later on, the Hamiltonian formalism is of special relevance, due to its symplectic structure, in which the phase-space coordinates of position \mathbf{q} and momentum \mathbf{p} appear symmetrically.

Two important limiting cases of Hamiltonian systems are given by integrable and fully chaotic systems. In integrable systems with f degrees of freedom, there exists a maximum number of f independent constants of motion, which restricts the dynamics to invariant tori in phase space. The motion on these f -dimensional tori is always regular in the sense, that it reacts weakly to a change in the initial conditions. On the other hand, in fully chaotic systems almost all solutions depend sensitively on their initial conditions and explore higher-dimensional regions in phase space.

However, typical Hamiltonian systems lie between these limiting cases and have a mixed phase space, where regions of regular and chaotic motion coexist [1]. This situation is illustrated in Fig. 1.1(a) for a symplectic 2D map showing regular orbits (lines) which form a regular island embedded in a chaotic sea (dots). Similar to the integrable case, the regular island is composed of invariant tori, but additionally includes a rich self-similar structure with nonlinear resonance chains and thin chaotic layers on all scales (not shown).

For many applications it turns out as extremely useful to replace the complicated fine details of the dynamics inside the regular islands of a mixed Hamiltonian H by an integrable approximation H_{reg} . Such applications arise in plasma physics [2], Hamiltonian transport [3], celestial mechanics [4], and dynamical tunneling (see below). The required integrable system H_{reg} should resemble the dynamics of the regular tori in the island as closely as possible and smoothly interpolate through regions of nonlinear resonance chains and chaotic layers. An example for such an integrable approximation is

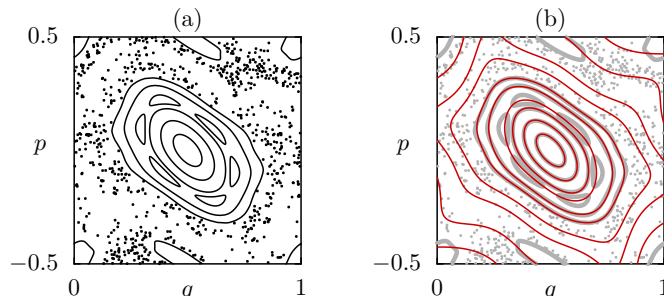


Figure 1.1.: (a) Phase space of the standard map (4.4) at $\kappa = 1.25$, with regular orbits (black lines) and chaotic orbits (black dots) and (b) of an integrable approximation H_{reg} (thin red lines).

shown in Fig. 1.1(b).

Our main motivation for constructing integrable approximations is the theoretical description of dynamical tunneling [5, 6] between classically disconnected regions in phase space. For this, two theoretical approaches have been developed, which both rely on an appropriate integrable approximation H_{reg} . In the semiclassical regime, where Planck's constant is small compared to the size of the involved regular island, $h \ll \mathcal{A}$, tunneling is strongly influenced by nonlinear resonance chains in phase space. Here, the theory of *resonance-assisted tunneling* can be applied [7–11]. In the contrary quantum regime $h \lesssim \mathcal{A}$, the role of resonances can be neglected and an appropriate description of tunneling is possible using the *fictitious integrable system approach* [12, 13]. Recently, this separation was overcome by a combined theory [14]. Currently, the main obstacle which constrains this research line is the question for a close integrable approximation.

Up to now, all methods for constructing such integrable approximations are either restricted to systems with only one degree of freedom [13], to systems of a special type [15, 16], to the local modeling of individual tori [4, 17], or to near-integrable systems (as, e.g., the methods of normal forms [18, 19] and Lie transforms [8, 20–22]). In this thesis, we introduce the *iterative canonical transformation method*, which overcomes all of these restrictions. We apply this method to symplectic 2D maps and to 2D billiards far from the near-integrable case. Moreover, we predict tunneling rates for both system classes by applying the fictitious integrable system approach.

This thesis is organized as follows: In Chpt. 2, we introduce Hamiltonian systems, canonical transformations, and the problem of integrable approximations. In Chpt. 3, we present the iterative canonical transformation method in general. In Chpt. 4, we apply our method to symplectic 2D maps, and, based on this intuition, discuss its convergence behavior, compare it to other methods, and work out several enhancements. In Chpt. 5, we apply our method to 2D billiards. In Chpt. 6, we review the fictitious integrable system approach and apply it to symplectic 2D maps and 2D billiards. Besides, we discuss the role of the quantization for the fictitious integrable system approach. In Chpt. 7, we summarize this thesis and give an outlook.

2. Fundamentals

In this chapter we lay out the basics of classical Hamiltonian physics with a strong focus on the distinction between integrable and non-integrable systems and their characteristic geometrical structure. First, we generally introduce Hamiltonian systems and their canonical transformation theory (Sec. 2.1). Then, we discuss integrable and non-integrable Hamiltonian systems (Secs. 2.2 and 2.3, respectively) and finally explain the concept of integrable approximations (Sec. 2.4).

2.1. Hamiltonian dynamical systems

Hamiltonian systems are possibly the most important type of dynamical systems in classical physics. They are used in many fields such as celestial mechanics, molecular physics, accelerator dynamics, or mesoscopic physics. Compared to the equivalent formulations of Newton and Lagrange, Hamilton's description of classical mechanics is better suited for perturbation theory and the geometrical understanding of the dynamics. Apart from classical mechanics, Hamiltonian systems are also relevant for semiclassical methods and form the conceptual basis of modern quantum mechanics and statistical physics.

2.1.1. Time-continuous Hamiltonian systems

In Hamilton's formulation of classical mechanics, the physical state of a system with f degrees of freedom is given by a point $\mathbf{x} = (\mathbf{q}, \mathbf{p})$ in the $2f$ -dimensional *phase space*. This point consists of f position coordinates $\mathbf{q} = (q_1, \dots, q_f)$ and their conjugated momentum coordinates $\mathbf{p} = (p_1, \dots, p_f)$. A dynamical system is called a (*time-continuous*) *Hamiltonian system*, if its time evolution can be written in the form,

$$\frac{d}{dt}\mathbf{q} = \frac{\partial H}{\partial \mathbf{p}}(\mathbf{q}, \mathbf{p}), \tag{2.1a}$$

$$\frac{d}{dt}\mathbf{p} = -\frac{\partial H}{\partial \mathbf{q}}(\mathbf{q}, \mathbf{p}), \tag{2.1b}$$

where t denotes time. Here $H(\mathbf{q}, \mathbf{p})$ is *Hamilton's function*, or the *Hamiltonian* of the system. We omit the discussion of time-dependent Hamiltonians $H(\mathbf{q}, \mathbf{p}, t)$, as they are formally equivalent to time-independent Hamiltonians with $f + 1$ degrees of freedom [22, Sec. 1.2b]. For a given initial condition $\mathbf{x}_0 = (\mathbf{q}_0, \mathbf{p}_0)$, the solution of Eqs. (2.1) is called a *trajectory*. Formally, this trajectory can

be written as

$$(\mathbf{q}, \mathbf{p})(t) = \mathcal{U}^t(\mathbf{q}_0, \mathbf{p}_0), \quad (2.2a)$$

or more compactly,

$$\mathbf{x}(t) = \mathcal{U}^t(\mathbf{x}_0). \quad (2.2b)$$

Here the map \mathcal{U}^t is the so-called *phase flow* of the system. For convenience, we refer to the solutions of Eqs. (2.1) simply as the solutions of H .

2.1.2. Canonical transformations

For a given Hamiltonian $H(\mathbf{q}, \mathbf{p})$, we now consider a change of phase-space coordinates, given by an invertible transformation

$$T : (\mathbf{q}, \mathbf{p}) \mapsto (\mathbf{q}', \mathbf{p}'). \quad (2.3)$$

If the dynamics in the new coordinates $(\mathbf{q}', \mathbf{p}')$ can also be expressed in Hamiltonian form (2.1), T is called a *canonical transformation*. This is the case if and only if the components $\mathbf{q}'(\mathbf{q}, \mathbf{p})$, $\mathbf{p}'(\mathbf{q}, \mathbf{p})$ of T satisfy

$$\{q'_i, p'_j\} = \delta_{ij}, \quad (2.4a)$$

$$\{q'_i, q'_j\} = 0, \quad (2.4b)$$

$$\{p'_i, p'_j\} = 0. \quad (2.4c)$$

Here we used the Poisson-bracket of two functions defined by $\{f, g\} := \frac{\partial f}{\partial q} \frac{\partial g}{\partial p} - \frac{\partial f}{\partial p} \frac{\partial g}{\partial q}$. The Hamiltonian in the new coordinates is then given by

$$H'(\mathbf{q}', \mathbf{p}') = H[\mathbf{q}(\mathbf{q}', \mathbf{p}'), \mathbf{p}(\mathbf{q}', \mathbf{p}')], \quad (2.5a)$$

$$= H[T^{-1}(\mathbf{q}', \mathbf{p}')], \quad (2.5b)$$

or in a more compact notation

$$H'(\mathbf{x}') = H[T^{-1}(\mathbf{x}')]. \quad (2.5c)$$

Although both Hamiltonians $H(\mathbf{x})$ and $H'(\mathbf{x}')$ describe physically the same system in different coordinates, we will use the term “system” as a synonym for “Hamiltonian”. Therefore, the reader should not be confused about statements of the form “the system $H(\mathbf{x})$ is transformed to the new system $H'(\mathbf{x}')$ ”.

By definition, the canonical transformation T switches between the phase flows of the connected

Hamiltonians,

$$\mathcal{U}'^t = T \circ \mathcal{U}^t \circ T^{-1}, \quad (2.6)$$

as illustrated in Fig. 2.1(a). This allows to reformulate the search for solutions of $H(\mathbf{x})$ as the search for a canonical transformation to a system with known solutions. More general, a popular practice to analyze $H(\mathbf{x})$ is to transform it to a system $H'(\mathbf{x}')$ that is more suitable for the considered analysis.

Although the motion might appear very different in the new coordinates, canonical transformations have several invariants. First of all, the maximum Lyapunov exponent, which quantifies the sensitivity of solutions with respect to their initial conditions, is unchanged under any canonical transformation [23]. Secondly, canonical transformations preserve certain integral invariants [24]. The two most relevant invariants are the volume of a phase-space region A ,

$$V[A] = \int_A d^f \mathbf{q} d^f \mathbf{p}, \quad (2.7)$$

and the *action integral* along a closed curve \mathcal{C} in phase space,

$$\mathcal{J}[\mathcal{C}] = \frac{1}{2\pi} \oint_{\mathcal{C}} \mathbf{p} d\mathbf{q}. \quad (2.8)$$

In the simplest case $f = 1$, the phase space is two-dimensional and these invariants coincide according to Stoke's theorem [25]. Hence 2D canonical transformations are area-preserving maps, see Fig. 2.1(b). In the general case, $V[A]$ is a $2f$ -dimensional volume of A and $\mathcal{J}[\mathcal{C}]$ is the sum over the areas inside the (q_i, p_i) -projections of \mathcal{C} .

Constructing a canonical transformation T for a given purpose can become difficult in practice, as Eqs. (2.4) impose $(3f - 1)f/2$ nonlinear side conditions on the partial derivatives of T . This situation is strongly simplified using the formalism of generating functions [24, 26], which brings two advantages. First, the vectorial canonical transformation $T : \mathbb{R}^{2f} \rightarrow \mathbb{R}^{2f}$ is represented by a scalar generating function $F : \mathbb{R}^{2f} \rightarrow \mathbb{R}^1$. Second, the formalism ensures that for any choice of F , the

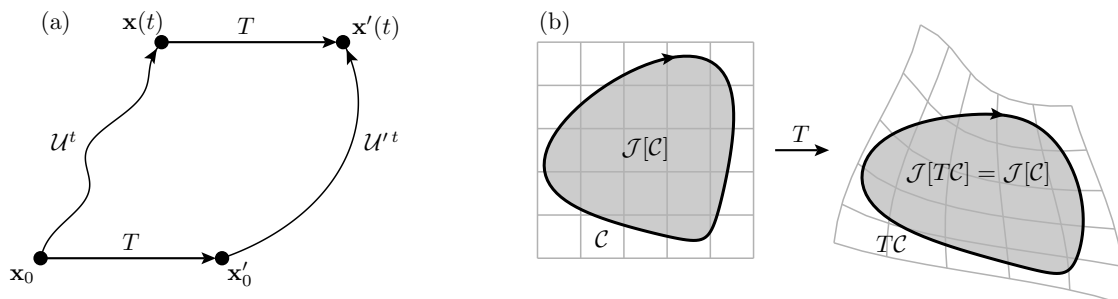


Figure 2.1.: (a) Illustration of the connection (2.6) between the two phase flows \mathcal{U}^t and \mathcal{U}'^t by means of the canonical transformation T . (b) Transformation of a closed curve \mathcal{C} in 2D phase space. The grid indicates the area-preserving property.

generated transformation T is canonical, i. e., the side conditions (2.4) are automatically fulfilled. Generating functions can be classified into different types [24], where the so-called second type will turn out to be of particular relevance for our subject. This type of generating function $F(\mathbf{q}, \mathbf{p}')$ has a hybrid dependence on the old position coordinates \mathbf{q} and the new momentum coordinates \mathbf{p}' . The canonical transformation T is generated by the equations

$$\mathbf{q}' = \frac{\partial F}{\partial \mathbf{p}'}(\mathbf{q}, \mathbf{p}'), \quad (2.9a)$$

$$\mathbf{p} = \frac{\partial F}{\partial \mathbf{q}}(\mathbf{q}, \mathbf{p}'), \quad (2.9b)$$

which implicitly connect the old coordinates (\mathbf{q}, \mathbf{p}) to the new coordinates $(\mathbf{q}', \mathbf{p}')$. The disadvantage of the generating function formalism is that this implicit description of T typically cannot be solved explicitly for $\mathbf{q}'(\mathbf{q}, \mathbf{p}), \mathbf{p}'(\mathbf{q}, \mathbf{p})$ in a closed form. Therefore, although T is well defined, its application requires the additional effort of solving Eqs. (2.9) numerically.

2.1.3. Time-discrete Hamiltonian systems

Finding the trajectories $\mathbf{x}(t)$ of a time-continuous Hamiltonian system requires the integration of Hamilton's equations of motion (2.1) in phase space, which is usually done numerically. In order to reduce the computational effort, one often considers time-discrete dynamical systems instead. Here the time evolution in phase space follows from a map \mathcal{M} according to

$$\mathbf{x}_{n+1} = \mathcal{M}(\mathbf{x}_n). \quad (2.10)$$

For a given initial condition \mathbf{x}_0 , the solution \mathbf{x}_n at discrete "times" $n \in \mathbb{N}_0$ is called an *orbit*.

Furthermore, the map \mathcal{M} is called *symplectic*, if its components fulfill Eqs. (2.4). Mathematically, symplectic maps are canonical transformations. However, to emphasize their physical context, we carefully distinguish between these terms. While a canonical transformation T is applied *once* to change the *spatial* description of a system, a symplectic map \mathcal{M} is applied *repeatedly*, to change the system's *temporal* state.

Symplectic maps are also called *time-discrete Hamiltonian systems*, as they are often derived as simplifications of time-continuous Hamiltonian systems. In the following we demonstrate two situations, where symplectic maps emerge from a time-continuous Hamiltonian system $H(\mathbf{q}, \mathbf{p})$. One concept to achieve this is the so-called *Poincaré section*. This is a common technique for the analysis of systems with $f \geq 2$ degrees of freedom. For this, one first defines a section through phase space by a $2(f-1)$ -dimensional manifold Σ . Secondly, the trajectories $\mathbf{x}(t)$ of $H(\mathbf{q}, \mathbf{p})$ are reduced to their intersection points \mathbf{x}_n with Σ . The time evolution of these points is then given by the so-called Poincaré map,

$$\mathbf{x}_{n+1} = \mathcal{P}(\mathbf{x}_n). \quad (2.11)$$

If the manifold Σ is parametrized by $2(f-1)$ coordinates $(q_1, \dots, q_{n-1}, p_1, \dots, p_{n-1})$, where $q(\mathbf{q}, \mathbf{p})$ and

$p(\mathbf{q}, \mathbf{p})$ fulfill the conditions (2.4), the Poincaré map \mathcal{P} is symplectic in (q, p) [24]. This reduces the time-continuous Hamiltonian system with f degrees of freedom to a symplectic map with $f - 1$ degrees of freedom, as sketched in Figs. 2.2(a) and (b).

Another symplectic map, induced by $H(\mathbf{q}, \mathbf{p})$, is its phase flow $\mathcal{U}^{\Delta t}$, Eq. (2.2), for a given, fixed timespan Δt [24]. This map reduces the dynamics of $H(\mathbf{q}, \mathbf{p})$ to times that are integer multiples of Δt , see Fig. 2.2(c). As this construction can be interpreted as a temporal analogue to the Poincaré section, it is called a *stroboscopic Poincaré section*.

As the orbits \mathbf{x}_n of the symplectic maps \mathcal{P} and $\mathcal{U}^{\Delta t}$ are discrete samples of the continuous trajectories $\mathbf{x}(t)$, their analysis also reveals insights into the motion of $H(\mathbf{q}, \mathbf{p})$. For example, if the maximum Lyapunov exponent exists, it must be the same for both $\mathbf{x}(t)$ and \mathbf{x}_n . Furthermore, any periodic orbit with $\mathbf{x}_{n+m} = \mathbf{x}_n$ refers to a periodic trajectory with $\mathbf{x}(t + T) = \mathbf{x}(t)$.

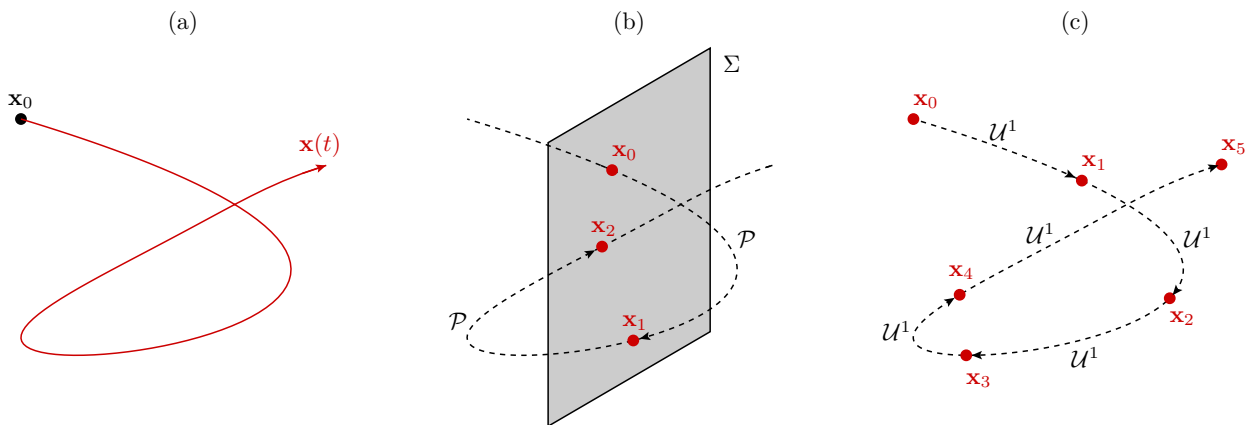


Figure 2.2.: (a) Trajectory $\mathbf{x}(t)$ of a time-continuous Hamiltonian system. (b) Discrete orbit \mathbf{x}_n of a Poincaré map \mathcal{P} induced from $\mathbf{x}(t)$ using the Poincaré section Σ . (c) Discrete orbit \mathbf{x}_n of the phase flow \mathcal{U}^1 induced from $\mathbf{x}(t)$.

2.2. Integrable systems and action–angle coordinates

For understanding a physical system, constants of motion are of great importance. From a geometrical point of view, energy-conservation restricts every solution of a Hamiltonian system $H(\mathbf{q}, \mathbf{p})$ to a $(2f - 1)$ -dimensional subregion of phase space, the so-called *energy shell*. Following this idea, every additional constant of motion reduces this accessible region by one dimension. In the most simple case, when there are as many independent constants of motion as there are degrees of freedom, the system is called integrable. In the following we will discuss the phase-space structure of such integrable systems.

We proceed with an alternative, equivalent definition of integrability: A system $H(\mathbf{q}, \mathbf{p})$ is called *integrable* on a certain domain of phase space, if there exists a canonical transformation

$$T : (\boldsymbol{\vartheta}, \mathbf{J}) \mapsto (\mathbf{q}, \mathbf{p}), \quad (2.12)$$

such that the Hamiltonian becomes independent of the positional coordinates $\boldsymbol{\vartheta}$, i.e.

$$\mathcal{H}(\boldsymbol{\vartheta}, \mathbf{J}) = \mathcal{H}(\mathbf{J}). \quad (2.13)$$

These special coordinates are called *angles* $\boldsymbol{\vartheta} = (\vartheta_1, \dots, \vartheta_f)$ and *actions* $\mathbf{J} = (J_1, \dots, J_f)$. For convenience we introduce the *frequency function* as

$$\boldsymbol{\omega}(\mathbf{J}) := \frac{\partial \mathcal{H}}{\partial \mathbf{J}}(\mathbf{J}). \quad (2.14)$$

As adding a constant to the Hamiltonian has no physical relevance, the frequency function $\boldsymbol{\omega}(\mathbf{J})$ contains the full information of the system $\mathcal{H}(\mathbf{J})$. Hamilton's Eqs. (2.1) in action–angle coordinates yield

$$\frac{d}{dt} \boldsymbol{\vartheta} = \boldsymbol{\omega}(\mathbf{J}), \quad (2.15a)$$

$$\frac{d}{dt} \mathbf{J} = \mathbf{0}, \quad (2.15b)$$

which can be integrated to

$$\boldsymbol{\vartheta}(t) = \boldsymbol{\vartheta}_0 + \boldsymbol{\omega}(\mathbf{J}_0) \cdot t, \quad (2.16a)$$

$$\mathbf{J}(t) = \mathbf{J}_0. \quad (2.16b)$$

Hence, the angles $\boldsymbol{\vartheta}$ process linearly in time with rates given by $\boldsymbol{\omega}(\mathbf{J})$, while the actions \mathbf{J} are preserved and play the role of the previously mentioned f constants of motion. The solutions in the original coordinates (\mathbf{q}, \mathbf{p}) can be obtained by applying the canonical transformation T .

In addition to the demonstrated algebraic simplification, integrability also has strong implications on the geometrical structure of the dynamics. According to the Poincaré–Hopf theorem [27], any integrable motion confined to a finite phase-space region takes place on invariant f -tori. These are

f -dimensional manifolds with the topology of a product of f independent circles. Consequently, the constant value of the actions $\mathbf{J} = \mathbf{J}_0$ fixes the invariant torus in phase space, while the angles ϑ parametrize the motion along this torus. Without loss of generality they can be chosen $\vartheta_i \in [0, 2\pi)$.

To get an intuitive understanding of integrability, we consider the most popular and simple example, the harmonic oscillator with one degree of freedom, described by the Hamiltonian

$$H_{\text{ho}}(x, p_x) = \frac{p_x^2}{2m} + \frac{m\Omega^2}{2}(x - x_0)^2, \quad (2.17)$$

where m is the particle's mass, Ω is the oscillation frequency, and x_0 is the oscillation center. To simplify the analysis, we shift the spatial origin to x_0 and express time, distance and mass in units of Ω^{-1} , x_0 , and m , respectively. This leads to the rescaled Hamiltonian

$$H(q, p) = \frac{1}{2}(p^2 + q^2), \quad (2.18)$$

as a function of the dimensionless position $q = (x - x_0)/x_0$ and momentum $p = p_x/(mx_0\Omega)$. As shown in Fig. 2.3(b), the phase space of this system contains a central fixed point at $(q^*, p^*) = (0, 0)$, where the motion is stationary. This fixed point is enwrapped by a smooth family of one-dimensional, circular tori. The system is brought to action–angle coordinates using the canonical transformation

$$q(\vartheta, J) = \sqrt{2J} \cos \vartheta, \quad (2.19a)$$

$$p(\vartheta, J) = -\sqrt{2J} \sin \vartheta. \quad (2.19b)$$

Figure 2.3 illustrates how the angle ϑ parametrizes the motion on a torus, while the action J parametrizes the family of tori. The figure also indicates, that the action coordinate J of a torus equals the action integral (2.8) along this torus. This fact is true for any system with $f = 1$ degree of freedom and follows from the invariance of the action integral under T :

$$\mathcal{J}[\mathcal{C}] = \mathcal{J}[T^{-1}\mathcal{C}] = \frac{1}{2\pi} \oint_{T^{-1}\mathcal{C}} J \, d\vartheta = \frac{J}{2\pi} \int_0^{2\pi} d\vartheta = J. \quad (2.20)$$

Here \mathcal{C} denotes the positively oriented curve along the torus in the (q, p) -plane. It follows that even

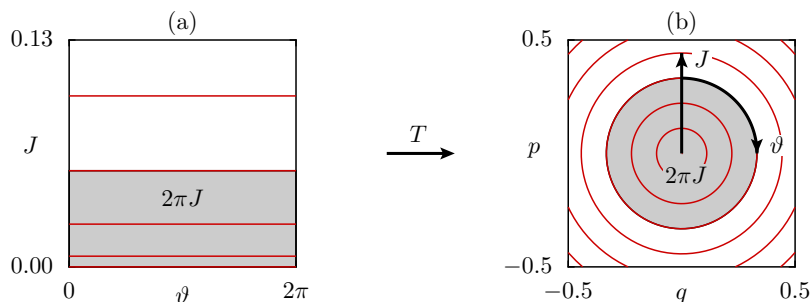


Figure 2.3.: Canonical transformation T from action–angle coordinates (a) to (q, p) -space (b) for the harmonic oscillator.

without explicit knowledge of the action–angle coordinates, the action coordinate of a torus is always accessible as its enclosed area divided by 2π .

To obtain the frequency function, we first insert the transformation T , Eq. (2.19) into Eq. (2.18) and find the Hamiltonian in action representation,

$$\mathcal{H}(J) = J. \quad (2.21)$$

With Eq. (2.14) the frequency function is $\omega(J) = 1$. The harmonic oscillator represents the trivial case of a globally constant frequency for all tori, see Fig. 2.4(a). Here the red arrows indicate the phase flow for a given timespan.

This example illustrates the importance of action–angle coordinates. They allow for a clean sepa-

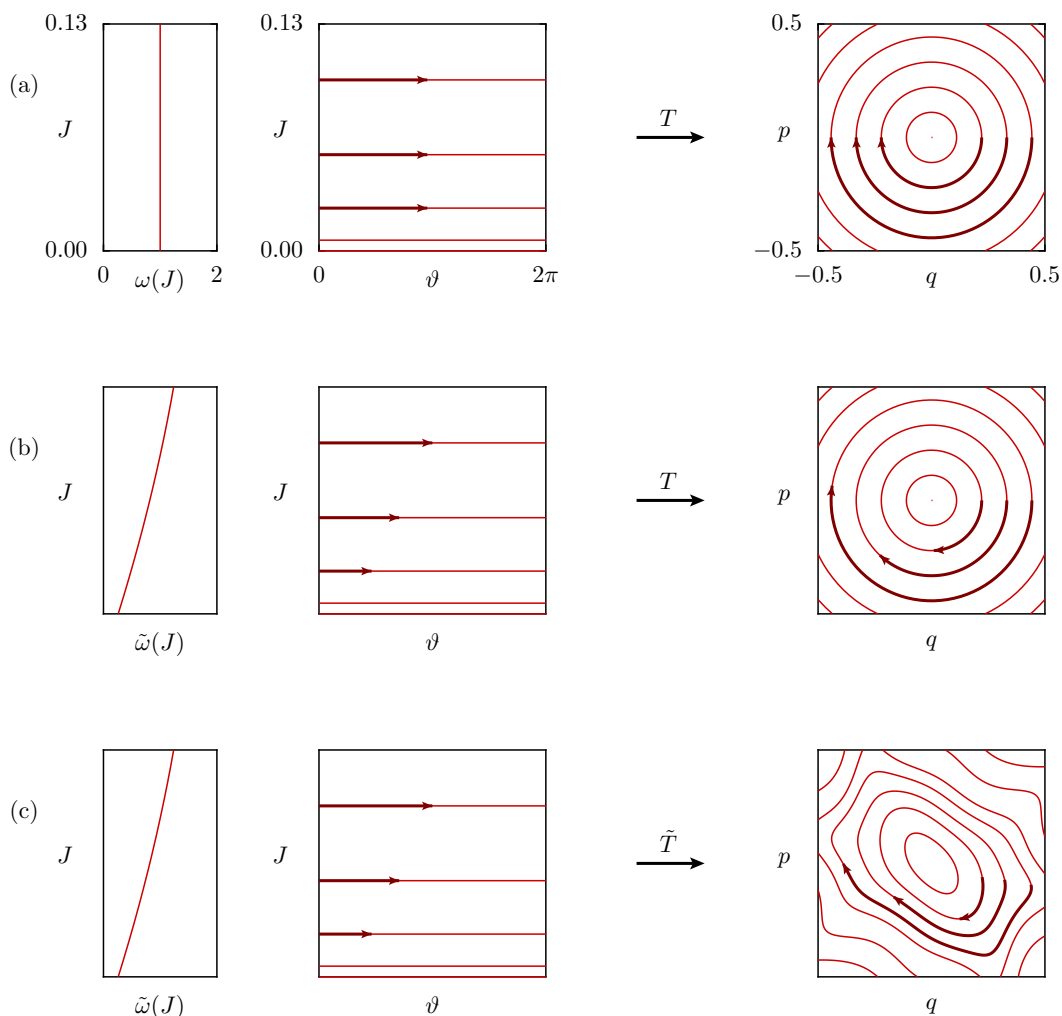


Figure 2.4.: (a) Illustration of the harmonic oscillator with constant frequency function $\omega(J)$ (left) and contour lines of the Hamiltonian in action–angle coordinates (center) and in the original phase-space coordinates (q, p) (right). Red arrows indicate the Hamiltonian flow for a given timespan $\Delta t = 3$. (b) Generalization of the previous system with a varying frequency function $\tilde{\omega}(J)$. (c) Generalization of the system from (b) with a different canonical transformation \tilde{T} .

ration of an integrable system into its two aspects frequency and shape, that are encoded in $\omega(J)$ and T , respectively. While $\omega(J)$ controls the frequency distribution over the tori, T generates their shape in the original phase-space coordinates (q, p) .

From this point of view, one can construct other integrable Hamiltonians by systematically changing either $\omega(J)$ or T . One could introduce, e. g., a new frequency function $\tilde{\omega}(J)$ by changing $\mathcal{H}(J)$. Combining this new action representation $\tilde{\mathcal{H}}(J)$ with the former transformation T produces a new Hamiltonian $\tilde{H}(q, p)$ with tori of the same shape but differently distributed frequencies, see Fig. 2.4(b). Finally, changing T to a different transformation \tilde{T} tunes the torus-geometry, see Fig. 2.4(c). This idea of constructing integrable systems due to a systematic, independent adjustment of $\omega(J)$ and T will become an important motif of this work.

In the following, we discuss the case $f = 2$. Here, we do not consider a concrete example system, but focus on the principal aspects of integrability in a 4D phase space. In this case two angles $\vartheta = (\vartheta_1, \vartheta_2)$ rotate with two constant frequencies $\omega(\mathbf{J}) = (\omega_1(\mathbf{J}), \omega_2(\mathbf{J}))$ according to Eq. (2.16a), as illustrated in Fig. 2.5(a). These angles parametrize the motion on a 2-torus, which is fixed by two actions $\mathbf{J} = (J_1, J_2)$. This 2-torus is a 2D manifold embedded in the 4D phase space. To visualize it, Fig. 2.5(b) shows a schematic projection into three dimensions.

If the two frequencies (ω_1, ω_2) of a given torus have a rational quotient, i. e. there exist $k_1, k_2 \in \mathbb{Z} \setminus \{0\}$ such that

$$k_1\omega_1 = k_2\omega_2, \quad (2.22)$$

the torus is called *resonant* and the motion is periodic, see Fig. 2.6(a) for an example. Otherwise, if the frequencies (ω_1, ω_2) have an irrational quotient, the torus is called *nonresonant*. The motion is quasiperiodic and densely fills out the torus, see Fig. 2.6(b). As the rational numbers \mathbb{Q} are dense in the real numbers \mathbb{R} , but still of measure zero, this also characterizes the distribution of resonant tori: The probability to randomly select such a resonant torus is zero, but still there exist infinitely many of them in an arbitrarily small phase-space region.

As introduced in Sec. 2.1.3, we now consider a 2D Poincaré section Σ in the 4D phase space. If Σ is chosen properly, its intersection with the 2-torus will be a 1-torus, i. e. a 1D closed curve, see Fig. 2.6.

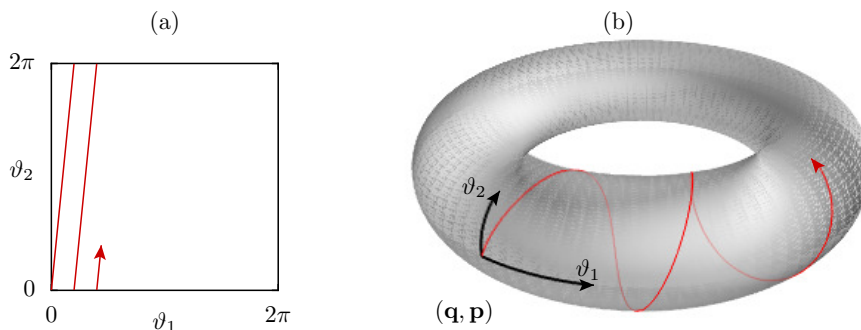


Figure 2.5.: Orbit of an integrable system (red line) in the $(\vartheta_1, \vartheta_2)$ -plane (a) and transformed to the phase-space coordinates (\mathbf{q}, \mathbf{p}) (b) with the corresponding torus (gray, schematic 3D projection)

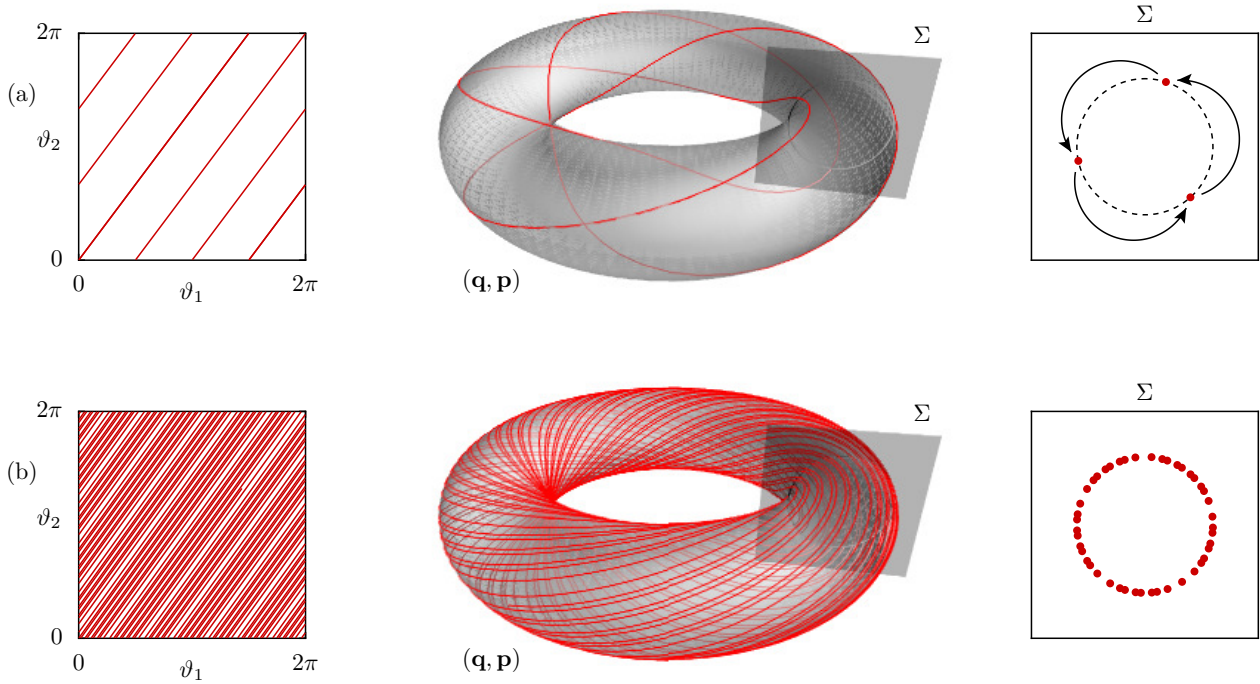


Figure 2.6.: Integrable dynamics on a resonant torus with frequencies $\omega_1/\omega_2 = 3/4$ (a) and on a nonresonant torus with frequencies $\omega_1/\omega_2 = 0.71817662680474015\dots$ (b). Each case is shown in the $(\vartheta_1, \vartheta_2)$ -plane (left), in the phase space coordinates (\mathbf{q}, \mathbf{p}) (center, schematic 3D projection), and in the Poincaré section Σ (right). Black arrows in (a) indicate the application of the Poincaré Map \mathcal{P} .

The time-continuous dynamics on the 2-torus is then reduced to the time-discrete dynamics on this 1-torus. Figure 2.6 illustrates the appearance of resonant and nonresonant dynamics in the Poincaré section. In the resonant case (2.22), the periodic motion of $H(\mathbf{q}, \mathbf{p})$ implies also a periodic orbit of \mathcal{P} . In the nonresonant case, the quasiperiodic motion of $H(\mathbf{q}, \mathbf{p})$ also implies a quasiperiodic orbit of \mathcal{P} , which densely fills the 1-torus.

Previously, we found the equality (2.20) between a torus' action coordinate and its action integral for $f = 1$. In the present situation $f = 2$, the action integral becomes ambiguous due to the free choice of the 1D integration curve \mathcal{C} on the 2-torus. In the following we explain the choice for \mathcal{C} which allows to generalize the equality (2.20). First, let \mathcal{C} be a closed curve on the torus with N_1 and N_2 rotations along the positive directions of ϑ_1 and ϑ_2 , respectively (Fig. 2.6(a) gives an example with $N_1 = 3, N_2 = 4$). The action integral along \mathcal{C} then evaluates to

$$\mathcal{J}[\mathcal{C}] = \mathcal{J}[T^{-1}\mathcal{C}] = \frac{1}{2\pi} \oint_{T^{-1}\mathcal{C}} \mathbf{J} d\boldsymbol{\vartheta} = \frac{1}{2\pi} \oint_{T^{-1}\mathcal{C}} (J_1 d\vartheta_1 + J_2 d\vartheta_2) \quad (2.23)$$

$$= \frac{1}{2\pi} \left(\oint_{T^{-1}\mathcal{C}|_1} J_1 d\vartheta_1 + \oint_{T^{-1}\mathcal{C}|_2} J_2 d\vartheta_2 \right) = \mathcal{J}[T^{-1}\mathcal{C}|_1] + \mathcal{J}[T^{-1}\mathcal{C}|_2]. \quad (2.24)$$

Here $T^{-1}\mathcal{C}|_i$ is the preimage of \mathcal{C} under T , projected to the (ϑ_i, J_i) -plane. As this projection represents

N_i rotations along ϑ_i , while J_i is constant on the torus, we find

$$\mathcal{J} [T^{-1}\mathcal{C}|_i] = \frac{1}{2\pi} \oint_{T^{-1}\mathcal{C}|_i} J_i d\vartheta_i = \frac{J_i}{2\pi} \int_0^{2\pi N_i} d\vartheta_i = N_i J_i, \quad (2.25)$$

and finally obtain the result

$$\mathcal{J} [\mathcal{C}] = N_1 J_1 + N_2 J_2. \quad (2.26)$$

The action integral just “counts” the rotations of \mathcal{C} along the angular directions, but ignores its concrete shape. Therefore, the actions J_i can be “measured” as integrals $\mathcal{J} [\mathcal{C}_i]$ along two fundamental loops $(\mathcal{C}_1, \mathcal{C}_2)$ on the torus, such that \mathcal{C}_i has one rotation along ϑ_i and zero rotations along the other angle, see Fig. 2.7. It is important to note, that the decomposition (2.26) of the action integral depends on the choice of the action–angle coordinates $(\boldsymbol{\vartheta}, \mathbf{J})$. Using a different set of angles $\boldsymbol{\vartheta}'$ would also lead to new actions \mathbf{J}' of the same torus and different rotation numbers N'_i while keeping $N'_1 J'_1 + N'_2 J'_2$ constant. Depending on the situation, this has two consequences. If the action–angle coordinates are known, the fundamental loops \mathcal{C}_i have to be *chosen* accordingly, such that

$$\mathcal{J} [\mathcal{C}_i] = J_i. \quad (2.27)$$

On the other hand, if the action–angle coordinates are unknown, they have to be *defined* according to Eq. (2.27) by choosing *any* pair of topologically independent, closed curves \mathcal{C}_i on the torus.

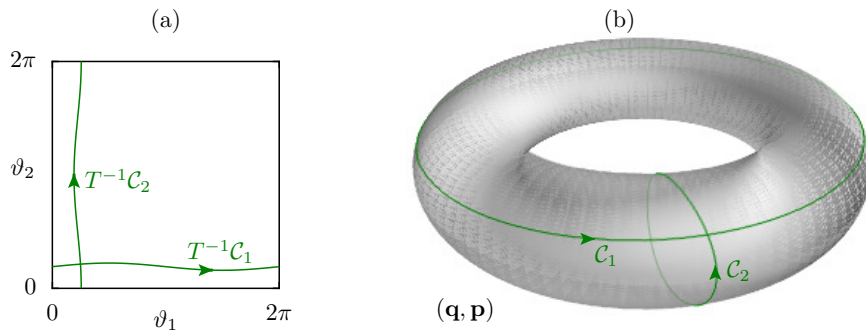


Figure 2.7.: Two fundamental loops $\mathcal{C}_1, \mathcal{C}_2$ in the $(\vartheta_1, \vartheta_2)$ -plane (a) and in the phase-space coordinates (\mathbf{q}, \mathbf{p}) (b) (schematic 3D projection).

2.3. Non-integrable systems

As mentioned in Sec. 2.2, integrable systems are rather special as they have the maximum number of constants of motion. In contrast to this, typical Hamiltonian systems are non-integrable [1]. As we show in the following, this leads to the coexistence of regular and chaotic motion in phase space.

Commonly, non-integrable systems are considered as perturbed integrable systems, i. e.

$$H = H_0 + \epsilon V, \quad (2.28)$$

where H_0 is integrable. This allows to study the geometrical modifications in phase space with increasing perturbation strength ϵ , starting from the known integrable case $\epsilon = 0$. For small perturbations, $|\epsilon| \ll 1$, the system is called *near-integrable* and allows for a perturbative treatment in ϵ . Here, two general theorems apply independently of H_0 and V . First, the Kolmogorov–Arnold–Moser (KAM) theorem [28–31] states, that almost all tori of H_0 are only deformed by the perturbation, but keep their topology. Here, no statement is made about the tori, which are in some sense “close” to resonant tori. This region is described by the Poincaré–Birkhoff theorem [32, 33], which states, that the resonant tori of H_0 are the first tori to break up under the perturbation. Following a universal mechanism, their collapse leaves a set of isolated, regular sub-regions. In its original version, the theorem only holds for symplectic 2D maps, where the set of regular sub-regions is geometrically well-understood. It is called a *nonlinear resonance chain* and discussed below. Typically these nonlinear resonance chains are surrounded by thin layers of chaotic motion. Although higher-dimensional generalizations of the Poincaré–Birkhoff theorem exist [34], getting a geometrical intuition is less trivial.

As the perturbation is increased towards $|\epsilon| \sim 1$, the system is called *mixed*. Here the chaotic regions which originated from the nonlinear resonance chains, have grown to reach about the same size as the regular regions.

At this point it should be mentioned, that the distinction of non-integrable systems into near-integrable ($|\epsilon| \ll 1$) and mixed systems ($|\epsilon| \sim 1$) might not be sharp, but matters. Residing beyond the breakdown of perturbation theory, mixed systems are technically more challenging, but also comprise new physical phenomena, e. g., regarding their diffusion behavior [35], their tunneling mechanisms [36–38], and their characteristic level statistics [39, 40].

In the following we illustrate the nonlinear phase-space structures using a paradigmatic example given by the standard map, Eq. (4.4). This time-discrete system represents a Poincaré map of a non-integrable system, where the perturbation strength is given by $\epsilon = \kappa$. Here we shall focus on the geometry of this system and shift its physical discussion to Sec. 4.1. The near-integrable case is illustrated in Fig. 2.8(a) for $\epsilon = 0.5$. In agreement to the KAM theorem, the phase space appears integrable, mainly consisting of regular tori (black lines in Fig. 2.8(a)), to which the orbits are confined. These tori surround a fixed point of the map at $(q^*, p^*) = (0.5, 0)$. However, a closer look reveals nonlinear resonances, as predicted by the Poincaré–Birkhoff theorem. As an example, the green lines in Fig. 2.8(a) show a nonlinear resonance chain which consists of 18 regular sub-regions. The central points of these sub-regions form a periodic orbit of the map (green dots). The nonlinear resonance

chain is surrounded by a new type of orbits (black dots) which turn out to be chaotic. In contrast to the regular orbits, these chaotic orbits occupy a 2D region in the (q, p) -plane.

The mixed case is illustrated in Fig. 2.8(b) for $\epsilon = 1.25$. This situation is often described by the picture of so-called *regular islands* which are embedded into a *chaotic sea*. However, this picture should not be taken too literally, as the composition of regular and chaotic regions is more complicated. As the resonant tori of the integrable system H_0 are dense in phase space, also the nonlinear resonance chains, which have emerged from these tori, can densely fill out the regular regions. Thus the regular island can be imagined similar to an integrable region, but densely interspersed with nonlinear resonance chains and chaotic layers on arbitrarily small scales. There is still a large set of remnant tori, but due to their dense interspersion, they do not form a smooth family. This is shown by a sequence of magnifications in Fig. 2.9(a).

For time-discrete systems with $f = 1$ degree of freedom, the nonlinear resonance chains can be classified by a tuple $(r:s)$ where r is the total number of sub-regions and s is the number of sub-regions which are surpassed in clockwise direction when the map is applied. Consequently, the central periodic orbit of such an $r:s$ -resonance then has a resonance frequency

$$\Omega_{r:s} = 2\pi \frac{s}{r}. \quad (2.29)$$

These nonlinear resonance chains also have an impact on the frequency function $\omega(J)$. As the system is non-integrable, the frequency function cannot be defined by Eq. (2.14). However, one can still define

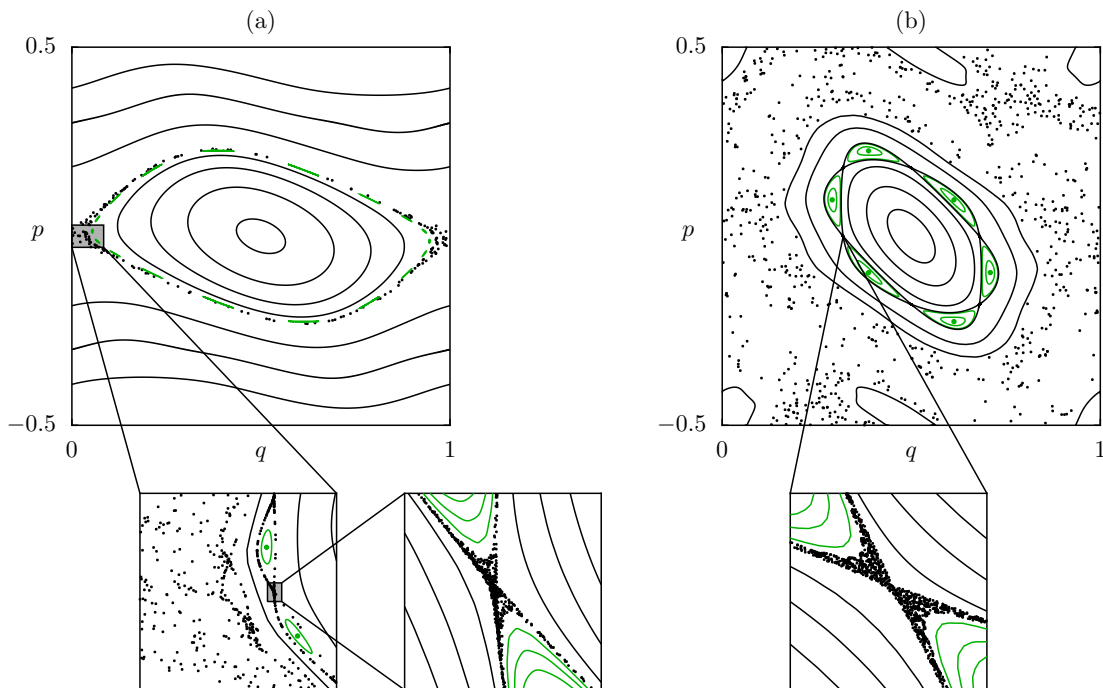


Figure 2.8.: Phase space of the standard map (4.4) with non-integrability parameter $\epsilon = \kappa$ for the near-integrable case $\epsilon = 0.5$ (a) and for the mixed case $\epsilon = 1.25$ (b). Shown are regular orbits (black lines) with nonlinear resonance chains (green lines) and chaotic orbits (black dots).

the action and main frequency of individual, remaining tori and compute them numerically. This data is shown in Fig. 2.9(b) for the main regular island of the system (for its practical computation we refer to Sec. 4.2). Each point (J, ω) in the plot corresponds to a torus of action J with a mean frequency ω . The action parametrizes the tori, starting near the center of the island at $J = 0$ and approaching larger tori for increasing J . The upper plot shows a gap of the frequency function around $J = 0.02$ caused by the dominant 6:1-resonance. Asymptotically, at this gap $\omega(J)$ approaches the resonance frequency $\Omega_{6:1} = 2\pi\frac{1}{6}$ with an infinite slope. As the action of a torus is proportional to its area, the gap's width is $A_{r:s}/(2\pi)$ where $A_{r:s}$ is the area occupied by the resonance. Inside this gap tori which encircle the central fixed point do not exist and thus action and frequency are not defined. However, there are more such gaps, which become visible on finer scales, as shown by the magnifications. Consequently,

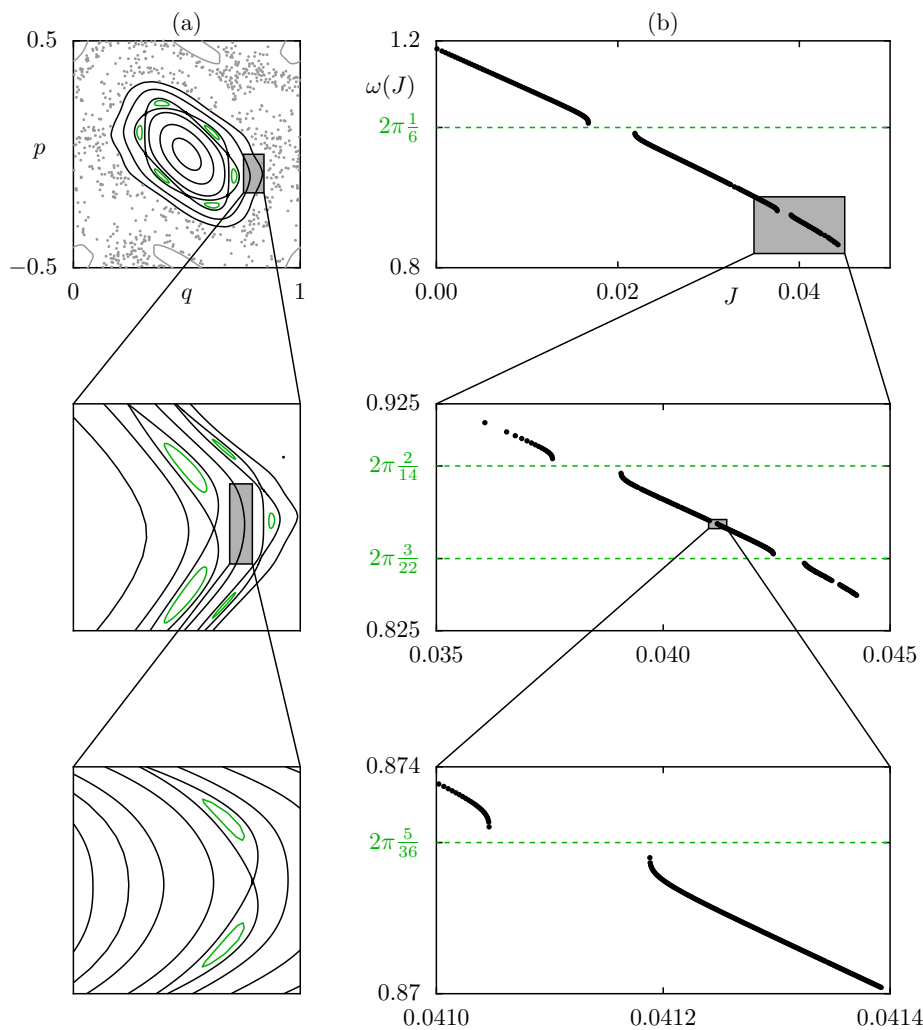


Figure 2.9.: (a) Phase space of the standard map (4.4) for $\kappa = 1.25$ with regular (lines) and chaotic orbits (dots). The magnifications demonstrate the existence of nonlinear resonance chains (green) on small scales. The shown resonance chains are of the type 6:1 (top), 14:2 and 3:22 (center), and 5:36 (bottom). (b) The frequency function $\omega(J)$ (black dots) for the tori, shown in (a) with the corresponding magnifications and the resonance frequencies $\Omega_{r:s} = 2\pi\frac{s}{r}$ of the $r:s$ -resonances (dashed green lines).

in any phase-space region there are gaps where the action J is undefined, as in any frequency interval (ω_a, ω_b) there are resonant frequencies with $\Omega_{r:s}/(2\pi) = \frac{s}{r} \in \mathbb{Q}$. Likewise, the frequency function appears smooth on a rough scale, but is interrupted by infinitely many gaps which occur on small scales and are distributed densely.

2.4. Integrable approximations

We close this chapter by stating the basic problem of this thesis, which is the construction of an *integrable approximation* for a given, mixed *target system*. Such an integrable approximation should mimic the dynamics of the target system in a given regular region as good as possible. More explicitly, for any torus of the target system with action \mathbf{J} (i) there should exist a corresponding torus of the integrable approximation with the same action \mathbf{J} and (ii) the dynamics on this integrable torus should approximate the dynamics on the target torus as closely as possible. Furthermore, the integrable approximation should interpolate through the nonlinear resonance chains of the target system and extrapolate its tori beyond the regular region. An example of such an integrable approximation is shown in Fig. 1.1(b), where the target system is given by the standard map, Fig. 1.1(a). Typically, only one particular region of the target system is modeled by the integrable approximation, which we refer to as the *target region*.

If the target system is given by a time-continuous Hamiltonian system H , its integrable approximation will be denoted by H_{reg} . If the target system is given by a symplectic map \mathcal{M} , the integrable approximation only needs to mimic its dynamics at discrete times. However, for a consistent description we also consider a time-continuous integrable approximation H_{reg} here, keeping in mind that its solutions are only relevant at integer times $t \in \mathbb{N}_0$. Thus the corresponding time-discrete integrable approximation would be the unit-time phase flow $\mathcal{U}_{\text{reg}}^1$ of H_{reg} .

3. Iterative canonical transformation method

In this chapter we introduce the *iterative canonical transformation method* for the construction of integrable approximations, which is one major result of this thesis and covered in Ref. [41]. First, we outline the basic idea of the method and its decomposition into two steps (Sec. 3.1), which we present afterwards (Secs. 3.2 and 3.3). Finally, we give an algorithmic overview (Sec. 3.4). While this chapter focuses on a formal presentation of the method, its illustration is shifted to its application in Ch. 4.2.

3.1. Basic idea

In the following we consider a given target system $H(\mathbf{q}, \mathbf{p})$ with f degrees of freedom. Although the following description remains valid, when choosing a symplectic map \mathcal{M} as target system, we will always denote the target system as $H(\mathbf{q}, \mathbf{p})$, to simplify our terminology. We assume $H(\mathbf{q}, \mathbf{p})$ to have a mixed phase space, where we consider a particular regular target region in phase space. This target region consists of f -tori, which are interspersed with other phase-space structures, such as chaotic layers and nonlinear resonance chains. Our goal is to construct an integrable approximation $H_{\text{reg}}(\mathbf{q}, \mathbf{p})$ which resembles the motion along the tori in this target region. Following Sec. 2.2, the integrable approximation $H_{\text{reg}}(\mathbf{q}, \mathbf{p})$ is represented by a tuple $(\boldsymbol{\omega}(\mathbf{J}), T)$ of its frequency function $\boldsymbol{\omega}(\mathbf{J})$ and the canonical transformation T , that translates the action–angle coordinates $(\boldsymbol{\vartheta}, \mathbf{J})$ to the original phase-space coordinates (\mathbf{q}, \mathbf{p}) . These two components $(\boldsymbol{\omega}(\mathbf{J}), T)$ completely define $H_{\text{reg}}(\mathbf{q}, \mathbf{p})$ and reflect its properties frequency and shape.

From this perspective, the integrable approximation $H_{\text{reg}}(\mathbf{q}, \mathbf{p})$ is constructed in two steps. We first construct the integrable approximation in action representation $\mathcal{H}_{\text{reg}}(\mathbf{J})$, which fixes the frequency function $\boldsymbol{\omega}(\mathbf{J})$ (*frequency approximation*). Secondly, we construct the transformation T to the original phase-space coordinates (\mathbf{q}, \mathbf{p}) , which generates the shape of the tori and fixes the final Hamiltonian $H_{\text{reg}}(\mathbf{q}, \mathbf{p})$ (*shape approximation*). These two steps are explained in the following two sections.

3.2. Frequency approximation

This section describes the first step of the iterative canonical transformation method, which is the construction of an integrable approximation in action representation $\mathcal{H}_{\text{reg}}(\mathbf{J})$. We obtain $\mathcal{H}_{\text{reg}}(\mathbf{J})$ from the actions of the tori in the target region of $H(\mathbf{q}, \mathbf{p})$. For this we choose a large, discrete sample of initial conditions $(\mathbf{q}_0^\tau, \mathbf{p}_0^\tau)$ on different tori τ . Using Eq. (2.1) we evolve each initial condition to a

long, discrete sample of times t_ℓ to obtain the sample points

$$\mathbf{x}_\ell^\tau = \mathcal{U}^{t_\ell}(\mathbf{q}_0^\tau, \mathbf{p}_0^\tau). \quad (3.1)$$

Here the index τ labels the tori, while the index ℓ describes the motion along these tori.

From each trajectory \mathbf{x}_ℓ^τ we numerically compute the actions \mathbf{J}^τ and the frequencies $\boldsymbol{\omega}^\tau$ of the torus τ . The actions $\mathbf{J}^\tau = (J_1^\tau, \dots, J_f^\tau)$ are determined by choosing a set of f fundamental loops \mathcal{C}_i on the torus τ (see Sec. 2.2) and evaluating the action integral (2.8) along these loops, which gives

$$J_i^\tau = \mathcal{J}[\mathcal{C}_i]. \quad (3.2)$$

The frequencies $\boldsymbol{\omega}^\tau = (\omega_1^\tau, \dots, \omega_f^\tau)$ are defined by the Fourier expansion of the trajectories

$$\mathbf{x}_\ell^\tau = \sum_{\mathbf{k} \in \mathbb{Z}^f} \mathbf{c}_{\mathbf{k}}^\tau e^{i\mathbf{k}\boldsymbol{\omega}^\tau t_\ell}. \quad (3.3)$$

Practically the computation of the actions \mathbf{J}^τ and the frequencies $\boldsymbol{\omega}^\tau$ based on Eqs. (3.2) and (3.3) is realized very differently depending on the number f of degrees of freedom. Explicit examples for $f = 1, 2$ are given in Secs. 4.2 and 5.4, respectively.

We now express $\mathcal{H}_{\text{reg}}(\mathbf{J})$ by a series expansion

$$\mathcal{H}_{\text{reg}}(\mathbf{J}) = \sum_{k_1=0}^{\mathcal{K}_1} \dots \sum_{k_f=0}^{\mathcal{K}_f} h_{k_1 \dots k_f} \mathcal{F}_{k_1 \dots k_f}(\mathbf{J}). \quad (3.4)$$

Practically this could be, e. g., a power series expansion $\mathcal{F}_{k_1 \dots k_f}(\mathbf{J}) = J_1^{k_1} \dots J_f^{k_f}$. Based on the data $(\mathbf{J}^\tau, \boldsymbol{\omega}^\tau)$, we determine the coefficients $h_{k_1 \dots k_f}$ of this expansion by minimizing

$$\chi^2(h) = \sum_{\tau} |\boldsymbol{\omega}^\tau - \boldsymbol{\omega}(\mathbf{J}^\tau)|^2 \quad (3.5a)$$

$$= \sum_{\tau} \sum_{i=1}^f \left| \omega_i^\tau - \frac{\partial \mathcal{H}_{\text{reg}}}{\partial J_i}(\mathbf{J}^\tau) \right|^2. \quad (3.5b)$$

In order to smoothly interpolate through zones of nonlinear resonance chains, tori close to them have to be excluded. If the target system is a time-continuous Hamiltonian system, another strategy is possible to determine the coefficients $h_{k_1 \dots k_f}$ by computing the energy of each torus as

$$E^\tau = H(\mathbf{q}_0^\tau, \mathbf{p}_0^\tau), \quad (3.6)$$

and minimizing

$$\chi^2(h) = \sum_{\tau} |E^\tau - \mathcal{H}_{\text{reg}}(\mathbf{J}^\tau)|^2. \quad (3.7)$$

This ensures, that corresponding pairs of tori from $\mathcal{H}_{\text{reg}}(\mathbf{J})$ and $H(\mathbf{q}, \mathbf{p})$ have the same energy. This also determines the frequency function $\boldsymbol{\omega}(\mathbf{J}) = \partial\mathcal{H}_{\text{reg}}(\mathbf{J})/\partial\mathbf{J}$ which characterizes the slope of energy perpendicular to the torus surfaces. Thereby, this minimization is equivalent to Eq. (3.5) but more convenient, as less terms are summed.

3.3. Shape approximation

This section describes the second step of the iterative canonical transformation method, which is the construction of the canonical transformation T , leading to the integrable approximation $H_{\text{reg}}(\mathbf{q}, \mathbf{p})$ in the original phase-space coordinates (\mathbf{q}, \mathbf{p}) of the target system $H(\mathbf{q}, \mathbf{p})$. Here T is not determined in one step, but is decomposed into a sequence of canonical transformations (T_0, T_1, T_2, \dots) . In Sec. 3.3.1 we use an initial canonical transformation T_0 leading to an initial integrable approximation $H_{\text{reg}}^0(\mathbf{q}, \mathbf{p})$. In Sec. 3.3.2 we introduce a family of canonical transformations. In Sec. 3.3.3 we use a cost function to iteratively select the optimal transformations (T_1, T_2, \dots) as members of the family, which successively improves the integrable approximation.

3.3.1. Initial integrable approximation

Starting from $\mathcal{H}_{\text{reg}}(\mathbf{J})$, we choose a simple, first-guess canonical transformation

$$T_0 : \quad (\boldsymbol{\vartheta}, \mathbf{J}) \mapsto (\mathbf{q}, \mathbf{p}), \quad (3.8)$$

which maps the tori of $\mathcal{H}_{\text{reg}}(\mathbf{J})$ to the neighborhood of the corresponding tori of $H(\mathbf{q}, \mathbf{p})$ with the same action \mathbf{J} such that they have the same topology and roughly the same shape. This canonical transformation leads to the *initial integrable approximation*

$$H_{\text{reg}}^0(\mathbf{q}, \mathbf{p}) = \mathcal{H}_{\text{reg}}(\mathbf{J}(\mathbf{q}, \mathbf{p})). \quad (3.9)$$

The transformation T_0 can be determined, e. g., from the linearized dynamics of $H(\mathbf{q}, \mathbf{p})$ at the center of the island. Explicit examples are given in Secs. 4.2 and 5.4.

3.3.2. Family of canonical transformations

We define a family of canonical transformations $\{T^{\mathbf{a}}\}$ whose members $T^{\mathbf{a}}$ are parametrized by a vector $\mathbf{a} = (a_1, \dots, a_{\mathcal{N}}) \in \mathbb{R}^{\mathcal{N}}$. This is realized using a second-type generating function of the form

$$F^{\mathbf{a}}(\mathbf{q}, \mathbf{p}') = \sum_{i=1}^f q_i p'_i + \sum_{\nu=1}^{\mathcal{N}} a_{\nu} G_{\nu}(\mathbf{q}, \mathbf{p}'). \quad (3.10)$$

The concrete family of transformations follows from the \mathcal{N} independent basis functions G_{ν} , whose particular choice depends on the considered target system and should account for its symmetries and periodicities. For examples see Secs. 4.2 and 5.4.

The canonical transformation $T^{\mathbf{a}}$ is then implicitly defined by the set of Eqs. (2.9), which take the form

$$\mathbf{q}' = \mathbf{q} + \sum_{\nu=1}^{\mathcal{N}} a_{\nu} \frac{\partial G_{\nu}}{\partial \mathbf{p}'}(\mathbf{q}, \mathbf{p}'), \quad (3.11a)$$

$$\mathbf{p} = \mathbf{p}' + \sum_{\nu=1}^{\mathcal{N}} a_{\nu} \frac{\partial G_{\nu}}{\partial \mathbf{q}}(\mathbf{q}, \mathbf{p}'). \quad (3.11b)$$

For $\mathbf{a} = \mathbf{0}$ one obtains the identity transformation. As the dynamics of H_{reg}^0 and H roughly agree, we consider only near-identity transformations to improve H_{reg}^0 assuming

$$|\mathbf{a}| \ll 1. \quad (3.12)$$

As we discuss in Sec. 4.3.1, this restriction ensures the global existence of a unique solution for the implicit Eqs. (3.11). Moreover, it allows to solve Eqs. (3.11) for $(\mathbf{q}', \mathbf{p}')$ in orders of \mathbf{a} , e. g., in first order one obtains

$$\mathbf{q}'_{\mathbf{a}}(\mathbf{q}, \mathbf{p}) = \mathbf{q} + \sum_{\nu=1}^{\mathcal{N}} a_{\nu} \frac{\partial G_{\nu}}{\partial \mathbf{p}}(\mathbf{q}, \mathbf{p}) + \mathcal{O}(|\mathbf{a}|^2), \quad (3.13a)$$

$$\mathbf{p}'_{\mathbf{a}}(\mathbf{q}, \mathbf{p}) = \mathbf{p} - \sum_{\nu=1}^{\mathcal{N}} a_{\nu} \frac{\partial G_{\nu}}{\partial \mathbf{q}}(\mathbf{q}, \mathbf{p}) + \mathcal{O}(|\mathbf{a}|^2). \quad (3.13b)$$

3.3.3. Iterative improvement

We now use the family of canonical transformations $\{T^{\mathbf{a}}\}$ to improve the agreement between the initial integrable approximation H_{reg}^0 , Eq. (3.9), and the target region of H . In principle it is tempting, to find a canonical transformation $T^{\mathbf{a}}$ leading to a new Hamiltonian which shows maximal agreement with the regular phase-space region of H . However, finding this optimal transformation, e. g., by using an infinite number of coefficients in Eqs. (3.10) is practically impossible. Therefore, we fix the number \mathcal{N} of coefficients, but use multiple transformations. This idea seems promising, as the family of canonical transformations does not form a group, i. e., $T^{\mathbf{a}} \circ T^{\mathbf{a}'} \neq T^{\mathbf{a}+\mathbf{a}'}$. Using such compositions effectively gives access to a larger class of transformations without increasing \mathcal{N} .

Subsequently we use a member from the family $\{T^{\mathbf{a}}\}$ to iteratively improve the agreement between the integrable approximation and the regular phase-space region of H . This gives a sequence of canonical transformations

$$T_n : (\mathbf{q}, \mathbf{p}) \mapsto (\mathbf{q}', \mathbf{p}'), \quad n = 1, \dots, N, \quad (3.14)$$

such that the n th integrable approximation

$$H_{\text{reg}}^n(\mathbf{q}, \mathbf{p}) = H_{\text{reg}}^0(T_1^{-1} \circ \dots \circ T_n^{-1}(\mathbf{q}, \mathbf{p})), \quad (3.15)$$

agrees more and more with the regular phase-space region of H when n is increased. Starting with H_{reg}^0 , this generates a sequence of integrable approximations

$$H_{\text{reg}}^0 \mapsto H_{\text{reg}}^1 \mapsto \dots \mapsto H_{\text{reg}}^N. \quad (3.16)$$

In the following we explain one iteration step, which is the selection of an optimal canonical transformation $T_{n+1} \in \{T^{\mathbf{a}}\}$ to improve H_{reg}^n . For this, T_{n+1} has to minimize the distance of points with corresponding action–angle coordinates in H_{reg}^n and H . To achieve this we define the corresponding sample points and set up a cost function to minimize their distance.

Sample points

Using Eq. (3.1), we obtain the sample points \mathbf{x}_ℓ^τ of H , which correspond to actions \mathbf{J}^τ and angles

$$\boldsymbol{\vartheta}_\ell^\tau = \boldsymbol{\vartheta}_0^\tau + \boldsymbol{\omega}^\tau t_\ell. \quad (3.17)$$

Here, the initial angle $\boldsymbol{\vartheta}_0^\tau$ can be chosen freely. For the integrable approximation H_{reg}^n , we define the corresponding sample points as

$$\mathbf{x}_\ell^{\tau,n} = T_n \circ \dots \circ T_1 \circ T_0(\boldsymbol{\vartheta}_\ell^\tau, \mathbf{J}^\tau), \quad (3.18)$$

using the same actions \mathbf{J}^τ and angles $\boldsymbol{\vartheta}_\ell^\tau$ as for the points \mathbf{x}_ℓ^τ . It is convenient to choose the initial angles $\boldsymbol{\vartheta}_0^\tau$ from Eq. (3.17), such that the initial sample points $\mathbf{x}_0^{\tau,0}$ are closest to \mathbf{x}_0^τ .

Cost function

To minimize the distance between \mathbf{x}_ℓ^τ and $\mathbf{x}_\ell^{\tau,n}$ in the $(n+1)$ st iteration step, we apply the canonical transformation $T^{\mathbf{a}}$ and minimize the cost function

$$\mathcal{L}(\mathbf{a}) = \frac{1}{N_p} \sum_\tau \sum_\ell |\mathbf{x}_\ell^\tau - T^{\mathbf{a}}(\mathbf{x}_\ell^{\tau,n})|^2. \quad (3.19)$$

Here N_p is the total number of sample points. This cost function $\mathcal{L}(\mathbf{a})$ measures how well a particular transformation $T^{\mathbf{a}}$ would improve the integrable approximation H_{reg}^n . The best transformation $T^{\mathbf{a}_0}$ is given by the parameter \mathbf{a}_0 which minimizes $\mathcal{L}(\mathbf{a})$.

Principally, finding this minimum would be difficult, as \mathcal{L} is defined on a high-dimensional parameter space $\mathbf{a} \in \mathbb{R}^{\mathcal{N}}$. However, as the tori of H_{reg}^n and H roughly agree, we can expect the minimum to be close to the origin of parameter space. In this case, we can replace $T^{\mathbf{a}}$ in Eq. (3.19) by its linear approximation (3.13) leading to

$$\mathcal{L}(\mathbf{a}) \approx \mathcal{L}(\mathbf{0}) - \frac{2}{N_p} \sum_{\nu=1}^{\mathcal{N}} B_\nu a_\nu + \frac{1}{N_p} \sum_{\mu,\nu=1}^{\mathcal{N}} a_\mu C_{\mu\nu} a_\nu, \quad (3.20)$$

where the coefficients are given by

$$B_\nu = \sum_{\tau,\ell} (\mathbf{q}_\ell^\tau - \mathbf{q}_\ell^{\tau,n}) \frac{\partial G_\nu}{\partial \mathbf{p}} (\mathbf{q}_\ell^{\tau,n}, \mathbf{p}_\ell^{\tau,n}) - \sum_{\tau,\ell} (\mathbf{p}_\ell^\tau - \mathbf{p}_\ell^{\tau,n}) \frac{\partial G_\nu}{\partial \mathbf{q}} (\mathbf{q}_\ell^{\tau,n}, \mathbf{p}_\ell^{\tau,n}), \quad (3.21a)$$

$$C_{\mu\nu} = \sum_{\tau,\ell} \frac{\partial G_\mu}{\partial \mathbf{p}} (\mathbf{q}_\ell^{\tau,n}, \mathbf{p}_\ell^{\tau,n}) \frac{\partial G_\nu}{\partial \mathbf{p}} (\mathbf{q}_\ell^{\tau,n}, \mathbf{p}_\ell^{\tau,n}) + \sum_{\tau,\ell} \frac{\partial G_\mu}{\partial \mathbf{q}} (\mathbf{q}_\ell^{\tau,n}, \mathbf{p}_\ell^{\tau,n}) \frac{\partial G_\nu}{\partial \mathbf{q}} (\mathbf{q}_\ell^{\tau,n}, \mathbf{p}_\ell^{\tau,n}), \quad (3.21b)$$

as derived in App. A.

The optimal parameter is the solution of the extremal condition $\partial \mathcal{L} / \partial \mathbf{a} = \mathbf{0}$, which under the approximation (3.20) obtains the linear form

$$\sum_{\nu=1}^{\mathcal{N}} C_{\mu\nu} a_\nu = B_\mu. \quad (3.22)$$

Solving this linear system of equations gives an estimate \mathbf{a}^* for the true minimum of $\mathcal{L}(\mathbf{a})$. For this parameter \mathbf{a}^* one solves the canonical transformation (3.11) numerically using Newton's method. If for this parameter \mathbf{a}^* Eq. (3.11) is not invertible on the relevant domain of phase-space, we rescale it according to

$$\mathbf{a}^* \mapsto \eta \mathbf{a}^*, \quad (3.23)$$

using a *damping factor* $\eta \in (0, 1)$. This is possible as $\mathcal{L}(\mathbf{a}^*) \leq \mathcal{L}(\eta \mathbf{a}^*) \leq \mathcal{L}(\mathbf{0})$, but requires to increase the number N of iteration steps by a factor of $1/\eta$. A detailed discussion of this damping mechanism is given in Sec. 4.3.

Finally, we obtain the transformation $T_{n+1} = T^{\mathbf{a}^*}$ leading to an improved integrable approximation H_{reg}^{n+1} of H , Eq. (3.15). Typically, after a finite number N of iterations, the cost function saturates and one can stop the iterative process. This leads to the final integrable approximation H_{reg}^N of H . Note that H_{reg}^N is not given in a closed form, as the transformations T_n^{-1} in Eq. (3.15) have to be evaluated numerically from Eqs. (3.11). However, in App. B we discuss, how such a closed form can be derived in principle.

3.4. Overview

In order to summarize this section, we give an algorithmic overview of the iterative canonical transformation method.

1. For a chosen set of tori τ of H , compute the actions \mathbf{J}^τ and frequencies $\boldsymbol{\omega}^\tau$.
2. Determine $\mathcal{H}_{\text{reg}}(\mathbf{J})$ by minimizing Eq. (3.5) or (3.7).
3. Define $H_{\text{reg}}^0(\mathbf{q}, \mathbf{p})$, Eq. (3.9), by choosing a simple transformation T_0 , Eq. (3.8), that roughly mimics the shape of the target tori τ .

4. For a chosen set of tori τ of H , determine a sample of points \mathbf{x}_ℓ^τ at times t_ℓ .
5. For $n = 0, 1, \dots, N - 1$:
 - a) Compute the points $\mathbf{x}_\ell^{\tau, n}$, Eq. (3.18). For $n > 0$ the transformation T_n is evaluated numerically using Eqs. (3.11).
 - b) Compute the coefficients B_ν and $C_{\mu\nu}$ of the cost function $\mathcal{L}(\mathbf{a})$, Eqs. (3.21).
 - c) Determine \mathbf{a}^* by solving Eq. (3.22) and possibly applying a damping, Eq. (3.23).
 - d) Set $T_{n+1} := T^{\mathbf{a}^*}$.
6. Determine H_{reg}^N with Eq. (3.15).

4. Integrable approximation of symplectic 2D maps

In this chapter, we apply the iterative canonical transformation method to symplectic 2D maps. Provided with a 2D intuition, we also explain general aspects of the method. First, we introduce a generic example system (Sec. 4.1) to which we apply the method (Sec. 4.2). Then, we discuss the damping mechanism (Sec. 4.3) and the method's high order asymptotics (Sec. 4.4). Furthermore, we give a comparison to alternative methods for constructing integrable approximations (Sec. 4.5). Finally, we adapt the iterative canonical transformation method to include a separatrix (Sec. 4.6) or a nonlinear resonance chain into the integrable approximation (Sec. 4.7).

4.1. Example system

A very simple class of non-integrable models is given by periodically time-dependent systems with $f = 1$ degree of freedom. These are systems with a Hamiltonian $H(q, p, t + \Theta) = H(q, p, t)$, where we choose the period $\Theta = 1$ without loss of generality. Especially convenient are so-called kicked systems, which are given by

$$H(q, p, t) = T(p) + V(q) \sum_{n \in \mathbb{Z}} \delta(t - n), \quad (4.1)$$

where $\delta(\cdot)$ denotes Dirac's delta-function, $T(p)$ is the kinetic energy, and $V(q)$ is a kicking potential that is switched on instantly at integer times. A popular example of a kicked system is the kicked rotor, which describes a pendulum that is impulsively exposed to gravity. Choosing appropriate units for the angular displacement q and its conjugated momentum p , this system is described by

$$T(p) = \frac{p^2}{2}, \quad (4.2a)$$

$$V(q) = \frac{\kappa}{2\pi} \cos(2\pi q). \quad (4.2b)$$

Here, the non-integrable force is controlled by the parameter of the kicking strength κ . The time evolution over a unit timestep from a state at time t to time $t + 1$ is given by a symplectic map

$$(q_{t+1}, p_{t+1}) = \mathcal{U}^{t,t+1}(q_t, p_t). \quad (4.3)$$

Due to the system's time-periodicity, this map only depends on the relative position of t to the driving period $\Theta = 1$, i. e. $\mathcal{U}^{t,t+1} = \mathcal{U}^{t_0}$ with $t_0 = (t \bmod 1)$.

Hence, the sequence of states in the (q, p) -plane at times $t_n = t_0 + n$ for $t_0 \in [0, 1)$ and $n \in \mathbb{N}_0$ is generated by the same symplectic map. In the limit of positive $t_0 \rightarrow 0+$, this map connects the states at times immediately after the kicks. It is called the *standard map* and given by

$$q_{n+1} = q_n + p_n, \quad (4.4a)$$

$$p_{n+1} = p_n + \frac{\kappa}{2\pi} \sin(2\pi(q_n + p_n)). \quad (4.4b)$$

In the following we consider this map on the (q, p) -plane $[0, 1) \times [-0.5, 0.5)$ with periodic boundary conditions. This map is a paradigmatic model for non-integrable systems. Its phase-space structures have been discussed in Sec. 2.3.

4.2. Application of the iterative canonical transformation method

We now apply the iterative canonical transformation method from Sec. 3 to symplectic 2D maps. Although we use only one example system, the following implementation is independent of this choice. Moreover, having a 2D phase space, this section allows for a simple illustration of the general ideas behind the method.

In the following we consider the standard map \mathcal{U}^1 given by Eqs. (4.4) on the phase-space $(q, p) \in [0, 1) \times [-0.5, 0.5)$ with periodic boundary conditions. For $\kappa \in (0, 4)$ this map has a stable fixed point at $(q^*, p^*) = (0.5, 0)$. We consider the standard map for $\kappa = 1.25$, see Fig. 2.8(b). The fixed point (q^*, p^*) is surrounded by an island of regular tori, which is embedded into a chaotic sea. We choose this regular island as our target region, for which we construct an integrable approximation $H_{\text{reg}}(q, p)$.

4.2.1. Frequency approximation

In this section we perform the frequency approximation as explained in Sec. 3.2. We first compute the sample points \mathbf{x}_ℓ^τ , Eq. (3.1). For this we choose a set of initial conditions on a line from the center of the regular island to its border (i. e. the outermost torus shown in Fig. 4.1(a)). Specifically, we use the points $(q_0^\tau, p_0^\tau) = (q^* + \frac{\tau}{60}\Delta q, p^*)$ with $\tau = 1, 2, \dots, 60$ and $\Delta q = 0.293$ (see the green line in Fig. 4.1(a)). For each initial condition, we compute 10^4 iterates by applying the map \mathcal{U}^1 . The resulting sample points \mathbf{x}_ℓ^τ are shown in Fig. 4.1(a) (black dots).

From these sample points \mathbf{x}_ℓ^τ on the tori τ , we compute the action J^τ and the frequency ω^τ . In the given case of a 2D phase space, the computation of the action J^τ from Eq. (3.2) is straightforward. Here, the choice of the fundamental loop \mathcal{C} on the torus becomes unambiguous and J^τ equals the area inside the torus τ divided by a factor of (2π) . We compute this action numerically from the sample points \mathbf{x}_ℓ^τ on the torus τ . The frequency ω^τ is computed from the points \mathbf{x}_ℓ^τ using the frequency map analysis [42, 43]. The resulting data (J^τ, ω^τ) is shown in Fig. 4.1(b) (black dots).

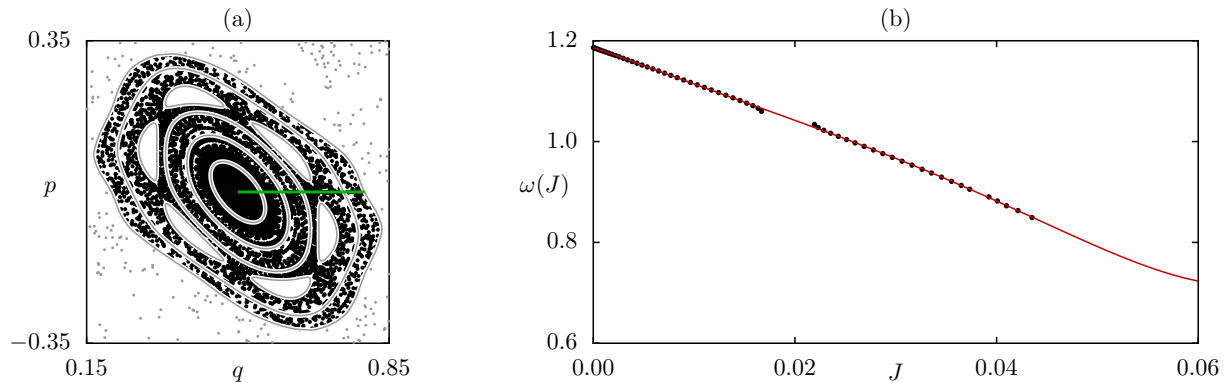


Figure 4.1.: (a) Phase space of the standard map (gray) with regular tori (lines), chaotic orbits (dots), and the sample points \mathbf{x}_ℓ^τ (black dots) used for the frequency approximation. (b) Numerically determined actions J^τ and frequencies ω^τ (black dots) fitted by Eq. (4.6) with $\mathcal{K} = 6$ (red line) and extrapolated beyond the boundary of the regular island.

For Eq. (3.4) we use the polynomial ansatz

$$\mathcal{H}_{\text{reg}}(J) = \sum_{k=0}^{\mathcal{K}} h_k J^k, \quad (4.5)$$

where we set $h_0 = 0$. This implies the frequency function

$$\omega(J) = \sum_{k=1}^{\mathcal{K}} k h_k J^{k-1}, \quad (4.6)$$

which we fit to the data (J^τ, ω^τ) by minimizing Eq. (3.5). Up to order $\mathcal{K} = 6$ (red curve in Fig. 4.1(b)) we find a significant improvement of the fit.

4.2.2. Shape approximation

In this section we perform the shape approximation as explained in Sec. 3.3.

Initial integrable approximation

To obtain $H_{\text{reg}}^0(q, p)$, we transform the dynamics of $\mathcal{H}_{\text{reg}}(J)$ to new coordinates (q, p) , according to the linearized dynamics of the symplectic map \mathcal{U}^1 around the fixed point (q^*, p^*) . This is realized by the transformation

$$T_0 : \begin{pmatrix} \vartheta \\ J \end{pmatrix} \mapsto \begin{pmatrix} q(\vartheta, J) \\ p(\vartheta, J) \end{pmatrix} = \begin{pmatrix} q^* \\ p^* \end{pmatrix} + \mathcal{R} \begin{pmatrix} \sqrt{2J} \cos \vartheta \\ -\sqrt{2J} \sin \vartheta \end{pmatrix}, \quad (4.7)$$

where

$$\mathcal{R} = \begin{pmatrix} \cos \beta & -\sin \beta \\ \sin \beta & \cos \beta \end{pmatrix} \begin{pmatrix} 1/\sqrt{\sigma} & 0 \\ 0 & \sqrt{\sigma} \end{pmatrix}. \quad (4.8)$$

This transformation generates elliptic tori centered around (q^*, p^*) with a tilting angle β and an axial ratio σ as shown by the red lines in Fig. 4.2(a). It includes the transformation (2.19) given by $\beta = 0$ and $\sigma = 1$ such that $\mathcal{R} = \mathbf{1}$. In general, β and σ are properties of the linearized dynamics of \mathcal{U}^1 and can be determined as [22, Sec. 3.3b]

$$\tan 2\beta = \frac{M_{11} - M_{22}}{M_{12} + M_{21}}, \quad (4.9)$$

$$\sigma^2 = \frac{|M_{12} - M_{21}| - c}{|M_{12} - M_{21}| + c}, \quad (4.10)$$

with

$$c = \sqrt{(M_{12} + M_{21})^2 + (M_{22} - M_{11})^2}. \quad (4.11)$$

Here M is the monodromy matrix of the standard map \mathcal{U}^1 at the stable fixed point (q^*, p^*) ,

$$M = \left(\begin{array}{cc} \frac{\partial q_{n+1}}{\partial q_n} & \frac{\partial q_{n+1}}{\partial p_n} \\ \frac{\partial p_{n+1}}{\partial q_n} & \frac{\partial p_{n+1}}{\partial p_n} \end{array} \right) \Big|_{(q^*, p^*)} = \begin{pmatrix} 1 & 1 \\ -\kappa & 1 - \kappa \end{pmatrix}. \quad (4.12)$$

The inverted transformation T_0^{-1} generates the Hamiltonian $H_{\text{reg}}^0(q, p)$ according to Eq. (3.15). Note that $H_{\text{reg}}^0(q, p)$ does not obey the periodic boundary conditions of the map \mathcal{U}^1 , which is not relevant for approximating the regular island. We stress that in contrast to the linearized dynamics of M , $H_{\text{reg}}^0(q, p)$ contains the global frequency information of the regular island of \mathcal{U}^1 . As shown in Fig. 4.2(a), the tori of $H_{\text{reg}}^0(q, p)$ agree with those of \mathcal{U}^1 only in the vicinity of the fixed point. In the remaining part of the regular island, H_{reg}^0 needs to be improved.

Family of canonical transformations

First we define a family of canonical transformations $T^{\mathbf{a}}$ by choosing a functional basis G_ν for the generating function (3.10). Since the tori of H_{reg}^0 and \mathcal{U}^1 are symmetric with respect to the fixed point, the transformations $T^{\mathbf{a}}$ should preserve this symmetry and commute with the symmetry operation

$$(q - q^*, p - p^*) \mapsto -(q - q^*), -(p - p^*), \quad (4.13)$$

i. e. we restrict to generators which satisfy

$$G_\nu(-(q - q^*), -(p' - p^*)) = G_\nu(q - q^*, p' - p^*). \quad (4.14)$$

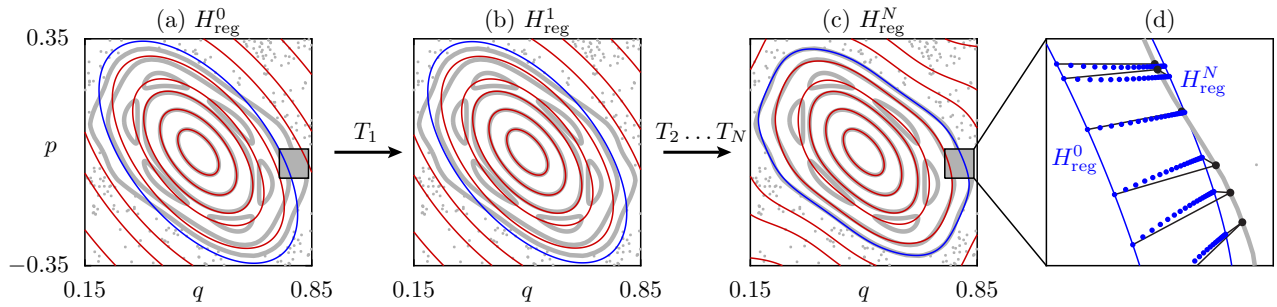


Figure 4.2.: The phase space of the standard map (4.4), at $\kappa = 1.25$ (thick gray lines and dots) compared to the tori (thin colored lines) of (a) the initial integrable approximation H_{reg}^0 , (b) its transformation after the first iteration step T_1 , and (c) after the final iteration step T_N , $N = 60$. (d) Magnification of the border torus of H_{reg}^0 and H_{reg}^N (thin blue lines) and the standard map (thick gray line) together with the individual points $\mathbf{x}_\ell^{\tau,n}$ (blue dots) approaching the reference points \mathbf{x}_ℓ^τ (big black dots) of the standard map. Straight lines (black) indicate the initial and final distances that contribute to the cost function, Eq. (3.19).

Furthermore, we choose a Fourier basis for the G_ν which brings Eq. (3.10) into the form

$$F^{\mathbf{a}}(q, p') = qp' + \sum_{\nu_1=0}^{\mathcal{N}_q} \sum_{\nu_2=0}^{\mathcal{N}_p} a_{\nu_1\nu_2}^+ f_{\nu_1}^+ \left(\frac{q - q^*}{\mathcal{L}_q} \right) f_{\nu_2}^+ \left(\frac{p' - p^*}{\mathcal{L}_p} \right) + \sum_{\nu_1=1}^{\mathcal{N}_q} \sum_{\nu_2=1}^{\mathcal{N}_p} a_{\nu_1\nu_2}^- f_{\nu_1}^- \left(\frac{q - q^*}{\mathcal{L}_q} \right) f_{\nu_2}^- \left(\frac{p' - p^*}{\mathcal{L}_p} \right), \quad (4.15)$$

with basis functions

$$f_\nu^+(x) = \cos(2\pi\nu x), \quad (4.16a)$$

$$f_\nu^-(x) = \sin(2\pi\nu x). \quad (4.16b)$$

Thus the coefficients to be optimized are $\mathbf{a} = (a_{\nu_1\nu_2}^+, a_{\nu_1\nu_2}^-)$ with $a_{00}^+ = 0$. The orders $\mathcal{N}_q, \mathcal{N}_p$ and the periods $\mathcal{L}_q, \mathcal{L}_p$ can still be chosen.

Iterative improvement

We now perform the iterative improvement in order to transform the tori of H_{reg}^0 closer to the tori of \mathcal{U}^1 . First we compute the coefficients B_ν and $C_{\mu\nu}$ of the cost function, Eqs. (3.21), summing over all sample points \mathbf{x}_ℓ^τ determined in Sec. 4.2.1. For the generating function (4.15) we choose period lengths $\mathcal{L}_{q,p} \approx 1$ and low orders $\mathcal{N}_{q,p}$, specifically $\mathcal{L}_q = \mathcal{L}_p = 1.33$ and $\mathcal{N}_q = \mathcal{N}_p = 2$. Finally we obtain a solution \mathbf{a} of Eq. (3.22) which we rescale using the strong damping factor $\eta = 0.05$, Eq. (3.23). This solution \mathbf{a} defines the first canonical transformation $T_1 = T^{\mathbf{a}}$. As shown in Fig. 4.2(b) this transformation slightly deforms the tori of the initial integrable approximation H_{reg}^0 .

We repeat this procedure iteratively to obtain a sequence of transformations (T_1, T_2, \dots) leading to improved integrable approximations $(H_{\text{reg}}^1, H_{\text{reg}}^2, \dots)$, see Fig. 4.2. To quantify this iterative improve-

ment we evaluate the cost function \mathcal{L} after each iteration step n , see Fig. 4.3. For large n the cost function saturates as T_n converges to the identity transformation and the iteration is stopped after $N = 60$ steps. The final integrable approximation $H_{\text{reg}}^N(q, p)$ closely resembles the dynamics of the original map \mathcal{U}^1 , as shown in Fig. 4.2(c) for the shape of the tori and in Fig. 4.2(d) for the individual points that are used for the cost function, Eq. (3.19).

One would expect further optimization of the results by choosing higher orders $\mathcal{N}_{q,p}$ in Eq. (4.15) which increases the number of parameters of the transformation $T^{\mathbf{a}}$. However, it turns out that increasing $\mathcal{N}_{q,p}$ requires very small damping factors η and hence more iteration steps, which reduces the performance. A possible improvement might be the increase of $\mathcal{N}_{q,p}$ only during the last iteration steps.

4.3. Damping mechanism

In this section we explain the damping mechanism, Eq. (3.23). For this, we first examine the problem of invertibility for the family of canonical transformations $\{T^{\mathbf{a}}\}$ (Sec. 4.3.1). Then we show how the damping mechanism can restore this invertibility (Sec. 4.3.2). Finally we illustrate these results using the example of the standard map (Sec. 4.3.3) and present an adapted damping mechanism to achieve faster convergence (Sec. 4.3.4).

4.3.1. Invertibility

Formally, the family of canonical transformations $\{T^{\mathbf{a}}\}$ that is used for the presented method is induced by the generating function $F^{\mathbf{a}}$, Eq. (3.10) and a choice of basis functions G_ν . However, for a particular parameter \mathbf{a} , the transformation $T^{\mathbf{a}}$ only exists, if the implicit Eqs. (3.11) can be solved for new variables $\mathbf{x}' = (\mathbf{q}', \mathbf{p}')$ in terms of the old variables $\mathbf{x} = (\mathbf{q}, \mathbf{p})$. We now derive a condition to ensure this invertibility, based on implicit function theory.

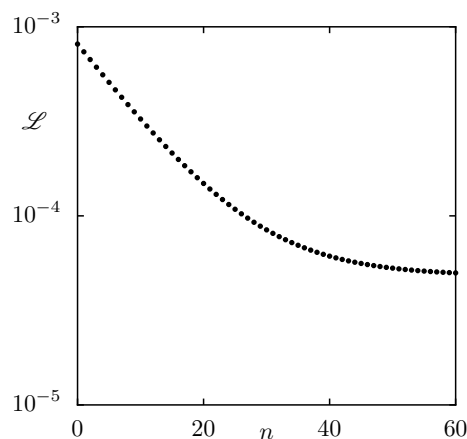


Figure 4.3.: Cost function \mathcal{L} , Eq. (3.19), vs. iteration step n .

Formally, the implicit Eqs. (3.11) can be written as

$$\phi(\mathbf{x}, \mathbf{x}') = \mathbf{0}, \quad (4.17)$$

where the function $\phi : \mathbb{R}^{2f} \times \mathbb{R}^{2f} \mapsto \mathbb{R}^{2f}$ is given by a tuple $\phi = (\phi_1, \phi_2)$ with the components

$$\phi_{1,k}(\mathbf{q}, \mathbf{p}, \mathbf{q}', \mathbf{p}') = \frac{\partial F^{\mathbf{a}}}{\partial p'_k}(\mathbf{q}, \mathbf{p}') - q'_k, \quad (4.18a)$$

$$\phi_{2,k}(\mathbf{q}, \mathbf{p}, \mathbf{q}', \mathbf{p}') = \frac{\partial F^{\mathbf{a}}}{\partial q_k}(\mathbf{q}, \mathbf{p}') - p_k, \quad (4.18b)$$

for $k = 1, \dots, f$. Given a two-point solution $(\mathbf{x}, \mathbf{x}')$ of Eq. (4.17), the transformation $T^{\mathbf{a}}$ is defined locally, if the solution can be uniquely extended in its neighborhood. According to the implicit function theorem [44], this requires the function $\phi(\cdot, \mathbf{x}')$ to have a nonzero Jacobian,

$$\det \left(\frac{D\phi}{D\mathbf{x}} \right) \neq 0. \quad (4.19)$$

Here $D\mathbf{u}/D\mathbf{v}$ denotes the matrix of the partial derivatives $\partial u_i / \partial v_j$. Using Eq. (4.18), we have

$$\frac{D\phi}{D\mathbf{x}} = \left(\begin{array}{c|c} \frac{D\phi_1}{D\mathbf{q}} & \frac{D\phi_1}{D\mathbf{p}} \\ \hline \frac{D\phi_2}{D\mathbf{q}} & \frac{D\phi_2}{D\mathbf{p}} \end{array} \right) = \left(\begin{array}{c|c} \frac{\partial^2 F^{\mathbf{a}}}{\partial q_j \partial p'_i} & 0 \\ \hline \frac{\partial^2 F^{\mathbf{a}}}{\partial q_j \partial q_i} & \delta_{ij} \end{array} \right), \quad (4.20)$$

and the condition (4.19) for the local existence of $T^{\mathbf{a}}$ reduces to

$$\mathcal{J}(\mathbf{q}, \mathbf{p}') := \det \left(\frac{\partial^2 F^{\mathbf{a}}}{\partial q_j \partial p'_i}(\mathbf{q}, \mathbf{p}') \right) \neq 0. \quad (4.21)$$

We now translate this condition for the generator $F^{\mathbf{a}}$ into a condition for the parameter \mathbf{a} . Using the special form (3.10) of $F^{\mathbf{a}}$, we have

$$\mathcal{J}(\mathbf{q}, \mathbf{p}') = \det \left(\delta_{ij} + \sum_{\nu} a_{\nu} \frac{\partial^2 G_{\nu}}{\partial q_j \partial p'_i}(\mathbf{q}, \mathbf{p}') \right). \quad (4.22)$$

Assuming the basis functions G_{ν} to be bounded and C^2 , this can be estimated as

$$\mathcal{J}(\mathbf{q}, \mathbf{p}') = 1 + \mathcal{O}(|\mathbf{a}|). \quad (4.23)$$

Hence, there exists an upper bound a_{crit} such that for near-zero parameters with

$$|\mathbf{a}| < a_{\text{crit}}, \quad (4.24)$$

Eq. (4.21) is guaranteed everywhere in phase space. Consequently, for sufficiently small \mathbf{a} , the trans-

formation $T^{\mathbf{a}}$ is locally defined everywhere. Additionally the function $\phi(\cdot, \mathbf{x}')$ is proper, as shown in App. C. This allows to apply Hadamard's global inverse function theorem [44], which for $|\mathbf{a}| \ll 1$ also ensures *global* invertibility and thus the unique existence of $T^{\mathbf{a}}$.

4.3.2. Existence of damped solutions

The analysis of the previous section has shown, that small parameters \mathbf{a} lead to a globally well defined transformation $T^{\mathbf{a}}$. The iterative improvement algorithm introduced in Sec. 3.3.3 also assumes small parameters, which, however, does not guarantee the solution parameter \mathbf{a} of Eq. (3.22) to be small. For the case where this solution parameter \mathbf{a} is too large, the damping mechanism, Eq. (3.23), was introduced. Traditionally, "damping" refers to a widespread concept, which essentially means to stabilize an iterative algorithm by an additional reduction of its step width [45]. Here this is realized by downscaling the solution parameters \mathbf{a} of the transformation $T^{\mathbf{a}}$ to $\eta\mathbf{a}$ using a damping factor $\eta \in (0, 1]$. Obviously, by choosing η sufficiently small we can reach the valid parameter range (4.24) and restore invertibility.

However, to justify the damping mechanism, we further need to prove that the downscaled transformation $T^{\eta\mathbf{a}}$ is still able to mimic the original transformation $T^{\mathbf{a}}$ in some sense, which we will do in the following. For this we need to study the parameter dependence of the family of transformations $\{T^{\mathbf{a}}\}$ defined by Eqs. (3.11). First, we consider the expansions of $T^{\mathbf{a}}$ in \mathbf{a} up to second and first order, which are given by

$$T^{\mathbf{a}}(\mathbf{x}) = \mathbf{x} + \mathbf{a}\mathbf{f}_1(\mathbf{x}) + \mathcal{O}(|\mathbf{a}|^2), \quad (4.25a)$$

$$= \mathbf{x} + \mathcal{O}(|\mathbf{a}|), \quad (4.25b)$$

respectively. The linear coefficients \mathbf{f}_1 are given by Eq. (3.13), which, however, is not relevant in the following. Note that the dependence on \mathbf{x} is suppressed in the \mathcal{O} -notation for convenience. Using the linear expansion (4.25a), we compute the linear expansion of two nested transformations as

$$T^{\mathbf{a}'}[T^{\mathbf{a}}(\mathbf{x})] = T^{\mathbf{a}}(\mathbf{x}) + \mathbf{a}'\mathbf{f}_1[T^{\mathbf{a}}(\mathbf{x})] + \mathcal{O}(|\mathbf{a}'|^2). \quad (4.26)$$

By repeatedly applying Eqs. (4.25), this simplifies to

$$T^{\mathbf{a}'}[T^{\mathbf{a}}(\mathbf{x})] = \underbrace{T^{\mathbf{a}}(\mathbf{x})}_{\mathbf{x} + \mathbf{a}\mathbf{f}_1(\mathbf{x}) + \mathcal{O}(|\mathbf{a}|^2)} + \mathbf{a}' \underbrace{\mathbf{f}_1[T^{\mathbf{a}}(\mathbf{x})]}_{\mathbf{f}_1[\mathbf{x} + \mathcal{O}(|\mathbf{a}|)]} + \mathcal{O}(|\mathbf{a}'|^2), \quad (4.27a)$$

$$= \mathbf{x} + \underbrace{\mathbf{a}\mathbf{f}_1(\mathbf{x}) + \mathbf{a}'\mathbf{f}_1(\mathbf{x})}_{(\mathbf{a} + \mathbf{a}')\mathbf{f}_1(\mathbf{x})} + \underbrace{\mathcal{O}(|\mathbf{a}|^2) + \mathbf{a}'\mathcal{O}(|\mathbf{a}|) + \mathcal{O}(|\mathbf{a}'|^2)}_{\mathcal{O}_2(|\mathbf{a}|, |\mathbf{a}'|)}. \quad (4.27b)$$

Here, the multivariate symbol $\mathcal{O}_k(y_1, y_2, \dots, y_n)$ denotes a function which only has components $y_1^{k_1} y_2^{k_2} \dots y_n^{k_n}$ of total order $k_1 + \dots + k_n \geq k$. However, up to first order this equals $T^{\mathbf{a}+\mathbf{a}'}$. If we totally suppress

the dependence on \mathbf{x} , we obtain

$$T^{\mathbf{a}'} \circ T^{\mathbf{a}} = T^{\mathbf{a}+\mathbf{a}'} + \mathcal{O}_2(|\mathbf{a}|, |\mathbf{a}'|). \quad (4.28)$$

This result can be interpreted as an approximate group property, i. e., the family $\{T^{\mathbf{a}}\}$ forms a group in the small parameter limit. Using this identity, we can derive a 3-fold composition as

$$T^{\mathbf{a}} \circ T^{\mathbf{a}'} \circ T^{\mathbf{a}''} = T^{\mathbf{a}+\mathbf{a}'+\mathbf{a}''} + \mathcal{O}_2(|\mathbf{a}|, |\mathbf{a}'|, |\mathbf{a}''|), \quad (4.29)$$

and by induction we arrive at the corresponding identity for an N -fold composition,

$$T^{\mathbf{a}_1} \circ \dots \circ T^{\mathbf{a}_N} = T^{\mathbf{a}_1+\dots+\mathbf{a}_N} + \mathcal{O}_2(|\mathbf{a}_1|, \dots, |\mathbf{a}_N|). \quad (4.30)$$

Using this idea backwards, we can split up a single parameter \mathbf{a} into a sequence of N identical fractions,

$$T^{\mathbf{a}/N} \circ \dots \circ T^{\mathbf{a}/N} = T^{\mathbf{a}} + \mathcal{O}(|\mathbf{a}|^2/N^2). \quad (4.31)$$

Introducing the damping factor $\eta = 1/N$, this can be rewritten as

$$\left| T^{\mathbf{a}} - T^{\eta\mathbf{a}} \circ \dots \circ T^{\eta\mathbf{a}} \right| = \mathcal{O}(\eta^2|\mathbf{a}|^2). \quad (4.32)$$

Consequently $T^{\mathbf{a}}$ is approximated by a chain of damped transformations $T^{\eta\mathbf{a}}$. This approximation can reach any precision, by choosing η sufficiently small. Moreover, even if $T^{\mathbf{a}}$ is not defined globally, $T^{\eta\mathbf{a}}$ and thus also $T^{\eta\mathbf{a}} \circ \dots \circ T^{\eta\mathbf{a}}$ will be for $|\eta| \ll 1$. Having ensured the existence of this approximating chain, we can ask for even better approximations of the more general form $T^{\eta\mathbf{a}} \circ T^{\mathbf{a}_2} \circ \dots \circ T^{\mathbf{a}_N}$ where $\mathbf{a}_2, \dots, \mathbf{a}_N$ are chosen freely. Using Eq. (4.32) as an upper bound, we can expect a solution whose quality will be at least

$$\left| T^{\mathbf{a}} - T^{\eta\mathbf{a}} \circ T^{\mathbf{a}_2} \dots \circ T^{\mathbf{a}_N} \right| \leq \mathcal{O}(\eta^2|\mathbf{a}|^2). \quad (4.33)$$

For the iterative scheme presented in Sec. 3.3.3, this estimation justifies to approximate $T^{\mathbf{a}}$ by a chain of transformations where the first element is $T^{\eta\mathbf{a}}$ and the other elements $T^{\mathbf{a}_2} \circ \dots \circ T^{\mathbf{a}_N}$ are to be determined in the remaining iteration steps.

4.3.3. Illustration for 2D maps

To illustrate the damping mechanism, we now return to the example of the standard map, Eq. (4.4). We consider this system for the parameter $\kappa = 0.9$, see Fig. 4.4(a). For the target region we choose the central regular island (black lines).

We implement the iterative canonical transformation method according to Sec. 4.2 using the parameters $(\Delta q, \mathcal{K}, \mathcal{L}_q, \mathcal{L}_p, \mathcal{N}_q, \mathcal{N}_p) = (0.3537, 5, 2.8, 1.3, 2, 3)$. First, we consider the undamped algorithm,

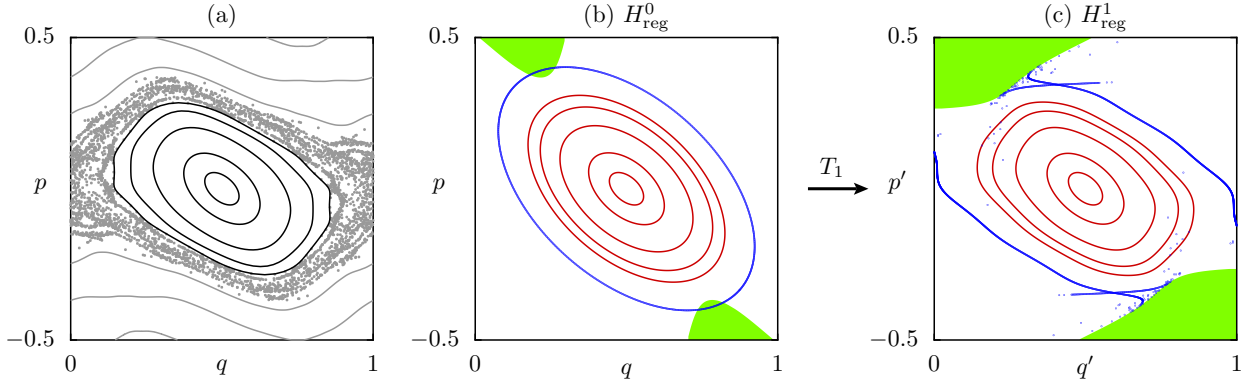


Figure 4.4.: (a) Phase space of the standard map (4.4) for $\kappa = 0.9$ with regular orbits (lines) and chaotic orbits (dots). (b–c) Regions of positive (white) and negative (green) Jacobian \mathcal{J} (b) in (q, p) -space and (c) in (q', p') -space. Furthermore, tori of the integrable approximations (b) H_{reg}^0 and (c) H_{reg}^1 are shown (red lines). As the blue torus in (q, p) -space (b) crosses regions $\mathcal{J} = 0$, its transformation to (q', p') -space fails (c).

$\eta = 1$. In the first iteration step, Eq. (3.22) is solved for the parameter \mathbf{a} . Given this parameter, we compute the Jacobian (4.21), which in this case reduces to the scalar function

$$\mathcal{J}(q, p') = \frac{\partial F^{\mathbf{a}}}{\partial q \partial p'}(q, p'). \quad (4.34)$$

Due to the choice of the Fourier basis (4.15) for G_ν , this function is periodic in q and p' with period lengths \mathcal{L}_q and $\mathcal{L}_{p'}$, respectively. The upper plot of Fig. 4.5(a) shows the sign of $\mathcal{J}(q, p')$ in one unit cell of the (q, p') -plane. As one finds regions of both signs, the invertibility condition (4.21) is violated at the boundary between these regions and $T^{\mathbf{a}}$ is not globally defined. Using Eqs. (3.11) we map these regions to the (q, p) - and (q', p') -plane, as shown in Figs. 4.4(b) and (c), respectively. Avoiding the lines $\mathcal{J} = 0$, the transformation $T_1 = T^{\mathbf{a}}$ can only be defined locally in each connected subregion $\mathcal{J} < 0$ or $\mathcal{J} > 0$. Here, the central white region of Fig. 4.4(b) is chosen, as it contains the target region for the integrable approximation. For tori which penetrate these lines, the transformation expectably fails, as shown for the blue torus in Figs. 4.4(b) and (c). However, if one restricts to the white region $\mathcal{J} > 0$, the Hamiltonian H_{reg}^1 is defined and the iteration can be continued. In principle, each iteration step would lead to further restrictions of the domain of definition. However, practically no confinement of the domain of definition occurs, as the following transformations (T_2, T_3, \dots) will only add smaller corrections. After $N = 5$ iteration steps, the cost function saturates, see Fig. 4.5(a).

In the following, we consider the damped algorithm for $\eta = 1/10$. The first transformation is now given by $T_1 = T^{\eta \mathbf{a}}$. As proposed in Sec. 4.3.2, this expands the white region where H_{reg}^1 is defined, see Fig. 4.5(b). However, as the rescaled transformation $T^{\eta \mathbf{a}}$ is located closer to the identity transformation than $T^{\mathbf{a}}$, less improvement is achieved in one iteration step and the algorithm becomes slower. Enhancing the total iteration time by the factor η^{-1} to $N = 50$ leads to a final integrable approximation H_{reg}^{50} that is similar to the previous result H_{reg}^5 for $\eta = 1$.

Finally, by choosing a stronger damping $\eta = 1/100$, the regions $\mathcal{J} < 0$ completely disappear, see

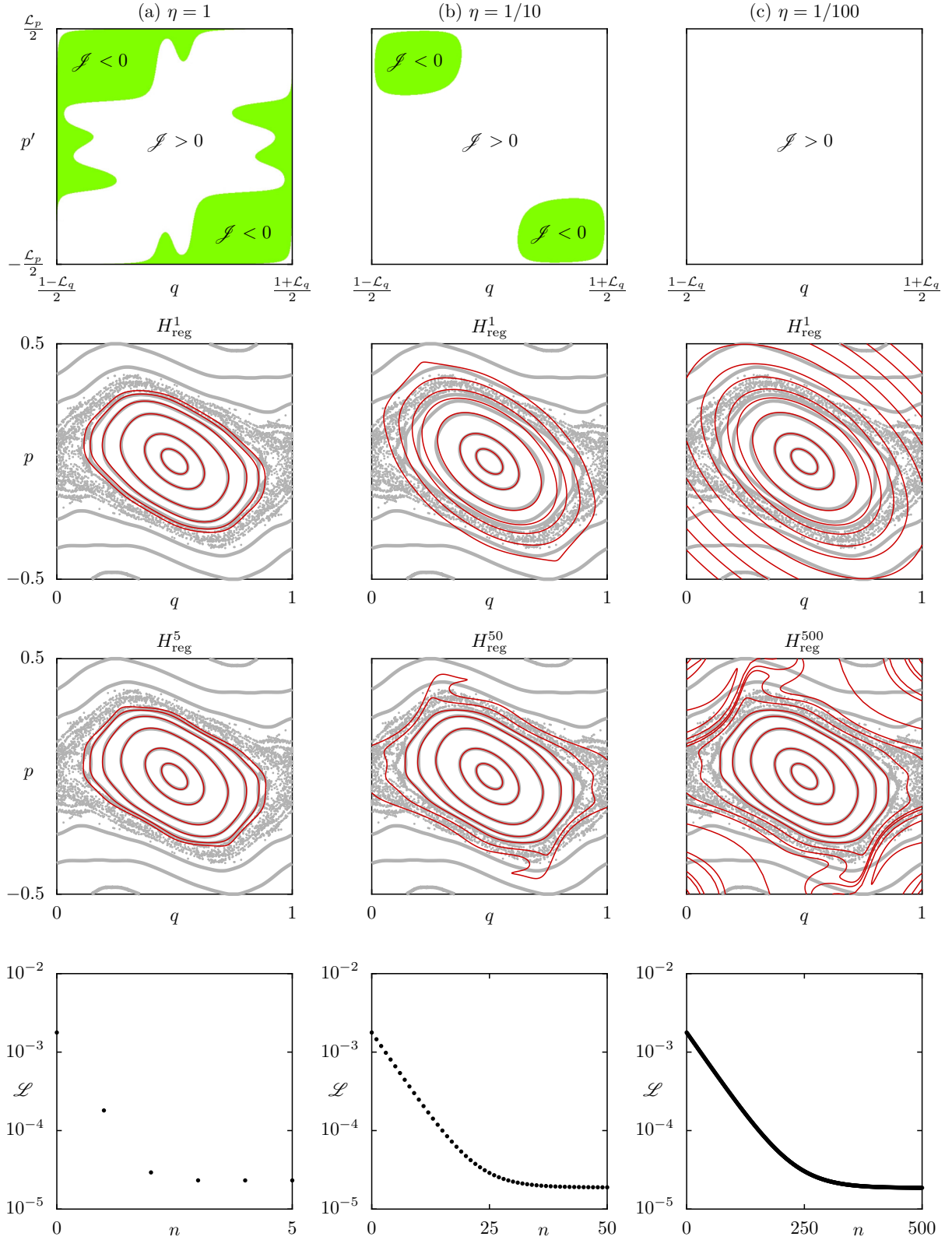


Figure 4.5.: Illustration of the damping mechanism for the iterative improvement algorithm. Results are shown for the undamped algorithm $\eta = 1$ (a) and the damped algorithm with $\eta = 1/10$ (b) and $\eta = 1/100$ (c). First row: regions of positive (white) and negative (green) Jacobian \mathcal{J} in (q, p') -space, evaluated for the first transformation T_1 . Second and third row: orbits of the standard map (4.4) for $\kappa = 0.9$ (gray lines and dots) with tori of the integrable approximations H_{reg}^1 (second row) and $H_{\text{reg}}^{5/\eta}$ (third row) (red lines). Fourth row: Cost function \mathcal{L} , Eq. (3.19), vs. iteration step n .

Fig. 4.5(c). The rescaled parameter $\eta\mathbf{a}$ now is located in the valid parameter range (4.24) such that $T^{\eta\mathbf{a}}$, H_{reg}^1 , and also the final integrable approximation H_{reg}^{500} are globally defined. Furthermore, the agreement of the final integrable approximations indicates the stability of the algorithm when η is changed. This is also supported by the behavior of the cost function for different η , which nearly agree if the iteration time n is rescaled by η^{-1} . This example shows, how the damping mechanism allows to extend the integrable approximation to a larger domain of definition.

4.3.4. Adapted damping

The main drawback of the damping mechanism is the slowdown of convergence. It is of interest to use as few iteration steps as possible. To this end we use, that even for the undamped algorithm the transformations T_n become smaller when n is increased. Thus the damping becomes less necessary for growing n and it is reasonable, to gradually turn it off during the algorithm. This is realized using an adapted damping factor for each iteration step n ,

$$\eta \rightarrow \eta_n. \quad (4.35)$$

In the following we derive the optimal sequence η_n from the structure of the family of canonical transformations $\{T^{\mathbf{a}}\}$. For this, we assume all involved transformations to be sufficiently small such that the group property,

$$T^{\mathbf{a}+\mathbf{a}'} = T^{\mathbf{a}} \circ T^{\mathbf{a}'}, \quad (4.36)$$

becomes exact, see Eq. (4.28). Let $(\bar{\mathbf{a}}_1, \bar{\mathbf{a}}_2, \dots)$ and $(\mathbf{a}_1, \mathbf{a}_2, \dots)$ denote the parameter sequences of the undamped and the damped algorithm, respectively. As for the undamped algorithm, the first transformation $T^{\bar{\mathbf{a}}_1}$ typically gives the main contribution, our next approximation is to neglect the corrections $(T^{\bar{\mathbf{a}}_2}, T^{\bar{\mathbf{a}}_3}, \dots)$. In this approximation order, the full result of the undamped algorithm is given by its first iteration step $T_1 = T^{\bar{\mathbf{a}}_1}$. We now express all parameters $(\mathbf{a}_1, \mathbf{a}_2, \dots)$ of the damped algorithm as a function of $\bar{\mathbf{a}}_1$. Obviously, the first step yields the parameter $\mathbf{a}_1 = \eta_1 \bar{\mathbf{a}}_1$. According to the group property (4.36), the remaining transformation would be given by $\bar{\mathbf{a}}_1 - \mathbf{a}_1$ and after applying the damping factor η_2 , the second step yields the parameter $\mathbf{a}_2 = \eta_2(\bar{\mathbf{a}}_1 - \mathbf{a}_1)$. Continuing this way, we obtain

$$\mathbf{a}_1 = \eta_1 \bar{\mathbf{a}}_1, \quad (4.37a)$$

$$\mathbf{a}_{n+1} = \eta_{n+1} \left(\bar{\mathbf{a}}_1 - \sum_{m=1}^n \mathbf{a}_m \right). \quad (4.37b)$$

As the solution \mathbf{a}_n of this convolution recursion must be linear in $\bar{\mathbf{a}}_1$, we make the ansatz

$$\mathbf{a}_n = \eta_n R_n \bar{\mathbf{a}}_1. \quad (4.38)$$

Inserting this into Eq. (4.37) leads to a recursion for the prefactors R_n given by

$$R_1 = 1, \quad (4.39a)$$

$$R_{n+1} = (1 - \eta_n)R_n. \quad (4.39b)$$

The most effective choice for the damping factors η_n would make each transformation $T^{\mathbf{a}_n}$ equally strong. Thus we fix η_n by requiring all parameters to be of the same magnitude, i.e., $|\mathbf{a}_n| = |\mathbf{a}_1|$. Using Eq. (4.38) this condition becomes

$$\eta_n = \eta_1 \frac{R_1}{R_n}, \quad (4.40)$$

where we assumed $\eta_n \geq 0$. This allows to eliminate η_n in Eq. (4.39b), leading to the linear recursion

$$R_1 = 1 \quad (4.41)$$

$$R_{n+1} = R_n - \eta_1 \quad (4.42)$$

for R_n only, which has the solution $R_n = 1 + (1 - n)\eta_1$. Finally, inserting this back into Eq. (4.40) leads to the ideal damping sequence

$$\eta_n = \frac{\eta_1}{1 + (1 - n)\eta_1}. \quad (4.43)$$

This sequence behaves differently, depending on the choice of the initial damping factor η_1 . For $\eta_1 = 1/N$ with $N \in \mathbb{N}$, the sequence monotonically approaches $\eta_N = 1$ at step $n = N$, see Fig. 4.6(a). In this case, evaluating Eq. (4.37b) for $n = N$ gives

$$\bar{\mathbf{a}}_1 = \sum_{m=1}^N \mathbf{a}_m, \quad (4.44)$$

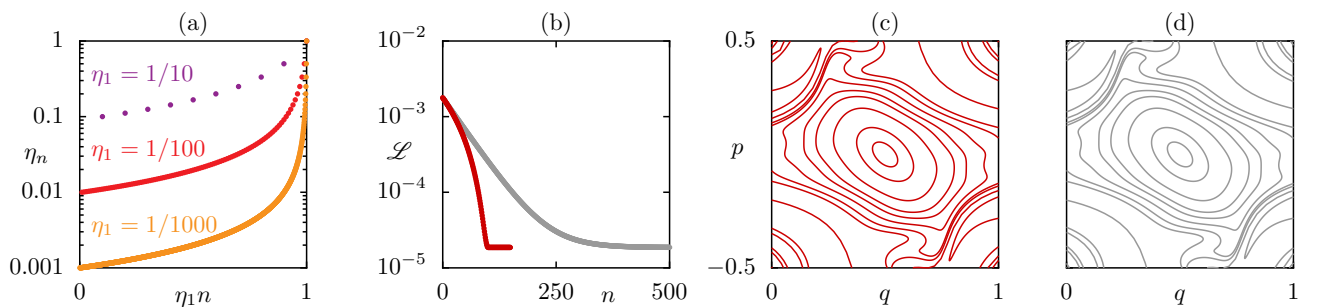


Figure 4.6.: (a) Ideal damping sequence η_n , Eq. (4.43), vs. rescaled iteration time $\eta_1 n$, shown for different initial conditions $\eta_1 = 1/10$, $1/100$, and $1/1000$. (b–d) Illustration of the adapted damping mechanism using the standard map (4.4) with $\kappa = 0.9$: (b) Cost function \mathcal{L} , Eq. (3.19), vs. iteration step n for the iterative algorithm with constant damping $\eta = 1/100$ (gray) and with adapted damping using $\eta_1 = 1/100$ (red). (c,d) Integrable approximations H_{reg}^{100} obtained using adapted damping (c) and H_{reg}^{500} obtained using constant damping (d).

i. e., the full result $\bar{\mathbf{a}}_1$ is reached and the algorithm finishes after the N -th step. Thus, the choice $\eta_1 = 1/N$ also suggests an ideal runtime of N steps for the algorithm. If η_1 is not an inverse integer, negative values for η_n occur, before the algorithm terminates. As we required $\eta_n \geq 0$, these values for η_1 are invalid.

We now demonstrate the adapted damping mechanism by constructing an integrable approximation of the standard map at $\kappa = 0.9$. Figure 4.6(b) shows the cost function for the algorithm applied with constant damping $\eta = 1/100$ (gray), as implemented in the previous section, and for the algorithm with adapted damping using $\eta_1 = 1/100$ (red). After $N = 100$ iteration steps, the adapted algorithm is continued without damping by setting $\eta_n = 1$ for $n > 100$. As the cost function abruptly becomes constant for $98 \leq n \leq 102$ (not shown), the predicted termination after $N = 100$ steps is verified. Moreover, we find a close agreement between the integrable approximations H_{reg}^{100} resulting from the algorithm with adapted damping and H_{reg}^{500} resulting from the algorithm with constant damping, as shown in Figs. 4.6(c-d).

4.4. Choice of the orders \mathcal{N} and convergence

For the iterative improvement of the presented method, a family of canonical transformations $\{T^{\mathbf{a}}\}$ is used. Until now, the entire discussion was based on one given family. However, this family is constituted by the order \mathcal{N} at which the generating function (3.10) is truncated. In the following we discuss how changing this truncation order \mathcal{N} influences the convergence of the algorithm and investigate the asymptotics $\mathcal{N} \rightarrow \infty$.

To this end, we consider the standard map at $\kappa = 2.9$. This choice is convenient for studying the convergence, as the large perturbation causes a stronger tendency for the algorithm to diverge. Following Sec. 4.2, the truncation order \mathcal{N} is represented by two integers $(\mathcal{N}_q, \mathcal{N}_p)$ in Eq. (4.15). First, we consider the undamped algorithm, $\eta = 1$. We vary the truncation orders in the range $0 \leq \mathcal{N}_q, \mathcal{N}_p \leq 6$ and for each choice $(\mathcal{N}_q, \mathcal{N}_p)$ we run the iterative canonical transformation method according to Sec. 4.2 using the parameters $(\Delta q, \mathcal{K}, \mathcal{L}_q, \mathcal{L}_p) = (0.1012, 5, 2.8, 1.3)$. For each $(\mathcal{N}_q, \mathcal{N}_p)$ we compute the final, saturated value of the cost function \mathcal{L}_N after a sufficiently long iteration time N , see Fig. 4.7(a). As expected, we find that increasing $(\mathcal{N}_q, \mathcal{N}_p)$ improves the final integrable approximation. However, when a critical domain $(\mathcal{N}_q \geq 3) \wedge (\mathcal{N}_p \geq 3)$ is reached, the algorithm diverges, as indicated by the red area. This behavior is also expected, as for growing orders more terms can shift the determinant (4.22) away from unity, which effectively contracts the valid parameter range (4.24). The inset at $(\mathcal{N}_q, \mathcal{N}_p) = (4, 4)$ shows the integrable approximation $H_{\text{reg}}^1(q, p)$. Here the transformation T_1 fails for the outer torus. Hence, due to the contraction of the valid parameter range (4.24), the target region is not fully included in the domain of definition for the used transformation T_1 .

In Fig. 4.7(b) we show the analogous results for the damped algorithm with $\eta = 1/5$. It turns out that the region of convergence in the $(\mathcal{N}_q, \mathcal{N}_p)$ -plane is enlarged as compared to $\eta = 1$. Hence, the damping mechanism stabilizes the algorithm and allows to increase the orders $(\mathcal{N}_q, \mathcal{N}_p)$ to improve the final integrable approximation.

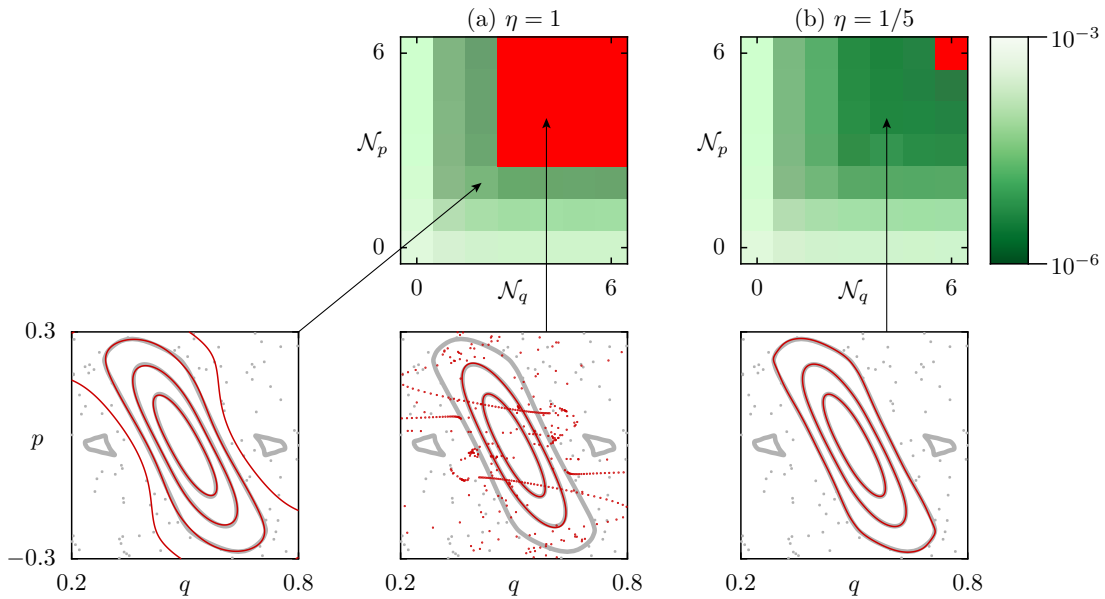


Figure 4.7.: Saturated value of the cost function \mathcal{L}_N (green) after a sufficiently long iteration time N for different orders $(\mathcal{N}_q, \mathcal{N}_p)$ in Eq. (4.15) and damping factors $\eta = 1$ (a) and $\eta = 1/5$ (b). Red areas indicate the divergence of the iterative improvement algorithm. The insets show the phase space of the standard map (4.4) for $\kappa = 2.9$ (gray) with tori (red) of the corresponding integrable approximations H_{reg}^N for $(\mathcal{N}_q, \mathcal{N}_p, \eta) = (2, 2, 1)$ (left), H_{reg}^1 for $(\mathcal{N}_q, \mathcal{N}_p, \eta) = (4, 4, 1)$ (center), and H_{reg}^N for $(\mathcal{N}_q, \mathcal{N}_p, \eta) = (4, 4, 1/5)$ (right).

However, this improvement is limited, as Fig. 4.7(b) shows a saturation of \mathcal{L}_N for large $(\mathcal{N}_q, \mathcal{N}_p)$. This indicates the general observation, that for $\mathcal{N} \rightarrow \infty$ a final, unremovable error $\mathcal{L}^* > 0$ is left. In the following we discuss the source of this final error. One source is the general fact, that the integrable approximation of a non-integrable regular target region can, of course, never be exact. The reason for this are the nonlinear resonance chains, which are densely distributed in the target region. Although these resonances are not included in the sample points for the cost function, their signature is still present, as they deform all tori of the system.

Apart from this *principal* error, which cannot be overcome, the final error \mathcal{L}^* might also include a *specific* error caused by insufficiencies of the iterative improvement algorithm. To investigate the existence of that specific error, we switch off the principal error by considering an integrable target system $H_{\text{bench}}(q, p)$. According to Sec. 2.2, this system is defined by a frequency function $\omega_{\text{bench}}(J)$ and a canonical transformation T_{bench} . As our focus is on the shape approximation, we set $\omega_{\text{bench}}(J) = 1$. For T_{bench} we use the combination

$$T_{\text{bench}} = \tilde{T} \circ T_0, \quad (4.45)$$

where T_0 is given by Eqs. (4.7) and (4.8) with $(q^*, p^*) = (0, 0)$, $\sigma = 1$, and $\beta = 0$. The second

contribution \tilde{T} is given by

$$\tilde{T} : \begin{pmatrix} q \\ p \end{pmatrix} \mapsto \begin{pmatrix} q + g(p) \\ p \end{pmatrix}, \quad (4.46)$$

with

$$g(p) = (b_1 p + b_3 p^3 + b_5 p^5) e^{-bp^2}. \quad (4.47)$$

Note that $g(-p) = -g(p)$ such that $H_{\text{bench}}(q, p)$ has the same symmetry (4.13) as the standard map. In the following we consider this benchmark system H_{bench} for $b_1 = 0.5$, $b_3 = -b_5 = 0.087$, and $b = 0.23$, see the gray lines in Fig. 4.8(a). For different values of $(\mathcal{N}_q, \mathcal{N}_p)$ we run the iterative canonical transformation method using the parameters $(\Delta q, \mathcal{L}_q, \mathcal{L}_p) = (3.2, 10, 10)$ and a damping $\eta = 1/5$. The saturated values of the cost function \mathcal{L}_N are shown in Fig. 4.8(b). As \mathcal{L}_N is nearly independent of \mathcal{N}_q , very low orders \mathcal{N}_q are sufficient for this example system. Moreover, by increasing \mathcal{N}_p , the quality \mathcal{L}_N of the integrable approximation can be brought to the order 10^{-16} of machine precision. As no relevant specific error can be observed, numerical or conceptual insufficiencies of the iterative canonical transformation method can be excluded. Thus, the finite, asymptotic error $\mathcal{L}^* > 0$ which is found for non-integrable target systems, originates from non-integrable phase-space structures only.

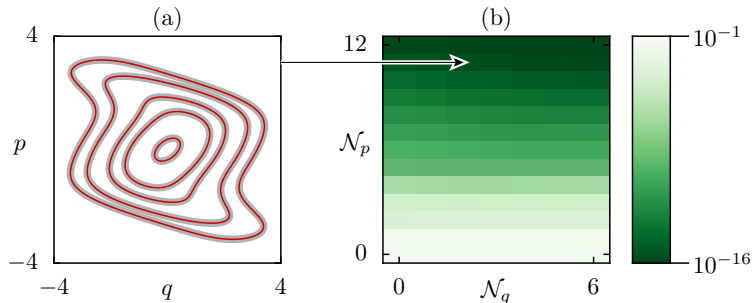


Figure 4.8.: (a) Phase space of the integrable target system H_{bench} (gray) and its integrable approximation H_{reg}^N for $(\mathcal{N}_q, \mathcal{N}_p) = (2, 11)$ (red). (b) Saturated value of the cost function \mathcal{L}_N after a sufficiently long iteration time N for different orders $(\mathcal{N}_q, \mathcal{N}_p)$ in Eq. (4.15).

4.5. Comparison to other methods

In the literature, there exist a couple of methods for the construction of integrable approximations. In this section, we present two prominent methods and compare them to the iterative canonical transformation method. Namely, we consider the method of normal forms [18, 19] and the method of Lie transforms [8, 20–22]. A third method based on a Baker–Campbell–Hausdorff expansion is known [46, 47]. However, for the standard map (4.4) it produces the same results as the Lie method, and is thus not treated in the following.

4.5.1. Method of normal forms

The first considered method is the method of normal forms, which we review here following Refs. [18, 19]. Although this method is also valid for time-continuous Hamiltonian systems, we present it directly for the modeling of symplectic maps. Thus our starting point is a symplectic 2D map \mathcal{U}^1 with a mixed phase space. For convenience, we consider its simplified representation $\mathcal{F} = C^{-1} \circ \mathcal{U}^1 \circ C$, using the Courant–Snyder transformation

$$C : \quad \mathbf{x} \mapsto \mathbf{x}^* + \mathcal{R}\mathbf{x}. \quad (4.48)$$

Here \mathcal{R} is given by Eq. (4.8) and $\mathbf{x}^* = (q^*, p^*)$ is the central fixed point of the map \mathcal{U}^1 . Moreover, we introduce the complex phase-space coordinates

$$z = q - ip, \quad (4.49a)$$

$$z^* = q + ip, \quad (4.49b)$$

and rewrite the time evolution as

$$z' = \mathcal{F}(z, z^*), \quad (4.50a)$$

$$(z^*)' = \mathcal{F}(z, z^*)^*. \quad (4.50b)$$

Now we consider another canonical transformation $T : \xi \mapsto z$ which leads to the following diagram:

$$\begin{array}{ccc} z & \xrightarrow{\mathcal{F}} & z' \\ T \uparrow & & \uparrow T \\ \xi & \xrightarrow{U} & \xi' \end{array} \quad (4.51)$$

The goal is to construct the objects T and U of this diagram, such that U is integrable. As \mathcal{F} is not integrable, this cannot be fulfilled exactly, but rather approximately. Therefore, T and U are constructed, to *nearly* obey the diagram (4.51) while keeping U integrable. The conditions for this

are

$$\mathcal{F} \circ T = T \circ U, \quad (4.52a)$$

$$\frac{\partial T}{\partial \xi} \frac{\partial T^*}{\partial \xi^*} - \frac{\partial T}{\partial \xi^*} \frac{\partial T^*}{\partial \xi} = 1. \quad (4.52b)$$

Here Eq. (4.52a) just expresses the diagram (4.51) while Eq. (4.52b) ensures the transformation T to be canonical. Now the functions \mathcal{F} , T , and U are expanded in orders of z and ξ , i. e.,

$$z' = \mathcal{F}(z, z^*) = \sum_{n=1}^{\infty} \sum_{k=0}^n \mathcal{F}_{k,n-k} z^k (z^*)^{n-k}, \quad (4.53a)$$

$$z = T(\xi, \xi^*) = \sum_{n=1}^{\infty} \sum_{k=0}^n T_{k,n-k} \xi^k (\xi^*)^{n-k}, \quad (4.53b)$$

$$\xi' = U(\xi, \xi^*) = \sum_{n=1}^{\infty} \sum_{k=0}^n U_{k,n-k} \xi^k (\xi^*)^{n-k}. \quad (4.53c)$$

If \mathcal{F} is symplectic, U obtains the simpler form

$$U(\xi, \xi^*) = e^{i\Omega(|\xi|^2)} \xi, \quad (4.54)$$

with one real-valued function $\Omega(\cdot)$. Thus U performs a circular rotation of ξ with a frequency depending on the radius $|\xi|$. As, due to the Courant–Snyder transformation (4.48), the local dynamics of \mathcal{F} around $|z| = 0$ is also circular, the lowest order of T is the identity transformation. This leads to

$$\mathcal{F}_{1,0} = e^{i\omega}, \quad \mathcal{F}_{0,1} = 0, \quad (4.55a)$$

$$U_{1,0} = e^{i\omega}, \quad U_{0,1} = 0, \quad (4.55b)$$

$$T_{1,0} = 1, \quad T_{0,1} = 0, \quad (4.55c)$$

where ω is the local frequency of \mathcal{F} around $z = 0$.

Given these initial values and \mathcal{F} , one systematically constructs the higher orders of T and U . More precisely, for $n = 2, 3, \dots$ one determines $U_{k,n-k}$ and $T_{k,n-k}$ by solving the projections of Eqs. (4.52a) and (4.52b) to order $|\xi|^n$ and $|\xi|^{n-1}$, respectively. After step n this allows to compute the n -th integrable approximation

$$\mathcal{F}_{\text{reg}}^n = [T \circ U \circ T^{-1}]_n, \quad (4.56)$$

where $[\cdot]_n$ denotes the truncated expansion up to order n . As the frequency function is given by $\omega(J) = \Omega(2J)$ with Ω from Eq. (4.54), the corresponding Hamiltonian reads

$$\mathcal{H}_{\text{nf}}^n(\xi, \xi^*) = \left[\int_0^{|\xi|^2/2} dJ \Omega(2J) \right]_n, \quad (4.57)$$

as follows from Eq. (2.14) and $J = |\xi|^2/2$. As mentioned, the underlying approach (4.51) is intrinsically paradox, as the non-integrable system \mathcal{F} cannot be canonically connected to an integrable system U . Typically, this leads to the divergence of the series (4.53b) and (4.53c).

4.5.2. Comparison to the method of normal forms

We now apply the method of normal forms to the standard map. Following the presented algorithm, we construct the integrable approximations $\mathcal{F}_{\text{reg}}^n$, Eq. (4.56), up to order $n = 8$. We evaluate these integrable approximations for the map parameters $\kappa = 0.5, 1.25$, and 2.9 . For comparison we use the integrable approximations H_{reg}^n from the iterative canonical transformation method with the following settings

$$\kappa = 0.5 : \quad (\Delta p, \mathcal{K}, \mathcal{L}_q, \mathcal{L}_p, \mathcal{N}_q, \mathcal{N}_p, \eta) = (0.5, 5, 1, 3, 7, 7, 1/3) \quad (\text{Sec. 4.6}), \quad (4.58a)$$

$$\kappa = 1.25 : \quad (\Delta q, \mathcal{K}, \mathcal{L}_q, \mathcal{L}_p, \mathcal{N}_q, \mathcal{N}_p, \eta) = (0.293, 6, 1.33, 1.33, 2, 2, 1/20) \quad (\text{Sec. 4.2}), \quad (4.58b)$$

$$\kappa = 2.9 : \quad (\Delta q, \mathcal{K}, \mathcal{L}_q, \mathcal{L}_p, \mathcal{N}_q, \mathcal{N}_p, \eta) = (0.1012, 5, 2.8, 1.3, 1, 2, 1/10) \quad (\text{Sec. 4.4}). \quad (4.58c)$$

Note that the implementation for $\kappa = 0.5$ uses an enhanced ansatz for H_{reg}^0 including a separatrix, which will be explained in Sec. 4.6, while the results for $\kappa = 1.25$ and $\kappa = 2.9$ have been determined previously.

To estimate the quality of the normal-form approximations $\mathcal{F}_{\text{reg}}^n$, we compute their frequency function and their cost function. The frequency function of $\mathcal{F}_{\text{reg}}^n$ is evaluated straightforwardly as $\omega_n(J) = [\Omega(2J)]_n$ with Ω from Eq. (4.54). Note that, in contrast to the iterative canonical transformation method, this frequency function $\omega_n(J)$ changes during the iteration. The cost function of $\mathcal{F}_{\text{reg}}^n$ is evaluated as

$$\mathcal{L} = \frac{1}{N_p} \sum_{\tau} \sum_{\ell} |\mathbf{x}_{\ell}^{\tau} - \mathbf{x}_{\ell}^{\tau,n}|^2. \quad (4.59)$$

Here the normalization N_p and the sample points \mathbf{x}_{ℓ}^{τ} of the standard map are chosen as in Eq. (3.19). Moreover, the sample points $\mathbf{x}_{\ell}^{\tau,n}$ of the map $C \circ \mathcal{F}_{\text{reg}}^n \circ C^{-1}$ are chosen as follows. Based on the action computation of Sec. 4.2.1, we perform a bisection search on a line of initial conditions for a point with action $J = J^{\tau}$. Using this point $\mathbf{x}_0^{\tau,n}$ and the corresponding frequency ω^{τ} of the standard map, we compute

$$\mathbf{x}_{\ell}^{\tau,n} = (C \circ T) \left(e^{i\omega^{\tau}\ell} \cdot (C \circ T)^{-1}(\mathbf{x}_0^{\tau,n}) \right). \quad (4.60)$$

We first discuss the near-integrable case $\kappa = 0.5$. Here, the integrable approximations $\mathcal{F}_{\text{reg}}^n$ converge, showing no significant improvement after step $n = 8$. In Fig. 4.9(a) we show the numerically determined frequency function $\omega_8(J)$ of the normal-form approximation $\mathcal{F}_{\text{reg}}^8$ (violet line). For comparison, we also show the frequency data of the target system (dots) and the frequency function $\omega(J)$ of H_{reg}^n (red line). In Fig. 4.9(b) we show the cost function \mathcal{L} for $\mathcal{F}_{\text{reg}}^n$ (violet) and H_{reg}^n (red). Moreover, we

only find local invertibility for the truncated transformation $[T]_n$, thus the normal-form approximations $\mathcal{F}_{\text{reg}}^n$ have a restricted domain, see the white region in Fig. 4.9(c) for $n = 8$. This domain becomes smaller when the order n is increased. The restriction of the domain of $\mathcal{F}_{\text{reg}}^n$ is a manifestation of the invertibility problem, as discussed in Sec. 4.3.1 for the iterative canonical transformation method without damping. Note that, due to this restriction, only sample points from the elliptic phase-space region have been included in the cost functions in Fig. 4.9(b).

We now consider the case $\kappa = 1.25$. Here, the best normal-form approximation is obtained at step $n = 5$, see Fig. 4.10. For higher orders $n > 5$, the domain of $\mathcal{F}_{\text{reg}}^n$ becomes smaller than the target region, as shown in Fig. 4.10(d) for $\mathcal{F}_{\text{reg}}^8$. In the strongly non-integrable case $\kappa = 2.9$, the same phenomenon occurs, see Fig. 4.11. Generally, for higher perturbations κ , the domain of $\mathcal{F}_{\text{reg}}^n$ collapses faster with n .

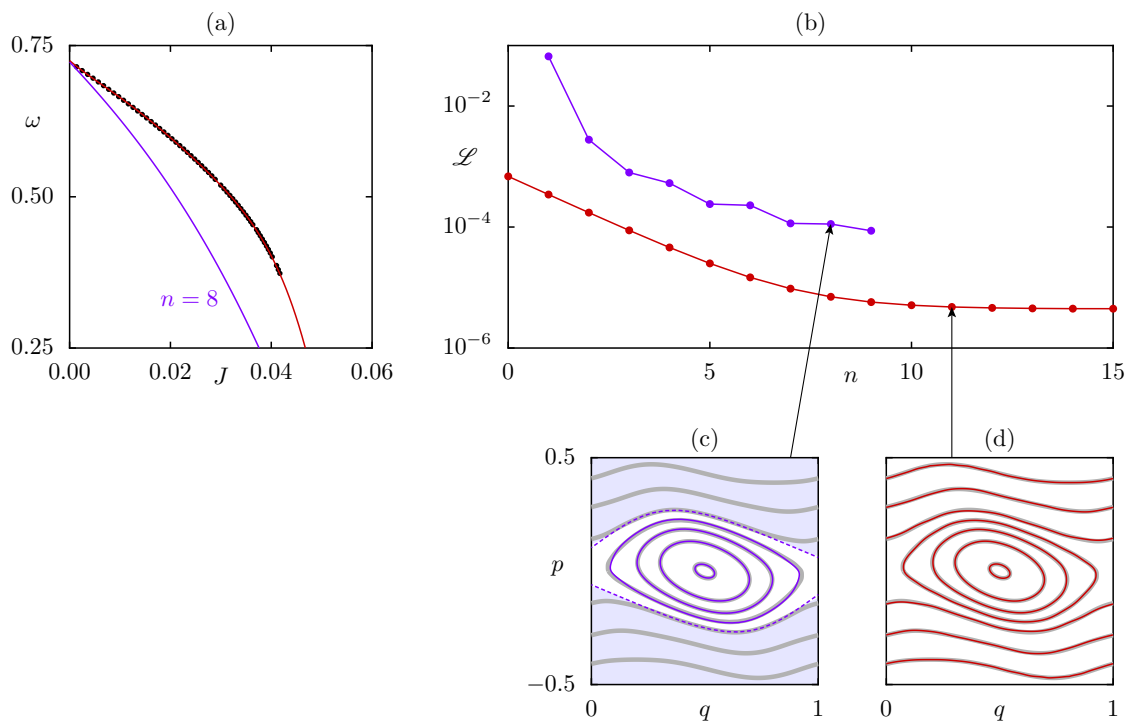


Figure 4.9.: Comparison of integrable approximations $\mathcal{F}_{\text{reg}}^n$ and H_{reg}^n of the standard map (4.4), for $\kappa = 0.5$. (a) Actions and frequencies (J^τ, ω^τ) of the standard map (black dots) with the frequency functions $\omega_8(J)$ of $\mathcal{F}_{\text{reg}}^8$ (violet) and $\omega(J)$ of H_{reg}^n (red). (b) Cost function \mathcal{L} vs. iteration step n for $\mathcal{F}_{\text{reg}}^n$ (violet), Eq. (4.59), and for H_{reg}^n (red), Eq. (3.19). (c–d) Phase space of the standard map (gray) and the integrable approximations $C \circ \mathcal{F}_{\text{reg}}^8 \circ C^{-1}$ (violet) (c), and H_{reg}^{11} (red) (d). In (c) the domain of $\mathcal{F}_{\text{reg}}^8$ is restricted to the white region inside the dashed torus.

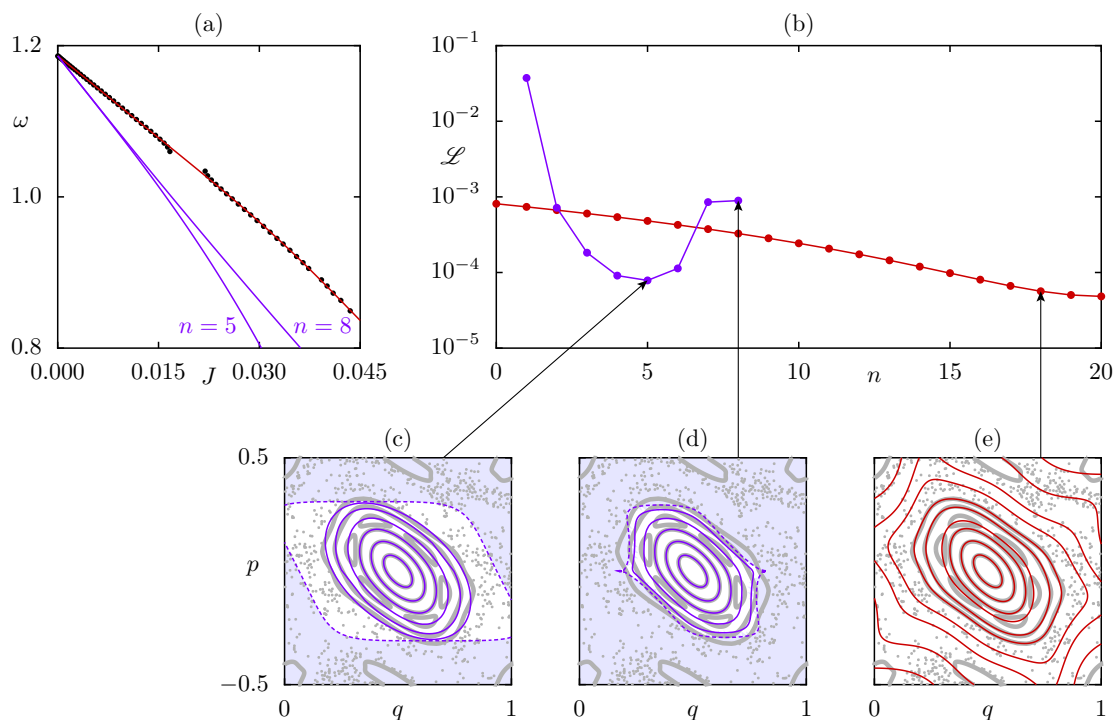


Figure 4.10.: Same as Fig. 4.9, but for $\kappa = 1.25$, $\mathcal{F}_{\text{reg}}^5$, $\mathcal{F}_{\text{reg}}^8$, and H_{reg}^{18} .

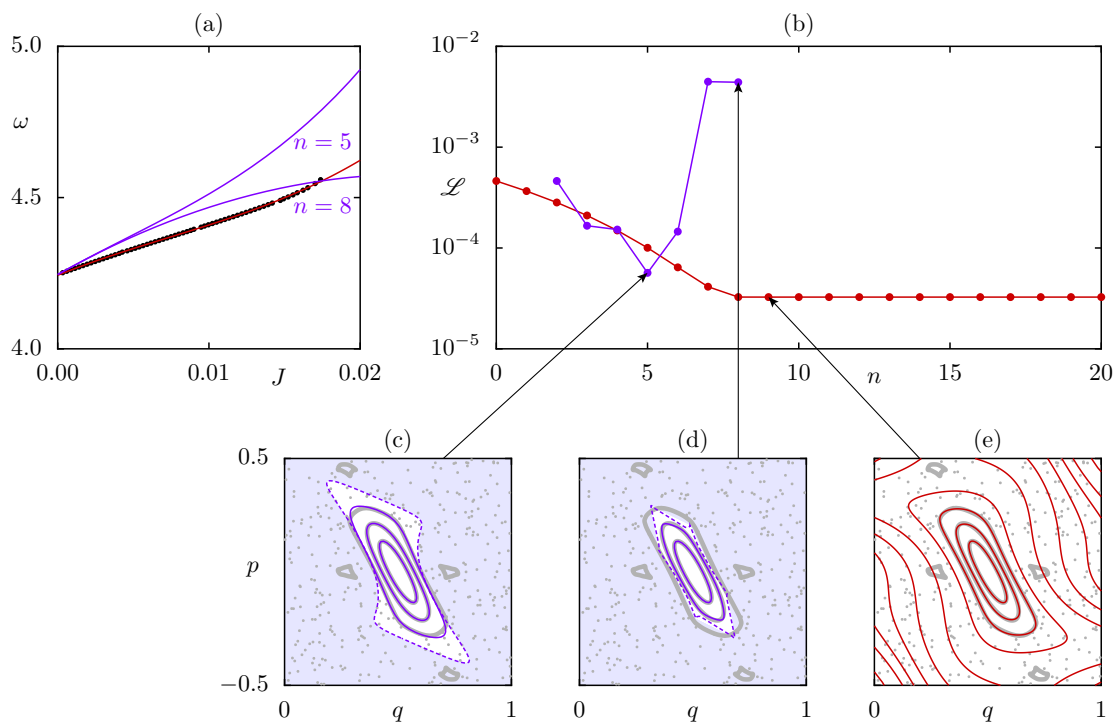


Figure 4.11.: Same as Fig. 4.9, but for $\kappa = 2.9$, $\mathcal{F}_{\text{reg}}^5$, $\mathcal{F}_{\text{reg}}^8$, and H_{reg}^9 .

4.5.3. Method of Lie transforms

The next considered method is the method of Lie transforms [8, 20–22], which we review in the following. Here, the starting point is a given Hamiltonian system $H(\mathbf{q}, \mathbf{p})$. The application of a certain canonical transformation $T : (\mathbf{q}, \mathbf{p}) \mapsto (\mathbf{q}', \mathbf{p}')$ would imply a new Hamiltonian, given by

$$K(\mathbf{q}', \mathbf{p}') = H [T^{-1}(\mathbf{q}', \mathbf{p}')]. \quad (4.61)$$

This idea is equivalent to the normal-form diagram (4.51) where the Hamiltonians H and K correspond to the maps \mathcal{F} and U , respectively. Generally, Lie transforms provide a systematic technique to construct the canonical transformation T when K is given. For this, T is represented by a Lie generating function $w(\mathbf{q}, \mathbf{p})$. Now, we assume the objects H , K , and w to depend on a small parameter ϵ and consider their expansions in ϵ , i. e.,

$$H = H_0 + \epsilon H_1 + \epsilon^2 H_2 + \dots, \quad (4.62a)$$

$$K = K_0 + \epsilon K_1 + \epsilon^2 K_2 + \dots, \quad (4.62b)$$

$$w = w_0 + \epsilon w_1 + \epsilon^2 w_2 + \dots \quad (4.62c)$$

From Eq. (4.61) one can derive a connection between K and w which is the Lie equation

$$\mathcal{D}_0 w_n = n(K_n - H_n) - \sum_{m=1}^{n-1} (L_{n-m} K_m - m \mathcal{T}_{n-m}^- H_m), \quad (n = 0, 1, 2, \dots). \quad (4.63)$$

Here, the differential operators \mathcal{D}_0 , L_n , and \mathcal{T}_n^- are given by

$$\mathcal{D}_0 = \frac{\partial}{\partial t} - \{H_0, \cdot\}, \quad (4.64a)$$

$$L_n = \{w_n, \cdot\}, \quad (4.64b)$$

$$\mathcal{T}_0^- = 1, \quad (4.64c)$$

$$\mathcal{T}_n^- = \frac{1}{n} \sum_{m=0}^{n-1} L_{n-m} \mathcal{T}_m^-, \quad (n = 1, 2, \dots). \quad (4.64d)$$

Now, given K , the Lie equation (4.63) allows to systematically construct the Lie generating function w in ascending orders of ϵ .

If we consider H as the target system with a mixed phase space, this scheme allows to construct integrable approximations as follows. First, we choose the decomposition (4.62a) such that H_0 is integrable and set $w_0 = 0$, which implies $K_0 = H_0$. Then, we iteratively choose K_n to be integrable and integrate Eq. (4.63) for w_n . After step n , we obtain a truncated integrable approximation

$$K_{\text{reg}}^n = \sum_{m=0}^n \epsilon^m K_m. \quad (4.65)$$

This strategy is commonly denoted as the *method of Lie transforms (for constructing integrable approximations)*, or sometimes also as *Deprit's method*. Also superconvergent versions of this method have been developed [48]. Although the Lie ansatz (4.61) is equivalent to the normal-form ansatz (4.52a), the two methods use principally different expansions. While the Lie expansion (4.62) is based on an arbitrary system parameter ϵ , the normal-form expansion (4.53) is done locally around the central fixed point in phase space.

4.5.4. Comparison to the method of Lie transforms

We now return to the special case of the standard map (4.4), which is the unit flow of a time-periodic Hamiltonian. For this class of systems, an implementation of the method of Lie transforms is given in Ref. [8]. Following this reference, we iteratively construct the integrable approximations K_{reg}^n up to order $n = 9$. Again, we consider the map parameters $\kappa = 0.5, 1.25$, and 2.9 .

Proceeding analogously to Sec. 4.5.2, we compute the frequency function and the cost function of the Lie approximations K_{reg}^n . Here some additional technical effort is necessary. As the frequency function $\omega_n(J)$ is not given explicitly, we compute a discrete sample by applying the numerical procedure of Sec. 4.2.1 to K_{reg}^n . Second, for the cost function (4.59), also the sample points $\mathbf{x}_\ell^{\tau,n}$ are computed numerically from $\mathbf{x}_0^{\tau,n}$. This is realized by the time evolution of K_{reg}^n over the timespan $\Delta t = \ell\omega^\tau/\omega_{\text{lie}}^\tau$. Here ω^τ and ω_{lie}^τ are the frequencies of the standard map \mathcal{U}^1 and of K_{reg}^n , respectively.

We begin with the near-integrable case $\kappa = 0.5$. Here the integrable approximation K_{reg}^n rapidly converges, such that no significant change is visible after $n = 6$ iteration steps. In Fig. 4.12(a) we show the numerically determined frequency function $\omega_6(J)$ (green line), which closely approximates the frequencies of the standard map (dots). For comparison, Fig. 4.12 also includes the corresponding information for the integrable approximations H_{reg}^n (red). We also show the cost function \mathcal{L} of H_{reg}^n and the phase space of H_{reg}^{11} for comparison (red). Regarding the frequency function, as well as the cost function, the results K_{reg}^6 and H_{reg}^{11} are of a comparable quality.

We now consider the case $\kappa = 1.25$. Here we also observe convergence of K_{reg}^n and stop the iteration at step $n = 9$, where no further improvement is achieved. In Fig. 4.13 we show the frequency function $\omega_9(J)$ and the cost function \mathcal{L} for K_{reg}^n (green) compared to the integrable approximation H_{reg}^{18} (red) obtained from the iterative canonical transformation method. Again the results K_{reg}^9 and H_{reg}^{18} are of a comparable quality, but less accurate compared to the near-integrable case $\kappa = 0.9$.

Finally, we look at the strongly non-integrable case $\kappa = 2.9$. Here, no convergence is observed, see Fig. 4.14, and K_{reg}^n does not reach a precision comparable to H_{reg}^9 . We again show the frequency function $\omega_5(J)$, the cost function \mathcal{L} , and the phase space of K_{reg}^5 (green) compared to the integrable approximation H_{reg}^9 (red) obtained from the iterative canonical transformation method. Here, K_{reg}^n does not reach a precision comparable to H_{reg}^9 .

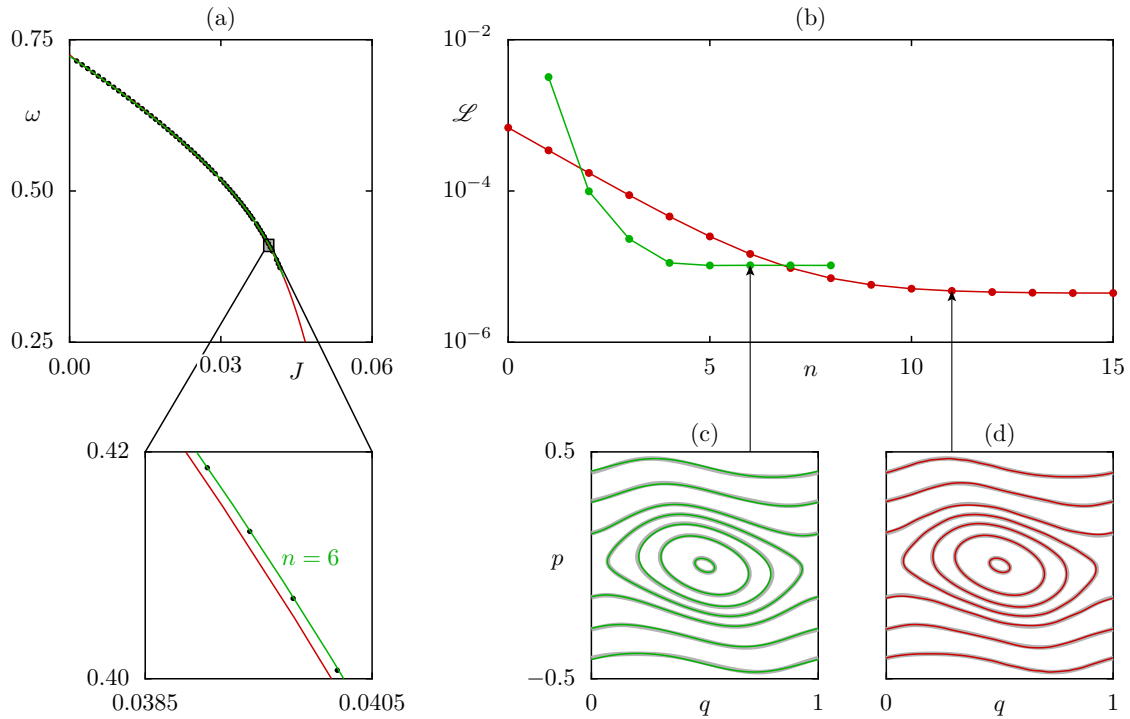


Figure 4.12.: Comparison of integrable approximations K_{reg}^n and H_{reg}^n of the standard map (4.4) for $\kappa = 0.5$. (a) Actions and frequencies (J^τ, ω^τ) of the standard map (black dots) with the frequency functions $\omega_6(J)$ of K_{reg}^6 (green) and $\omega(J)$ of H_{reg}^n (red). (b) Cost function \mathcal{L} vs. iteration step n for K_{reg}^n (green), Eq. (4.59), and for H_{reg}^n (red), Eq. (3.19). (c-d) Phase space of the standard map (gray) and the integrable approximations K_{reg}^6 (green) (c), and H_{reg}^{11} (red) (d).

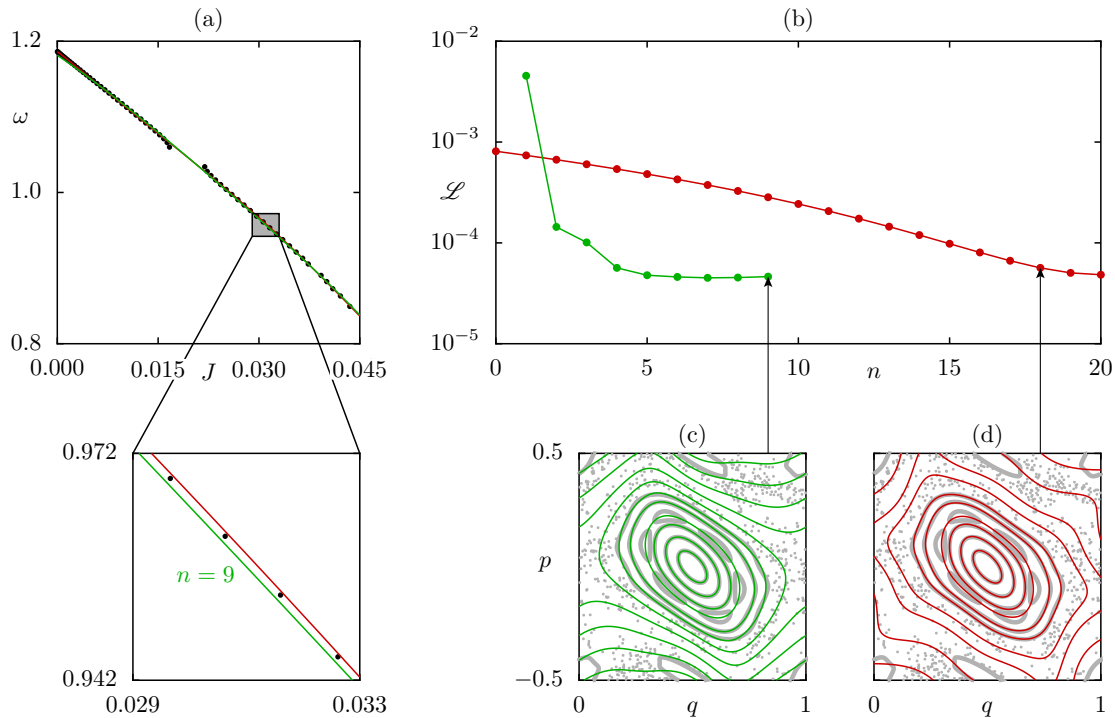


Figure 4.13.: Same as Fig. 4.12, but for $\kappa = 1.25$, K_{reg}^9 , and H_{reg}^{18} .

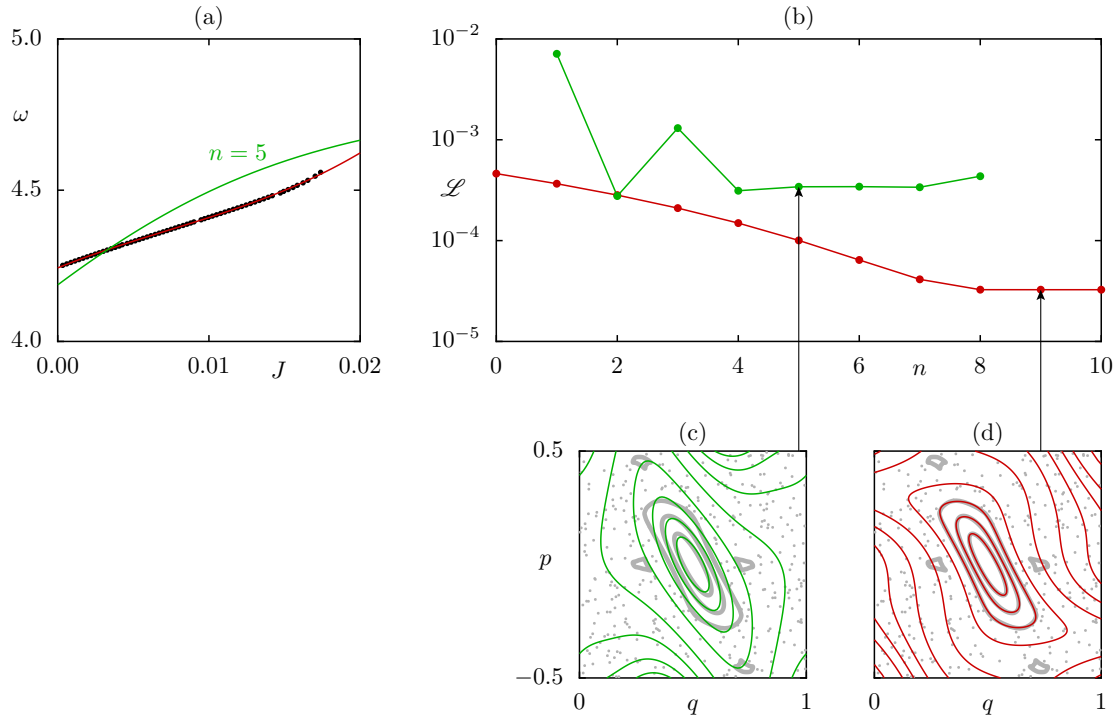


Figure 4.14.: Same as Fig. 4.12, but for $\kappa = 2.9$, K_{reg}^5 , and H_{reg}^9 .

4.5.5. Conclusion

We now summarize the results from Secs. 4.5.2 and 4.5.4. First, we discuss the complexity of the considered methods. Figure 4.15 shows the total computation time t_n (in seconds) after each iteration step n for the application to the standard map at $\kappa = 0.5$. Here our focus is not on the absolute time – which strongly depends on the architecture and programming language – but on the asymptotics. For the iterative canonical transformation method, we find a linear behavior $t_n \propto n$ (red line). This is expected, as each iteration step consists of the same number of operations. In contrast, both, the normal-form method (violet line) and the Lie method (green line) show an asymptotic behavior of at least $t_n \propto n^3$. This is characteristic for analytical methods, as the growing number of coefficients also requires more algebraic operations in each step.

Considering the quality of the presented results, we find that the iterative canonical transformation method provides integrable approximations which are comparable to, or even better than the Lie and normal-form approximations. This is verified when comparing the frequency functions as well as the cost functions.

For the near integrable case $\kappa = 0.5$, the results from the iterative canonical transformation method and the method of Lie transforms are comparable, while the method of normal forms fails to give a satisfactory approximation. This is due to the contraction of the domain of definition, which is faster than the convergence of the frequency function ω_n .

For $\kappa = 1.25$ the normal-form method becomes unstable, while the Lie approximation stays com-

parable to the approximation from the iterative canonical transformation method.

In the generic case $\kappa = 2.9$, both the Lie method and the method of normal forms fail to give a close approximation of the standard map, while the iterative canonical transformation method remains applicable. This is possible due to the damping mechanism, which stabilizes the iterative canonical transformation method.

These examples illustrate the inapplicability of traditional methods for strongly perturbed systems. Typically, this inapplicability manifests in integrable approximations, which either (i) give an inaccurate agreement to H (see Fig. 4.14(c)), (ii) diverge in the limit of high orders \mathcal{N} (see Fig. 4.11(c)), or (iii) converge only locally (see the inset at $(\mathcal{N}_q, \mathcal{N}_p) = (4, 4)$ in Fig. 4.7(a)). As expected, the damping mechanism solves these problems by (i–ii) allowing arbitrarily large truncation orders \mathcal{N} of the family of canonical transformations (Sec. 4.4) and by (iii) extending the region of convergence of H_{reg} (Sec. 4.3.3). With the invertibility problem of the generating function, we provided a perspective, where the connection between these three problems becomes obvious (Sec. 4.3.1).

The confirmed applicability of the iterative canonical transformation method to strongly non-integrable systems is the main achievement of this method. It is expected to be true also in higher dimensions, as is the theoretical foundation of the damping mechanism given in Sec. 4.3.

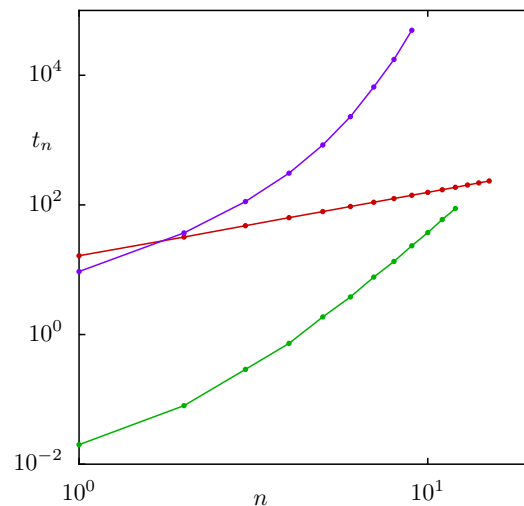


Figure 4.15.: Computation time t_n (in seconds) vs. iteration step n for the normal-form method (violet), the method of Lie transforms (green), and the iterative canonical transformation method (red).

4.6. Integrable approximations including a separatrix

In general, integrable systems can have phase-space structures of various topologies. In the iterative canonical transformation method, the topology is generated by the initial canonical transformation T_0 , Eq. (3.8). Up to now, T_0 was chosen from Eq. (4.7), which produces a phase space filled with elliptic tori, see Fig. 4.2(a). In many situations, this choice for T_0 is not suitable, as e. g., for the standard map with $\kappa = 0.5$. Here, the phase space consists of regions with topologically different dynamics, which are separated by a thin chaotic layer, see Fig. 4.16(a). In such a situation, integrable approximations with a purely elliptic structure are inconvenient. Even approximating only the yellow region in Fig. 4.16(a) is hard, as its outer tori tend to an edgy shape that is not well obtained from a smooth deformation of ellipses. The considered phase space is similar to that of a pendulum, see Fig. 4.16(b). In the following, we adapt the iterative canonical transformation method to this situation by choosing the transformation T_0 from the pendulum. As our focus is on the topological features, we only discuss the shape approximation. For the special features of the frequency function in pendulum-like systems, see, e. g., Ref. [22] or Sec. 4.7 for a more general case.

We consider the integrable pendulum Hamiltonian, given by

$$H_{\text{pend}}(q, p) = \frac{G}{2}p^2 - \cos q, \quad (4.66)$$

where $G > 0$ and $(q, p) \in [-\pi, \pi) \times \mathbb{R}$ with periodic boundary conditions in q -direction. As shown in Fig. 4.16(b), the phase space of this system is decomposed into three disjoint regions, which are separated by a one-dimensional, so-called *separatrix* (dashed red line). One finds a central region of libration (yellow) and two regions of rotation (green and white). As the two latter regions are connected by symmetry, we only discuss the green region where $p > 0$.

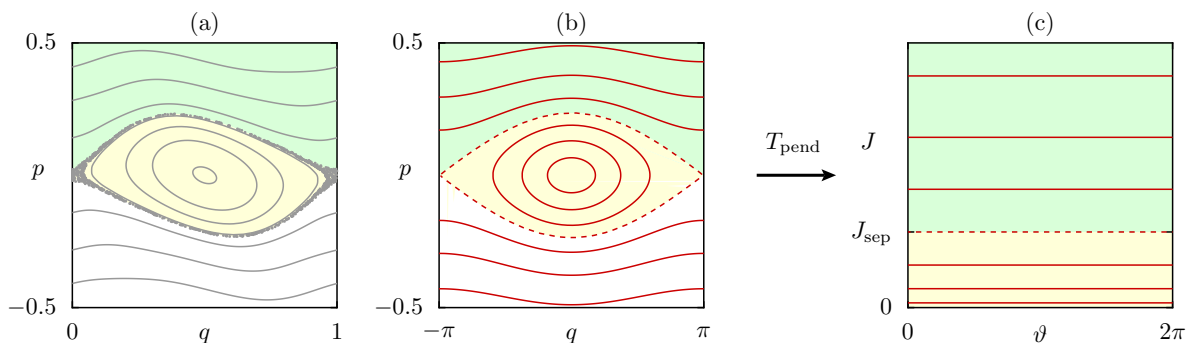


Figure 4.16.: (a) Phase space of the standard map (4.4), for $\kappa = 0.5$. (b–c) Phase space of the pendulum Hamiltonian (4.66), in its original coordinates (q, p) (b) and in action–angle coordinates (ϑ, J) (c). In all figures, the colors indicate different types of regular dynamics, i. e., libration (yellow) and rotation (green, white).

The motion of this system is mapped to action–angle coordinates using the transformation

$$T_{\text{pend}} : \quad \begin{pmatrix} q \\ p \end{pmatrix} \mapsto \begin{pmatrix} \vartheta(q, p) \\ J(q, p) \end{pmatrix}, \quad (4.67a)$$

given by [22],

$$\vartheta(q, p) = \pi \cdot \begin{cases} \frac{1}{2} \mathcal{K} [k(q, p)]^{-1} \mathcal{F} [\eta(q, p), k(q, p)] & k(q, p) < 1, \\ \mathcal{K} [k(q, p)^{-1}]^{-1} \mathcal{F} [\frac{1}{2}q, k(q, p)^{-1}] & k(q, p) > 1, \end{cases} \quad (4.67b)$$

$$J(q, p) = J_{\text{sep}} \cdot \begin{cases} \mathcal{E} [k(q, p)] - [1 - k(q, p)^2] \mathcal{K} [k(q, p)] & k(q, p) < 1, \\ \frac{1}{2} k(q, p) \mathcal{E} [k(q, p)^{-1}] & k(q, p) > 1. \end{cases} \quad (4.67c)$$

Here, $\mathcal{K}(k)$ and $\mathcal{E}(k)$ are the complete elliptic integrals of the first and second kind, respectively, and $\mathcal{F}(\eta, k)$ is the incomplete integral of the first kind [49]. Moreover we used

$$\eta(q, p) = \arcsin \left[\frac{\sin(\frac{1}{2}q)}{k(q, p)} \right], \quad (4.68)$$

$$k(q, p) = \sqrt{\frac{1 + H_{\text{pend}}(q, p)/G}{2}}, \quad (4.69)$$

and the action of the separatrix,

$$J_{\text{sep}} = \frac{8}{\pi\sqrt{G}}. \quad (4.70)$$

As follows from Eqs. (4.67), the transformation T_{pend} is discontinuous at the separatrix where $k(q, p) = 1$. In action–angle coordinates, this corresponds to the action $J = J_{\text{sep}}$, see Fig. 4.16(c). For the iterative canonical transformation method, the inverse transformation T_{pend}^{-1} would serve as a suitable choice for T_0 . To apply T_{pend}^{-1} , Eqs. (4.67) need to be inverted for (q, p) , which requires some technical effort, as discussed in App. D.

We now apply the iterative canonical transformation method using this transformation in order to produce an integrable approximation with a separatrix. More general, we choose the initial canonical transformation to be

$$T_0 = T_{\text{scale}} \circ T_{\text{pend}}^{-1}, \quad (4.71)$$

where T_{scale} shifts the stable fixed point to (q^*, p^*) and rescales the periodic q -domain to width δ , i. e.,

$$T_{\text{scale}} : \quad \begin{pmatrix} q \\ p \end{pmatrix} \mapsto \begin{pmatrix} q^* + \frac{\delta}{\pi} q \\ p^* + \frac{\pi}{\delta} p \end{pmatrix}. \quad (4.72)$$

The transformation T_0 thus depends on the parameters (q^*, p^*) , δ , and J_{sep} . For the standard map we set $(q^*, p^*) = (0.5, 0)$ and $\delta = 1$. To match the yellow areas of the librational phase-space

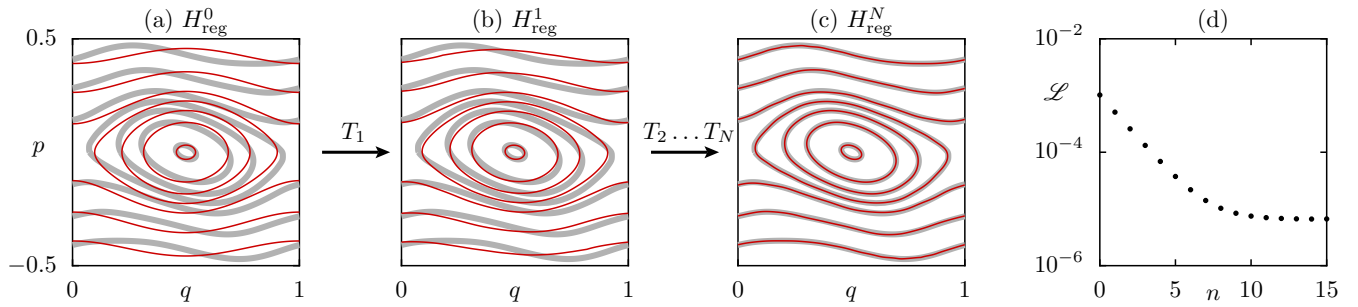


Figure 4.17.: (a–c) Phase space of the standard map (4.4), at $\kappa = 0.5$ (gray) compared to the tori (thin red lines) of (a) the initial integrable approximation H_{reg}^0 , (b) its transformation after the first iteration step T_1 , and (c) after the final iteration step T_N , $N = 15$. (d) Cost function \mathcal{L} , Eq. (3.19), vs. iteration step n .

regions in Figs. 4.16(a) and (b), we numerically determine this area A for the standard map and choose $J_{\text{sep}} = A/(2\pi)$, which for $\kappa = 0.5$ yields $J_{\text{sep}} = 0.048$. This leads to the initial integrable approximation H_{reg}^0 shown in Fig. 4.17(a) (red lines).

For the iterative improvement, we choose a set of initial conditions on a line going through both phase-space regions. Specifically, we use the points $(q_0^\tau, p_0^\tau) = (q^*, p^* + \frac{\tau}{100}\Delta p)$ with $\tau = 1, 2, \dots, 100$ and $\Delta p = 0.5$. Using these initial conditions, we perform the iterative improvement according to Sec. 4.2.2 with the parameters $(\mathcal{L}_q, \mathcal{L}_p) = (1, 3)$, $(\mathcal{N}_q, \mathcal{N}_p) = (7, 7)$, and a damping factor $\eta = 1/3$. Here, the choice $\mathcal{L}_q = 1$ is essential to preserve the phase-space periodicity in q -direction during each transformation. After $N = 15$ iteration steps, we obtain an integrable approximation H_{reg}^N which accurately resembles the shape of the target tori, see Fig. 4.17(c). We observe an improvement of the cost function over two orders of magnitude, see Fig. 4.17(d).

4.7. Integrable approximations including a nonlinear resonance chain

In this section, we present a further generalization of the iterative canonical transformation method, which generates integrable approximations including a nonlinear resonance chain. Note that this work was done in cooperation with my co-workers Julius Kullig and Normann Mertig and its results are reported in Refs. [50, 51].

4.7.1. Basic idea

As discussed in Sec. 2.3, the phase space of mixed systems is densely filled with nonlinear resonances. Up to now, integrable approximations have been constructed to interpolate through these resonances. In the following, we construct an integrable approximation to a regular phase-space region and one nonlinear resonance chain. This is preferable for certain applications, especially when one resonance is large and thus important for the physics of the target system.

Such a situation is shown in Fig. 4.18(a) for the standard map at $\kappa = 3.4$. This system has a dominant $r:s = 6:2$ resonance consisting of $r = 6$ resonance regions (green). Here s denotes the number

of resonance regions that are surpassed in one iteration step of \mathcal{U}^1 . Consequently, the r resonance regions are connected by the dynamics of \mathcal{U}^1 , see Fig. 4.18(a), a property which cannot be modeled by a time-independent integrable approximation. However, applying the r -fold map \mathcal{U}^r gives the same phase-space structure as \mathcal{U}^1 , while each resonance region is mapped onto itself. Therefore, we consider \mathcal{U}^r for constructing the integrable approximation. More specifically, the integrable approximation $H_{\text{reg}}(q, p)$ is constructed such that the final point of a time evolution over the timespan $\Delta t = r$ is close to $\mathcal{U}^r(q, p)$, if the initial point (q, p) is chosen from the target region.

Having said that, we now discuss how to choose the initial integrable approximation $H_{\text{reg}}^0(q, p)$, Eq. (3.9), with the appropriate phase-space topology to model the target region of \mathcal{U}^r including the resonance. As shown in Fig. 4.18(a), the resonance divides the phase space into r resonance regions of size $\bar{A}_{r:s}$ (green), an inner region of size \bar{A}_1 (yellow), and an outer region (white). A similar phase-space structure is described by the normal-form Hamiltonian [7, 8, 14, 52–55]

$$\mathcal{H}_{r:s}(\theta, I) = \mathcal{H}_0(I) + \mathcal{V}(I) \cos(r\theta), \quad (4.73)$$

where r is the order of the resonance. The phase space of this Hamiltonian consists of three integrable parts, see Fig. 4.18(c), which correspond to the different regions of \mathcal{U}^r from Fig. 4.18(a). This ansatz for $\mathcal{H}_{r:s}(\theta, I)$ contains two arbitrary functions $\mathcal{H}_0(I)$ and $\mathcal{V}(I)$ which will be determined in Sec. 4.7.2. Finally, the initial integrable approximation $H_{\text{reg}}^0(q, p)$ follows from $\mathcal{H}_{r:s}(\theta, I)$ by applying a simple canonical transformation

$$\tilde{T}_0 : \quad (\theta, I) \mapsto (q, p). \quad (4.74)$$

This transformation should map the tori of $\mathcal{H}_{r:s}(\theta, I)$ to the neighborhood of the corresponding tori of \mathcal{U}^r . In particular the torus with action $J = 0$ should be mapped onto the fixed point (q^*, p^*) of \mathcal{U}^r , see Fig. 4.18(b). An example is given in Sec. 4.7.3.

We mention, that the normal-form Hamiltonian $\mathcal{H}_{r:s}(\theta, I)$, Eq. (4.73), is not in action–angle coor-

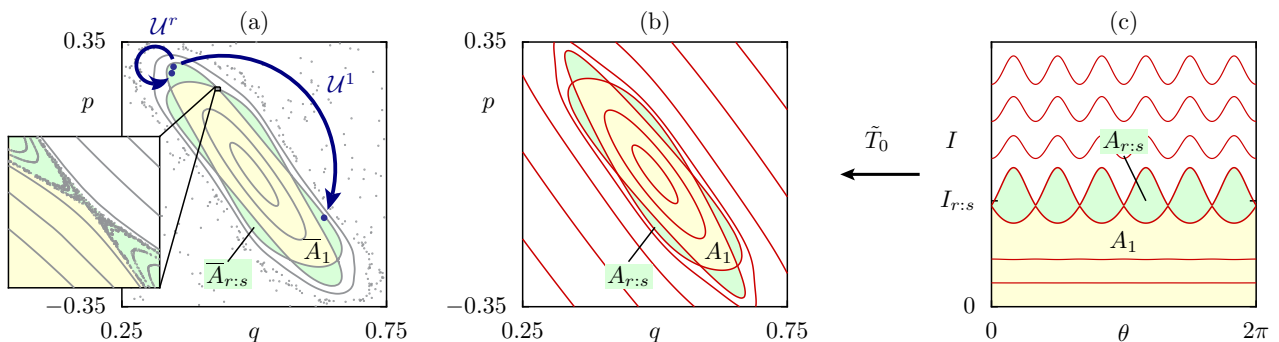


Figure 4.18.: (a) Phase space of the standard map at $\kappa = 3.4$ (gray) including the dominant 6:2 resonance chain of size $\bar{A}_{r:s}$ (green) with a chaotic layer (inset), and the central region of size \bar{A}_1 (yellow). The arrows indicate one iteration step, when applying the maps \mathcal{U}^1 and \mathcal{U}^r . (b) Phase space of $H_{\text{reg}}^0(q, p)$ (lines) with resonance regions of size $A_{r:s}$ (green) and the central region of size A_1 (yellow). (c) Phase space of $\mathcal{H}_{\text{reg}}(\theta, I)$ (lines) with the regions corresponding to (b).

dinates. However, integrability ensures a transformation to action–angle coordinates,

$$T^* : (\vartheta, J) \mapsto (\theta, I), \quad (4.75)$$

to exist for each integrable region in Fig. 4.18(c). Formally, the initial canonical transformation T_0 of the iterative canonical transformation method, Eq. (3.8), equals

$$T_0 = \tilde{T}_0 \circ T^*. \quad (4.76)$$

However, apart from special cases like the pendulum Hamiltonian [22], the transformation T^* is not known in a closed form. To use the normal-form ansatz (4.73), we thus start the construction in the coordinates (θ, I) , and, if necessary, use T^* numerically. The technical details of this numerical implementation of T^* are discussed in App. E.

The lack of a closed form for T_0 disables a direct access to the frequency function $\omega(J)$ and therefore a direct fit of $\mathcal{H}_{r:s}(\theta, I)$ via Eq. (3.5) is impossible. To apply the frequency approximation (Sec. 4.2.1), we solve this issue in the next section. However, the shape approximation (Sec. 4.2.2) is straightforward.

4.7.2. Frequency approximation

For the frequency approximation (Sec. 4.2.1) we first compute the sample points $\mathbf{x}_{\ell r}^\tau$ of \mathcal{U}^r given by Eq. (3.1) with the sample times $t_\ell = \ell r$. Secondly, we compute the action J^τ and frequency ω^τ of each orbit from Eqs. (3.2) and (3.3), respectively. Note that, according to this definition we have $\omega^\tau \in [-\frac{\pi}{r}, \frac{\pi}{r}]$ where $r\omega^\tau \in [-\pi, \pi]$ is the frequency of the discrete sequence $(\mathbf{x}_0^\tau, \mathbf{x}_r^\tau, \mathbf{x}_{2r}^\tau, \dots)$. Finally this leads to the dataset of actions and frequencies (J^τ, ω^τ) .

The next step is to adjust the integrable approximation $\mathcal{H}_{r:s}(\theta, I)$, Eq. (4.73), to this dataset according to the following criterion: For every torus of the map \mathcal{U}^r with action J^τ and frequency ω^τ , there should (i) exist a torus of $\mathcal{H}_{r:s}(\theta, I)$ with the same action $J = J^\tau$ having (ii) a similar frequency $\omega(J = J^\tau) \approx \omega^\tau$. Here $\omega(J)$ is the frequency function induced by the Hamiltonian $\mathcal{H}_{r:s}(\theta, I)$ in the corresponding parts of phase space. To achieve (i), $\mathcal{H}_{r:s}(\theta, I)$ must be chosen such that the total area $A_{r:s}$ of the resonance regions and the area A_1 below the resonance region agree with the corresponding areas of \mathcal{U}^r , see Fig. 4.18,

$$A_{r:s} \approx \bar{A}_{r:s}, \quad (4.77a)$$

$$A_1 \approx \bar{A}_1. \quad (4.77b)$$

To achieve (ii), $\mathcal{H}_{r:s}(\theta, I)$ must be chosen with frequencies close to those of \mathcal{U}^r such that Eq. (3.5) is minimized. Following Sec. 4.2.1, one would determine the integrable approximation from a direct fit of $\omega(J)$. However, as in the present situation the integrable approximation $\mathcal{H}_{r:s}(\theta, I)$ is not constructed in action–angle coordinates, a direct fit is impossible. Instead an enhanced strategy is needed, which we develop in the following.

We begin by choosing an expansion of the normal-form Hamiltonian $\mathcal{H}_{r:s}(\theta, I)$, Eq. (4.73), as

$$\mathcal{H}_0(I) = \frac{(I - I_{r:s})^2}{2M_{r:s}} + \sum_{k=3}^{\mathcal{K}} h_k (I - I_{r:s})^k, \quad (4.78)$$

and the lowest order ansatz for a resonance chain encircling a fixed point [14, 54, 55],

$$\mathcal{V}(I) = 2V_{r:s} \left(\frac{I}{I_{r:s}} \right)^{r/2}. \quad (4.79)$$

In the following, we determine the unknown parameters $\{I_{r:s}, M_{r:s}, V_{r:s}, h_k\}$ from the conditions (4.77) and (3.5) by analyzing $\mathcal{H}_{r:s}(\theta, I)$ first close to the resonance and secondly far away from the resonance.

Close to the resonance, the leading order expansion of $\mathcal{H}_{r:s}(\theta, I)$ around $I_{r:s}$ is the pendulum Hamiltonian [7, 8, 53]

$$\mathcal{H}_{r:s}(\theta, I) \approx \frac{(I - I_{r:s})^2}{2M_{r:s}} + 2V_{r:s} \cos(r\theta). \quad (4.80)$$

Here $I_{r:s}$ gives the location of the resonance, while $M_{r:s}$ and $V_{r:s}$ control the size $A_{r:s}$ of the resonance and the frequency at the center of the resonance region. We compute these parameters according to [9]

$$I_{r:s} = \frac{1}{2\pi} (\bar{A}_1 + \frac{1}{2}\bar{A}_{r:s}), \quad (4.81a)$$

$$M_{r:s} = \frac{\mu r^2}{16} \bar{A}_{r:s} \arccos \left(\frac{1}{2} \text{Tr} \bar{\mathcal{M}}_{r:s} \right)^{-1}, \quad (4.81b)$$

$$V_{r:s} = \frac{\mu}{32r^2} \bar{A}_{r:s} \arccos \left(\frac{1}{2} \text{Tr} \bar{\mathcal{M}}_{r:s} \right). \quad (4.81c)$$

This accounts for conditions (4.77) by matching the areas $\bar{A}_{r:s}$ and \bar{A}_1 of \mathcal{U}^r , see Fig. 4.18. Furthermore, the frequency at the center of the resonance region enters via the monodromy matrix $\bar{\mathcal{M}}_{r:s}$. Note that these parameters contain the essential information on action and frequency within the resonance regions. Finally, the sign μ can still be chosen.

We now determine the parameters $\{h_k\}$ which describe the frequency behavior far away from the resonance regions. There the frequency function is approximately

$$\omega(J) \approx \mathcal{H}'_0(J) = \frac{J - I_{r:s}}{M_{r:s}} + \sum_{k=3}^{\mathcal{K}} k h_k (J - I_{r:s})^{k-1}, \quad (4.82)$$

which neglects the resonance as a perturbation. In this approximation, Eq. (3.5) becomes

$$\sum_{\tau} |\omega^{\tau} - \mathcal{H}'_0(J^{\tau})|^2. \quad (4.83)$$

As \mathcal{H}'_0 is linear in the coefficients $\{h_k\}$, we determine them directly by minimizing Eq. (4.83).

4.7.3. Application to the standard map

We now apply the iterative canonical transformation method with resonance to the standard map. We first consider the parameter $\kappa = 3.4$ with a dominant 6:2 resonance, see Fig. 4.18(a).

Frequency approximation

We first compute the sample points $\mathbf{x}_{\ell_r}^\tau$ of \mathcal{U}^τ using $\ell_{\max} = 10^4$ iterates of 80 initial conditions on a line $(q^* + \lambda, p^*)$ with $\lambda \in (0, \Delta q]$ and $\Delta q = 0.0931$. We compute the dataset of actions and frequencies (J^τ, ω^τ) , which is depicted by the black dots in Fig. 4.19(a). Note that a similar procedure could be applied to the tori inside the considered resonance chain. However, for convenience we do not use those tori which will turn out to be sufficient.

By computing orbits close to the chaotic layer in Fig. 4.18(a), we approximate the areas \bar{A}_1 and $\bar{A}_{r:s}$ leading to the coefficients $\{I_{r:s}, M_{r:s}, V_{r:s}\}$ via Eqs. (4.81). For the involved sign we find $\mu = -1$, as the frequencies decrease with increasing action, see Fig. 4.19(a). Moreover, we determine the coefficients $\{h_k\}$ by minimizing Eq. (4.83). For $\mathcal{K} = 4$ we find a satisfactory agreement between the dataset (J^τ, ω^τ) and $\mathcal{H}'_0(J)$, see the red line in Fig. 4.19(a). Note that this comparison is meaningful only far from the resonance, where the approximation (4.82) is justified.

The resulting parameters determine the Hamiltonian $\mathcal{H}_{r:s}(\theta, I)$, see Fig. 4.18(c). For a global comparison, we perform a numerical evaluation of the exact frequency function $\omega(J)$ of $\mathcal{H}_{r:s}(\theta, I)$. We obtain a good agreement with a mean error of $\Delta\omega = 0.0002$ for the dataset (J^τ, ω^τ) and also near the resonance (light blue dots in Fig. 4.19(b)) we have $\Delta\omega < 0.001$. Moreover, even inside the resonance regions where no data of tori has been used for the optimization, but only the parameters of Eqs. (4.81), the frequency is well approximated, see Fig. 4.19(c).

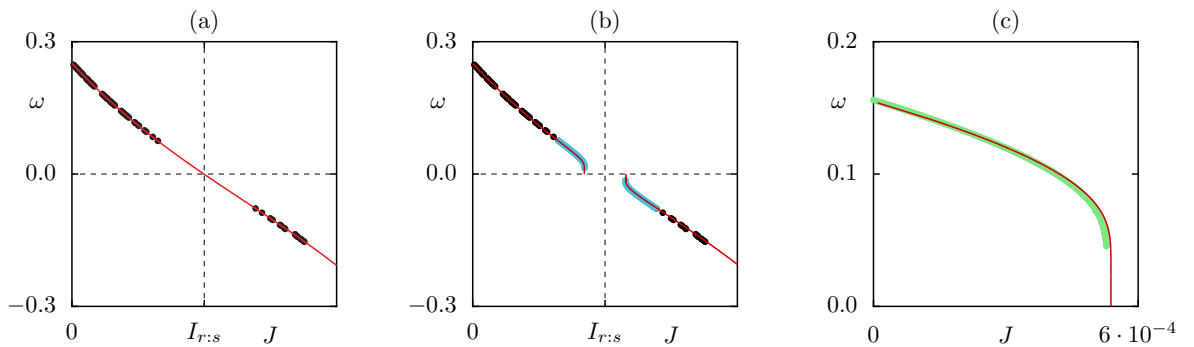


Figure 4.19.: (a) Numerically determined actions J^τ and frequencies ω^τ (black dots) fitted by $\mathcal{H}'_0(J)$, Eq. (4.82), with $\mathcal{K} = 4$ (red line). (b–c) Comparison of the frequency function $\omega(J)$ of the determined integrable approximation $\mathcal{H}_{r:s}(\theta, I)$ (red lines) to frequencies of \mathcal{U}^τ (dots): (b) the determined frequencies ω^τ (black dots), frequencies close to the resonance region (light blue dots), and (c) frequencies inside the resonance region (green dots).

Shape approximation

We now perform the shape approximation according to Sec. 4.2.2. For the transformation \tilde{T}_0 , Eq. (4.74), we choose

$$\tilde{T}_0 : \quad \begin{pmatrix} \theta \\ I \end{pmatrix} \mapsto \begin{pmatrix} q^* \\ p^* \end{pmatrix} + \mathcal{R} \begin{pmatrix} \sqrt{2J} \cos \vartheta \\ -\sqrt{2J} \sin \vartheta \end{pmatrix}, \quad (4.84)$$

with

$$\mathcal{R} = \begin{pmatrix} 1 & 1/2 \\ 0 & 1 \end{pmatrix} \begin{pmatrix} 1/\sqrt{\sigma} & 0 \\ 0 & \sqrt{\sigma} \end{pmatrix}. \quad (4.85)$$

Here, $\sigma = 3.96851$ is chosen such that the hyperbolic periodic points of the nonlinear resonance chain along the line $p = 0$ agree both for the standard map \mathcal{U}^r and $H_{\text{reg}}^0(q, p)$. The resulting initial integrable approximation $H_{\text{reg}}^0(q, p)$ is shown in Fig. 4.18(b).

The iterative improvement is performed according to Sec. 4.2.2 without any modifications. However, note that due to Eq. (4.76), computing the sample points requires the numerical application of T^* . Using the parameters $\mathcal{L}_q = \mathcal{L}_p = 1.1$, $\mathcal{N}_q = \mathcal{N}_p = 3$, $\eta = 1/4$, and $N = 15$ iteration steps, we obtain a sequence of improved integrable approximations H_{reg}^n as shown in Fig. 4.20.

The final integrable approximation H_{reg}^N gives a very good description of the regular region and the 6:2 resonance regions. Even the tori inside the resonance regions which have not yet been included in the cost function, are well approximated.

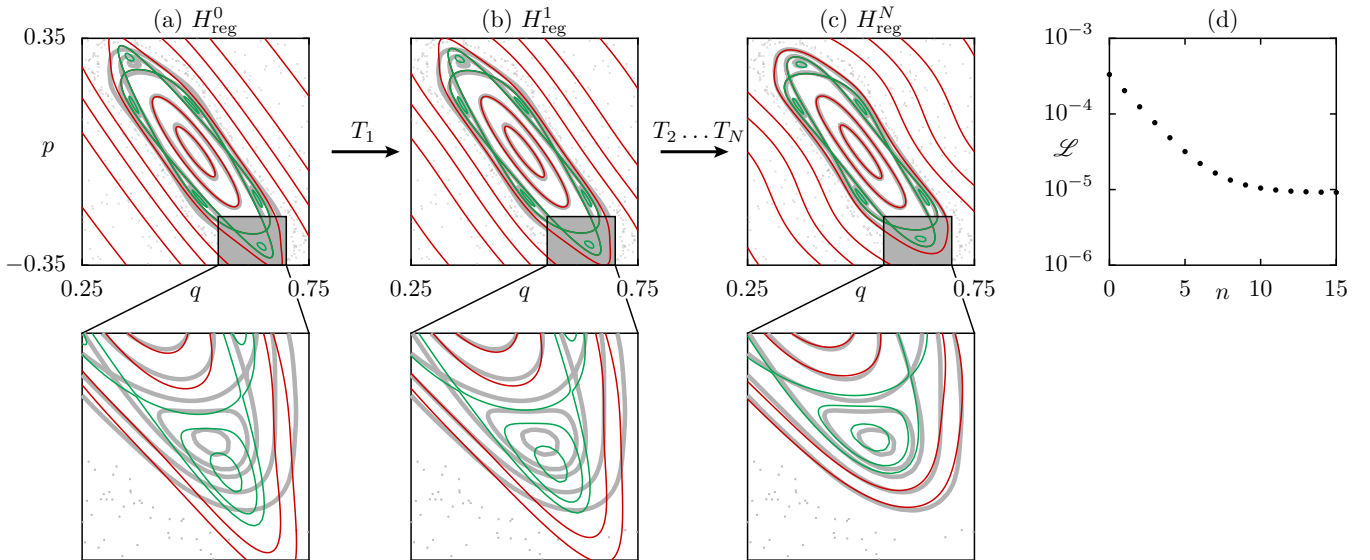


Figure 4.20.: (a–c) Phase space of the standard map (4.4), at $\kappa = 3.4$ (gray) compared to the tori (thin colored lines) of (a) the initial integrable approximation H_{reg}^0 , (b) its transformation after the first iteration step T_1 , and (c) after the final iteration step T_N , $N = 15$. (d) Cost function \mathcal{L} , Eq. (3.19), vs. iteration step n .

5. Integrable approximation of 2D billiards

In this chapter, we construct integrable approximations for 2D billiards. We first give an introduction to these billiard systems (Sec. 5.1) and develop a geometrically convenient description (Sec. 5.2). Then we explain their underlying scaling behavior (Sec. 5.3) and finally apply the iterative canonical transformation method (Sec. 5.4). This work is covered in Ref. [41].

5.1. Billiards

One very important class of Hamiltonian model systems are so-called *billiards*. They are important models to study questions of quantum chaos [56] and classical nonlinear dynamics [57]. This is done both numerically and experimentally, where microwave billiards are used [56, 58]. Relevant applications lie mainly in optics [59], especially in optical cavities and fibers.

Classically, a billiard describes a particle which is confined in a bounded domain $\Omega \subset \mathbb{R}^f$. While the particle moves freely inside Ω , it is elastically reflected on the boundary $\partial\Omega$. Hence, the dynamics is described by the Hamiltonian

$$H(\mathbf{q}, \mathbf{p}) = \begin{cases} \mathbf{p}^2 & \mathbf{q} \in \Omega \\ \infty & \mathbf{q} \notin \Omega \end{cases}. \quad (5.1)$$

Note that the particle's mass was set to $2m = 1$ for convenience. As $\frac{\partial H}{\partial \mathbf{q}}$ becomes infinite at the boundary $\partial\Omega$, the solutions of Hamilton's equations (2.1) are only defined in an asymptotical sense. More precisely, one considers a family of smooth Hamiltonians H_r which approach H as $r \rightarrow \infty$. By definition, the solutions of H are obtained from the solutions of H_r in this "hard wall limit". However, the practical determination of the solutions is much simpler. Here, one successively computes the intersections between straight rays of free motion and the boundary $\partial\Omega$. At each intersection point one reflects the momentum perpendicular to the boundary's tangential manifold.

In the following, we restrict to 2D billiards with $f = 2$ degrees of freedom, denoting the phase-space coordinates by $\mathbf{q} = (x, y)$ and $\mathbf{p} = (p_x, p_y)$. Hence, 2D billiards have a 4D phase space. The example system for this chapter will be the cosine billiard, which is a rectangle with $\mathbf{q} \in [-0.5, 0.5] \times \mathbb{R}_+$ whose upper boundary is replaced by the curve

$$r(x) = h + \frac{w}{2}[1 + \cos(2\pi x)]. \quad (5.2)$$

For $w = 0$, this system describes a rectangle billiard, which is integrable, see Fig. 5.1(a). Here, only periodic and quasiperiodic trajectories exist. For $w > 0$, the system becomes non-integrable. Figure

5.1(b) shows a generic case, $w = 0.033$, where one finds both regular (red, black) and chaotic solutions (blue). For sufficiently large deformations the system becomes macroscopically chaotic, as shown in Fig. 5.1(c) for $w = 0.22$.

We now take a closer look at the generic example $(h, w) = (0.2, 0.066)$ from Fig. 5.1(b). Here the vertical periodic trajectory at $x = 0$ (black line) is stable, see App. G. Therefore, it is surrounded by

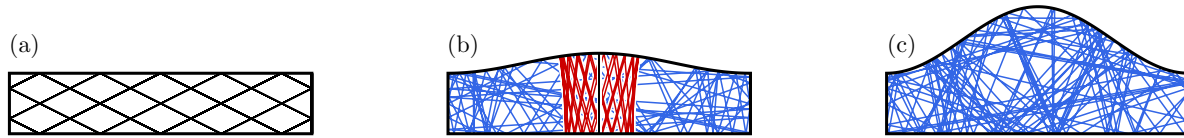


Figure 5.1.: Dynamics in the 2D cosine billiard (5.2), with $h = 0.2$. (a) Integrable case, $w = 0$, (b) generic case, $w = 0.033$, and (c) macroscopically chaotic case, $w = 0.22$. Shown are periodic (black), quasiperiodic (red), and chaotic trajectories (blue).

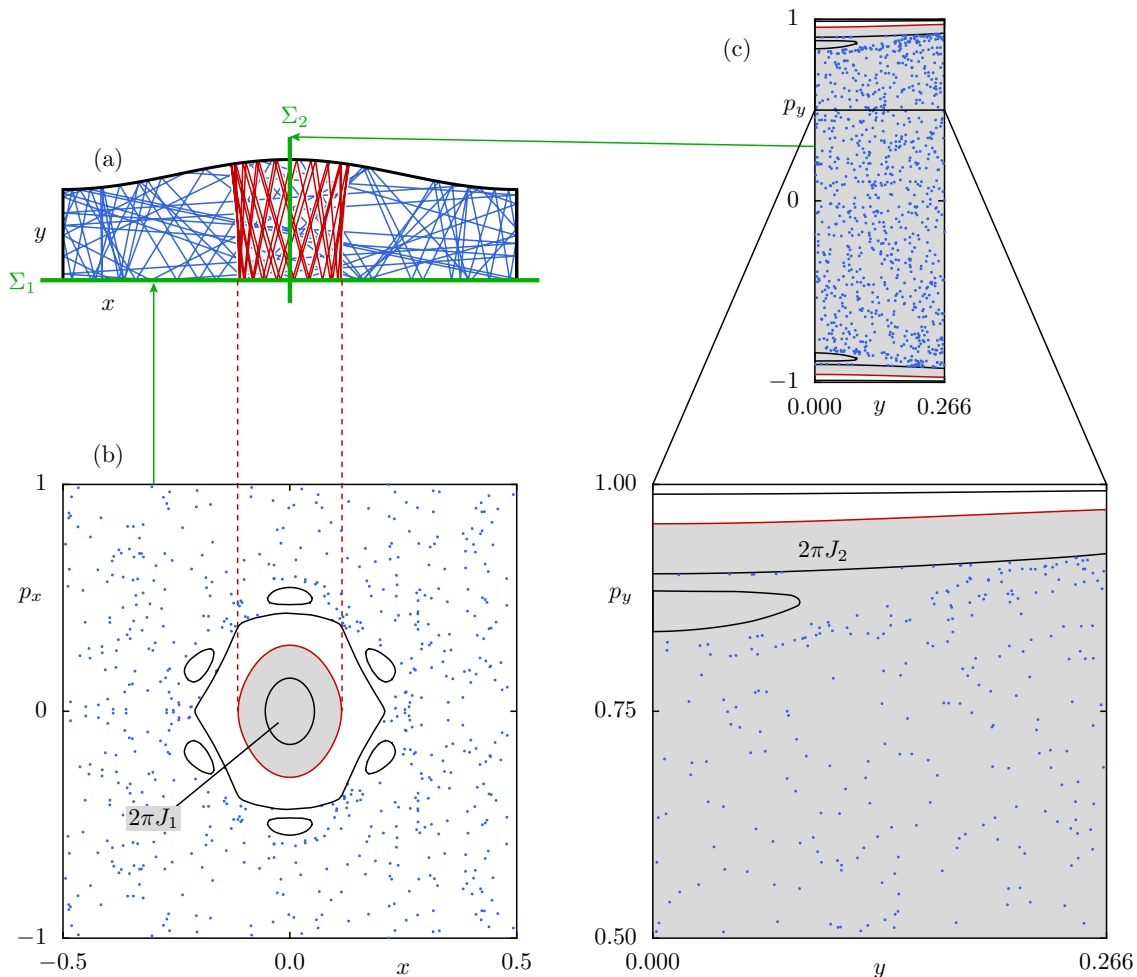


Figure 5.2.: (a) Cosine billiard (5.2), for $(h, w) = (0.2, 0.066)$ with a regular trajectory (red), a chaotic trajectory (blue), and the positions of the Poincaré sections Σ_1 and Σ_2 (green lines). (b) Dynamics of the induced Poincaré map \mathcal{P}_1 in Σ_1 with regular orbits (lines) and a chaotic orbit (dots). The gray area defines the action J_1 that is enclosed by the red orbit. (c) Same as (b), but for \mathcal{P}_2 , Σ_2 , and J_2 with a magnification of the region to $p_y \in [0.5, 1]$.

regular, quasiperiodic trajectories (red lines). According to Sec. 2, this quasiperiodic motion takes place on 2-tori in 4D phase space. To visualize these KAM tori, we define two Poincaré sections Σ_i given by $\Sigma_1 : (y = 0, p_y > 0)$ and $\Sigma_2 : (x = 0, p_x > 0)$, as indicated by the green lines in Fig. 5.2(a). Figures 5.2(b) and (c) show the intersections of some trajectories with these Poincaré sections Σ_1 and Σ_2 , respectively. In each Poincaré section Σ_i the quasiperiodic trajectory (red) induces a regular orbit of the Poincaré map \mathcal{P}_i , which densely fills a 1D curve, as expected from the dimensional analysis in Sec. 2.2. In Σ_1 , Fig. 5.2(b), this 1D curve is an elliptic 1-torus, enwrapping the stable fixed point $(x^*, p_x^*) = (0, 0)$ of the Poincaré map \mathcal{P}_1 , leading to a situation as known from the standard map. In Σ_2 , Fig. 5.2(c), this 1D curve has two disjoint segments with $p_y > 0$ and $p_y < 0$ (red lines). This is caused by the reflections at $y = 0$ and $y = h + w = 0.266$, which are visible in Σ_2 only, as this section lies perpendicular to the billiard boundary.

The two intersection curves of the torus with Σ_1 and Σ_2 are topologically independent, because they cannot be smoothly deformed into each other without leaving the torus. Hence, these intersection curves \mathcal{C}_i can be used as fundamental loops to define two actions J_i of the torus according to Eq. (2.27), see also Fig. 2.7. Then the J_i represent the areas enclosed in these loops, as indicated by the gray areas in Figs. 5.2(b) and (c).

5.2. Boundary simplification

Among other systems with $f = 2$ degrees of freedom, 2D billiards have certain advantages. Their trajectories follow from a purely geometrical construction, which simplifies their numerical and analytical treatment. Moreover, as will turn out in Sec. 5.3, the analysis can be effectively reduced by one dimension. However, one drawback of billiards is that the momentum solutions $\mathbf{p}(t)$ are discontinuous due to the reflections at the boundary. Therefore regular tori consist of disjoint parts in phase space, whose edges are related in a nontrivial way, depending on the shape of the billiard boundary. It seems difficult to directly find an integrable approximation $H_{\text{reg}}(\mathbf{q}, \mathbf{p})$ whose trajectories reproduce these properties. However, from a more general perspective, the fragmentation of the tori appears as a property of the present coordinate system (\mathbf{q}, \mathbf{p}) . Following this idea, one could “repair” the tori by introducing appropriate coordinates

$$\mathcal{T} : (\mathbf{q}, \mathbf{p}) \mapsto (\mathbf{Q}, \mathbf{P}), \quad (5.3)$$

in which they appear connected, such that the transformed solutions $(\mathbf{Q}(t), \mathbf{P}(t))$ are continuous.

In the following we construct such a transformation \mathcal{T} as a composition of two transformations

$$\mathcal{T} = \mathcal{T}_2 \circ \mathcal{T}_1. \quad (5.4)$$

Here, \mathcal{T}_1 is given by a point transformation

$$\mathcal{T}_1 : \begin{pmatrix} \mathbf{q} \\ \mathbf{p} \end{pmatrix} \mapsto \begin{pmatrix} \bar{\mathbf{q}}(\mathbf{q}) \\ \bar{\mathbf{p}}(\mathbf{q}, \mathbf{p}) \end{pmatrix}, \quad (5.5)$$

that maps the given billiard to a new system which should (i) have a preferably regular boundary shape and (ii) show elastic reflections on this boundary. If the original billiard domain Ω has \mathcal{C} corners, this number is necessarily preserved under smooth invertible transformations [60]. Therefore, the boundary simplification needs to be discussed separately for each class \mathcal{C} of billiards. In Fig. 5.3 we show such a transformation \mathcal{T}_1 in position space for a deformed circle billiard $\mathcal{C} = 0$ (a) and the cosine billiard $\mathcal{C} = 4$ (b). A derivation of \mathcal{T}_1 for these cases $\mathcal{C} = 0$ and $\mathcal{C} = 4$ is given in App. H, where we consider an arbitrary boundary shape. In the following, we sketch this derivation for the latter case. More precisely, we consider the general class of rectangular-like billiards, where the upper boundary curve $r(x)$ is arbitrary.

First we introduce the point transformation $(x, y) \mapsto (\bar{x}, \bar{y})$ in position space. We fill the inner billiard domain with a family of curves (see the vertical curves in Fig. 5.4) which define the contour lines of $\bar{x}(x, y)$. This family of curves is given by $x = f(\bar{x}, y)$ where the function f has to be determined. The transformation equations are

$$x(\bar{x}, \bar{y}) = f[\bar{x}, y(\bar{x}, \bar{y})], \quad (5.6a)$$

$$y(\bar{x}, \bar{y}) = r(\bar{x})\bar{y}. \quad (5.6b)$$

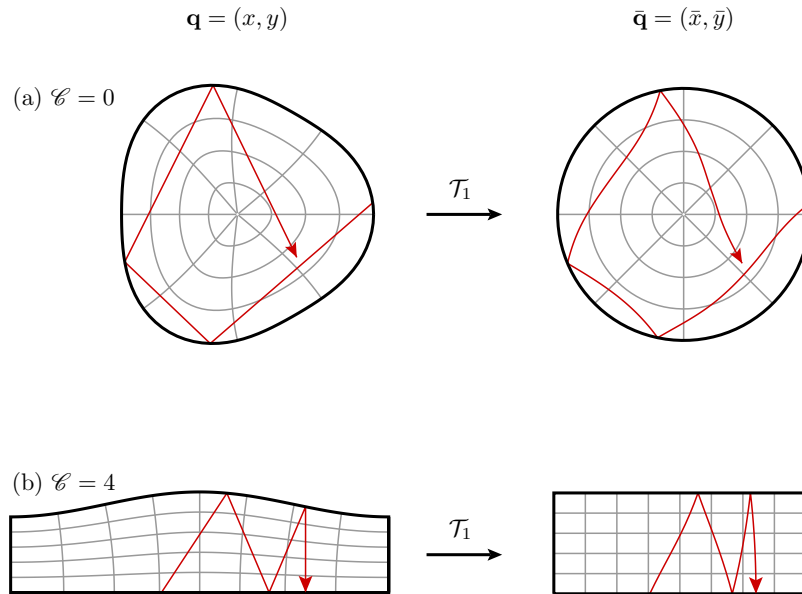


Figure 5.3.: Visualization of the transformation \mathcal{T}_1 used for the boundary simplification for billiards with \mathcal{C} corners, shown for $\mathcal{C} = 0$ (a) and $\mathcal{C} = 4$ (b). The transformed system in the new coordinates $\bar{\mathbf{q}} = (\bar{x}, \bar{y})$ (right) has a regular geometry and its trajectories (red lines) are elastically reflected at the boundary. Specifically, (a) shows a deformed circle given by $r(\phi) = 1 + \epsilon \cos(3\phi)$ with $\epsilon = 0.08$ and (b) shows the cosine billiard (5.2), with $(h, w) = (0.2, 0.066)$.

For practical reasons we require the coordinates x and \bar{x} to coincide at the upper boundary which leads to

$$f[\bar{x}, r(\bar{x})] = \bar{x}, \quad (5.7)$$

and ensures that $\bar{y} \in [0, 1]$. This position transformation (5.6) implies a canonical transformation in phase space, described by the generating function

$$F(\bar{x}, \bar{y}, p_x, p_y) = x(\bar{x}, \bar{y})p_x + y(\bar{x}, \bar{y})p_y. \quad (5.8)$$

Solving Eq. (2.9b) leads to the corresponding momentum transformation

$$\begin{pmatrix} p_x(\bar{x}, \bar{y}, \bar{p}_x, \bar{p}_y) \\ p_y(\bar{x}, \bar{y}, \bar{p}_x, \bar{p}_y) \end{pmatrix} = \begin{pmatrix} \frac{\partial x}{\partial \bar{x}} & \frac{\partial y}{\partial \bar{x}} \\ \frac{\partial x}{\partial \bar{y}} & \frac{\partial y}{\partial \bar{y}} \end{pmatrix} \Big|_{(\bar{x}, \bar{y})}^{-1} \begin{pmatrix} \bar{p}_x \\ \bar{p}_y \end{pmatrix}. \quad (5.9)$$

Here, the inverse matrix exists, if the underlying position transformation (5.6) is invertible. Taken together, Eqs. (5.6) and (5.9) define the transformation \mathcal{T}_1 which depends on the function f .

We now specify f by demanding elastic reflections at the boundary of the transformed system. Specifically, we require the transformed reflections to be of the form

$$\begin{pmatrix} \bar{p}_x \\ \bar{p}_y \end{pmatrix} \mapsto \begin{pmatrix} \bar{p}_x \\ -\bar{p}_y \end{pmatrix}, \quad \begin{pmatrix} \dot{\bar{x}} \\ \dot{\bar{y}} \end{pmatrix} \mapsto \begin{pmatrix} \dot{\bar{x}} \\ -\dot{\bar{y}} \end{pmatrix}, \quad (5.10)$$

at the lower ($\bar{y} = 0$) and upper boundary ($\bar{y} = 1$). As we show in App. H.3, this leads to the following

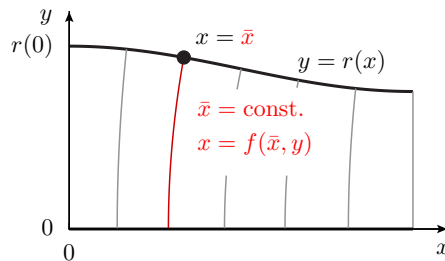


Figure 5.4.: Visualization of the billiard point transformation (5.6). The billiard domain is filled with a family of curves (vertical lines) that represent the contour lines of $\bar{x}(x, y)$ and intersect the upper boundary $y = r(x)$ at $x = \bar{x}$.

conditions for the function f

$$\frac{\partial f}{\partial \bar{x}}[\bar{x}, r(\bar{x})] = 1 + r'(\bar{x})^2, \quad (5.11a)$$

$$\frac{\partial f}{\partial y}[\bar{x}, r(\bar{x})] = -r'(\bar{x}), \quad (5.11b)$$

$$\frac{\partial f}{\partial y}(\bar{x}, 0) = 0, \quad (5.11c)$$

$$\frac{\partial^2 f}{\partial \bar{x} \partial y}(\bar{x}, 0) = -\frac{r'(\bar{x})}{r(\bar{x})} \frac{\partial f}{\partial y}(\bar{x}, 0). \quad (5.11d)$$

We solve the set of conditions (5.7) and (5.11) and obtain

$$f(\bar{x}, y) = \bar{x} + \frac{1}{2}r(\bar{x})r'(\bar{x}) - \frac{r'(\bar{x})y^2}{2r(\bar{x})}. \quad (5.12)$$

We verify that for the special case of the cosine billiard with $r(x)$ given by Eq. (5.2), the canonical transformation \mathcal{T}_1 is invertible everywhere in phase space if the parameters satisfy

$$\pi^2 w(h+w) < 1, \quad (5.13)$$

see App. H.4, Eq. (H.41). This includes all configurations of interest for which the central orbit is stable, see App. G.1, Eq. (G.5).

In Fig. 5.5(a) we visualize this transformation \mathcal{T}_1 , which maps the cosine billiard $H(\mathbf{q}, \mathbf{p})$ (left) to a system $H(\bar{\mathbf{q}}, \bar{\mathbf{p}})$ with a rectangular spatial domain (center). As required, the new system $H(\bar{\mathbf{q}}, \bar{\mathbf{p}})$ has elastic reflections at the boundary, but a nontrivial time evolution inside the rectangle, as shown for an example trajectory (red curve). In Fig. 5.5(b–c) we show the corresponding momentum components of the trajectory before (left) and after applying \mathcal{T}_1 (center). Here, as required, \bar{p}_x becomes continuous (Fig. 5.5(b), center) while \bar{p}_y flips its sign on the boundary (Fig. 5.5(c), center).

Furthermore, the sign flips of \bar{p}_y are removed by applying a simple unfolding transformation of the rectangle, $\mathcal{T}_2 : (\bar{\mathbf{q}}, \bar{\mathbf{p}}) \mapsto (\mathbf{Q}, \mathbf{P})$, given by

$$X = \bar{x}, \quad (5.14a)$$

$$Y = \begin{cases} \bar{y} & \bar{p}_y \geq 0 \\ 2 - \bar{y} & \bar{p}_y < 0 \end{cases}, \quad (5.14b)$$

$$P_x = \bar{p}_x, \quad (5.14c)$$

$$P_y = |\bar{p}_y|. \quad (5.14d)$$

As shown in Fig. 5.5(a), this flips the trajectory segments with $\bar{p}_y < 0$. The resulting components (X, Y) become smooth at $Y = 1$, where (\bar{x}, \bar{y}) visits the upper boundary. By imposing periodic boundary conditions, the jump from $Y = 2$ to $Y = 0$ is formally removed, leading to overall smooth trajectories (X, Y) . Also the momentum component P_y becomes continuous, see Fig. 5.5(c, right).

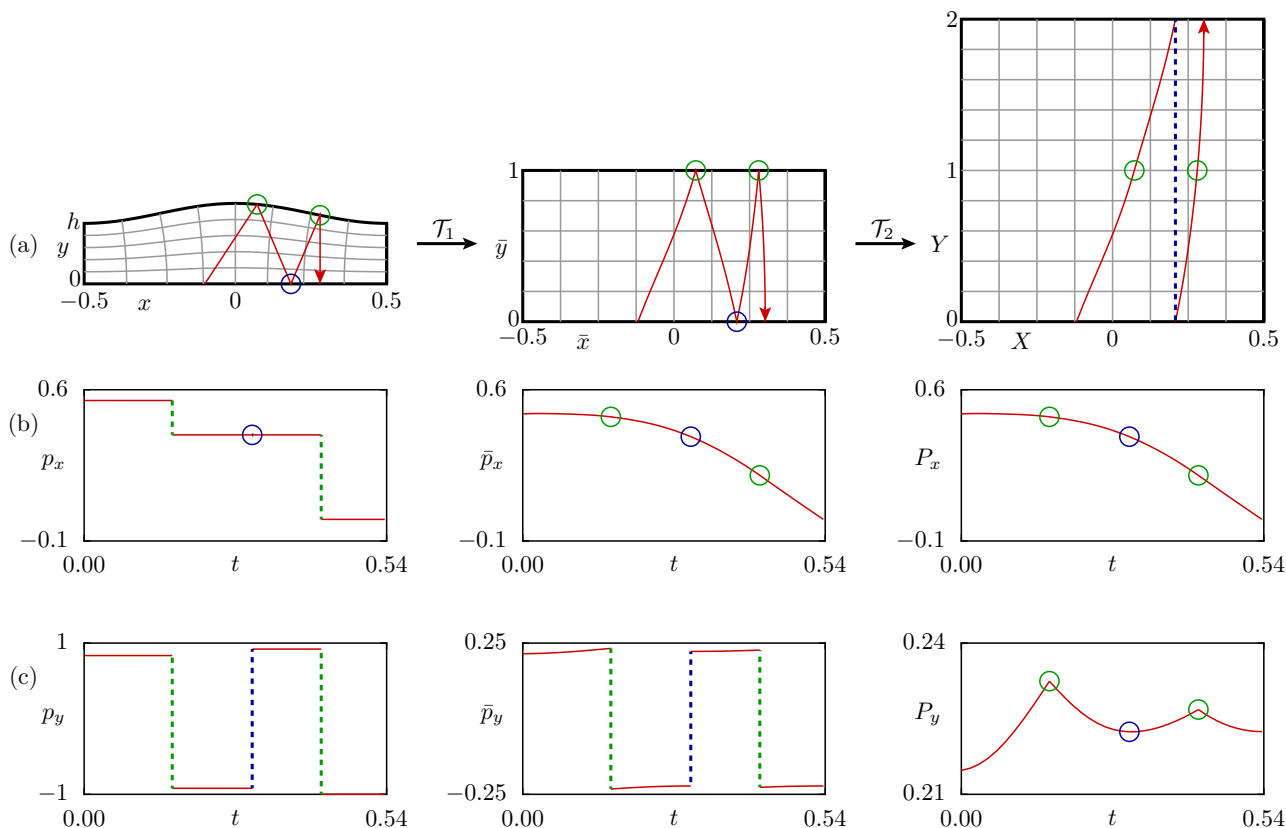


Figure 5.5.: (a) Cosine billiard and a trajectory (red line) in the coordinates $\mathbf{q} = (x, y)$ (left), $\bar{\mathbf{q}} = (\bar{x}, \bar{y})$ (center), and $\mathbf{Q} = (X, Y)$ (right) using the transformations \mathcal{T}_1 , Eq. (5.5), and \mathcal{T}_2 , Eq. (5.14). The colored dots correspond to the reflection points on the lower (blue) and upper boundary (green) of the original billiard trajectory (left). The gray grid shows lines of constant X and lines of constant Y . (b) Momentum components p_x (left), \bar{p}_x (center), and P_x (right) of the trajectory and its transformations (red). Colored circles and dashed lines indicate the corresponding reflection events from (a). (c) Same as (b), but for p_y , \bar{p}_y , and P_y .

Even, as shown in App. H.3, all trajectory components (X, Y, P_x, P_y) become also C^1 , except for the kinks in P_y at $Y = 1$ (green circles in Fig. 5.5(c, right)). Although the goal of continuous trajectories is achieved, one could go further and ask for a transformation \mathcal{T}_1 which also removes all higher order discontinuities. We verify, that this is impossible for any point transformation \mathcal{T}_1 . A proof is given in App. H.2.

5.3. Scaling systems

In the following we work out the characteristic scaling behavior of billiards and derive consequences for their integrable approximations. If we consider a particular billiard trajectory $(\mathbf{q}(t), \mathbf{p}(t))$ and a scaling factor $\lambda > 0$, then also the modified initial conditions $(\mathbf{q}(0), \lambda \mathbf{p}(0))$ would lead to a similar trajectory passing through the same path in \mathbf{q} -space, but slower or faster depending on λ . More

formally, if the solution $(\mathbf{q}(t), \mathbf{p}(t))$ has energy E , then for any $\lambda > 0$ the rescaled trajectory

$$\mathbf{q}_\lambda(t) := \mathbf{q}(\lambda t), \quad (5.15a)$$

$$\mathbf{p}_\lambda(t) := \lambda \mathbf{p}(\lambda t), \quad (5.15b)$$

is also a solution of the billiard and has energy $\lambda^2 E$. As we show in App. F, this behavior follows from the Hamiltonian's scaling property

$$H(\mathbf{q}, \lambda \mathbf{p}) = \lambda^2 H(\mathbf{q}, \mathbf{p}). \quad (5.16)$$

If we introduce the scaling operator in phase space

$$S_\lambda : (\mathbf{q}, \mathbf{p}) \mapsto (\mathbf{q}, \lambda \mathbf{p}), \quad (5.17)$$

we can rewrite this scaling property as

$$H \circ S_\lambda = \lambda^2 H, \quad (5.18)$$

and the rescaled solutions (5.15) as

$$(\mathbf{q}_\lambda, \mathbf{p}_\lambda)(t) := S_\lambda(\mathbf{q}, \mathbf{p})(\lambda t). \quad (5.19)$$

We now discuss some important properties of this general class of scaling Hamiltonians (5.16), which includes all billiards. According to Sec. 2.1, any solution is restricted to a $(2f - 1)$ -dimensional energy shell where $H(\mathbf{q}, \mathbf{p}) = E$. In scaling systems (5.16) such a solution of energy E is rescaled to a solution of unit energy $E' = 1$ by applying S_λ with $\lambda = 1/\sqrt{E}$. As this is true for *all solutions* of energy E , the operator S_λ relates the whole energy shell E to the unit energy shell $E' = 1$. As S_λ is invertible with $S_\lambda^{-1} = S_{\lambda^{-1}}$, this relation is bijective. Finally, as this is true for *all energies* $E > 0$, the unit energy shell contains the full information of the system¹. Consequently, any analysis of a scaling system (5.16) is reduced by one dimension to this unit energy shell, which for 2D billiards is a 3D region.

Moreover, for the action integral (2.8) we find the scaling

$$\mathcal{J}[S_\lambda \mathcal{C}] = \frac{1}{2\pi} \oint_{S_\lambda \mathcal{C}} \mathbf{p} d\mathbf{q} = \frac{1}{2\pi} \oint_{\mathcal{C}} (\lambda \mathbf{p}) d\mathbf{q} = \lambda \mathcal{J}[\mathcal{C}]. \quad (5.20)$$

Note that this is just a geometrical property of the operator S_λ for an arbitrary curve \mathcal{C} and thus holds independently of any underlying Hamiltonian system.

We now consider the subclass of scaling Hamiltonians (5.16) which are integrable. Following the decomposition of integrable systems into their frequency function $\boldsymbol{\omega}(\mathbf{J})$ and their canonical transfor-

¹If also negative energies are relevant, two unit energy shells $E' = \pm 1$ need to be considered, which, however, is not necessary for billiards.

mation T (see Sec. 2.2), we conclude special properties of these two objects. By combining the linear scaling (5.20) of the action with the quadratic scaling (5.16) of energy, we obtain a scaling of the action representation,

$$\mathcal{H}(\lambda\mathbf{J}) = \lambda^2\mathcal{H}(\mathbf{J}), \quad (5.21)$$

or equivalently for the frequency function

$$\omega(\lambda\mathbf{J}) = \lambda\omega(\mathbf{J}), \quad (5.22)$$

as follows from differentiating Eq. (5.21) with respect to action \mathbf{J} . Note that, as the action is a momentum variable, the scaling relation (5.21) is also of the form (5.18). As both Hamiltonians $\mathcal{H}(\mathbf{J})$ and $H(\mathbf{q}, \mathbf{p})$ fulfill the same scaling relation, their connecting canonical transformation $(\mathbf{q}, \mathbf{p}) = T(\boldsymbol{\vartheta}, \mathbf{J})$ must preserve this scaling, i. e.,

$$T \circ S_\lambda = S_\lambda \circ T. \quad (5.23)$$

Finally, if T is implied by a type-two generating function F , the scaling invariance (5.23) translates to a condition of F , which we derive in the following. For generality we consider a transformation between two arbitrary sets of coordinates $T : (\mathbf{q}, \mathbf{p}) \mapsto (\mathbf{q}', \mathbf{p}')$, which do not necessarily include action–angle coordinates. Considering the implicit-function description of T via Eq. (4.17), the condition (5.23) reads

$$\phi(\mathbf{x}, \mathbf{x}') = 0 \quad \Leftrightarrow \quad \phi(S_\lambda\mathbf{x}, S_\lambda\mathbf{x}') = 0. \quad (5.24)$$

Here, we only need to consider the implication from left to right, as the inverse direction is still included when replacing $\lambda \mapsto \lambda^{-1}$. Written in components, Eq. (4.18), this statement becomes²

$$\begin{pmatrix} \mathbf{q}' \\ \mathbf{p} \end{pmatrix} = \begin{pmatrix} \frac{\partial F}{\partial \mathbf{p}'}(\mathbf{q}, \mathbf{p}') \\ \frac{\partial F}{\partial \mathbf{q}}(\mathbf{q}, \mathbf{p}') \end{pmatrix} \quad \Rightarrow \quad \begin{pmatrix} \mathbf{q}' \\ \lambda\mathbf{p} \end{pmatrix} = \begin{pmatrix} \frac{\partial F}{\partial \mathbf{p}'}(\mathbf{q}, \lambda\mathbf{p}') \\ \frac{\partial F}{\partial \mathbf{q}}(\mathbf{q}, \lambda\mathbf{p}') \end{pmatrix}. \quad (5.25)$$

Substituting the left equations into the right ones, we obtain two purely functional equations

$$\frac{\partial F}{\partial \mathbf{p}'}(\mathbf{q}, \lambda\mathbf{p}') = \frac{\partial F}{\partial \mathbf{p}'}(\mathbf{q}, \mathbf{p}'), \quad (5.26a)$$

$$\frac{\partial F}{\partial \mathbf{q}}(\mathbf{q}, \lambda\mathbf{p}') = \lambda \frac{\partial F}{\partial \mathbf{q}}(\mathbf{q}, \mathbf{p}'). \quad (5.26b)$$

Neglecting the freedom of an additive constant in F , which is practically irrelevant, this is equivalent

²For convenience, the symbol $\frac{\partial F}{\partial \mathbf{p}'}(\cdot, \cdot)$ denotes the derivative of F with respect to the second argument regardless of its value, e. g., $\frac{\partial F}{\partial \mathbf{p}'}F(\mathbf{q}, \lambda\mathbf{p}') = \lambda \frac{\partial F}{\partial \mathbf{p}'}(\mathbf{q}, \lambda\mathbf{p}')$.

to

$$F(\mathbf{q}, \lambda \mathbf{p}') = \lambda F(\mathbf{q}, \mathbf{p}'). \quad (5.27)$$

This scaling relation of the generating function F ensures the scaling invariance (5.23) of the induced canonical transformation T .

5.4. Application of the iterative canonical transformation method

In this section we show the construction of integrable approximations for 2D billiards via the iterative canonical transformation method. For this we take advantage of the special coordinates (\mathbf{Q}, \mathbf{P}) (Sec. 5.2) and the billiard-specific scaling (Sec. 5.3). As a generic example system we consider the cosine billiard (5.2), at the parameters $(h, w) = (0.2, 0.066)$ where it is strongly non-integrable, see Fig. 5.2.

5.4.1. Frequency approximation

To define the action representation $\mathcal{H}_{\text{reg}}(\mathbf{J})$ of the integrable approximation, we first compute points on a set of tori of the billiard H . As these tori are 2D manifolds in the 4D phase space, there exist 2 independent directions perpendicular to a given torus. As discussed in Sec. 5.3, it suffices to explore the phase space only along one direction of constant energy $E = 1$ while requiring the scaling relation (5.21) for $\mathcal{H}_{\text{reg}}(\mathbf{J})$. For this curve we choose a fixed position at the top of the billiard and a momentum parametrized by an angle α ,

$$x_0 = 0, \quad (5.28a)$$

$$y_0 = h + w, \quad (5.28b)$$

$$p_{x0} = \sin \alpha, \quad (5.28c)$$

$$p_{y0} = -\cos \alpha, \quad (5.28d)$$

with $\alpha \in (0, 0.3926]$. For 100 initial conditions on this curve we calculate a trajectory with 10^4 reflections, sampling the regular tori. We compute their intersections with Σ_1 and Σ_2 to determine the actions $\mathbf{J}^\tau = (J_1^\tau, J_2^\tau)$ using Eq. (2.8), see the dots in Fig. 5.6(a). We compute the frequencies $\boldsymbol{\omega}^\tau = (\omega_1^\tau, \omega_2^\tau)$ for each torus.

According to Sec. 3.2 we now determine the Hamiltonian $\mathcal{H}_{\text{reg}}(\mathbf{J})$ which connects the actions to the corresponding energies. As it must fulfill the scaling relation (5.21), it can be written, e. g., as

$$\mathcal{H}_{\text{reg}}(\mathbf{J}) = J_2^2 \cdot \mathcal{F}(J_1/J_2), \quad (5.29)$$

with some scalar function \mathcal{F} . Expressing \mathcal{F} as a power series, the general ansatz (3.4) obtains the

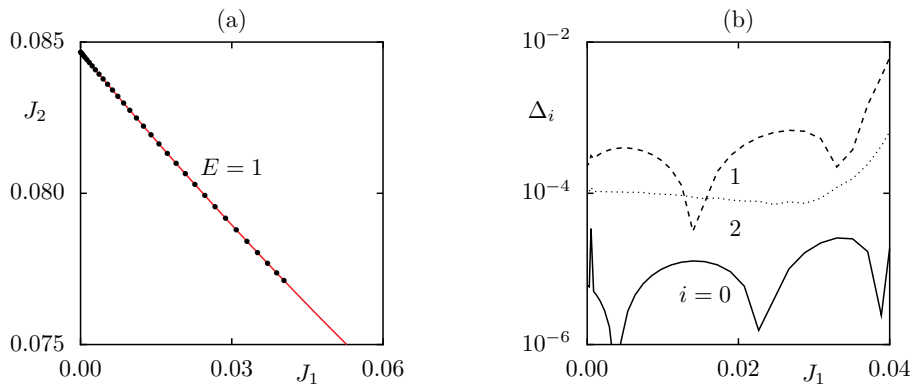


Figure 5.6.: (a) Numerically determined actions $\mathbf{J}^\tau = (J_1^\tau, J_2^\tau)$ of the cosine billiard (dots) and contour line $E = 1$ (red) of the integrable Hamiltonian $\mathcal{H}_{\text{reg}}(\mathbf{J})$, Eq. (5.29). (b) Relative error Δ_0 of the energy (solid) and the frequencies Δ_1 (dashed) and Δ_2 (dotted).

form

$$\mathcal{H}_{\text{reg}}(\mathbf{J}) = J_2^2 \cdot \sum_{k=0}^{\mathcal{K}} h_k \cdot (J_1/J_2)^k. \quad (5.30)$$

With $k \geq 0$ this ensures finite energies in the center of the regular island, where $J_1 = 0$, see Fig. 5.2. We determine the coefficients $\{h_k\}$ such that Eq. (3.7) is minimized. For $\mathcal{K} = 2$ we show in Fig. 5.6(a) the contour line $E = 1$ of $\mathcal{H}_{\text{reg}}(\mathbf{J})$ in good agreement with the numerical actions \mathbf{J}^τ . In Fig. 5.6(b) we plot the relative errors of the energy $\Delta_0 = |[\mathcal{H}_{\text{reg}}(\mathbf{J}^\tau) - E]/E|$ for $E = 1$ and of the frequencies $\Delta_i = |[\partial\mathcal{H}_{\text{reg}}(\mathbf{J}^\tau)/\partial J_i - \omega_i^\tau]/\omega_i^\tau|$ with $i = 1, 2$. Here we use the numerically determined frequencies ω_i^τ of the cosine billiard for comparison. All relative errors Δ_i are lower than 10^{-2} .

5.4.2. Shape approximation

In the following we use the special coordinates (\mathbf{Q}, \mathbf{P}) defined in Sec. 5.2, which give a continuous representation of trajectories in phase space. In these coordinates we determine an integrable approximation $H_{\text{reg}}(\mathbf{Q}, \mathbf{P})$ of $H(\mathbf{Q}, \mathbf{P})$. Finally by returning to the original billiard coordinates (\mathbf{q}, \mathbf{p}) we find the integrable approximation $H_{\text{reg}}(\mathbf{q}, \mathbf{p})$ of $H(\mathbf{q}, \mathbf{p})$.

Note that the transformation \mathcal{T} leading to (\mathbf{Q}, \mathbf{P}) preserves the scaling, Eq. (5.23), such that $H(\mathbf{Q}, \mathbf{P})$ also fulfills the scaling relation (5.16). Moreover, both actions $\mathbf{J} = (J_1, J_2)$ are preserved under \mathcal{T} , individually, such that the previously determined Hamiltonian $H_{\text{reg}}(\mathbf{J})$ remains valid for $H(\mathbf{Q}, \mathbf{P})$.

Initial integrable approximation

We now define the initial transformation T_0 which generates the topology of the tori. As shown in Figs. 5.7(a) and (d), these tori combine a libration in the (X, P_x) -projection with a rotation along the

periodic Y -direction. This behavior is modeled by choosing T_0 as

$$X = \sqrt{\frac{2J_1}{\delta J_2}} \cos \vartheta_1, \quad (5.31a)$$

$$P_x = -\sqrt{2\delta J_1 J_2} \sin \vartheta_1, \quad (5.31b)$$

$$Y = \frac{1}{\pi} \vartheta_2 + \frac{J_1}{\pi J_2} \sin \vartheta_1 \cos \vartheta_1, \quad (5.31c)$$

$$P_y = \pi J_2. \quad (5.31d)$$

The first two Eqs. (5.31a) and (5.31b) lead to the desired, elliptic dynamics in the (X, P_x) -projection with action J_1 and half-axis ratio δJ_2 , see the red lines in Fig. 5.7(b). We choose the constant parameter δ to reproduce the linearized dynamics around the stable periodic orbit at $Y = 0$. For this we derive an analytical expression for δ as a function of the cosine billiard parameters h and w , see App. G.2, Eq. (G.8). Equations (5.31c) and (5.31d) describe dynamics with constant momentum P_y , see the red lines in Fig. 5.7(e). On average Y increases linearly with ϑ_2 such that $\vartheta_2 \in [0, 2\pi)$ is mapped to $Y \in [0, 2)$ with periodic boundary conditions, see the red lines in Fig. 5.7(e). The second, oscillatory term in Eq. (5.31c) is required to make the transformation canonical. As the average of this term vanishes, the coordinates Y and ϑ_2 both move with the same frequency ω_2 . We finally obtain an initial integrable approximation $H_{\text{reg}}^0(\mathbf{Q}, \mathbf{P})$. As T_0 fulfills Eq. (5.23), the scaling relation (5.16) is ensured for $H_{\text{reg}}^0(\mathbf{Q}, \mathbf{P})$. Figures 5.7(b) and (e) show that the tori of H and H_{reg}^0 agree close to the central trajectory.

Family of canonical transformations

To improve H_{reg}^0 , we introduce a family of canonical transformations $T^{\mathbf{a}}$, given by a generating function

$$F^{\mathbf{a}}(\mathbf{Q}, \mathbf{P}') = \mathbf{Q}\mathbf{P}' + G(\mathbf{Q}, \mathbf{P}'), \quad (5.32)$$

with the perturbation

$$G(\mathbf{Q}, \mathbf{P}') = \sum_{\nu=1}^{\mathcal{N}} a_{\nu} G_{\nu}(\mathbf{Q}, \mathbf{P}'). \quad (5.33)$$

In the following, we specify the perturbation $G(\mathbf{Q}, \mathbf{P}')$ according to (i) the scaling relation, (ii) the symmetries, and (iii) the phase-space geometry.

(i) To preserve the scaling relation (5.18), $F^{\mathbf{a}}$, and thus also G , must satisfy the conditions (5.27). This is ensured by the form

$$G(\mathbf{Q}, \mathbf{P}') = P' g(\mathbf{Q}, \theta'), \quad (5.34)$$

which uses the polar representation $\mathbf{P}' = (P' \cos \theta', P' \sin \theta')$ with $\theta' \in [0, \pi)$ and an arbitrary function $g(X, Y, \theta')$ of 3 variables only.

(ii) The systems H and H_{reg}^0 both have two symmetries, namely the parity in X -direction and the time reversal symmetry. In the coordinates (\mathbf{Q}, \mathbf{P}) , these symmetries are represented by

$$(X, Y, P_x, P_y) \mapsto (-X, Y, -P_x, P_y), \quad (5.35a)$$

$$(X, Y, P_x, P_y) \mapsto (X, 2 - Y, -P_x, P_y), \quad (5.35b)$$

respectively. To preserve these symmetries, the function g must satisfy

$$g(-X, Y, \pi - \theta') = g(X, Y, \theta'), \quad (5.36a)$$

$$g(X, 2 - Y, \pi - \theta') = -g(X, Y, \theta'). \quad (5.36b)$$

(iii) To match the Y -periodic structure of the phase space we require

$$g(X, Y + 2, \theta') = g(X, Y, \theta'). \quad (5.37)$$

We express g as a truncated Fourier series in X , Y , and θ' with periodicities $\mathcal{L}_x = 1$, $\mathcal{L}_y = 2$, and $\mathcal{L}_\theta = 2\pi$. Regarding the conditions (5.36) this leads to the expansion

$$\begin{aligned} g(X, Y, \theta') = & \sum_{n=0}^{\mathcal{N}_x} \sum_{m=1}^{\mathcal{N}_y} \sum_{l=0}^{\mathcal{N}_\theta} a_{nml}^1 f_n^+ \left(\frac{X}{\mathcal{L}_x} \right) f_m^- \left(\frac{Y-1}{\mathcal{L}_y} \right) f_l^+ \left(\frac{\theta' - \frac{\pi}{2}}{\mathcal{L}_\theta} \right) \\ & + \sum_{n=1}^{\mathcal{N}_x} \sum_{m=0}^{\mathcal{N}_y} \sum_{l=1}^{\mathcal{N}_\theta} a_{nml}^2 f_n^- \left(\frac{X}{\mathcal{L}_x} \right) f_m^+ \left(\frac{Y-1}{\mathcal{L}_y} \right) f_l^- \left(\frac{\theta' - \frac{\pi}{2}}{\mathcal{L}_\theta} \right), \end{aligned} \quad (5.38)$$

with the Fourier basis functions f_ν^\pm from Eqs. (4.16). In the following example, we choose for the orders $\mathcal{N}_x = \mathcal{N}_y = \mathcal{N}_\theta = 2$.

Iterative improvement

According to Sec. 3.3.3 we use the family of canonical transformations $T^{\mathbf{a}}$ to successively determine the parameters $\mathbf{a}_1, \mathbf{a}_2, \dots$ of the transformations T_1, T_2, \dots by minimizing the cost function $\mathcal{L}(\mathbf{a})$, Eq. (3.19). Here, we use $\ell = 1, 2, \dots, 10^3$ sample points \mathbf{x}_ℓ^τ of H on each of the previously used tori $\tau = 1, 2, \dots, 100$. With a damping factor $\eta = 0.3$, we obtain a satisfying agreement. After $N = 6$ steps convergence is achieved. The final integrable approximation $H_{\text{reg}}^N(\mathbf{Q}, \mathbf{P})$ is given by Eq. (3.15). In Figs. 5.7(c) and (f) we compare the Poincaré sections of $H(\mathbf{Q}, \mathbf{P})$ (gray) and $H_{\text{reg}}^N(\mathbf{Q}, \mathbf{P})$ (red lines). We have confirmed that the improvement is of the same quality also in other sections of phase space (not shown). Figure 5.8 shows the evaluated cost function \mathcal{L} after each iteration step n . Its final value is about a factor of 2 larger than for a comparable 2D example with a strong perturbation, see, e. g., Fig. 4.3. However, as \mathcal{L} is defined as a squared distance, Eq. (3.19), it scales linear in the number f of degrees of freedom. From that perspective the results are comparable in quality. One would expect further improvements when choosing a larger family of canonical transformations by increasing the orders $\mathcal{N}_x, \mathcal{N}_y, \mathcal{N}_\theta$ in Eq. (5.38).

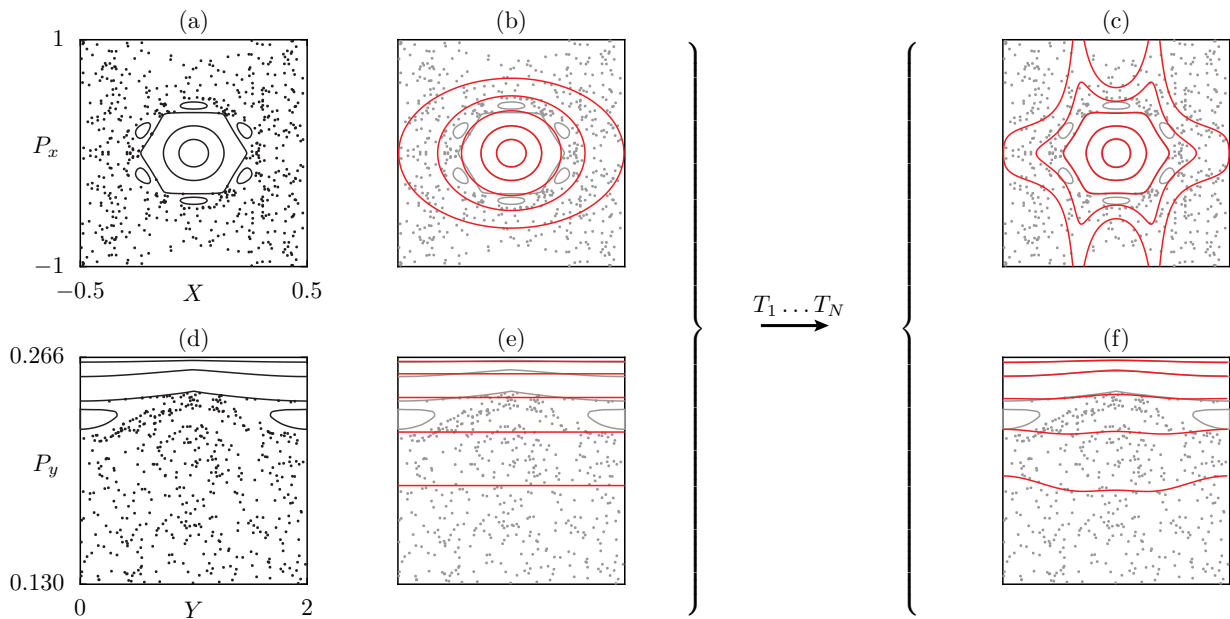


Figure 5.7.: Poincaré sections Σ_1 and Σ_2 for the cosine billiard $H(\mathbf{Q}, \mathbf{P})$, (a,d), its initial integrable approximation $H_{\text{reg}}^0(\mathbf{Q}, \mathbf{P})$, (b,e), and its final integrable approximation $H_{\text{reg}}^N(\mathbf{Q}, \mathbf{P})$, $N = 6$, (c,f).

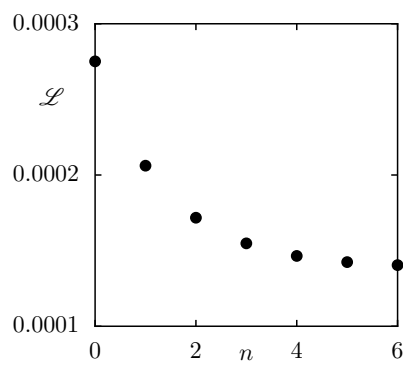


Figure 5.8.: Cost function \mathcal{L} , Eq. (3.19), vs. iteration step n .

6. Dynamical tunneling

In this chapter, the integrable approximations from the iterative canonical transformation method are used to describe dynamical tunneling. We first introduce the concept of dynamical tunneling and its theoretical prediction (Sec. 6.1) which we then demonstrate for symplectic 2D maps (Sec. 6.2). After this, we discuss the quantization of integrable approximations (Sec. 6.3). Finally, we derive tunneling predictions for generic 2D billiards (Sec. 6.4).

6.1. Dynamical tunneling and the fictitious integrable system approach

Tunneling is one of the most important effects in quantum mechanics. It is possibly the most illustrative example among the many ways in which quantum theory challenges an insufficient, classical picture of the physical reality. In the early times of quantum mechanics, the process of *barrier tunneling* was investigated [61, 62]. This is the transport of probability density through an energetic barrier, which would be classically impossible. The discovery and theoretical foundation of this effect explained many important phenomena (e. g., alpha decay, nuclear fusion in stars, or spontaneous DNA mutation) and led to numerous technical developments, from the tunnel diode and the scanning tunnel microscope towards flash memory cards.

Later, the concept of *dynamical tunneling* [5, 6] was established, which denotes any probability transport between classically disjoint regions in *phase space*. While this generalization includes barrier tunneling as a special case, it also comprises new tunneling processes where the classical barrier becomes visible from a phase-space perspective only. Given a non-integrable system, one such perspective is to divide the phase space into regions of regular and chaotic dynamics, leading to the process of *regular-to-chaotic tunneling* [63, 64]. It has been shown, that nonlinear resonance chains of the regular phase-space regions can strongly enhance dynamical tunneling, which is then termed *resonance-assisted tunneling* [7–11]. In this thesis we focus on regular-to-chaotic tunneling in the contrary situation, where resonances can be neglected, which is called *direct* (regular-to-chaotic) tunneling.

In a non-integrable system represented by its unit-time evolution operator \hat{U} , the regular-to-chaotic tunneling effect can be characterized by a set of tunneling rates $\gamma_{\mathbf{n}}$. These rates describe the transport from the system's \mathbf{n} -th quantizing torus in the regular phase-space region towards the chaotic phase-space region. Here \mathbf{n} is a set of suitable quantum numbers. For a more precise definition of $\gamma_{\mathbf{n}}$ it

seems suggestive to use the eigenstates of \hat{U} ,

$$\hat{U} |\psi_{\mathbf{n}}\rangle = \xi_{\mathbf{n}} |\psi_{\mathbf{n}}\rangle. \quad (6.1)$$

This basis includes “regular” eigenstates $|\psi_{\mathbf{n}}\rangle$, which typically localize on these regular quantizing tori. However, as these eigenstates are invariant under \hat{U} , their propagation shows no tunneling transport. Instead, $\gamma_{\mathbf{n}}$ can be defined based on the corresponding open system [65]

$$\hat{U}_{\text{open}} = (1 - \hat{P}_{\text{abs}})\hat{U}(1 - \hat{P}_{\text{abs}}), \quad (6.2)$$

where \hat{P}_{abs} is a projector onto an absorbing domain in the chaotic phase-space region. Due to the absorption, the modified eigenstates

$$\hat{U}_{\text{open}} |\mathbf{n}\rangle = z_{\mathbf{n}} |\mathbf{n}\rangle, \quad (6.3)$$

show a propagation towards the chaotic region. Due to the subunitarity of \hat{U}_{open} , their magnitude $|\langle \mathbf{n} | \mathbf{n} \rangle|$ decreases by a factor $|z_{\mathbf{n}}|^2 \leq 1$ per iteration step. Consequently, the tunneling rate is defined as their decay rate

$$\gamma_{\mathbf{n}} = -2 \log |z_{\mathbf{n}}|. \quad (6.4)$$

For the theoretical prediction of regular-to-chaotic tunneling rates, the *fictitious integrable system approach* was developed [12–14]. This approach is based on an integrable approximation H_{reg} for the considered non-integrable system. First, the classical function H_{reg} is translated to an operator

$$\hat{H}_{\text{reg}} = \mathcal{Q}(H_{\text{reg}}), \quad (6.5)$$

by applying an appropriate quantization rule \mathcal{Q} . The discussion of this step is shifted to Sec 6.3. Then the eigenvalue problem of the quantum system \hat{H}_{reg} is considered,

$$\hat{H}_{\text{reg}} |\psi_{\text{reg}}^{\mathbf{n}}\rangle = E_{\text{reg}}^{\mathbf{n}} |\psi_{\text{reg}}^{\mathbf{n}}\rangle. \quad (6.6)$$

Here, the eigenstates $|\psi_{\text{reg}}^{\mathbf{n}}\rangle$ are called *quasimodes*. When ordered appropriately, $|\psi_{\text{reg}}^{\mathbf{n}}\rangle$ localizes on the \mathbf{n} -th quantizing torus of H_{reg} . Consequently, if H_{reg} closely approximates the regular region of the given, non-integrable system H , also the quasimodes $|\psi_{\text{reg}}^{\mathbf{n}}\rangle$ approximate the states $|\psi_{\mathbf{n}}\rangle$ in the regular region. However, while the $|\psi_{\mathbf{n}}\rangle$ also couple to the chaotic regions due to dynamical tunneling, the quasimodes $|\psi_{\text{reg}}^{\mathbf{n}}\rangle$ decay exponentially outside the quantizing torus, as H_{reg} is integrable. Due to this sharp localization, the quasimodes $|\psi_{\text{reg}}^{\mathbf{n}}\rangle$ provide an orthogonal basis to accurately measure the quantizing tori. Following this idea, the fictitious integrable system approach gives a prediction of the

direct regular-to-chaotic tunneling rate as

$$\gamma_{\mathbf{n}} = \left| \hat{P}_{\text{abs}} \hat{U} |\psi_{\text{reg}}^{\mathbf{n}}\rangle \right|^2. \quad (6.7)$$

The underlying intuition is to model $\gamma_{\mathbf{n}}$ as the weight of the quasimode $|\psi_{\text{reg}}^{\mathbf{n}}\rangle$ that is propagated into the absorber via the unit-time operator \hat{U} .

Apart from this prediction, which will be used in this thesis, there are also other descriptions of dynamical tunneling which rely on an integrable approximation H_{reg} . One example is a perturbative extension of Eq. (6.7), which can also account for resonance-assisted regular-to-chaotic tunneling [14]. Also a perturbation-free extension for this case has been developed, which is based on an integrable approximation with resonance, as constructed in Sec. 4.7 [50, 66]. Another important concept is the semiclassical description of dynamical tunneling based on complex paths. Here, the tunneling process is expanded in terms of trajectories in the complexified phase space of the integrable approximation H_{reg} . This has been accomplished for tunneling in purely integrable systems [55], for regular-to-chaotic tunneling in near-integrable microcavities [67, 68] and generic 2D maps [37, 69], as well as for resonance-assisted regular-to-chaotic tunneling in generic 2D maps [70], where the iterative canonical transformation method was used.

6.2. Tunneling predictions in 2D maps using integrable approximations

In this section, we apply the fictitious integrable system approach to symplectic 2D maps, proceeding along the lines of Ref. [65]. Our purpose is both to illustrate the fictitious integrable system approach and to verify its applicability with the integrable approximations from the iterative canonical transformation method. Specifically, we consider the standard map (4.4) with $\kappa = 2.9$. Quantizing this map leads to a quantum map \hat{U} [71]. For this quantization we choose an inverse integer value for the effective Planck's constant $\hbar_{\text{eff}} = 1/N$. Together with the 2π -periodic boundary conditions in both q and p , this leads to an N -dimensional Hilbert space that is spanned by a finite, discrete subset of, e. g., the position eigenstates $|q\rangle$. Using this discrete basis, we define the open system \hat{U}_{open} , Eq. (6.2), by choosing an absorber in position space,

$$\hat{P}_{\text{abs}} = \sum_{\text{abs}} |q\rangle \langle q|, \quad (6.8)$$

summing over all (quantized) positions which additionally fulfill $q \in [0, q_{\text{abs}}] \cup [1 - q_{\text{abs}}, 1]$. For the specific system $\kappa = 2.9$, we choose $q_{\text{abs}} = 0.2713$, such that the absorber is located close to but outside the regular region, see the gray areas in Fig. 6.1(e).

For H_{reg} we choose the integrable approximation obtained from the iterative canonical transformation method in Sec. 4.4 with $(\mathcal{N}_q, \mathcal{N}_p) = (1, 2)$ and $N = 40$, see Fig. 6.1(a). For the numerical

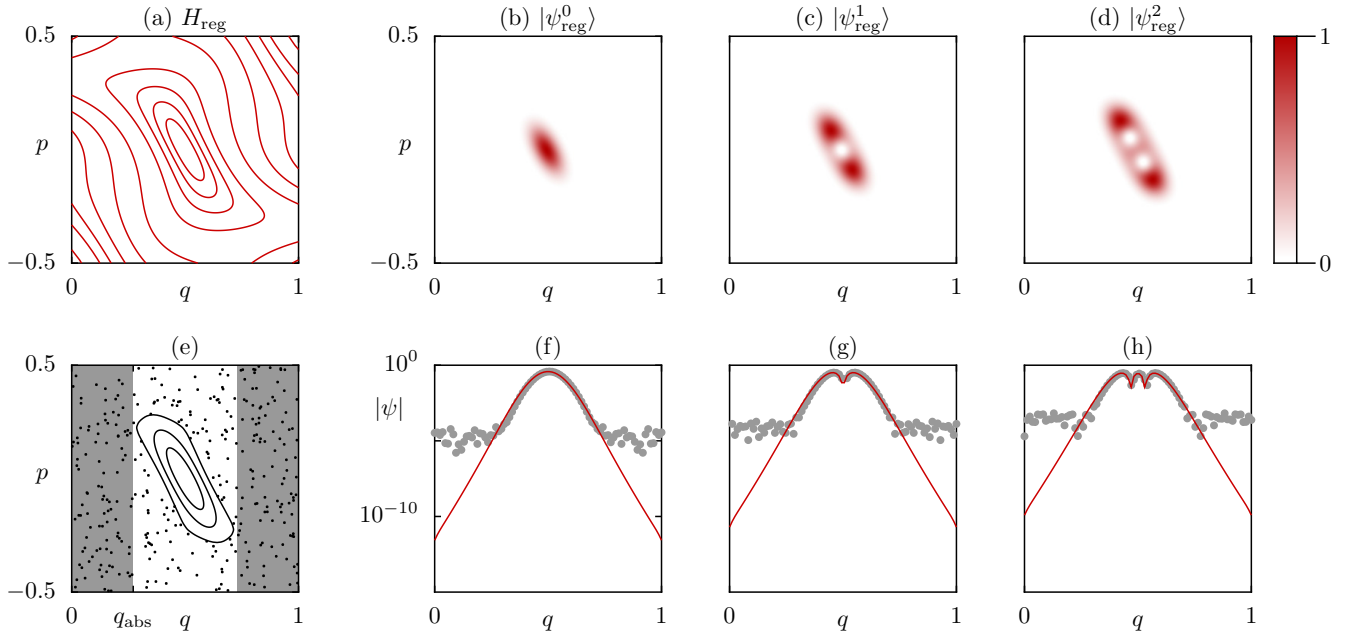


Figure 6.1.: (a) Phase space of an integrable approximation H_{reg} obtained from the iterative canonical transformation method. (b–d) Husimi function of the quasimodes $|\psi_{\text{reg}}^n\rangle$ for $n = 0$ (b), $n = 1$ (c), and $n = 2$ (d) and $h_{\text{eff}} = 1/86$, shown on a linear scale. (e) Phase space of the standard map (4.4) (black) for $\kappa = 2.9$ with an absorbing region (gray) located at $q \in [0, q_{\text{abs}}] \cup [1 - q_{\text{abs}}, 1]$ with $q_{\text{abs}} = 0.2713$. (f–h) Modulus $|\psi_{\text{reg}}^n(q)|$ of the quasimodes from (b–d) in position representation, shown on a logarithmic scale (red). The gray dots show the corresponding eigenstates $|\psi_n(q)\rangle$ of the quantum map \hat{U} .

evaluation it is convenient to set

$$\mathcal{H}_{\text{reg}}(J) = J, \quad (6.9)$$

for the action representation of H_{reg} . This enforces a parabolic energy landscape, preventing artificial couplings due to eventual oscillations in $\mathcal{H}_{\text{reg}}(J)$. Note that this leaves the torus geometry unchanged. We quantize $H_{\text{reg}}(q, p)$ according to the Weyl rule, as will be explained in the next section. For the resulting operator \hat{H}_{reg} we determine the quasimodes $|\psi_{\text{reg}}^n\rangle$ numerically from Eq. (6.6). In Figs. 6.1(b–d) we show the Husimi phase-space distribution of the ground state $|\psi_{\text{reg}}^0\rangle$, $n = 0$ (b) and the first two excited states $n = 1$ (c) and $n = 2$ (d) for $h_{\text{eff}} = 1/86$. The red lines in Figs. 6.1(f–h) show the modulus $|\psi_{\text{reg}}^n(q)|$ of these states in position representation on a logarithmic scale. For comparison we also show the corresponding eigenstates $|\psi_n(q)\rangle$ of the quantum map \hat{U} (gray dots). Apart from their close agreement in the regular region, $\psi_{\text{reg}}^n(q)$ and $\psi_n(q)$ differ significantly outside of this region, as mentioned in Sec. 6.1. Here, $\psi_n(q)$ has fluctuations of the order 10^{-5} which are caused by dynamical tunneling, while $\psi_{\text{reg}}^n(q)$ decays exponentially.

Using the quasimodes $|\psi_{\text{reg}}^n\rangle$ of \hat{H}_{reg} , we now apply the fictitious integrable system approach to predict direct regular-to-chaotic tunneling rates γ_n , Eq. (6.7). We evaluate this prediction for values of the effective Planck's constant h_{eff} where $1/h_{\text{eff}}$ is an even integer. In Fig. 6.2 we show this

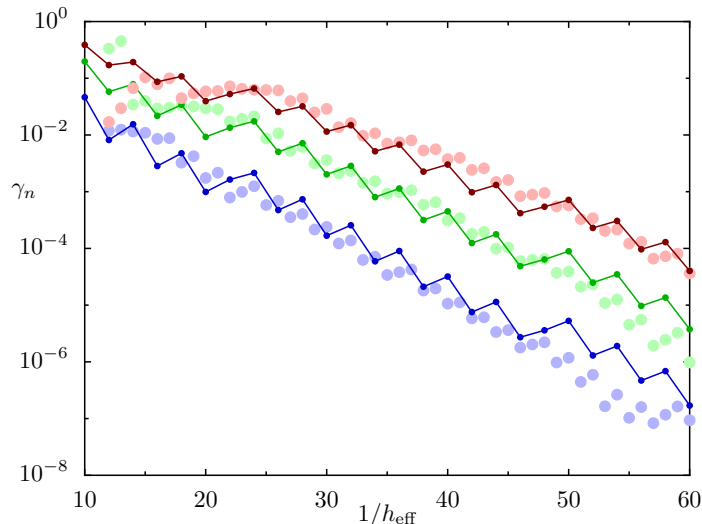


Figure 6.2.: Tunneling rates γ_n of the quantized standard map at $\kappa = 2.9$ (bright dots) for $n = 0$ (violet), $n = 1$ (green), and $n = 2$ (red) with their predictions (dark dots and lines) obtained from the fictitious integrable system approach.

prediction (dark dots and line) for the rates γ_0 (blue), γ_1 (green), and γ_2 (red). For visual clarity, the predicted values are connected by lines. For comparison, the bright dots depict the numerically determined values γ_n computed from Eq. (6.4). The prediction shows a rough agreement with the numerical data with a loss of relative precision in the semiclassical regime where $1/h_{\text{eff}}$ becomes large. Here, the small deviations between H_{reg} and the regular island of the standard map become more relevant. The prediction could be improved by using a better integrable approximation H_{reg} . The local fluctuations of the prediction are an inherent characteristic of the fictitious integrable system approach [13]. The prediction based on the integrable approximation H_{reg} obtained from the iterative canonical transformation method is of a comparable quality to previous results for the same system, where other methods have been used to construct H_{reg} , see, e. g., Ref. [12, Fig. 4].

6.3. Influence of the quantization rule

As explained in Sec. 6.1, the fictitious integrable system approach requires a classical integrable approximation H_{reg} which is quantized using a quantization rule \mathcal{Q} , Eq. (6.5). Hence, the resulting prediction of tunneling rates depends on both H_{reg} and \mathcal{Q} . While the influence of H_{reg} has been discussed [13], the influence of the quantization rule \mathcal{Q} was not considered so far. In this section, we give a numerical evidence for the relevance of this choice. Although this has general implications, we restrict to the case of $f = 1$ degree of freedom for convenience.

Basically, a quantization rule \mathcal{Q} is an instruction which associates a quantum observable \hat{A} to any classical, scalar observable $A : \mathbb{R}^{2f} \mapsto \mathbb{C}$. As \hat{A} depends on the behavior of $A(q, p)$ everywhere in phase space, \hat{A} is a functional of $A(q, p)$. As we will see later, this functional is linear, thus it can be

expressed as an integral operator

$$\hat{A} = \mathcal{Q}(A) = \frac{1}{(2\pi)^2} \int dq \int dp \int d\theta \int d\tau w(\theta, \tau) e^{-i\theta q} e^{-i\tau p} e^{i\theta \hat{q}} e^{i\tau \hat{p}} A(q, p). \quad (6.10)$$

Here the integrals are taken over the real domain \mathbb{R} . The operators \hat{q} and \hat{p} denote position and momentum with the well known commutation relation

$$[\hat{q}, \hat{p}] = i\hbar. \quad (6.11)$$

The function $w(\theta, \tau)$ is the integral kernel which defines \mathcal{Q} . For $w(\theta, \tau) = 1$, Eq. (6.10) would simply describe a two-step Fourier transform, where (q, p) are first transformed to their conjugated variables (θ, τ) , and then back to the quantum mechanical operators (\hat{q}, \hat{p}) . However, due to the commutation relation (6.11) the choice of the exponential term $e^{i\theta \hat{q}} e^{i\tau \hat{p}}$ is arbitrary. One could also choose it, e. g., in the reverse order $e^{i\tau \hat{p}} e^{i\theta \hat{q}}$, which using the Baker–Campbell–Hausdorff formula, equals

$$e^{i\tau \hat{p}} e^{i\theta \hat{q}} = e^{i\theta \tau \hbar} e^{i\theta \hat{q}} e^{i\tau \hat{p}}. \quad (6.12)$$

Thus, using this reverse order of the exponential factors would imply an integral kernel $w(\theta, \tau) = e^{i\theta \tau \hbar}$ in Eq. (6.10). At this point one might ask for the general class of integral kernels $w(\theta, \tau)$ which are reasonable from a physical perspective. For this, the transformation rule should fulfill the following properties

$$\mathcal{Q}(1) = 1, \quad (6.13a)$$

$$\mathcal{Q}(A^*) = \mathcal{Q}(A)^\dagger, \quad (6.13b)$$

$$\lim_{\hbar \rightarrow 0} \mathcal{Q}(A) = A(q, p), \quad (6.13c)$$

$$A(q, p) = A(q) \quad \Rightarrow \quad \mathcal{Q}(A) = A(\hat{q}), \quad (6.13d)$$

$$A(q, p) = A(p) \quad \Rightarrow \quad \mathcal{Q}(A) = A(\hat{p}). \quad (6.13e)$$

Here, property (6.13a) is a normalization, while property (6.13b) ensures the correspondence of real-valued functions to self-adjoint operators. Property (6.13c) states that any quantized observable approaches its classical analogue in the semiclassical limit. The reasoning behind properties (6.13d) and (6.13e) is to allow single-operator functions to be expressed by their series expansions. Note that this fact also implies, that all Hamiltonians of the so-called *Schrödinger form*

$$H(\mathbf{q}, \mathbf{p}) = T(\mathbf{p}) + V(\mathbf{q}), \quad (6.14)$$

have a *unique* quantization $\hat{H} = T(\hat{\mathbf{p}}) + V(\hat{\mathbf{q}})$. As this is the case in many fields of physics, the quantization is often a straightforward issue. Also, linear coupling terms known from electromagnetics have a unique form $\mathcal{Q}(qp) = (\hat{q}\hat{p} + \hat{p}\hat{q})/2$ due to property (6.13b). However, for more complicated Hamiltonians, the quantization becomes ambiguous and needs more consideration, as it is the case

for integrable approximations. Here, arbitrary couplings between q and p occur due to the canonical transformations in Eq. (3.15). As we show in App. I, the properties (6.13) translate to the following conditions on the kernel function, given in respective order,

$$w(0, 0) = 1, \quad (6.15a)$$

$$w(-\theta, -\tau)^* = w(\theta, \tau)e^{-i\theta\tau\hbar}, \quad (6.15b)$$

$$\lim_{\hbar \rightarrow 0} w(\theta, \tau) = 1, \quad (6.15c)$$

$$\frac{\partial^n w}{\partial \theta^n}(0, 0) = 0, \quad \forall n \in \mathbb{N}, \quad (6.15d)$$

$$\frac{\partial^n w}{\partial \tau^n}(0, 0) = 0, \quad \forall n \in \mathbb{N}. \quad (6.15e)$$

One specific family of quantizations, which solves these conditions is given by

$$w_\alpha(\theta, \tau) = \frac{1}{2} \left(e^{i\theta\tau\hbar\left(\frac{1}{2}-\alpha\right)} + e^{i\theta\tau\hbar\left(\frac{1}{2}+\alpha\right)} \right), \quad \alpha \in \left[0, \frac{1}{2}\right]. \quad (6.16)$$

A similar family of quantization rules also appears in Ref. [72]¹. It includes two well known special cases, namely the Weyl rule [73] for $\alpha = 0$ and the Rivier rule [74] for $\alpha = \frac{1}{2}$. In the context of the fictitious integrable system approach, both rules have been used in the past, see, e. g., Ref. [65, Eq. (3.41)] for the Weyl rule and Ref. [75, Eq. (3.154)] for the Rivier rule. In the following we construct a larger class of quantization rules from Eq. (6.16), given by

$$w(\theta, \tau) = \sum_{i=1}^n c_i w_{\alpha_i}(\theta, \tau), \quad (6.17)$$

where we use n parameters $\alpha_i \in \left[0, \frac{1}{2}\right]$ with normalized, real coefficients

$$\sum_{i=1}^n c_i = 1. \quad (6.18)$$

This is valid, since the conditions (6.15b), (6.15d), and (6.15e) are linear in w , while the normalization (6.18) ensures conditions (6.15a) and (6.15c). We construct an ensemble of quantizations by choosing α_i and c_i randomly. More specifically, we once pick n parameters α_i uniformly from $\left[0, \frac{1}{2}\right]$. With this choice fixed, we construct an ensemble of quantizations by picking different parameter sets c_i uniformly from $[-1, 1]$, and normalizing them according to Eq. (6.18). This strategy of fixing the α_i reduces the computational effort, as the resulting operator is given by $c_1 \mathcal{Q}_{\alpha_1}(A) + \dots + c_n \mathcal{Q}_{\alpha_n}(A)$. Hence, the operators $\mathcal{Q}_{\alpha_i}(A)$ are determined only once for the whole ensemble, and then just recombined with different coefficients c_i for each ensemble element.

To estimate the influence of the quantization rule on the fictitious integrable system approach, we set $n = 10$ and choose an ensemble of $M = 60$ quantization rules. For each quantization rule, we

¹More specifically, Eq. (6.16) represents a symmetrized version of Ref. [72, Eq. (4.1.3)].

compute the prediction of direct regular-to-chaotic tunneling rates, using the same setting as specified in Sec. 6.2. In Fig. 6.3(a) we show the prediction for the tunneling rates γ_0 . Here the solid line shows the prediction averaged over the ensemble, while the dashed lines mark the minimum and maximum predictions.

To quantify the spreading of the predicted tunneling rate γ_0 , we compute its standard deviation σ_{γ_0} . Note that σ_{γ_0} must be evaluated with respect to the average predicted tunneling rate $\bar{\gamma}_0$, but not to the numerically determined tunneling rate, as our interest is on the error between the predictions. In Fig. 6.3(b) we show this standard deviation (dots). Apart from the absolute deviation, which might strongly depend on the considered system and the construction of the ensemble, we find an asymptotically exponential decay $\sigma_{\gamma_0} \propto e^{-\text{const.}/h_{\text{eff}}}$.

The triangles in Fig. 6.3(b) show the standard deviation for a prediction based on the initial integrable approximation H_{reg}^0 instead of H_{reg}^N . Here, all predictions agree up to the order of machine precision. This can be understood as follows. According to Eqs. (3.9), (4.7), and (6.9), H_{reg}^0 is the harmonic oscillator, modified by a linear canonical transformation \mathcal{R} , Eq. (4.8). As the harmonic oscillator is in Schrödinger form (6.14) and linear transformations have a unique quantum mechanical representation [76], the quantization $\mathcal{Q}(H_{\text{reg}}^0)$ must be unique. Consequently, the deviations observed for the predictions based on H_{reg}^N must arise from the canonical transformations T_n , Eq. (3.15). The observed relevance of the chosen quantization for H_{reg}^N will be revisited in the end of the next section.

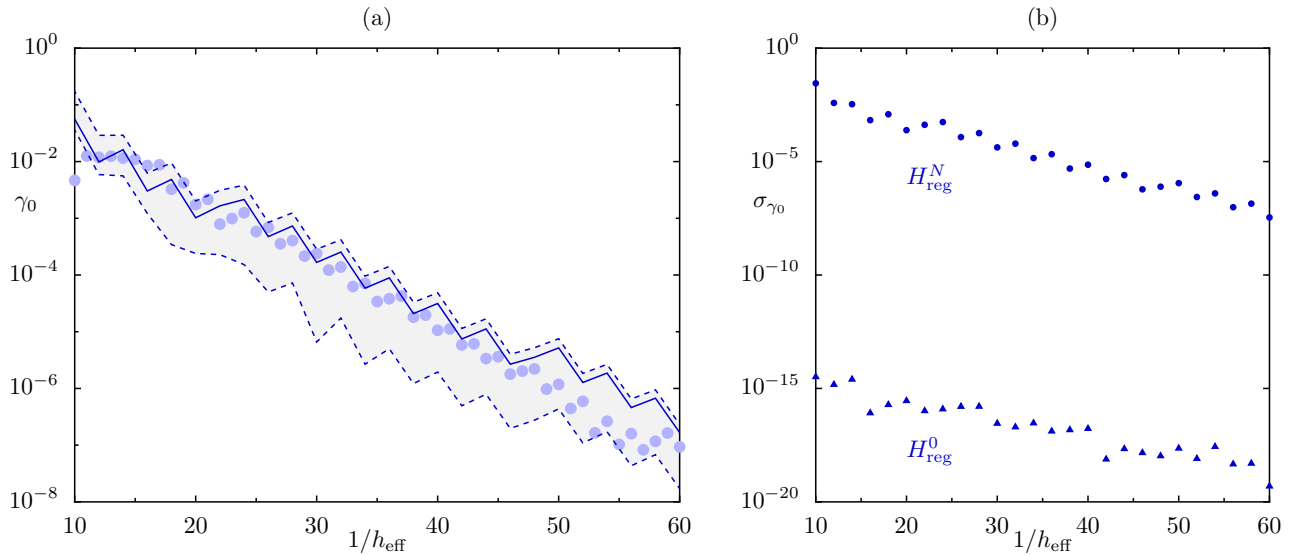


Figure 6.3.: (a) Tunneling rates γ_0 of the quantized standard map at $\kappa = 2.9$ (bright dots) compared to their prediction obtained from the fictitious integrable system approach using an ensemble of $M = 60$ quantization rules \mathcal{Q} defined by Eq. (6.17) with $n = 10$. We show the minimum and maximum predicted value (dashed lines) and the mean prediction (solid line). (b) Standard deviation σ_{γ_0} for this prediction (dots), and for a prediction based on the initial integrable approximation H_{reg}^0 (triangles).

6.4. Tunneling predictions in 2D billiards using integrable approximations

In this section we implement the fictitious integrable system approach for generic 2D billiards. After a short recapitulation of this approach adapted to billiards (Sec. 6.4.1), we derive an effective numerical scheme for computing quasimodes in 2D confined systems (Sec. 6.4.2). Finally, we present the application of the fictitious integrable system approach (Sec. 6.4.3). Note that this application contains unresolved problems, which, however, make its detailed documentation even more important.

6.4.1. Fictitious integrable system approach for 2D billiards

We now formulate the fictitious integrable system approach for 2D billiards. In contrast to time-discrete systems, billiards have no special time scale, which allows to consider tunneling rates either as differential [15] or as absolute transport rates with respect to time. Following Sec. 6.1, we take the latter perspective and consider the time-discrete open system \hat{U}_{open} , Eq. (6.2), where the unitary part is given by

$$\hat{U} = e^{-i\hat{H}t_0/\hbar}. \quad (6.19)$$

Here, t_0 is the time period between the instantaneous absorption events. Due to the scaling relation (5.16) of H , we can rewrite this as

$$\hat{U} = \left(\hat{U}_0\right)^{t_0\hbar}, \quad (6.20)$$

where $\hat{U}_0 = e^{-i\hat{H}_0}$ and $\hat{H}_0 = \hat{H}/\hbar^2$ are dimensionless operators which do not depend on t_0 and \hbar . Consequently, for scaling systems (5.16), such as billiards, the tunneling process depends only on the product $t_0\hbar$ and the semiclassical limit $\hbar \rightarrow 0$ coincides with the transition to short times $t_0 \rightarrow 0$. To avoid computational effort, it is convenient to express \hat{U} in the eigenbasis of \hat{H}_0 as

$$\hat{U} = \sum_{\mathbf{n}} e^{-iE_{0,\mathbf{n}}t_0\hbar} |\psi_{\mathbf{n}}\rangle \langle \psi_{\mathbf{n}}|, \quad (6.21)$$

using the eigenvalues $E_{0,\mathbf{n}}$ of \hat{H}_0 . This way, tunneling rates may be computed for different values of t_0 or \hbar by just replacing $t_0\hbar$ in Eq. (6.21) without solving the eigenvalue problem of \hat{H} again. Moreover, Eq. (6.21) also allows an enhanced evaluation of the open quantum map \hat{U}_{open} , Eq. (6.2). Using an arbitrary basis $|\varphi_{\mathbf{n}}\rangle$ and a projector \hat{P}_{abs} onto a region defined in position space, we can write the

matrix elements of \hat{U}_{open} as

$$\langle \varphi_{\mathbf{n}} | \hat{U}_{\text{open}} | \varphi_{\mathbf{m}} \rangle = \langle \varphi_{\mathbf{n}} | (1 - \hat{P}_{\text{abs}}) \hat{U} (1 - \hat{P}_{\text{abs}}) | \varphi_{\mathbf{m}} \rangle \quad (6.22a)$$

$$= \int d^2 \mathbf{q} \int d^2 \mathbf{q}' \langle \varphi_{\mathbf{n}} | (1 - \hat{P}_{\text{abs}}) | \mathbf{q} \rangle \langle \mathbf{q} | \hat{U} | \mathbf{q}' \rangle \langle \mathbf{q}' | (1 - \hat{P}_{\text{abs}}) | \varphi_{\mathbf{m}} \rangle, \quad (6.22b)$$

$$= \sum_{\mathbf{k}} e^{-iE_{0,\mathbf{k}}t_0\hbar} \int d^2 \mathbf{q} \int d^2 \mathbf{q}' \langle \varphi_{\mathbf{n}} | (1 - \hat{P}_{\text{abs}}) | \mathbf{q} \rangle \langle \mathbf{q} | \psi_{\mathbf{k}} \rangle \langle \psi_{\mathbf{k}} | \mathbf{q}' \rangle \langle \mathbf{q}' | (1 - \hat{P}_{\text{abs}}) | \varphi_{\mathbf{m}} \rangle, \quad (6.22c)$$

$$= \sum_{\mathbf{k}} e^{-iE_{0,\mathbf{k}}t_0\hbar} \underbrace{\left(\int_{\mathbf{q} \notin \text{abs}} d^2 \mathbf{q} \langle \varphi_{\mathbf{n}} | \mathbf{q} \rangle \langle \mathbf{q} | \psi_{\mathbf{k}} \rangle \right)}_{=: \mathcal{I}_{\mathbf{n}}^{\mathbf{k}}} \left(\int_{\mathbf{q}' \notin \text{abs}} d^2 \mathbf{q}' \langle \psi_{\mathbf{k}} | \mathbf{q}' \rangle \langle \mathbf{q}' | \varphi_{\mathbf{m}} \rangle \right), \quad (6.22d)$$

$$= \sum_{\mathbf{k}} e^{-iE_{0,\mathbf{k}}t_0\hbar} \cdot \mathcal{I}_{\mathbf{n}}^{\mathbf{k}} \cdot \mathcal{I}_{\mathbf{m}}^{\mathbf{k}*}. \quad (6.22e)$$

Thus, for N basis states $|\varphi_{\mathbf{n}}\rangle$, instead of N^2 4D integrals (6.22b), only N^2 2D integrals $\mathcal{I}_{\mathbf{n}}^{\mathbf{k}}$ need to be computed. Moreover, as the latter are independent of t_0 and \hbar , they only have to be computed once. Keeping this in mind, we use dimensionless units from here, setting $t_0\hbar = 1$.

6.4.2. Numerical computation of eigenstates in 2D confined systems

To employ the integrable approximations H_{reg} constructed in Sec. 5.4 for the fictitious integrable system approach, the quasimodes $|\psi_{\text{reg}}^{\mathbf{n}}\rangle$ need to be determined. Here, we encounter the difficulty that H_{reg} is not in Schrödinger form (6.14), due to the canonical transformations in Eq. (3.15). Therefore, traditional numerical methods for the eigenvalue problem of Hamiltonian systems cannot be used, as they implicitly assume this form (6.14) with $T(\mathbf{p}) = \mathbf{p}^2$, where the stationary Schrödinger equation translates to its well known form $(-\hbar^2\Delta + V - E)\psi = 0$, which is a second order partial differential equation. For Hamiltonians which are not in Schrödinger form, however, a differential equation approach becomes impractical. Therefore, we develop an alternative numerical scheme for computing the eigenstates of such Hamiltonians in the present section.

For this we proceed in three steps. After formulating the problem (step 1), we derive an analogue of the Weyl quantization rule for 2D confined systems (step 2) and finally test the computation scheme with a toy Hamiltonian (step 3).

Problem

In the following we consider the integrable approximation H_{reg} of a 2D billiard. For convenience, we use the coordinates $(\bar{\mathbf{q}}, \bar{\mathbf{p}})$ introduced in Sec. 5.2, where the system is confined to a unit square in position space,

$$\bar{\mathbf{q}} \in \mathcal{S}, \quad \mathcal{S} = [0, 1] \times [0, 1]. \quad (6.23)$$

To emphasize the generality of this problem, and for a more convenient notation, we ignore the context of integrable approximations in this section by omitting the overbars of $(\bar{\mathbf{q}}, \bar{\mathbf{p}})$ and formally consider $H_{\text{reg}}(\bar{\mathbf{q}}, \bar{\mathbf{p}})$ as a general observable $A(\mathbf{q}, \mathbf{p})$.

Thus we aim to solve the eigenvalue problem

$$\hat{A}|\psi_{\mathbf{n}}\rangle = \lambda_{\mathbf{n}}|\psi_{\mathbf{n}}\rangle, \quad (6.24)$$

of an operator \hat{A} whose classical representation $A(\mathbf{q}, \mathbf{p})$ is not necessarily in Schrödinger form (6.14) and confined to the unit square $\mathbf{q} \in \mathcal{S}$. Assuming the classical system to feature elastic reflections, we propose Dirichlet boundary conditions

$$\langle \mathbf{q} | \psi_{\mathbf{n}} \rangle |_{\mathbf{q} \in \partial \mathcal{S}} = 0. \quad (6.25)$$

Consequently, the spectrum is discrete and labeled by two quantum numbers $\mathbf{n} = (n_1, n_2) \in \mathbb{N}^2$ corresponding to the two degrees of freedom.

First, we rewrite the eigenstates in an orthonormal basis

$$|\psi_{\mathbf{n}}\rangle = \sum_{\mathbf{m} \in \mathbb{N}^2} c_{\mathbf{m}}^{\mathbf{n}} |\varphi_{\mathbf{m}}\rangle, \quad \langle \varphi_{\mathbf{n}} | \varphi_{\mathbf{m}} \rangle = \delta_{\mathbf{n}, \mathbf{m}}. \quad (6.26)$$

By projecting Eq. (6.24) to this basis, we obtain the eigenvalue problem

$$\sum_{\mathbf{m} \in \mathbb{N}^2} A_{\mathbf{km}} c_{\mathbf{m}}^{\mathbf{n}} = \lambda_{\mathbf{n}} c_{\mathbf{k}}^{\mathbf{n}}, \quad (6.27)$$

for the coefficients $c_{\mathbf{k}}^{\mathbf{n}}$ with the matrix

$$A_{\mathbf{nm}} = \langle \varphi_{\mathbf{n}} | \hat{A} | \varphi_{\mathbf{m}} \rangle. \quad (6.28)$$

Furthermore, we truncate the basis at a cutoff (N_1, N_2) , i. e., we only consider states $|\varphi_{\mathbf{n}}\rangle$ with $n_i \leq N_i$, such that the eigenvalue problem (6.27) becomes finite and can be solved numerically.

Weyl quantization for 2D confined systems

The remaining task is to compute the matrix elements $A_{\mathbf{nm}} = \langle \varphi_{\mathbf{n}} | \hat{A} | \varphi_{\mathbf{m}} \rangle$, Eq. (6.28). For this we choose the basis states from the square billiard $|\varphi_{\mathbf{n}}\rangle = |\varphi_{n_1}\rangle |\varphi_{n_2}\rangle$, which have the position representation

$$\langle \mathbf{q} | \varphi_{\mathbf{n}} \rangle = \langle q_1 | \varphi_{n_1} \rangle \langle q_2 | \varphi_{n_2} \rangle = 2 \sin(n_1 \pi q_1) \sin(n_2 \pi q_2), \quad (6.29)$$

see Fig. 6.4. Note that expressing $|\psi_{\mathbf{n}}\rangle$ in the $|\varphi_{\mathbf{m}}\rangle$ automatically satisfies the boundary conditions (6.25).

In this basis, we derive an analogue of the Weyl quantization adapted to 2D confined systems,

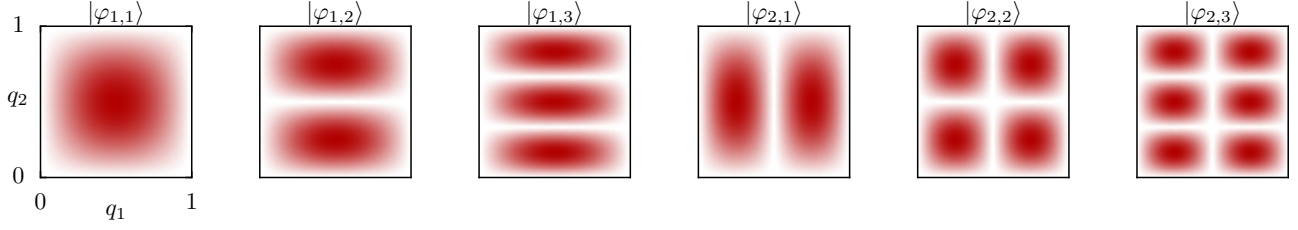


Figure 6.4.: Modulus $|\langle \mathbf{q} | \varphi_{\mathbf{n}} \rangle|$ of the square billiard eigenstates in position representation, Eq. (6.29), with $\mathbf{n} = (n_1, n_2)$ for $n_1 \leq 2$ and $n_2 \leq 3$, shown on a linear scale.

which will result in Eq. (6.50). As the position is confined to the unit square (6.23), the Hilbert space is spanned by the states $|\varphi_{\mathbf{n}}\rangle$ and we have

$$1 = \sum_{\mathbf{n} \in \mathbb{N}^2} |\varphi_{\mathbf{n}}\rangle \langle \varphi_{\mathbf{n}}|, \quad \langle \varphi_{\mathbf{n}} | \varphi_{\mathbf{m}} \rangle = \delta_{\mathbf{n}, \mathbf{m}}, \quad (6.30a)$$

$$1 = \int_{\mathcal{S}} d^2 \mathbf{q} |\mathbf{q}\rangle \langle \mathbf{q}|, \quad \langle \mathbf{q} | \mathbf{q}' \rangle = \delta(\mathbf{q} - \mathbf{q}'). \quad (6.30b)$$

Here, the Weyl quantization cannot be applied directly, as it is defined for systems with an unbounded position domain $\mathbf{q} \in \mathbb{R}^2$ only. The Hilbert space spanned by the $|\varphi_{\mathbf{n}}\rangle$, however, has different properties, e. g., the momentum has a discrete spectrum

$$\mathbf{p}_{\mathbf{n}} = \pi \hbar \begin{pmatrix} n_1 \\ n_2 \end{pmatrix}, \quad n_1, n_2 \in \mathbb{Z} \setminus \{0\}. \quad (6.31)$$

Moreover, as the momentum operator $\hat{\mathbf{p}}$ is self-adjoint, but not Hermitian, its eigenstates $|\mathbf{p}_{\mathbf{n}}\rangle = |p_{n_1}\rangle |p_{n_2}\rangle$ are not orthogonal, but fulfill

$$\langle \mathbf{p}_{\mathbf{n}} | \mathbf{p}_{\mathbf{m}} \rangle = \langle p_{n_1} | p_{m_1} \rangle \langle p_{n_2} | p_{m_2} \rangle, \quad \text{with} \quad \langle p_n | p_m \rangle = \begin{cases} 1 & n = m \\ \frac{(-1)^{m-n} - 1}{i\pi(m-n)} & n \neq m \end{cases}, \quad (6.32)$$

as can be shown by inserting $1 = \int_{\mathcal{S}} d^2 \mathbf{q} |\mathbf{q}\rangle \langle \mathbf{q}|$. As the position representation $\langle \mathbf{q} | \mathbf{p}_{\mathbf{n}} \rangle = \exp(i\pi \mathbf{n} \mathbf{q})$ vanishes nowhere, it violates the boundary conditions on $\partial \mathcal{S}$, thus the momentum eigenstates $|\mathbf{p}_{\mathbf{n}}\rangle$ cannot be expressed in the Hilbert-space basis $|\varphi_{\mathbf{n}}\rangle$. However, special linear combinations of the $|\mathbf{p}_{\mathbf{n}}\rangle$ can still be used to express valid states. For example, comparing the exponential representation of the sine function with Eq. (6.29), we can write $|\varphi_{\mathbf{n}}\rangle$ as

$$|\varphi_{\mathbf{n}}\rangle = |\varphi_{n_1}\rangle |\varphi_{n_2}\rangle = \left(\frac{-i}{\sqrt{2}} \right)^2 (|p_{n_1}\rangle - |p_{-n_1}\rangle) (|p_{n_2}\rangle - |p_{-n_2}\rangle) = -\frac{1}{2} \sum_{s_1, s_2}^{\pm} s_1 s_2 |\mathbf{p}_{s_1 n_1, s_2 n_2}\rangle. \quad (6.33)$$

Here, in the latter, more compact expression, we used the index notation (6.31) summing over two signs $s_1, s_2 \in \{+, -\}$, which will turn out as convenient for the following derivation.

We first recall the Weyl formula \mathcal{Q}_0 for an unbounded position domain $\mathbf{q} \in \mathbb{R}^2$, given by

$$\mathcal{Q}_0(A) = \frac{1}{(2\pi)^4} \int_{\mathbb{R}^2} d^2\mathbf{q} \int_{\mathbb{R}^2} d^2\mathbf{p} \int_{\mathbb{R}^2} d^2\boldsymbol{\theta} \int_{\mathbb{R}^2} d^2\boldsymbol{\tau} e^{-i\boldsymbol{\theta}\mathbf{q}} e^{-i\boldsymbol{\tau}\mathbf{p}} w(\boldsymbol{\theta}, \boldsymbol{\tau}) e^{i\boldsymbol{\theta}\hat{\mathbf{q}}} e^{i\boldsymbol{\tau}\hat{\mathbf{p}}} A(\mathbf{q}, \mathbf{p}), \quad (6.34)$$

where the kernel is given by Eq. (6.16) with $\alpha = 0$, i. e., $w(\boldsymbol{\theta}, \boldsymbol{\tau}) = e^{i\boldsymbol{\theta}\boldsymbol{\tau}\hbar/2}$. We remark, that the exponential operators in the integrand can be symmetrically expressed as

$$w(\boldsymbol{\theta}, \boldsymbol{\tau}) e^{i\boldsymbol{\theta}\hat{\mathbf{q}}} e^{i\boldsymbol{\tau}\hat{\mathbf{p}}} = e^{i\boldsymbol{\tau}\hat{\mathbf{p}}/2} e^{i\boldsymbol{\theta}\hat{\mathbf{q}}} e^{i\boldsymbol{\tau}\hat{\mathbf{p}}/2}. \quad (6.35)$$

The general idea behind Eq. (6.34) is a two-fold Fourier transform according to the scheme

$$(\mathbf{q}, \mathbf{p}) \xrightarrow{\text{FT}} (\boldsymbol{\theta}, \boldsymbol{\tau}) \xrightarrow{\text{FT}^{-1}} (\hat{\mathbf{q}}, \hat{\mathbf{p}}). \quad (6.36)$$

Based on this idea, we define the analogue of this quantization rule for the confined system, where the position variables are restricted to $\mathbf{q} \in \mathcal{S}$, by replacing the corresponding Fourier integral transformations with the Fourier *series* transformations, i. e.,

$$\frac{1}{2\pi} \int_{\mathbb{R}} dq_j \int_{\mathbb{R}} d\theta_j e^{-i\theta_j q_j} e^{i\theta_j \hat{q}_j} \quad \mapsto \quad \int_0^1 dq_j \sum_{\theta_j \in \mathbb{Z}} e^{-i2\pi\theta_j q_j} e^{i2\pi\theta_j \hat{q}_j}. \quad (6.37)$$

This transfers Eq. (6.34) into

$$\mathcal{Q}_0(A) = \frac{1}{(2\pi)^2} \int_{\mathcal{S}} d^2\mathbf{q} \int_{\mathbb{R}^2} d^2\mathbf{p} \sum_{\boldsymbol{\theta} \in \mathbb{Z}^2} \int_{\mathbb{R}^2} d^2\boldsymbol{\tau} e^{-i2\pi\boldsymbol{\theta}\mathbf{q}} e^{-i\boldsymbol{\tau}\mathbf{p}} e^{i\boldsymbol{\tau}\hat{\mathbf{p}}/2} e^{i2\pi\boldsymbol{\theta}\hat{\mathbf{q}}} e^{i\boldsymbol{\tau}\hat{\mathbf{p}}/2} A(\mathbf{q}, \mathbf{p}). \quad (6.38)$$

Considering the exponential operator terms in this integral, we derive their matrix representation in the $|\varphi_{\mathbf{n}}\rangle$ -basis as

$$\langle \varphi_{\mathbf{n}} | e^{i\boldsymbol{\tau}\hat{\mathbf{p}}/2} e^{i2\pi\boldsymbol{\theta}\hat{\mathbf{q}}} e^{i\boldsymbol{\tau}\hat{\mathbf{p}}/2} | \varphi_{\mathbf{m}} \rangle = \prod_{j=1,2} \langle \varphi_{n_j} | e^{i\tau_j \hat{p}_j / 2} e^{i2\pi\theta_j \hat{q}_j} e^{i\tau_j \hat{p}_j / 2} | \varphi_{m_j} \rangle, \quad (6.39a)$$

$$= \prod_{j=1,2} \frac{1}{2} \sum_{s_j, s'_j}^{\pm} s_j s'_j \langle p_{s_j n_j} | e^{i\tau_j \hat{p}_j / 2} e^{i2\pi\theta_j \hat{q}_j} e^{i\tau_j \hat{p}_j / 2} | p_{s'_j m_j} \rangle, \quad (6.39b)$$

$$= \frac{1}{4} \sum_{s_1, s_2, s'_1, s'_2}^{\pm} s_1 s_2 s'_1 s'_2 \prod_{j=1,2} \langle p_{s_j n_j} | e^{i\tau_j \hat{p}_j / 2} e^{i2\pi\theta_j \hat{q}_j} e^{i\tau_j \hat{p}_j / 2} | p_{s'_j m_j} \rangle, \quad (6.39c)$$

$$= \frac{1}{4} \sum_{s_1, s_2, s'_1, s'_2}^{\pm} s_1 s_2 s'_1 s'_2 \prod_{j=1,2} e^{i\tau_j (p_{s_j n_j} + p_{s'_j m_j}) / 2} \langle p_{s_j n_j} | e^{i2\pi\theta_j \hat{q}_j} | p_{s'_j m_j} \rangle, \quad (6.39d)$$

$$= \frac{1}{4} \sum_{s_1, s_2, s'_1, s'_2}^{\pm} s_1 s_2 s'_1 s'_2 \prod_{j=1,2} e^{i\tau_j(p_{s_j n_j} + p_{s'_j m_j})/2} \langle p_{s_j n_j} | p_{s'_j m_j + 2\theta_j} \rangle. \quad (6.39e)$$

Here, in step (6.39b), we used Eq. (6.33), in step (6.39d) we applied \hat{p}_j , and in step (6.39e) we used the translation operator $\exp(ia\hat{q})|p\rangle = |p+a\hbar\rangle$. For a shorter notation, we define

$$\mathbf{p}_{\mathbf{n}, \mathbf{m}}^{\mathbf{s}, \mathbf{s}', \pm} := \pi\hbar \begin{pmatrix} s_1 n_1 \pm s'_1 m_1 \\ s_2 n_2 \pm s'_2 m_2 \end{pmatrix}, \quad (6.40)$$

and exploit the invariance

$$\langle p_n | p_{m+\Delta} \rangle = \langle p_{n-\Delta} | p_m \rangle, \quad (6.41)$$

to rewrite Eq. (6.39e) as

$$= \frac{1}{4} \sum_{s_1, s_2, s'_1, s'_2}^{\pm} s_1 s_2 s'_1 s'_2 \prod_{j=1,2} e^{i\tau_j(p_{s_j n_j} + p_{s'_j m_j})/2} \langle p_{s_j n_j - s'_j m_j} | p_{2\theta_j} \rangle, \quad (6.42a)$$

$$= \frac{1}{4} \sum_{s_1, s_2, s'_1, s'_2}^{\pm} s_1 s_2 s'_1 s'_2 e^{i\tau \mathbf{p}_{\mathbf{n}, \mathbf{m}}^{\mathbf{s}, \mathbf{s}', +} / 2} \langle \mathbf{p}_{\mathbf{n}, \mathbf{m}}^{\mathbf{s}, \mathbf{s}', -} | \mathbf{p}_{2\theta} \rangle. \quad (6.42b)$$

Note that, by using the invariance (6.41), also scalar products involving $|p_0\rangle$ might occur formally, e. g., $\langle p_1 | p_1 \rangle = \langle p_0 | p_0 \rangle = 1$, thus we also allow $n_j = 0$ in Eq. (6.31) from now on.

Using Eqs. (6.42b) and (6.38), we derive the Weyl rule in $|\varphi_{\mathbf{n}}\rangle$ representation as

$$A_{\mathbf{nm}} = \langle \varphi_{\mathbf{n}} | \mathcal{Q}_0(A) | \varphi_{\mathbf{m}} \rangle, \quad (6.43a)$$

$$= \frac{1}{(2\pi)^2} \int_S d^2 \mathbf{q} \int_{\mathbb{R}} d^2 \mathbf{p} \sum_{\boldsymbol{\theta} \in \mathbb{Z}^2} \int_{\mathbb{R}} d^2 \boldsymbol{\tau} e^{-i2\pi \boldsymbol{\theta} \mathbf{q}} e^{-i\tau \mathbf{p}} \underbrace{\langle \varphi_{\mathbf{n}} | e^{i\tau \hat{\mathbf{p}}/2} e^{i2\pi \boldsymbol{\theta} \hat{\mathbf{q}}} e^{i\tau \hat{\mathbf{p}}/2} | \varphi_{\mathbf{m}} \rangle}_{= (6.42b)} A(\mathbf{q}, \mathbf{p}), \quad (6.43b)$$

$$= \frac{1}{(4\pi)^2} \sum_{s_1, s_2, s'_1, s'_2}^{\pm} s_1 s_2 s'_1 s'_2 \int_S d^2 \mathbf{q} \int_{\mathbb{R}} d^2 \mathbf{p} \sum_{\boldsymbol{\theta} \in \mathbb{Z}^2} e^{-i2\pi \boldsymbol{\theta} \mathbf{q}} \quad (6.43c)$$

$$\times \underbrace{\int_{\mathbb{R}} d^2 \boldsymbol{\tau} e^{i\tau (\mathbf{p}_{\mathbf{n}, \mathbf{m}}^{\mathbf{s}, \mathbf{s}', +} / 2 - \mathbf{p})}}_{= (2\pi)^2 \delta(\mathbf{p} - \mathbf{p}_{\mathbf{n}, \mathbf{m}}^{\mathbf{s}, \mathbf{s}', +} / 2)} \langle \mathbf{p}_{\mathbf{n}, \mathbf{m}}^{\mathbf{s}, \mathbf{s}', -} | \mathbf{p}_{2\theta} \rangle A(\mathbf{q}, \mathbf{p}), \quad (6.43d)$$

$$= \frac{1}{4} \sum_{s_1, s_2, s'_1, s'_2}^{\pm} s_1 s_2 s'_1 s'_2 \int_S d^2 \mathbf{q} A\left(\mathbf{q}, \mathbf{p}_{\mathbf{n}, \mathbf{m}}^{\mathbf{s}, \mathbf{s}', +} / 2\right) \sum_{\boldsymbol{\theta} \in \mathbb{Z}^2} e^{-i2\pi \boldsymbol{\theta} \mathbf{q}} \langle \mathbf{p}_{\mathbf{n}, \mathbf{m}}^{\mathbf{s}, \mathbf{s}', -} | \mathbf{p}_{2\theta} \rangle. \quad (6.43e)$$

The last step is to evaluate the double-sum over $\boldsymbol{\theta} = (\theta_1, \theta_2)$. This sum factorizes to $\mathcal{K}_1 \mathcal{K}_2$ with the

components

$$\mathcal{K}_j := \sum_{\theta_j \in \mathbb{Z}} e^{-i2\pi\theta_j q_j} \langle p_{s_j n_j - s'_j m_j} | p_{2\theta_j} \rangle. \quad (6.44)$$

We first consider the case, where $(n_j + m_j)$ is an even number. Note that this implies that also $(s_j n_j - s'_j m_j)$ is even for all signs (s_j, s'_j) . As $2\theta_j$ is even too, only the term with $(s_j n_j - s'_j m_j) = 2\theta_j$ contributes according to Eq. (6.32) and we obtain

$$\mathcal{K}_j = e^{-i\pi(s_j n_j - s'_j m_j) q_j}. \quad (6.45)$$

Secondly, we consider $(n_j + m_j)$ to be odd. With Eq. (6.32), we have

$$\mathcal{K}_j = \sum_{\theta_j \in \mathbb{Z}} e^{-i2\pi\theta_j q_j} \frac{(-1)^{2\theta_j - (s_j n_j - s'_j m_j)} - 1}{i\pi [2\theta_j - (s_j n_j - s'_j m_j)]}. \quad (6.46)$$

As $2\theta_j - (s_j n_j - s'_j m_j)$ is odd too, the numerator evaluates to (-2) , and we obtain

$$\mathcal{K}_j = -\frac{2}{i\pi} \sum_{\theta_j \in \mathbb{Z}} \frac{e^{-i2\pi\theta_j q_j}}{2\theta_j - (s_j n_j - s'_j m_j)}. \quad (6.47)$$

We evaluate this sum using that

$$\sum_{\theta \in \mathbb{Z}} \frac{e^{-i2\pi\theta q}}{2\theta - \xi} = -\frac{i\pi}{2} e^{-i\pi\xi q} \quad \text{for } q \in [0, 1) \text{ and } \xi \text{ odd}, \quad (6.48)$$

which can be shown by elementary methods. For $\xi = (s_j n_j - s'_j m_j)$ this leads to the same result \mathcal{K}_j as for the even case (6.45). Finally, by reinserting \mathcal{K}_j into Eq. (6.43e), we obtain the matrix elements of the Weyl quantized observable,

$$A_{\mathbf{nm}} = \frac{1}{4} \sum_{s_1, s_2, s'_1, s'_2}^{\pm} s_1 s_2 s'_1 s'_2 \int_{\mathcal{S}} d^2 \mathbf{q} A \left(\mathbf{q}, \mathbf{p}_{\mathbf{n}, \mathbf{m}}^{\mathbf{s}, \mathbf{s}', +} / 2 \right) e^{-i\mathbf{q} \mathbf{p}_{\mathbf{n}, \mathbf{m}}^{\mathbf{s}, \mathbf{s}', -} / \hbar}. \quad (6.49)$$

By resubstituting the $\mathbf{p}_{\mathbf{n}, \mathbf{m}}^{\mathbf{s}, \mathbf{s}', \pm}$ and assuming the scaling relation (5.16) for the classical observable $A(\mathbf{q}, \mathbf{p})$, this is simplified to

$$A_{\mathbf{nm}} = \left(\frac{\pi \hbar}{4} \right)^2 \sum_{s_1, s_2, s'_1, s'_2}^{\pm} s_1 s_2 s'_1 s'_2 \int_{\mathcal{S}} d^2 \mathbf{q} A \left[\mathbf{q}, \begin{pmatrix} s_1 n_1 + s'_1 m_1 \\ s_2 n_2 + s'_2 m_2 \end{pmatrix} \right] \exp \left[-i\pi \mathbf{q} \begin{pmatrix} s_1 n_1 - s'_1 m_1 \\ s_2 n_2 - s'_2 m_2 \end{pmatrix} \right]. \quad (6.50)$$

To evaluate the integrals, we discretize the position domain \mathcal{S} into N_q points along each direction q_1 and q_2 . As $(\mathbf{n}, \mathbf{m}) = (n_1, n_2, m_1, m_2)$, the matrix size of $A_{\mathbf{nm}}$ is $N_{\text{mat}} = N_1 N_2$ and the total

computation time grows like $\mathcal{O}(N_{\text{mat}}^2)$. In App. J, we present an optimized algorithm which reduces this to $\mathcal{O}(N_{\text{mat}})$.

Numerical test

To test the presented computation scheme, we first consider a toy Hamiltonian \hat{H} , whose eigenvalues and eigenvectors are known exactly. Here, any textbook system seems out of the question, as we require \hat{H} to be not in Schrödinger form. However, we can construct a non-Schrödinger Hamiltonian by considering, e. g., the modified square billiard on the unit square $\mathbf{q}' \in \mathcal{S}$, given by

$$H'(\mathbf{p}') = p_1'^2 + Z p_2'^2. \quad (6.51)$$

Here the factor $Z = \sqrt{3}$ is chosen to circumvent eigenvalue degeneracies between the uncoupled degrees of freedom. Compared to the square billiard $Z = 1$, this only changes the spectrum, while the eigenfunctions remain unchanged and are given by

$$\langle \mathbf{q}' | \psi_{\mathbf{n}} \rangle = 2 \sin(n_1 \pi q_1') \sin(n_2 \pi q_2'). \quad (6.52)$$

Then by applying a canonical transformation $\mathcal{T}_{\text{toy}} : (\mathbf{q}', \mathbf{p}') \mapsto (\mathbf{q}, \mathbf{p})$, we construct a new classical Hamiltonian

$$H(\mathbf{q}, \mathbf{p}) = H'[\mathcal{T}_{\text{toy}}^{-1}(\mathbf{q}, \mathbf{p})], \quad (6.53)$$

that is not in Schrödinger form. If we choose \mathcal{T}_{toy} as a point transformation, there is a unique relation between the eigenfunctions in both coordinates, given by [77, Eq. (1.2)]

$$\langle \mathbf{q} | \psi_{\mathbf{n}} \rangle = \sqrt{\left| \frac{d\mathbf{q}'}{d\mathbf{q}}(\mathbf{q}) \right|} \cdot \langle \mathbf{q}' | \psi_{\mathbf{n}} \rangle \Big|_{\mathbf{q}'=\mathbf{q}'(\mathbf{q})}. \quad (6.54)$$

Here $|\mathbf{q}\rangle$ and $|\mathbf{q}'\rangle$ denote the (different) eigenbases of $\hat{\mathbf{q}}$ and $\hat{\mathbf{q}}'$, respectively. This relation follows directly from the probability conservation $\rho(\mathbf{q})d\mathbf{q} = \rho'(\mathbf{q}')d\mathbf{q}'$ for $\rho(\mathbf{q}) = \langle \mathbf{q} | \psi_{\mathbf{n}} \rangle$ and $\rho'(\mathbf{q}') = \langle \mathbf{q}' | \psi_{\mathbf{n}} \rangle$. For the present purpose, the point transformation \mathcal{T}_{toy} should preserve the unit square \mathcal{S} , which is fulfilled, e. g., by the polynomial transformation

$$x'(x, y) = x + \epsilon \left[1 - 4\left(x - \frac{1}{2}\right)^2 \right] \left[1 - 2(2y - 1)^2 + (2y - 1)^4 \right], \quad (6.55a)$$

$$y'(x, y) = y, \quad (6.55b)$$

where we choose $\epsilon = 0.1$ in the following. Figure 6.5 shows the eigenfunction $\langle \mathbf{q}' | \psi_{\mathbf{n}} \rangle$ for $\mathbf{n} = (3, 5)$ (a), Eq. (6.52), and the transformed eigenfunction $\langle \mathbf{q} | \psi_{\mathbf{n}} \rangle$ (b), Eq. (6.54).

We now test our computation scheme by computing numerical solutions $|\psi_{\mathbf{n}}^{\text{num}}\rangle$ for the transformed toy Hamiltonian (6.53) using the parameters $(N_1, N_2, N_q) = (30, 30, 100)$. We compute the matrix elements (6.50) for the observable $A(\mathbf{q}, \mathbf{p}) = H(\mathbf{q}, \mathbf{p})$ and from its eigenvectors $\mathbf{c}_{\mathbf{m}}^{\mathbf{n}}$ we obtain the

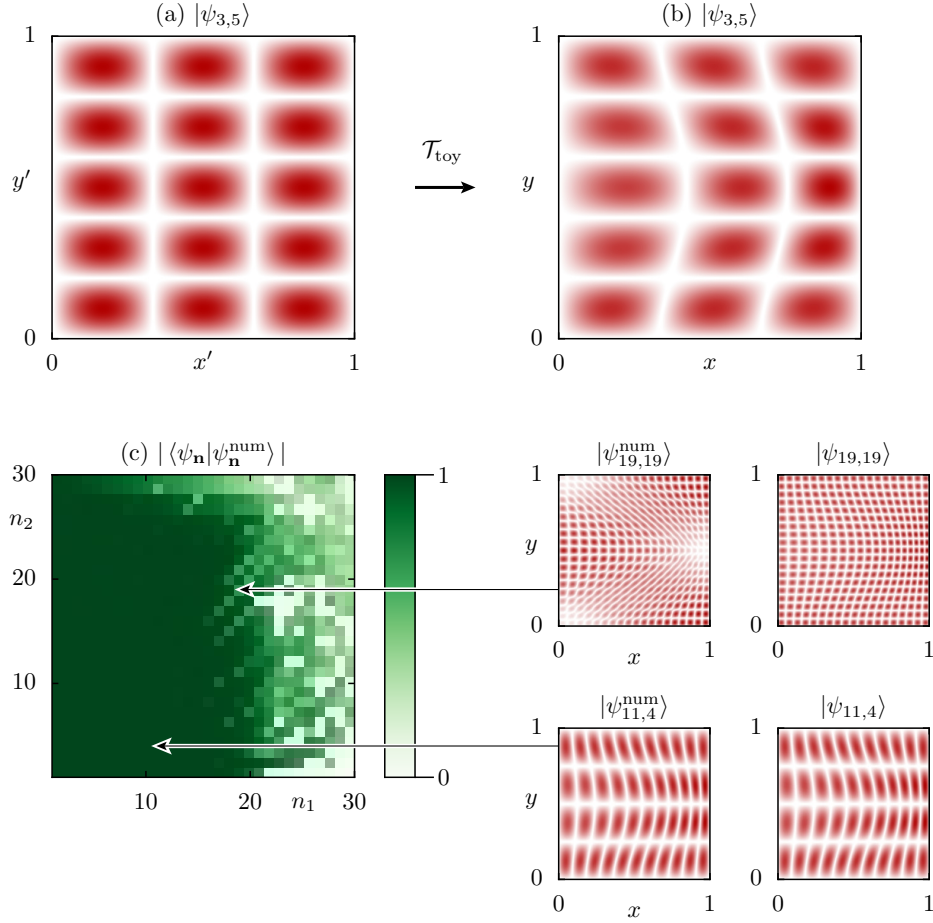


Figure 6.5.: (a) Modulus $|\langle \mathbf{q}' | \psi_{2,4} \rangle|$ of an eigenstate in $\mathbf{q}' = (x', y')$ -representation for the modified square billiard (6.51), shown on a linear scale. (b) Transformed eigenstate $|\langle \mathbf{q} | \psi_{2,4} \rangle|$, corresponding to the toy Hamiltonian (6.54). (c) Scalar product $|\langle \psi_{\mathbf{n}} | \psi_{\mathbf{n}}^{\text{num}} \rangle|$ of the predicted and the numerically computed eigenstates for different quantum numbers $\mathbf{n} = (n_1, n_2)$, together with insets (right) which show $|\langle \mathbf{q} | \psi_{\mathbf{n}}^{\text{num}} \rangle|$ and $|\langle \mathbf{q} | \psi_{\mathbf{n}} \rangle|$ for a state near the critical threshold $\mathbf{n} = (19, 19)$ and a well approximated state $\mathbf{n} = (11, 4)$.

eigenstates $|\psi_{\mathbf{n}}^{\text{num}}\rangle$. Note that due to the scaling relation (5.16) of $H(\mathbf{q}, \mathbf{p})$, Planck's constant \hbar does not influence the eigenstates, while the eigenvalues scale with \hbar^2 . We sort the resulting eigenstates, such that $|\psi_{\mathbf{n}}^{\text{num}}\rangle$ has n_j modes along each direction q_j . To compare these eigenstates to the exact solutions, we compute the scalar product $|\langle \psi_{\mathbf{n}} | \psi_{\mathbf{n}}^{\text{num}} \rangle|$, see Fig. 6.5(c). Below a critical threshold $n_1 < 15$, $n_2 < 25$, the eigenstates are well approximated. For states outside of this threshold, the cutoff parameters (N_1, N_2) do not suffice. This is illustrated in Fig. 6.5(c) where we compare $|\langle \mathbf{q} | \psi_{\mathbf{n}} \rangle|$ and $|\langle \mathbf{q} | \psi_{\mathbf{n}}^{\text{num}} \rangle|$ for $\mathbf{n} = (11, 4)$ and $\mathbf{n} = (19, 19)$. Apparently, choosing higher cutoff parameters (N_1, N_2) increases the critical threshold. As this increase leaves any well approximated state $|\psi_{\mathbf{n}}^{\text{num}}\rangle$ invariant, it also serves as a check for convergence when the true solutions $|\psi_{\mathbf{n}}\rangle$ are unknown.

6.4.3. Application

We now apply the fictitious integrable system approach to the cosine billiard (5.2). We use the parameters $(h, w) = (0.2, 0.066)$ where the system has a generic, mixed phase space and an integrable approximation has been determined in Sec. 5.4. We consider the Hamiltonians of the billiard H , Eq. (5.1), and its integrable approximation H_{reg} , Eq. (3.15), additionally transformed to the coordinates (\bar{q}, \bar{p}) defined in Sec. 5.2. Moreover, we shift \bar{x} to the interval $[0, 1]$ according to the convention (6.23).

Applying the computation scheme from Sec. 6.4.2 with the numerical parameters $(N_1, N_2, N_q) = (40, 40, 100)$, we obtain the eigenstates of \hat{H} and \hat{H}_{reg} . The first row in Fig. 6.6 shows different regular eigenstates $|\psi_{\mathbf{n}}\rangle$ of the cosine billiard \hat{H} in \mathbf{q} -representation, which locate in the regular region, see also Fig. 5.2(a). In the second row, we show the same eigenstates in $\bar{\mathbf{q}}$ -representation. For comparison, the third row (d–f) shows the corresponding eigenstates $|\psi_{\text{reg}}^{\mathbf{n}}\rangle$ of \hat{H}_{reg} . Note that, as the connection (5.5) between the coordinates (\bar{q}, \bar{p}) and the original billiard coordinates (\mathbf{q}, \mathbf{p}) is a point transformation, also the transformation between quantum states $\langle \bar{\mathbf{q}} | \psi \rangle$ and $\langle \mathbf{q} | \psi \rangle$ follows straightforwardly from Eq. (6.54).

Due to the mixed phase space of H , the basis $|\psi_{\mathbf{n}}\rangle$ contains “regular” states which localize on a quantizing torus (see Fig. 6.6(a–c)) and “chaotic” states (not shown). In contrast, the basis $|\psi_{\text{reg}}^{\mathbf{n}}\rangle$ only contains “regular” quasimodes, as the integrable approximation H_{reg} globally extrapolates the regular

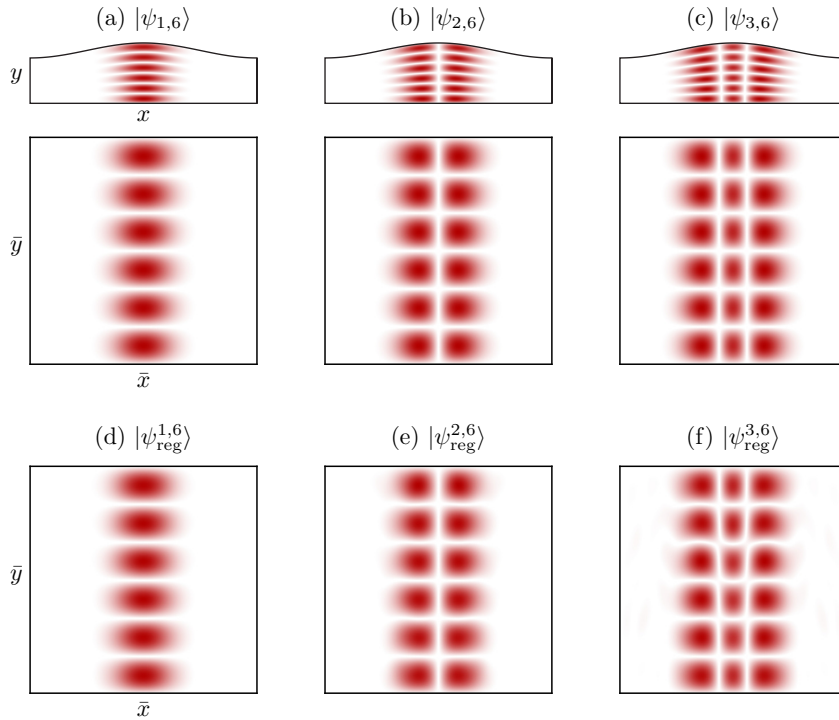


Figure 6.6.: (a–c) Billiard eigenstates $|\psi_{\mathbf{n}}\rangle$ in $\mathbf{q} = (x, y)$ -representation (first row) and $\bar{\mathbf{q}} = (\bar{x}, \bar{y})$ -representation (second row), for $\mathbf{n} = (1, 6)$ (a), $\mathbf{n} = (2, 6)$ (b), and $\mathbf{n} = (3, 6)$ (c), shown on a linear scale. (d–f) Corresponding quasimodes $|\psi_{\text{reg}}^{\mathbf{n}}\rangle$ in $\bar{\mathbf{q}} = (\bar{x}, \bar{y})$ -representation.

region of H . Thus, some of the quasimodes $|\psi_{\text{reg}}^{\mathbf{n}}\rangle$ are located in the regular region of H , and some are located outside. These two parts of the basis $|\psi_{\text{reg}}^{\mathbf{n}}\rangle$ can be distinguished very easily by considering the action–angle coordinates $(\boldsymbol{\vartheta}, \mathbf{J})$, where each torus corresponds to a point \mathbf{J} in the action plane. Here, according to the EBK quantization [78], the eigenstates $|\psi_{\text{reg}}^{\mathbf{n}}\rangle$ localize on quantizing actions given by

$$\mathbf{J}_{\mathbf{n}} = \left(\mathbf{n} + \frac{\boldsymbol{\mu}}{4} \right) \hbar + \mathcal{O}(\hbar^2), \quad \mathbf{n} \in \mathbb{N}^2. \quad (6.56)$$

The numbers $\boldsymbol{\mu} = (\mu_1, \mu_2)$ are the Maslov indices of the fundamental loops $(\mathcal{C}_1, \mathcal{C}_2)$ on the considered torus. As discussed in Sec. 5.1, \mathcal{C}_1 includes two turning points, while \mathcal{C}_2 includes two hard-wall reflections. This leads to $\mu_1 = 2$ and $\mu_2 = 4$ [78, App. D.2]. Neglecting $\mathcal{O}(\hbar^2)$, the resulting grid of quantizing actions (6.56) is sketched in Fig. 6.7. Now, the scaling relation (5.21) of $H_{\text{reg}}(\mathbf{J})$ decomposes the action plane into families of similar tori located on radial lines through the origin $\mathbf{J} = \mathbf{0}$. Particularly, the line $J_1 = 0$ corresponds to the family of stable periodic orbits in the center of the regular region, see Sec. 5.1. Consequently, the border of the regular region is completely defined, if one point $\mathbf{J}^* = (J_1^*, J_2^*)$ on this border is known, see the dashed line in Fig. 6.7. Note that one such point \mathbf{J}^* is determined when applying the iterative canonical transformation method, see the rightmost dot in Fig. 5.6(a). Therefore, $|\psi_{\text{reg}}^{\mathbf{n}}\rangle$ belongs to the regular region of H if

$$\frac{n_1 + \frac{\mu_1}{4}}{n_2 + \frac{\mu_2}{4}} < \frac{J_1^*}{J_2^*}. \quad (6.57)$$

As the main regular island of the cosine billiard is restricted in \bar{x} -direction, we choose a position \bar{x}_{abs} slightly left of the outermost torus and introduce the symmetric absorber

$$\hat{P}_{\text{abs}} = \int_{\text{abs}} d^2 \bar{\mathbf{q}} |\bar{\mathbf{q}}\rangle \langle \bar{\mathbf{q}}|, \quad (6.58)$$

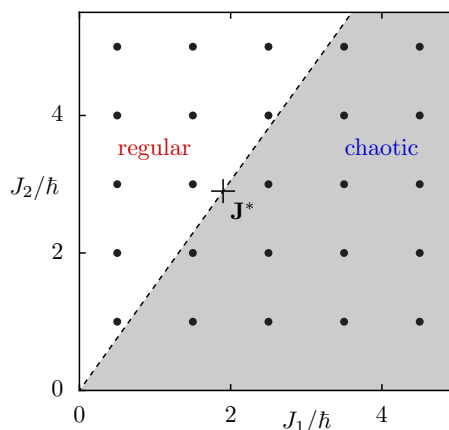


Figure 6.7.: Action plane with a grid of quantizing actions (6.56) (black dots), and a radial line through a point \mathbf{J}^* (cross) separating the regular from the chaotic phase-space region.

where the integral goes over all positions with $\bar{x} \in [0, \bar{x}_{\text{abs}}] \cup [1 - \bar{x}_{\text{abs}}, 1]$. For the considered system $(h, w) = (0.2, 0.066)$ we set $\bar{x}_{\text{abs}} = 0.26$. The inset in Fig. 6.8(a) shows this absorber in the billiard coordinates (x, y) (gray areas) and a trajectory on the outermost torus \mathbf{J}^* (red).

Using this absorber, we first compute the tunneling rates, Eq. (6.4), from the eigenvalues of the open system \hat{U}_{open} , which we evaluate with Eq. (6.22e). Secondly, we compute the predicted tunneling rates using the fictitious integrable system approach (6.7). For the following purpose it is sufficient to use the integrable approximation \hat{H}_{reg}^1 obtained after the first step of the iterative canonical transformation method. In Fig. 6.8(a) we compare the tunneling rates $\gamma_{\mathbf{n}}$ for $n_1 = 1$ (bright dots) with their prediction (dark dots and line). As can be seen, this prediction fails for the most values of n_2 , where it is systematically larger than the true rates. This behavior is caused by the quasimodes $|\psi_{\text{reg}}^{\mathbf{n}}\rangle$, which are not purely located at the \mathbf{n} -th quantizing tori but also include small couplings to other tori $\mathbf{n}' \neq \mathbf{n}$. This can be seen, e. g., for the states $|\psi_{\text{reg}}^{1,4}\rangle$ and $|\psi_{\text{reg}}^{7,3}\rangle$ in Figs. 6.8(b) and (c), where we find small contributions of $|\psi_{\text{reg}}^{1,4}\rangle$ located far from the central orbit $\bar{x} = \frac{1}{2}$ which replicate the structure of $|\psi_{\text{reg}}^{7,3}\rangle$. This hybridization is possible due to a quasi-degeneracy of the tori $\mathbf{n} = (1, 4)$ and $\mathbf{n}' = (7, 3)$ in energy with $\Delta E/E \approx 0.006$. This can be understood by considering the action plane, where the tori $\mathbf{n} = (1, 4)$ and $\mathbf{n}' = (7, 3)$ lie close to a contour line of the Hamiltonian $\mathcal{H}_{\text{reg}}(\mathbf{J})$, see the red line in Fig. 6.8(d). From this figure it becomes obvious, that quasi-degeneracies are unavoidable. They arise whenever a contour line of $\mathcal{H}_{\text{reg}}(\mathbf{J})$ passes the neighborhoods of multiple points from

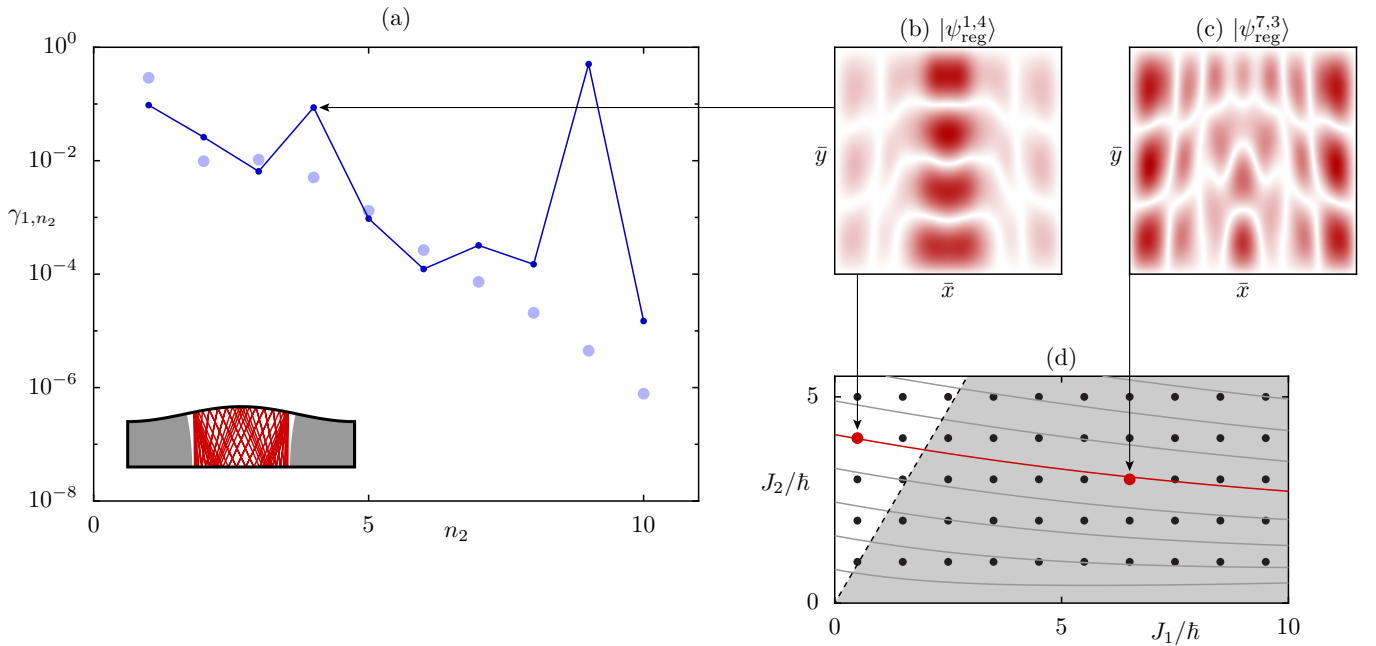


Figure 6.8.: (a) Tunneling rates γ_{1,n_2} of the cosine billiard (5.2) with $(h, w) = (0.2, 0.066)$ (bright dots) compared to their prediction obtained from the fictitious integrable system approach (dark dots and line) using an integrable approximation H_{reg}^1 obtained from the iterative canonical transformation method. (b–c) Quasimodes $\langle \bar{q} | \psi_{\text{reg}}^{\mathbf{n}} \rangle$ for (b) $\mathbf{n} = (1, 4)$ and (c) $\mathbf{n} = (7, 3)$. (d) Action plane with quantizing actions (6.56) (dots) and contour lines of the integrable approximation $\mathcal{H}_{\text{reg}}(\mathbf{J})$ (red and gray lines).

the quantizing grid (6.56), which happens systematically for an equidistant grid and is independent of the chosen function $\mathcal{H}_{\text{reg}}(\mathbf{J})$. This is in contrast to the situation of $f = 1$ degree of freedom, where such quasi-degeneracies can be removed by enforcing the monotony of $\mathcal{H}_{\text{reg}}(J)$, Eq. (6.9). Moreover, choosing higher basis cutoffs (N_1, N_2) enlarges the grid of quantizing actions (6.56), which incrementally enhances the appearance of quasi-degeneracies. Having stated the statistical necessity of quasi-degenerate states, however, only explains the possibility of couplings, but not their existence.

A hint to their origin comes up, if we consider the initial integrable approximation \hat{H}_{reg}^0 , Eq. (3.9), for which we obtain the prediction shown in Fig. 6.9. Here, the tunneling rate predictions for $\gamma_{\mathbf{n}}$ with $n_1 = 1, 2, 3$ (blue, green, and red, respectively) show a vague agreement, only. This is expected, as H_{reg}^0 gives only a rough approximation of H . Apart from this, however, we observe no couplings between energetically close tori, see Figs. 6.9(b) and (c). This example shows that the couplings in \hat{H}_{reg}^1 between different tori are caused by the canonical transformation T_1 . Although we could not resolve this issue, we emphasize an alternative interpretation. It was already exposed in Sec. 6.3, that the canonical transformations T_n , $n > 0$ give rise to quantum mechanical ambiguities, namely in the quantization rule \mathcal{Q} , which is related to the current problem. Denote by $|\mathbf{J}_{\mathbf{n}}\rangle$ a state purely localizing on the \mathbf{n} -th quantizing torus. Among all possible quantizations, the fictitious integrable system approach requires an integrable approximation $\hat{H}_{\text{reg}}^{n*}$ which is diagonal in this basis, i. e.,

$$\langle \mathbf{J}_{\mathbf{n}} | \hat{H}_{\text{reg}}^{n*} | \mathbf{J}_{\mathbf{m}} \rangle = \delta_{\mathbf{n}, \mathbf{m}}. \quad (6.59)$$

However, as the classical Hamiltonian H_{reg}^n has no unique quantization for $n \neq 0$, any two quantizations differ by a term $\mathcal{O}(\hbar)$, Eq. (6.13c). From a perturbative perspective it is clear, that even this small perturbation $\mathcal{Q}(H_{\text{reg}}^n) = \hat{H}_{\text{reg}}^{n*} + \mathcal{O}(\hbar)$ leads to significant couplings $\langle \mathbf{J}_{\mathbf{n}} | \mathcal{Q}(H_{\text{reg}}^n) | \mathbf{J}_{\mathbf{m}} \rangle$ between energetically close tori. Therefore, the unwanted couplings appear as the consequence of an improp-

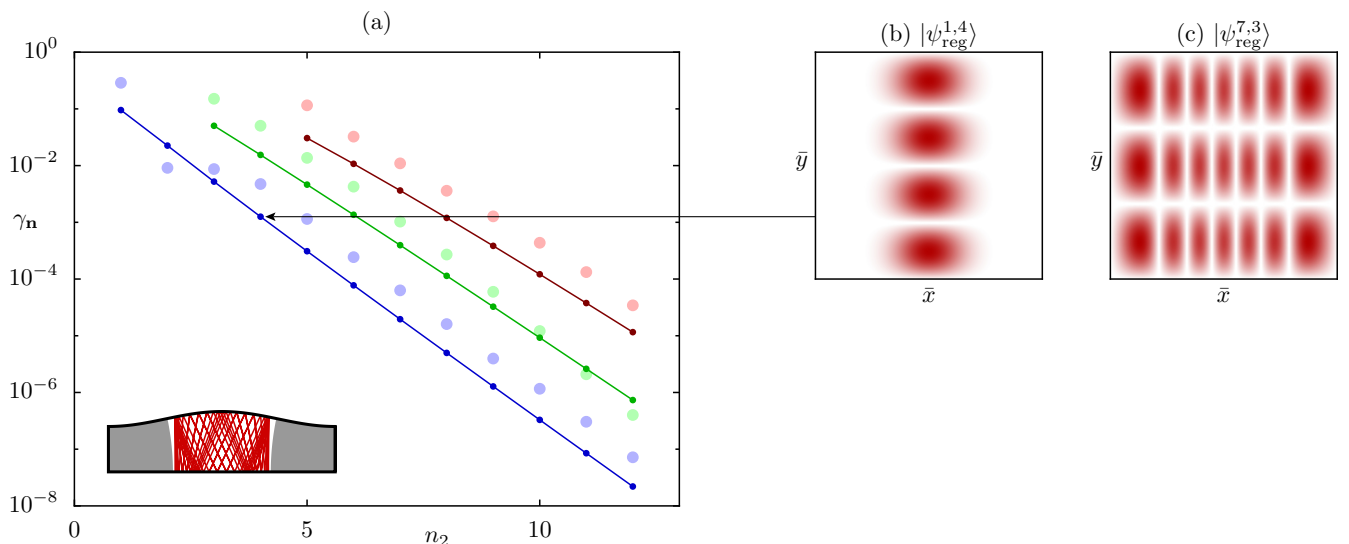


Figure 6.9.: (a) Tunneling rates $\gamma_{\mathbf{n}}$ as in Fig. 6.8(a) but for H_{reg}^0 and $n_1 = 1$ (blue), $n_1 = 2$ (green), and $n_1 = 3$ (red). (b–c) Quasimodes $\langle \bar{\mathbf{q}} | \psi_{\text{reg}}^{\mathbf{n}} \rangle$ for (b) $\mathbf{n} = (1, 4)$ and (c) $\mathbf{n} = (7, 3)$.

erly chosen quantization rule. An equivalent problem arose for $f = 1$ degree of freedom in Ref. [50, Sec. 4.3.2], where integrable approximations from the iterative canonical transformation method are used to describe resonance-assisted tunneling. There, the Weyl quantization also causes undesired couplings in \hat{H}_{reg}^n if $n \neq 0$. This is resolved by the author due to an analytical quantization procedure based on selection rules for the couplings, which requires to reset $\mathcal{H}_{\text{reg}}(J)$ according to Eq. (6.9). This way the quantization rule remains ambiguous, but its influence on the couplings is effectively suppressed by a selective removal of the quasi-degeneracies. However, as stated above, quasi-degeneracies are unavoidable in the present situation.

These considerations suggest, that the missing piece for a successful generalization of the fictitious integrable system approach to $f \geq 2$ can possibly be found from two perspectives. One option would be a deeper investigation of the interplay between canonical transformations and quantization, possibly including the role of the Egorov theorem. A second option would be, to not choose the quasimodes from the eigenbasis of \hat{H}_{reg} , but from the eigenbasis $|\mathbf{J}_n\rangle$ of the complete set of commuting observables $\hat{\mathbf{J}} = (\hat{J}_1, \dots, \hat{J}_f)$, whose classical counterparts $\mathbf{J}(\mathbf{q}, \mathbf{p})$ are also determined by the iterative canonical transformation method. Although this complete set formally defines a unique eigenbasis, its practical determination becomes difficult, as f operators need to be considered simultaneously, whose spectra are completely degenerate.

Finally, we apply the fictitious integrable system approach in the near-integrable case, where the integrable approximation H_{reg}^0 is sufficient. Specifically, we choose the cosine billiard with $(h, w) = (0.115, 0.06)$ and $\bar{x}_{\text{abs}} = 0.148$. We compute the quasimodes with the computation scheme from Sec. 6.4.2 with the numerical parameters $(N_1, N_2, N_q) = (60, 20, 100)$. The comparison of the tunneling rates with their prediction based on H_{reg}^0 is shown in Fig. 6.10. Here, for all numerically accessible tunneling rates $\gamma_n > 10^{-16}$, we obtain a closer prediction. This confirms the validity of our imple-

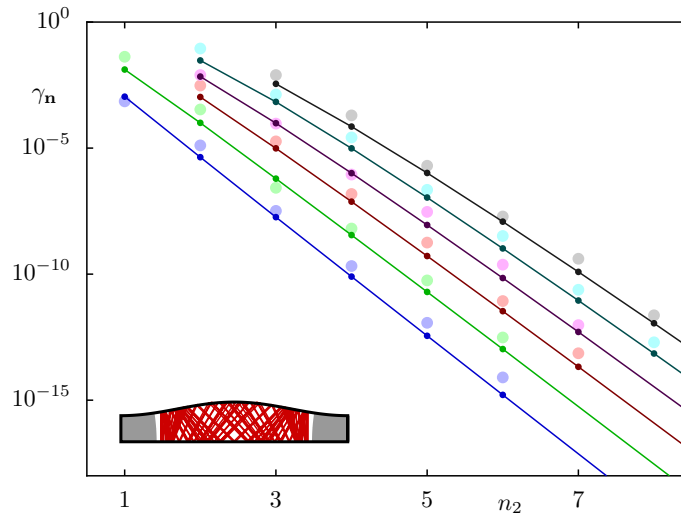


Figure 6.10.: Tunneling rates γ_n as in Fig. 6.8(a) but for $(h, w) = (0.115, 0.06)$, H_{reg}^0 , and the quantum numbers $n_1 = 1$ (blue), $n_1 = 2$ (green), $n_1 = 3$ (red), $n_1 = 4$ (purple), $n_1 = 5$ (light blue), and $n_1 = 6$ (gray).

mentation based on the derived Weyl quantization and demonstrates the principal applicability of the fictitious integrable system approach to 2D billiards.

7. Summary and outlook

In this thesis, we developed a new method which constructs an integrable approximation H_{reg} to a given, non-integrable system H (Sec. 3). This *iterative canonical transformation method* requires no specification on the system H or its dimension, aside from an increasing numerical effort for higher dimensions. The basic idea of this method is to determine H_{reg} by independently constructing its frequency function $\omega(\mathbf{J})$ (frequency approximation) and its canonical transformation T (shape approximation), where both $\omega(\mathbf{J})$ and T are optimized using sampled data of the target system H . In the second step, the canonical transformation T is decomposed into a sequence of individual transformations (T_0, T_1, \dots, T_N) which are chosen iteratively from a family of canonical transformations (iterative improvement).

Up to now, the construction of a globally accurate integrable approximation was practically restricted to near-integrable target systems, due to the perturbative character of traditional methods. The main result of this thesis was to overcome this restriction. Technically, this was achieved by a damping mechanism, which restabilizes the iterative improvement even for strongly perturbed systems. This advancement was confirmed by an explicit comparison to the methods of normal forms [18, 19] and Lie transforms [8, 20–22] (Sec. 4.5).

We demonstrated the applicability of the method to symplectic 2D maps (Sec. 4) and 2D billiards (Sec. 5) far from the near-integrable regime. For both system classes, we obtained comparably accurate results. Moreover, we have shown that the method is able to reach the insurmountable, optimal accuracy of any integrable approximation, which is caused by the presence of nonlinear resonances and chaotic layers (Sec. 4.4).

We have emphasized, that the proper choice of the initial canonical transformation T_0 allows to enhance the phase-space topology of H_{reg} . For symplectic 2D maps, we have used this to incorporate a separatrix (Sec. 4.6) or a nonlinear resonance chain (Sec. 4.7) into the integrable approximation H_{reg} . Here, the latter result was obtained in cooperation with Julius Kullig and Normann Mertig.

Finally, we have used the integrable approximations for the theoretical prediction of direct regular-to-chaotic tunneling rates (Sec. 6). This was accomplished by applying the fictitious integrable system approach [12–14] with the previously constructed integrable approximations H_{reg} .

For symplectic 2D maps, we performed this prediction with success (Sec. 6.2). We emphasized that the required quantized integrable approximation \hat{H}_{reg} is ambiguous due to the non-Schrödinger form of the classical Hamiltonian H_{reg} (Sec. 6.3). For the standard map, we gave numerical evidence for the resulting ambiguity of the tunneling predictions.

For generic 2D billiards, we also implemented this prediction (Sec. 6.4). We first derived an analogue of the Weyl quantization adapted to spatially confined systems. For the cosine billiard, a successful

prediction was only achieved in the near-integrable case, where the initial integrable approximation H_{reg}^0 is sufficient. For H_{reg}^n with $n > 0$, however, we found unexpected inter-torus couplings in the quantized integrable approximation \hat{H}_{reg}^n . The nature of these couplings represents the most important open question raised by this work, as it prevents a successful application of the fictitious integrable system approach to generic billiards, up to now. Our results give strong evidence, that these couplings occur generally for systems with $f > 1$ degrees of freedom. We related them to the ambiguity of the quantization of H_{reg} , which is inherent in the fictitious integrable system approach, and discussed possible solutions. We stress, that the occurring question for the “correct” quantization of a general Hamiltonian is equivalent to the question for the “correct” quantum analogue of a general canonical transformation, which has a long history and is not yet answered [79–82]. However, in the present context “correct” refers to the concrete requirement of vanishing inter-torus couplings, which might simplify the problem.

In principle, the fictitious integrable system approach allows to predict tunneling rates in 2D billiards and quality factors in open microcavities. Up to now, this was only possible for special boundary geometries [15, 16], where a direct construction of the quasimodes avoids to determine a proper quantization of H_{reg} . If, however, the fictitious integrable system approach can be extended by such a quantization, the iterative canonical transformation method allows its application to billiards and microcavities with arbitrary boundary geometries, as well as to higher-dimensional smooth-potential systems.

Apart from that, the results of this thesis allow to readily extend some tunneling applications, where the torus-coupling problem is not relevant. The first application is based on Ref. [14]. Here, the authors extend the prediction of direct tunneling from the fictitious integrable system approach with the theory of resonance-assisted tunneling [7–11]. While the direct tunneling rate follows from an integrable approximation H_{reg} , the resonant contributions appear as perturbative corrections based on properties of the dominant resonance chain. Recently, using the iterative canonical transformation method with resonance (Sec. 4.7) this prediction was simplified by including the resonance already in H_{reg} [50, 66].

Further applications arise in the semiclassical description of tunneling in complex phase space. Here, the tunneling mechanism is expressed by paths on the complexified torus, which can propagate into the classically forbidden regions in real phase space. However, as non-integrable tori are not analytic, their complex continuation is limited due to a “natural boundary” [7, 8, 83]. To avoid this, one uses analytic tori of an integrable approximation H_{reg} instead. The iterative canonical transformation method is especially suitable for this, as $T(\boldsymbol{\vartheta}, \mathbf{J})$ gives a direct parametrization of the complex tori in terms of complex angles $\boldsymbol{\vartheta}$. For the direct tunneling mechanism, this complex-path approach was applied before in 2D maps [37, 69] and near-integrable optical microcavities [67, 68]. Recently, with the iterative canonical transformation method with resonance for 2D maps, also complex paths for the resonance-assisted tunneling mechanism have been constructed successfully [70]. Moreover, the present results for 2D billiards would also allow for an application to strongly deformed microcavities. We mention, however, that this poses the additional challenge of finding the relevant tunneling paths

in the billiard's complexified, eight-dimensional phase space, which is complicated even for simple geometries [84].

We mention, that another general area of potential applications is transport in Hamiltonian systems, such as Arnold diffusion or random diffusion. Here, the diffusion between different tori is naturally described in action space. This requires a global, smooth function $\mathbf{J}(\mathbf{q}, \mathbf{p})$ in phase space, which is directly determined by the iterative canonical transformation method. Especially for the conceptually simple case of 2D maps, our results would allow to generalize works such as Ref. [3] to strongly-perturbed systems. Also, recent work on random diffusion in 2D maps which uses action coordinates equivalent to H_{reg}^0 [35] could be extended.

From the methodical perspective, it would be of interest to generalize the iterative canonical transformation method with resonance (i) to include multiple resonances and (ii) to higher dimensions. This would, however, require resonant normal forms (i) with multiple resonances or (ii) in higher dimensions. The first is still an open question, while for the second, the implementation of the correct actions and frequencies represents the main difficulty. If those requirements were given, however, the shape approximation using the iterative canonical transformation method should be straightforward.

Appendix

A. Approximation of the cost function \mathcal{L}

In the following we derive the coefficients B_ν and $C_{\mu\nu}$, Eqs. (3.21), for the quadratic approximation (3.20) of the cost function $\mathcal{L}(\mathbf{a})$. This approximation follows from inserting Eqs. (3.13) into Eq. (3.19) which gives

$$\mathcal{L}(\mathbf{a}) = \frac{1}{N_p} \sum_{\tau\ell} \left(\mathbf{q}_\ell^\tau - \mathbf{q}_\ell^{\tau,n} + \sum_\lambda a_\lambda \frac{\partial G_\lambda}{\partial \mathbf{p}}(\mathbf{q}_\ell^{\tau,n}, \mathbf{p}_\ell^{\tau,n}) \right)^2 \quad (\text{A.1})$$

$$+ \frac{1}{N_p} \sum_{\tau\ell} \left(\mathbf{p}_\ell^\tau - \mathbf{p}_\ell^{\tau,n} - \sum_\lambda a_\lambda \frac{\partial G_\lambda}{\partial \mathbf{q}}(\mathbf{q}_\ell^{\tau,n}, \mathbf{p}_\ell^{\tau,n}) \right)^2. \quad (\text{A.2})$$

Using the chain rule, we obtain the first derivatives

$$\frac{\partial \mathcal{L}}{\partial a_\nu}(\mathbf{a}) = \frac{2}{N_p} \sum_{\tau\ell} \left(\mathbf{q}_\ell^\tau - \mathbf{q}_\ell^{\tau,n} + \sum_\lambda a_\lambda \frac{\partial G_\lambda}{\partial \mathbf{p}}(\mathbf{q}_\ell^{\tau,n}, \mathbf{p}_\ell^{\tau,n}) \right) \frac{\partial G_\nu}{\partial \mathbf{p}}(\mathbf{q}_\ell^{\tau,n}, \mathbf{p}_\ell^{\tau,n}) \quad (\text{A.3})$$

$$- \frac{2}{N_p} \sum_{\tau\ell} \left(\mathbf{p}_\ell^\tau - \mathbf{p}_\ell^{\tau,n} - \sum_\lambda a_\lambda \frac{\partial G_\lambda}{\partial \mathbf{q}}(\mathbf{q}_\ell^{\tau,n}, \mathbf{p}_\ell^{\tau,n}) \right) \frac{\partial G_\nu}{\partial \mathbf{q}}(\mathbf{q}_\ell^{\tau,n}, \mathbf{p}_\ell^{\tau,n}), \quad (\text{A.4})$$

and the constant, second derivatives

$$\frac{\partial}{\partial a_\mu} \frac{\partial \mathcal{L}}{\partial a_\nu} = \frac{2}{N_p} \sum_{\tau\ell} \left(\frac{\partial G_\mu}{\partial \mathbf{p}}(\mathbf{q}_\ell^{\tau,n}, \mathbf{p}_\ell^{\tau,n}) \frac{\partial G_\nu}{\partial \mathbf{p}}(\mathbf{q}_\ell^{\tau,n}, \mathbf{p}_\ell^{\tau,n}) + \frac{\partial G_\mu}{\partial \mathbf{q}}(\mathbf{q}_\ell^{\tau,n}, \mathbf{p}_\ell^{\tau,n}) \frac{\partial G_\nu}{\partial \mathbf{q}}(\mathbf{q}_\ell^{\tau,n}, \mathbf{p}_\ell^{\tau,n}) \right). \quad (\text{A.5})$$

This allows to compute the coefficients appearing in Eq. (3.20) as

$$B_\nu = -\frac{N_p}{2} \frac{\partial \mathcal{L}}{\partial a_\nu}(\mathbf{a} = \mathbf{0}), \quad (\text{A.6})$$

$$C_{\mu\nu} = \frac{N_p}{2} \frac{\partial^2 \mathcal{L}}{\partial a_\mu \partial a_\nu}(\mathbf{a} = \mathbf{0}), \quad (\text{A.7})$$

which leads to the results (3.21).

B. Closed form for H_{reg}^N

One drawback of the iterative canonical transformation method is, that the resulting integrable approximation $H_{\text{reg}}^N(\mathbf{q}, \mathbf{p})$ is not constructed in a closed form. Instead, the canonical transformations T_n in Eq. (3.15) follow from the implicit Eqs. (3.11) and are applied only numerically. We remark that, however, such a closed form can be derived as a series expansion up to any order in the transformation parameters. In the following, we do not explicitly perform this expansion, but sketch its idea.

We start by denoting the phase-space point by $\mathbf{x} = (\mathbf{q}, \mathbf{p})$ and express the transformations by their parameters, $T_n = T^{\mathbf{a}^n}$. With this, Eq. (3.15) takes the form

$$H_{\text{reg}}^N(\mathbf{x}) = H_{\text{reg}}^0 \left[(T^{\mathbf{a}^1})^{-1} \circ \dots \circ (T^{\mathbf{a}^N})^{-1}(\mathbf{x}) \right]. \quad (\text{B.1})$$

Now, Eq. (3.11) allows in principle to derive an explicit expansion of $(T^{\mathbf{a}})^{-1}$ in \mathbf{a} up to any order r , which is of the general form

$$(T^{\mathbf{a}})^{-1}(\mathbf{x}) = \mathbf{x} + \sum_{\substack{\mathbf{k} \in \mathbb{N}_0^N \\ |\mathbf{k}| \leq r}} T_{\mathbf{k}}(\mathbf{x}) \cdot a_{\nu_1}^{k_1} \dots a_{\nu_N}^{k_N} + \mathcal{O}(|\mathbf{a}|^{r+1}). \quad (\text{B.2})$$

Here $|\mathbf{k}| = k_1 + \dots + k_N$. The explicit solution of Eqs. (3.11) gives the coefficients as polynomials of the generating function's partial derivatives,

$$T_{\mathbf{k}}(\mathbf{x}) \sim \frac{\partial^{r_1 + \dots + r_{2f}} G_{\nu}}{\partial x_1^{r_1} \dots \partial x_{2f}^{r_{2f}}}(\mathbf{x}), \quad r_1 + \dots + r_{2f} \leq r + 1. \quad (\text{B.3})$$

For example, the linear order solution $r = 1$ follows from inverting Eq. (3.13). As in linear order $(T^{\mathbf{a}})^{-1} = T^{-\mathbf{a}}$, this inversion reduces to exchanging \mathbf{x} and \mathbf{x}' and replacing $\mathbf{a} \mapsto -\mathbf{a}$.

By combining the expansions (B.2) into Eq. (B.1) and expanding the result again, one can finally derive a closed form

$$H_{\text{reg}}^N(\mathbf{x}) = H_{\text{reg}}^0(\mathbf{x}) + \sum_{\substack{\mathbf{k}_n \in \mathbb{N}_0^N \\ 1 \leq |\mathbf{k}_1| + \dots + |\mathbf{k}_N| \leq r}} H_{\text{reg}, \mathbf{k}_1, \dots, \mathbf{k}_N}(\mathbf{x}) \prod_{n=1}^N \prod_{\nu=1}^N (\mathbf{a}_n)_{\nu}^{(\mathbf{k}_n)_{\nu}} + \mathcal{O}_{r+1}(|\mathbf{a}_1|, \dots, |\mathbf{a}_N|). \quad (\text{B.4})$$

Formally, this result generalizes the Lie formula (4.65) to multiple transformations. However, in contrast to the Lie formula, this expansion converges for $r \rightarrow \infty$, as the underlying Hamiltonian H_{reg}^N is integrable. Once, this closed form (B.4) is derived up to order r , its error $\mathcal{O}_{r+1}(|\mathbf{a}_1|, \dots, |\mathbf{a}_N|)$ can be made arbitrarily small by choosing H_{reg}^N with a sufficiently strong damping.

C. Properness of the implicit function ϕ

In the following we show, that the function $\phi(\mathbf{x}, \mathbf{x}')$ given by Eq. (4.18) is proper in \mathbf{x} . Keeping \mathbf{x}' fixed, this function is of the type $\mathbb{R}^{2f} \mapsto \mathbb{R}^{2f}$, thus properness is ensured by [44]

$$\lim_{|\mathbf{x}| \rightarrow \infty} |\phi(\mathbf{x}, \mathbf{x}')|^2 = \infty. \quad (\text{C.1})$$

Using Eqs. (4.18) and (3.11), we have

$$|\phi(\mathbf{x}, \mathbf{x}')|^2 = |\phi_1(\mathbf{q}, \mathbf{p}, \mathbf{q}', \mathbf{p}')|^2 + |\phi_2(\mathbf{q}, \mathbf{p}, \mathbf{q}', \mathbf{p}')|^2 \quad (\text{C.2})$$

$$= |\mathbf{q} - \mathbf{\Delta}_1(\mathbf{q}, \mathbf{q}', \mathbf{p}')|^2 + |\mathbf{p} - \mathbf{\Delta}_2(\mathbf{q}, \mathbf{p}')|^2, \quad (\text{C.3})$$

where

$$\mathbf{\Delta}_1(\mathbf{q}, \mathbf{q}', \mathbf{p}') = \mathbf{q}' - \sum_{\nu} a_{\nu} \frac{\partial G_{\nu}}{\partial \mathbf{p}'}(\mathbf{q}, \mathbf{p}'), \quad (\text{C.4})$$

$$\mathbf{\Delta}_2(\mathbf{q}, \mathbf{p}') = -\mathbf{p}' - \sum_{\nu} a_{\nu} \frac{\partial G_{\nu}}{\partial \mathbf{q}}(\mathbf{q}, \mathbf{p}'). \quad (\text{C.5})$$

As the basis functions G_{ν} are bounded and C^2 with respect to \mathbf{q} , so are the functions $\mathbf{\Delta}_1$ and $\mathbf{\Delta}_2$. Thus, they can be estimated as

$$\mathbf{\Delta}_1(\mathbf{q}, \mathbf{q}', \mathbf{p}') < K_1(\mathbf{q}', \mathbf{p}'), \quad (\text{C.6})$$

$$\mathbf{\Delta}_2(\mathbf{q}, \mathbf{p}') < K_2(\mathbf{p}'). \quad (\text{C.7})$$

Using these bounds and the alternate triangle inequality, we obtain a lower estimate for Eq. (C.3) given by

$$|\phi(\mathbf{x}, \mathbf{x}')|^2 \geq (|\mathbf{q}| - |\mathbf{\Delta}_1(\mathbf{q}, \mathbf{q}', \mathbf{p}')|)^2 + (|\mathbf{p}| - |\mathbf{\Delta}_2(\mathbf{q}, \mathbf{p}')|)^2, \quad (\text{C.8})$$

$$= |\mathbf{q}|^2 - 2|\mathbf{\Delta}_1(\mathbf{q}, \mathbf{q}', \mathbf{p}')||\mathbf{q}| + \mathbf{\Delta}_1(\mathbf{q}, \mathbf{q}', \mathbf{p}')^2 + |\mathbf{p}|^2 - 2|\mathbf{\Delta}_2(\mathbf{q}, \mathbf{p}')||\mathbf{p}| + \mathbf{\Delta}_2(\mathbf{q}, \mathbf{p}')^2, \quad (\text{C.9})$$

$$> \underbrace{|\mathbf{q}|^2 + |\mathbf{p}|^2 - 2K_1(\mathbf{q}', \mathbf{p}')|\mathbf{q}| - 2K_2(\mathbf{p}')|\mathbf{p}|}_{=: A} + \underbrace{\mathbf{\Delta}_1(\mathbf{q}, \mathbf{q}', \mathbf{p}')^2 + \mathbf{\Delta}_2(\mathbf{q}, \mathbf{p}')^2}_{=: B}. \quad (\text{C.10})$$

This estimator consists of two contributions A and B . As for $|\mathbf{x}| \rightarrow \infty$ we have $A \rightarrow \infty$ while B is bounded in \mathbf{x} , also $(A + B) \rightarrow \infty$, which ensures Eq. (C.1).

D. Inversion of the pendulum transformation T_{pend}

In this appendix, we demonstrate the numerical inversion of the pendulum transformation T_{pend} , Eqs. (4.67). As these equations are discontinuous at the separatrix $k(q, p) = 1$, a straightforward

application of, e. g., the Newton–Raphson method [45], would fail. Instead, we invert Eqs. (4.67) by treating different phase-space regions separately. In each region, we decompose the 2D inversion problem into two subsequent 1D inversion problems and discuss appropriate inversion algorithms.

As the transformation parameter J_{sep} appears linearly in Eqs. (4.67c), also the inverse transformation has a trivial dependence on J_{sep} . Namely, for any value J_{sep} the inversion for (ϑ, J) gives $(q, p) = (q_0, J_{\text{sep}}p_0)$, where (q_0, p_0) is the corresponding result for $(\vartheta, J/J_{\text{sep}})$ and $J_{\text{sep}} = 1$. Therefore, we set $J_{\text{sep}} = 1$ in the following. As a second simplification, we restrict to the upper part of phase space $p > 0$. By symmetry, the inversion in the lower part for (ϑ, J) gives $(q, p) = (-q_0, -p_0)$, where (q_0, p_0) is the corresponding result of the inversion for $(\vartheta + \pi, J)$.

We first discuss the inversion in the region inside the separatrix, where $J < 1$ (yellow areas in Fig. 4.16(b–c)). Here it is suitable, to first invert Eq. (4.67c) for k , i. e., solve

$$J = \mathcal{E}(k) - (1 - k^2) \mathcal{K}(k) \quad =: A(k), \quad (\text{D.1})$$

for $k \in (0, 1)$. This is a 1D inversion problem of a continuous, monotonous function $A : (0, 1) \rightarrow (0, 1)$. A solution via the Newton–Raphson method turns out as sufficient for all k . Here we use the initial conditions $k_0 = J$. The next step is to invert Eq. (4.67b) with $k < 1$ for η , i. e., solve

$$\vartheta = \frac{\pi}{2} \cdot \frac{\mathcal{F}(\eta, k)}{\mathcal{K}(k)} \quad =: B(\eta), \quad (\text{D.2})$$

for $\eta \in [-\frac{\pi}{2}, \frac{\pi}{2})$. The introduced function $B : [-\frac{\pi}{2}, \frac{\pi}{2}) \rightarrow [-\frac{\pi}{2}, \frac{\pi}{2})$ is monotonous with $B(\pm\frac{\pi}{2}) = \pm\frac{\pi}{2}$. Again, we apply the Newton–Raphson method using the initial condition

$$\eta_0 = \frac{2\vartheta}{\pi} \cdot \frac{\mathcal{K}(k)}{\frac{\partial \mathcal{F}}{\partial \eta}(0, k)}, \quad (\text{D.3})$$

which is the first order solution of Eq. (D.2) near $\eta = 0$. This even works out when leaving the neighborhood of the solution $\eta = \vartheta = 0$ and approaching the solutions $\eta = \vartheta = \pm\frac{\pi}{2}$, as long as $k < 0.8$. However, for $k > 0.8$ and $|\vartheta| > 1$ the Newton–Raphson method fails, and we apply a less efficient bisection algorithm [85]. Here, we use the initial intervals $[\pm\frac{\pi}{2} - 0.5, \pm\frac{\pi}{2} + 0.5]$ for $\vartheta \gtrless 0$. Finally, using Eqs. (4.66), (4.68), and (4.69) we obtain the solution

$$q = 2 \arcsin(k \sin \eta). \quad (\text{D.4a})$$

$$p = \frac{\pi}{8} \sqrt{2(2k^2 - 1 + \cos q)}. \quad (\text{D.4b})$$

We now discuss the inversion in the region outside the separatrix, where $J > 1$ (green areas in Fig. 4.16(b–c)). Again, we first invert Eq. (4.67c) by solving

$$J = \frac{k}{2\mathcal{E}(k^{-1})} \quad =: C(k), \quad (\text{D.5})$$

for $k \in (1, \infty)$. Here the Newton–Raphson method with the initial condition $k_0 = 2J/\pi$ is applicable

only far from the separatrix where $J > 5$. For $J < 5$, we use a bisection algorithm with the initial k -interval $[1, 10]$. Given k , we then invert Eq. (4.67b) by solving

$$\vartheta = \frac{\pi \mathcal{F}(q/2, k)}{\mathcal{K}(k^{-1})} =: D(q), \tag{D.6}$$

for $q \in [-\pi, \pi)$. Here, the Newton–Raphson algorithm works out globally, using the initial condition $q_0 = \vartheta - \frac{\pi}{2}$. Finally, given q , we compute p from Eq. (D.4b).

E. Implementation of the normal-form transformation T^*

Here, we describe a numerical procedure to implement the transformation

$$T^* : (\vartheta, J) \mapsto (\theta, I), \tag{E.1}$$

which gives access to the action–angle coordinates (ϑ, J) of the normal-form Hamiltonian $\mathcal{H}_{r:s}(\theta, I)$, Eq. (4.73). Figure E.1(b) shows the phase space of $\mathcal{H}_{r:s}(\theta, I)$ with two regions of rotation (yellow, white) and one region of libration (green). Due to the topological change between these regions, the transformation T^* is not defined globally in phase space. Instead, it connects the phase-space coordinates (θ, I) of each region to action–angle coordinates $(\vartheta, J) \in [0, 2\pi) \times \mathcal{I}$. Here the intervals \mathcal{I} are given by $(0, J_-)$ for the yellow region, (J_+, ∞) for the white region, and $(0, J_{r:s})$ for the green

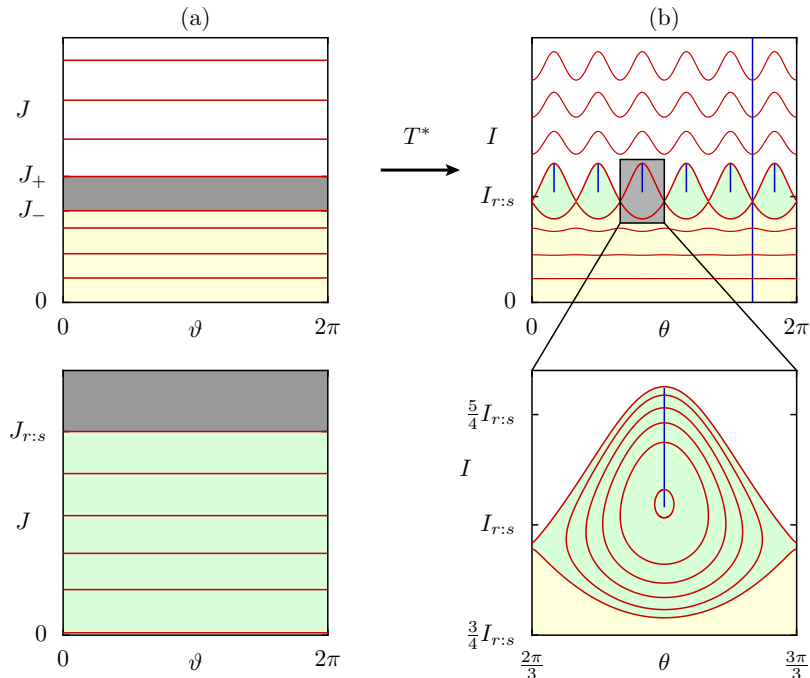


Figure E.1.: Visualization of the transformation T^* from action–angle coordinates (ϑ, J) (a) to the original coordinates (θ, I) (b) of the normal-form Hamiltonian $\mathcal{H}_{r:s}(\theta, I)$, Eq. (4.73). The colors indicate different regions, which are connected by the transformation.

region, see Fig. E.1(a). The interval boundaries follow from the phase-space areas A_1 and $A_{r:s}$ defined in Fig. 4.18(c) according to

$$J_- = \frac{A_1}{2\pi}, \quad (\text{E.2a})$$

$$J_+ = \frac{A_1 + A_{r:s}}{2\pi}, \quad (\text{E.2b})$$

$$J_{r:s} = \frac{A_{r:s}}{2\pi r}. \quad (\text{E.2c})$$

For a unique definition of the action–angle coordinates (ϑ, J) , in each region a curve \mathcal{C}_0 has to be chosen which defines $\vartheta = 0$, see the blue lines in Fig. E.1(b) for a convenient choice.

In the following we describe an algorithm for the application of T^* and $(T^*)^{-1}$. This algorithm is based on the numerical time evolution of $\mathcal{H}_{r:s}(\theta, I)$ in the (θ, I) -plane. Moreover, it uses the numerical computation of the action J and the frequency ω for a given, closed trajectory according to Sec. 4.2.1. The transformation of a point (ϑ, J) is computed as follows:

1. Search for an initial condition $(\theta_0, I_0) \in \mathcal{C}_0$ with action J using numerical time evolution.
2. For this initial condition (θ_0, I_0) compute a trajectory $(\theta, I)(t)$ and its frequency ω .
3. Compute the transformed point as

$$T^*(\vartheta, J) = (\theta, I)(t = \vartheta/\omega). \quad (\text{E.3})$$

The inverse transformation of a point (θ, I) is computed as follows:

1. For the initial condition (θ, I) compute a trajectory $(\theta, I)(t)$, its action J , and its frequency ω .
2. Compute the time t_0 , when this trajectory first intersects \mathcal{C}_0 .
3. Compute the transformed point as

$$(T^*)^{-1}(\theta, I) = (2\pi - \omega t_0, J). \quad (\text{E.4})$$

F. Scaling property

Here we show, that the scaling property (5.16) of a Hamiltonian $H(\mathbf{q}, \mathbf{p})$ implies the scaling behavior of its solutions as described in Sec. 5.3. This scaling behavior means, that for any solution $(\mathbf{q}, \mathbf{p})(t)$ with $H(\mathbf{q}, \mathbf{p}) = E$, the rescaled trajectory $(\mathbf{q}_\lambda, \mathbf{p}_\lambda)(t)$, Eq. (5.15), is also a solution of energy $\lambda^2 E$.

First, we mention that the scaling property (5.16) implies the scaling of the derivatives

$$\frac{\partial H}{\partial \mathbf{q}}(\mathbf{q}, \lambda \mathbf{p}) = \lambda^2 \frac{\partial H}{\partial \mathbf{q}}(\mathbf{q}, \mathbf{p}), \quad (\text{F.1a})$$

$$\frac{\partial H}{\partial \mathbf{p}}(\mathbf{q}, \lambda \mathbf{p}) = \lambda \frac{\partial H}{\partial \mathbf{p}}(\mathbf{q}, \mathbf{p}), \quad (\text{F.1b})$$

which we use in the following.

Next, we show that if $(\mathbf{q}, \mathbf{p})(t)$ fulfills Hamilton's equations (2.1), then also does $(\mathbf{q}_\lambda, \mathbf{p}_\lambda)(t)$. For the position component $\mathbf{q}_\lambda(t)$ we find

$$\frac{d}{dt}\mathbf{q}_\lambda(t) = \lambda\dot{\mathbf{q}}(\lambda t), \quad (\text{F.2a})$$

$$= \lambda \frac{\partial H}{\partial \mathbf{p}}[\mathbf{q}(\lambda t), \mathbf{p}(\lambda t)], \quad (\text{F.2b})$$

$$= \frac{\partial H}{\partial \mathbf{p}}[\mathbf{q}(\lambda t), \lambda \mathbf{p}(\lambda t)], \quad (\text{F.2c})$$

$$= \frac{\partial H}{\partial \mathbf{p}}[\mathbf{q}_\lambda(t), \mathbf{p}_\lambda(t)]. \quad (\text{F.2d})$$

Here we used Eqs. (2.1), (5.15), and (F.1b). For the momentum component $\mathbf{p}_\lambda(t)$ we find analogously

$$\frac{d}{dt}\mathbf{p}_\lambda(t) = \lambda^2 \dot{\mathbf{p}}(\lambda t), \quad (\text{F.3a})$$

$$= -\lambda^2 \frac{\partial H}{\partial \mathbf{q}}[\mathbf{q}(\lambda t), \mathbf{p}(\lambda t)], \quad (\text{F.3b})$$

$$= -\frac{\partial H}{\partial \mathbf{q}}[\mathbf{q}(\lambda t), \lambda \mathbf{p}(\lambda t)], \quad (\text{F.3c})$$

$$= -\frac{\partial H}{\partial \mathbf{q}}[\mathbf{q}_\lambda(t), \mathbf{p}_\lambda(t)]. \quad (\text{F.3d})$$

Thus, we obtain the equivalence between the scaling property (5.16) and the scaling behavior of the solutions $(\mathbf{q}_\lambda, \mathbf{p}_\lambda)(t)$ as claimed in Sec. 5.3.

G. Stability of the cosine billiard

Here, we analyze the stability of the vertical, periodic trajectory of the cosine billiard (5.2), see the black line in Fig. 5.1(b).

G.1. Stability condition

First we consider the Poincaré map $\mathcal{P}_1 : (x, p_x) \mapsto (x', p'_x)$ on the Poincaré section Σ_1 . This map has a fixed point $(x^*, p_x^*) = (0, 0)$ which corresponds to the central, periodic trajectory of the billiard. According to Ref. [86] we compute its monodromy matrix as

$$M = \begin{pmatrix} 1 - \ell\kappa & \ell(1 - \frac{\ell\kappa}{2}) \\ -2\kappa & 1 - \ell\kappa \end{pmatrix}. \quad (\text{G.1})$$

Here ℓ is the length of the periodic trajectory and κ is the curvature of its reflection point on the upper boundary. They are given by

$$\ell = 2(h + w), \quad (\text{G.2a})$$

$$\kappa = r''(0) = 2\pi^2 w. \quad (\text{G.2b})$$

For later use we mention, that the action of this trajectory is given by

$$J_2 = \frac{\ell}{2\pi}. \quad (\text{G.3})$$

The eigenvalues of M are

$$\beta_{\pm} = (1 - \ell\kappa) \pm \sqrt{2\ell\kappa \left(\frac{\ell\kappa}{2} - 1 \right)}. \quad (\text{G.4})$$

The considered central orbit is stable, if $\beta_{\pm} \in \mathbb{R}$, which requires the term under the root to be positive. Reexpressing ℓ and κ with Eqs. (G.2) this leads to the stability condition

$$\pi^2 w(h + w) < \frac{1}{2}. \quad (\text{G.5})$$

G.2. Derivation of the parameter δ for the cosine billiard

We now derive the parameter δ , Eqs. (5.31a) and (5.31b), which controls the half-axis ratio of the regular tori shown in Fig. 5.7(b) (red lines). Using Eqs. (4.10) and (4.11), the half-axis ratio σ of the local elliptic dynamics in Σ_1 can be expressed in terms of the monodromy matrix (G.1). When changing to the coordinates (\mathbf{Q}, \mathbf{P}) under the transformation \mathcal{T} , Eq. (5.4), this half-axis ratio changes to

$$\sigma' = \sigma \left(1 - \frac{\ell\kappa}{4} \right)^2. \quad (\text{G.6})$$

On the other hand, for $H_{\text{reg}}^0(\mathbf{Q}, \mathbf{P})$ this half-axis ratio is

$$\sigma' = \delta J_2, \quad (\text{G.7})$$

as follows from Eqs. (5.31a) and (5.31b). Finally, by combining Eqs. (G.3), (G.6), and (G.7) we obtain

$$\delta = \frac{2\pi}{\ell} \left(1 - \frac{\ell\kappa}{4} \right)^2 \sqrt{\frac{|2\kappa + \ell(1 - \frac{\ell\kappa}{2})| - |2\kappa - \ell(1 - \frac{\ell\kappa}{2})|}{|2\kappa + \ell(1 - \frac{\ell\kappa}{2})| + |2\kappa - \ell(1 - \frac{\ell\kappa}{2})|}}. \quad (\text{G.8})$$

H. Derivation of the boundary transformation \mathcal{T}_1

In this appendix we derive the boundary transformation \mathcal{T}_1 . As motivated in Sec. 5.2, this transformation should map a given billiard to a new system confined in a domain of a simple shape with elastic reflections. Proposing this, we first consider a billiard with $\mathcal{C} = 4$ corners and derive a general set of conditions for the boundary transformation (App. H.1). Then we prove that this set of conditions cannot be solved (App. H.2), as it was claimed in Sec. 5.2. By removing one condition, we obtain a relaxed problem and demonstrate its solution (App. H.3) which was outlined roughly in Sec. 5.2. Moreover, we give an invertibility condition for the transformation in the case of the cosine billiard (App. H.4). Finally, we derive the boundary transformation \mathcal{T}_1 for a class of billiards with a smooth domain $\mathcal{C} = 0$ (App. H.5).

H.1. Conditions

As outlined in Sec. 5.2, we consider a general billiard domain defined by a rectangle with an arbitrary upper boundary curve $r(x)$ according to $-0.5 \leq x \leq 0.5$ and $0 \leq y \leq r(x)$. Our goal is to derive an invertible point transformation

$$x = x(\bar{x}, \bar{y}), \quad (\text{H.1a})$$

$$y = y(\bar{x}, \bar{y}), \quad (\text{H.1b})$$

which maps the billiard domain to a square where $(\bar{x}, \bar{y}) \in [-0.5, 0.5] \times [0, 1]$. For reasons of continuity, the four boundary segments of the billiard need to be mapped onto the corresponding edges of the unit square, i. e.,

$$x(\pm 0.5, \bar{y}) = \pm 0.5, \quad (\text{H.2a})$$

$$y(\bar{x}, 0) = 0, \quad (\text{H.2b})$$

$$y(\bar{x}, 1) = r(x(\bar{x}, 1)). \quad (\text{H.2c})$$

In this section, we shall remain with this general form (H.1), which expands the following derivation, but will make the non-existence statement in App. H.2 universal.

In the following we denote the Jacobi matrix of the point transformation (H.1) by

$$\mathcal{A}(\bar{x}, \bar{y}) = \begin{pmatrix} \mathcal{A}_{11}(\bar{x}, \bar{y}) & \mathcal{A}_{12}(\bar{x}, \bar{y}) \\ \mathcal{A}_{21}(\bar{x}, \bar{y}) & \mathcal{A}_{22}(\bar{x}, \bar{y}) \end{pmatrix} = \begin{pmatrix} \frac{\partial x}{\partial \bar{x}}(\bar{x}, \bar{y}) & \frac{\partial x}{\partial \bar{y}}(\bar{x}, \bar{y}) \\ \frac{\partial y}{\partial \bar{x}}(\bar{x}, \bar{y}) & \frac{\partial y}{\partial \bar{y}}(\bar{x}, \bar{y}) \end{pmatrix}, \quad (\text{H.3})$$

and its determinant by

$$\mathcal{D}(\bar{x}, \bar{y}) = \mathcal{A}_{11}(\bar{x}, \bar{y})\mathcal{A}_{22}(\bar{x}, \bar{y}) - \mathcal{A}_{12}(\bar{x}, \bar{y})\mathcal{A}_{21}(\bar{x}, \bar{y}). \quad (\text{H.4})$$

Moreover, we mention that the point transformation (H.1) implies a momentum transformation ac-

cording to

$$\begin{pmatrix} p_x \\ p_y \end{pmatrix} = \mathcal{A}(\bar{x}, \bar{y})^{-1} \begin{pmatrix} \bar{p}_x \\ \bar{p}_y \end{pmatrix} = \frac{1}{\mathcal{D}(\bar{x}, \bar{y})} \begin{pmatrix} \mathcal{A}_{22}(\bar{x}, \bar{y}) & -\mathcal{A}_{12}(\bar{x}, \bar{y}) \\ -\mathcal{A}_{21}(\bar{x}, \bar{y}) & \mathcal{A}_{11}(\bar{x}, \bar{y}) \end{pmatrix} \begin{pmatrix} \bar{p}_x \\ \bar{p}_y \end{pmatrix}. \quad (\text{H.5})$$

The conditions to be evaluated in the following are those of elastic reflections

$$(\bar{p}_x, \bar{p}_y) \mapsto (\bar{p}_x, -\bar{p}_y), \quad (\text{H.6a})$$

$$(\dot{\bar{x}}, \dot{\bar{y}}) \mapsto (\dot{\bar{x}}, -\dot{\bar{y}}), \quad (\text{H.6b})$$

$$(\dot{\bar{p}}_x, \dot{\bar{p}}_y) \mapsto (\dot{\bar{p}}_x, -\dot{\bar{p}}_y), \quad (\text{H.6c})$$

which we require on the lower ($\bar{y} = 0$) and on the upper boundary ($\bar{y} = 1$).

The condition (H.6a) on the upper boundary $\bar{y} = 1$

On the upper billiard boundary, the momentum vector (p_x, p_y) is reflected perpendicular to the boundary curve $r(x)$. This immediate reflection corresponds to the action of a linear operator on (p_x, p_y) which is given by

$$R_2(\bar{x}) = \begin{pmatrix} 1 & 0 \\ 0 & -1 \end{pmatrix} + \frac{2r'[x(\bar{x}, 1)]}{1 + r'[x(\bar{x}, 1)]^2} \begin{pmatrix} -r'[x(\bar{x}, 1)] & 1 \\ 1 & r'[x(\bar{x}, 1)] \end{pmatrix}. \quad (\text{H.7})$$

The condition (H.6a) requires the transformed reflection operator to be

$$\bar{R}_2 = \begin{pmatrix} 1 & 0 \\ 0 & -1 \end{pmatrix}. \quad (\text{H.8})$$

According to Eq. (H.5), the matrices $R_2(\bar{x})$ and \bar{R}_2 are connected by

$$\mathcal{A}(\bar{x}, 1) \cdot R_2(\bar{x}) = \bar{R}_2 \cdot \mathcal{A}(\bar{x}, 1). \quad (\text{H.9})$$

With Eqs. (H.7) and (H.8) this leads to

$$\begin{pmatrix} \mathcal{A}_{11} & \mathcal{A}_{12} \\ \mathcal{A}_{21} & \mathcal{A}_{22} \end{pmatrix} \left[\begin{pmatrix} 1 & 0 \\ 0 & -1 \end{pmatrix} + \frac{2r'}{1 + r'^2} \begin{pmatrix} -r' & 1 \\ 1 & r' \end{pmatrix} \right] = \begin{pmatrix} 1 & 0 \\ 0 & -1 \end{pmatrix} \begin{pmatrix} \mathcal{A}_{11} & \mathcal{A}_{12} \\ \mathcal{A}_{21} & \mathcal{A}_{22} \end{pmatrix}. \quad (\text{H.10})$$

From now on, we suppress the positional arguments for convenience. For $r' \neq 0$ this matrix equation implies

$$\mathcal{A}_{21} = -r' \mathcal{A}_{22}, \quad (\text{H.11a})$$

$$\mathcal{A}_{12} = r' \mathcal{A}_{11}. \quad (\text{H.11b})$$

Geometrically, this states that the contour lines of \bar{x} and \bar{y} lie perpendicular and parallel to the boundary $y = r(x)$, respectively.

The condition (H.6a) on the lower boundary $\bar{y} = 0$

On the lower boundary, condition (H.6a) is evaluated analogously. Here the reflection of the old momentum (p_x, p_y) has the simple form

$$R_1 = \begin{pmatrix} 1 & 0 \\ 0 & -1 \end{pmatrix}, \quad (\text{H.12})$$

which corresponds to Eq. (H.7) with a straight boundary $r' = 0$. Hence, we find the same matrix equation (H.10) with $r' = 0$,

$$\begin{pmatrix} \mathcal{A}_{11} & \mathcal{A}_{12} \\ \mathcal{A}_{21} & \mathcal{A}_{22} \end{pmatrix} \begin{pmatrix} 1 & 0 \\ 0 & -1 \end{pmatrix} = \begin{pmatrix} 1 & 0 \\ 0 & -1 \end{pmatrix} \begin{pmatrix} \mathcal{A}_{11} & \mathcal{A}_{12} \\ \mathcal{A}_{21} & \mathcal{A}_{22} \end{pmatrix}, \quad (\text{H.13})$$

which leads to the condition

$$\mathcal{A}_{12} = \mathcal{A}_{21} = 0. \quad (\text{H.14})$$

The condition (H.6b) on both boundaries

To evaluate condition (H.6b) the velocities $\dot{\bar{\mathbf{q}}} = (\dot{\bar{x}}, \dot{\bar{y}})$ need to be expressed as functions of the phase-space coordinates $(\bar{\mathbf{q}}, \bar{\mathbf{p}})$ using Hamilton's equations (2.1) with the billiard Hamiltonian (5.1). For $\dot{\bar{x}}$ this is

$$\dot{\bar{x}} = \frac{\partial}{\partial \bar{p}_x} [p_x(\bar{\mathbf{q}}, \bar{\mathbf{p}})^2 + p_y(\bar{\mathbf{q}}, \bar{\mathbf{p}})^2], \quad (\text{H.15a})$$

$$= 2 \begin{pmatrix} p_x(\bar{\mathbf{q}}, \bar{\mathbf{p}}) \\ p_y(\bar{\mathbf{q}}, \bar{\mathbf{p}}) \end{pmatrix}^\top \frac{\partial}{\partial \bar{p}_x} \begin{pmatrix} p_x(\bar{\mathbf{q}}, \bar{\mathbf{p}}) \\ p_y(\bar{\mathbf{q}}, \bar{\mathbf{p}}) \end{pmatrix}. \quad (\text{H.15b})$$

Using Eq. (H.5) this becomes

$$\dot{\bar{x}} = \frac{2}{\mathcal{D}^2} \left[\begin{pmatrix} \mathcal{A}_{22} & -\mathcal{A}_{12} \\ -\mathcal{A}_{21} & \mathcal{A}_{11} \end{pmatrix} \begin{pmatrix} \bar{p}_x \\ \bar{p}_y \end{pmatrix} \right]^\top \begin{pmatrix} \mathcal{A}_{22} & -\mathcal{A}_{12} \\ -\mathcal{A}_{21} & \mathcal{A}_{11} \end{pmatrix} \frac{\partial}{\partial \bar{p}_x} \begin{pmatrix} \bar{p}_x \\ \bar{p}_y \end{pmatrix} \quad (\text{H.15c})$$

$$= \frac{2}{\mathcal{D}^2} [(\mathcal{A}_{21}^2 + \mathcal{A}_{22}^2)\bar{p}_x - (\mathcal{A}_{11}\mathcal{A}_{21} + \mathcal{A}_{12}\mathcal{A}_{22})\bar{p}_y]. \quad (\text{H.15d})$$

Keeping in mind that \mathcal{A}_{ij} and \mathcal{D} depend on $\bar{\mathbf{q}}$, this expresses $\dot{\bar{x}}$ in terms of $(\bar{\mathbf{q}}, \bar{\mathbf{p}})$. Considering an infinitesimal time interval around a reflection event, this equation translates the momentum reflection $(\bar{p}_x, \bar{p}_y) \mapsto (\bar{p}_x, -\bar{p}_y)$ to an intermediate change of $\dot{\bar{x}}$. To fulfill condition (H.6b), i. e., $\dot{\bar{x}} \mapsto \dot{\bar{x}}$, the

coefficient of \bar{p}_y must vanish, leading to

$$\mathcal{A}_{11}\mathcal{A}_{21} + \mathcal{A}_{12}\mathcal{A}_{22} = 0. \quad (\text{H.16})$$

Analogously, for $\dot{\bar{y}}$ we find

$$\dot{\bar{y}} = \frac{2}{\mathcal{D}^2} [(\mathcal{A}_{11}^2 + \mathcal{A}_{12}^2)\bar{p}_y - (\mathcal{A}_{11}\mathcal{A}_{21} + \mathcal{A}_{12}\mathcal{A}_{22})\bar{p}_x]. \quad (\text{H.17})$$

To obtain the reflection $\dot{\bar{y}} \mapsto -\dot{\bar{y}}$, the coefficient of \bar{p}_x must vanish, giving the same condition (H.16). Note that this derivation is valid for both boundaries $\bar{y} = 0$ and $\bar{y} = 1$.

The condition (H.6c) on both boundaries

Proceeding as before, we evaluate the last condition (H.6c) by expressing the momentum velocities $\dot{\bar{\mathbf{p}}} = (\dot{\bar{p}}_x, \dot{\bar{p}}_y)$ as functions of $(\bar{\mathbf{q}}, \bar{\mathbf{p}})$. For $\dot{\bar{p}}_x$ this is

$$\dot{\bar{p}}_x = -\frac{\partial}{\partial \bar{x}} [p_x(\bar{\mathbf{q}}, \bar{\mathbf{p}})^2 + p_y(\bar{\mathbf{q}}, \bar{\mathbf{p}})^2], \quad (\text{H.18a})$$

$$= -2 \begin{pmatrix} p_x(\bar{\mathbf{q}}, \bar{\mathbf{p}}) \\ p_y(\bar{\mathbf{q}}, \bar{\mathbf{p}}) \end{pmatrix}^\top \frac{\partial}{\partial \bar{x}} \begin{pmatrix} p_x(\bar{\mathbf{q}}, \bar{\mathbf{p}}) \\ p_y(\bar{\mathbf{q}}, \bar{\mathbf{p}}) \end{pmatrix}, \quad (\text{H.18b})$$

$$= -2 \left[\frac{1}{\mathcal{D}} \begin{pmatrix} \mathcal{A}_{22} & -\mathcal{A}_{12} \\ -\mathcal{A}_{21} & \mathcal{A}_{11} \end{pmatrix} \begin{pmatrix} \bar{p}_x \\ \bar{p}_y \end{pmatrix} \right]^\top \frac{\partial}{\partial \bar{x}} \frac{1}{\mathcal{D}} \begin{pmatrix} \mathcal{A}_{22} & -\mathcal{A}_{12} \\ -\mathcal{A}_{21} & \mathcal{A}_{11} \end{pmatrix} \begin{pmatrix} \bar{p}_x \\ \bar{p}_y \end{pmatrix}, \quad (\text{H.18c})$$

$$= -\frac{2}{\mathcal{D}} \begin{pmatrix} \bar{p}_x \\ \bar{p}_y \end{pmatrix}^\top \underbrace{\begin{pmatrix} \mathcal{A}_{22} & -\mathcal{A}_{21} \\ -\mathcal{A}_{12} & \mathcal{A}_{11} \end{pmatrix} \frac{\partial}{\partial \bar{x}} \frac{1}{\mathcal{D}} \begin{pmatrix} \mathcal{A}_{22} & -\mathcal{A}_{12} \\ -\mathcal{A}_{21} & \mathcal{A}_{11} \end{pmatrix}}_{=: \begin{pmatrix} \beta_{11} & \beta_{12} \\ \beta_{21} & \beta_{22} \end{pmatrix}} \begin{pmatrix} \bar{p}_x \\ \bar{p}_y \end{pmatrix}, \quad (\text{H.18d})$$

$$= -\frac{2}{\mathcal{D}} [\beta_{11}\bar{p}_x^2 + \beta_{22}\bar{p}_y^2 + (\beta_{12} + \beta_{21})\bar{p}_x\bar{p}_y]. \quad (\text{H.18e})$$

Thus, we obtain a quadratic form in $\bar{\mathbf{p}} = (\bar{p}_x, \bar{p}_y)$, whose coefficients are evaluated as

$$\beta_{11} = \mathcal{A}_{21} \frac{\partial}{\partial \bar{x}} \frac{1}{\mathcal{D}} \mathcal{A}_{21} + \mathcal{A}_{22} \frac{\partial}{\partial \bar{x}} \frac{1}{\mathcal{D}} \mathcal{A}_{22}, \quad (\text{H.19a})$$

$$\beta_{22} = \mathcal{A}_{11} \frac{\partial}{\partial \bar{x}} \frac{1}{\mathcal{D}} \mathcal{A}_{11} + \mathcal{A}_{12} \frac{\partial}{\partial \bar{x}} \frac{1}{\mathcal{D}} \mathcal{A}_{12}, \quad (\text{H.19b})$$

$$\beta_{12} + \beta_{21} = -\mathcal{A}_{11} \frac{\partial}{\partial \bar{x}} \frac{1}{\mathcal{D}} \mathcal{A}_{21} - \mathcal{A}_{21} \frac{\partial}{\partial \bar{x}} \frac{1}{\mathcal{D}} \mathcal{A}_{11} - \mathcal{A}_{12} \frac{\partial}{\partial \bar{x}} \frac{1}{\mathcal{D}} \mathcal{A}_{22} - \mathcal{A}_{22} \frac{\partial}{\partial \bar{x}} \frac{1}{\mathcal{D}} \mathcal{A}_{12}. \quad (\text{H.19c})$$

Condition (H.6c) requires that $\dot{\bar{p}}_x$ is preserved under the reflection $(\bar{p}_x, \bar{p}_y) \mapsto (\bar{p}_x, -\bar{p}_y)$, thus the coefficient $(\beta_{12} + \beta_{21})$ in Eq. (H.18e) must vanish. With Eq. (H.19c) this implies

$$0 = \mathcal{A}_{11} \frac{\partial}{\partial \bar{x}} \frac{1}{\mathcal{D}} \mathcal{A}_{21} + \mathcal{A}_{21} \frac{\partial}{\partial \bar{x}} \frac{1}{\mathcal{D}} \mathcal{A}_{11} + \mathcal{A}_{12} \frac{\partial}{\partial \bar{x}} \frac{1}{\mathcal{D}} \mathcal{A}_{22} + \mathcal{A}_{22} \frac{\partial}{\partial \bar{x}} \frac{1}{\mathcal{D}} \mathcal{A}_{12}, \quad (\text{H.20a})$$

$$\begin{aligned} &= \frac{\mathcal{A}_{12}}{\mathcal{D}} \left(\mathcal{A}_{22,x} - \frac{\partial \mathcal{D}}{\partial \bar{x}} \frac{\mathcal{A}_{22}}{\mathcal{D}} \right) + \frac{\mathcal{A}_{11}}{\mathcal{D}} \left(\mathcal{A}_{21,x} - \frac{\partial \mathcal{D}}{\partial \bar{x}} \frac{\mathcal{A}_{21}}{\mathcal{D}} \right) \\ &\quad + \frac{\mathcal{A}_{22}}{\mathcal{D}} \left(\mathcal{A}_{12,x} - \frac{\partial \mathcal{D}}{\partial \bar{x}} \frac{\mathcal{A}_{12}}{\mathcal{D}} \right) + \frac{\mathcal{A}_{21}}{\mathcal{D}} \left(\mathcal{A}_{11,x} - \frac{\partial \mathcal{D}}{\partial \bar{x}} \frac{\mathcal{A}_{11}}{\mathcal{D}} \right), \end{aligned} \quad (\text{H.20b})$$

and can be regrouped to

$$0 = \frac{\partial}{\partial \bar{x}} (\mathcal{A}_{11} \mathcal{A}_{21} + \mathcal{A}_{12} \mathcal{A}_{22}) - \frac{2}{\mathcal{D}} \frac{\partial \mathcal{D}}{\partial \bar{x}} (\mathcal{A}_{11} \mathcal{A}_{21} + \mathcal{A}_{12} \mathcal{A}_{22}). \quad (\text{H.21})$$

As the second term already vanishes due to condition (H.16), this simplifies to

$$0 = \frac{\partial}{\partial \bar{x}} (\mathcal{A}_{11} \mathcal{A}_{21} + \mathcal{A}_{12} \mathcal{A}_{22}). \quad (\text{H.22})$$

For the momentum velocity $\dot{\bar{p}}_y$, we proceed analogously, getting the same results (H.18e) and (H.19), but with $\partial/\partial \bar{x}$ being replaced by $\partial/\partial \bar{y}$. To satisfy condition (H.6c), i. e., $\dot{\bar{p}}_y \mapsto -\dot{\bar{p}}_y$, we must have $\beta_{11} = \beta_{22} = 0$, which leads to

$$0 = \frac{\partial}{\partial \bar{y}} (\mathcal{A}_{21}^2 + \mathcal{A}_{22}^2) - \frac{2}{\mathcal{D}} \frac{\partial \mathcal{D}}{\partial \bar{y}} (\mathcal{A}_{21}^2 + \mathcal{A}_{22}^2), \quad (\text{H.23a})$$

$$0 = \frac{\partial}{\partial \bar{y}} (\mathcal{A}_{11}^2 + \mathcal{A}_{12}^2) - \frac{2}{\mathcal{D}} \frac{\partial \mathcal{D}}{\partial \bar{y}} (\mathcal{A}_{11}^2 + \mathcal{A}_{12}^2). \quad (\text{H.23b})$$

Summary and reduction of the conditions

For clarity, we summarize the derived conditions

$$\mathcal{A}_{12} = \mathcal{A}_{21} = 0 \quad \text{at } \bar{y} = 0 \quad (\text{H.24a})$$

$$\mathcal{A}_{12} - r' \mathcal{A}_{11} = \mathcal{A}_{21} + r' \mathcal{A}_{22} = 0 \quad \text{at } \bar{y} = 1 \quad (\text{H.24b})$$

$$\mathcal{A}_{11} \mathcal{A}_{21} + \mathcal{A}_{12} \mathcal{A}_{22} = 0 \quad \text{at } \bar{y} = 0, 1 \quad (\text{H.24c})$$

$$\frac{\partial}{\partial \bar{x}} (\mathcal{A}_{11} \mathcal{A}_{21} + \mathcal{A}_{12} \mathcal{A}_{22}) = 0 \quad \text{at } \bar{y} = 0, 1 \quad (\text{H.24d})$$

$$\frac{\partial}{\partial \bar{y}} (\mathcal{A}_{21}^2 + \mathcal{A}_{22}^2) - \frac{2}{\mathcal{D}} \frac{\partial \mathcal{D}}{\partial \bar{y}} (\mathcal{A}_{21}^2 + \mathcal{A}_{22}^2) = 0 \quad \text{at } \bar{y} = 0, 1 \quad (\text{H.24e})$$

$$\frac{\partial}{\partial \bar{y}} (\mathcal{A}_{11}^2 + \mathcal{A}_{12}^2) - \frac{2}{\mathcal{D}} \frac{\partial \mathcal{D}}{\partial \bar{y}} (\mathcal{A}_{11}^2 + \mathcal{A}_{12}^2) = 0 \quad \text{at } \bar{y} = 0, 1. \quad (\text{H.24f})$$

We reduce this set of conditions as follows. First, we remove condition (H.24c), as (H.24a) \Rightarrow (H.24c) for $\bar{y} = 0$ and (H.24b) \Rightarrow (H.24c) for $\bar{y} = 1$. Second, we remove condition (H.24d), as (H.24c) \Rightarrow (H.24d). Finally, we simplify the conditions (H.24e) and (H.24f) as follows:

1. Condition (H.24e) for $\bar{y} = 0$: With Eq. (H.24a) and $\mathcal{D} = \mathcal{A}_{11}\mathcal{A}_{22}$ we obtain

$$0 = \frac{\partial}{\partial \bar{y}}(\mathcal{A}_{21}^2 + \mathcal{A}_{22}^2) - \frac{2}{\mathcal{D}} \frac{\partial \mathcal{D}}{\partial \bar{y}}(\mathcal{A}_{21}^2 + \mathcal{A}_{22}^2), \quad (\text{H.25a})$$

$$\begin{aligned} &= 2 \underbrace{\mathcal{A}_{21}}_0 \frac{\partial \mathcal{A}_{21}}{\partial \bar{y}} + 2\mathcal{A}_{22} \frac{\partial \mathcal{A}_{22}}{\partial \bar{y}} \\ &\quad - \frac{2}{\mathcal{D}} \left(\mathcal{A}_{22} \frac{\partial \mathcal{A}_{11}}{\partial \bar{y}} + \mathcal{A}_{11} \frac{\partial \mathcal{A}_{22}}{\partial \bar{y}} - \underbrace{\mathcal{A}_{21}}_0 \frac{\partial \mathcal{A}_{12}}{\partial \bar{y}} - \underbrace{\mathcal{A}_{12}}_0 \frac{\partial \mathcal{A}_{21}}{\partial \bar{y}} \right) \underbrace{(\mathcal{A}_{21}^2 + \mathcal{A}_{22}^2)}_0, \end{aligned} \quad (\text{H.25b})$$

$$= -\frac{2}{\mathcal{D}} \mathcal{A}_{22}^3 \frac{\partial \mathcal{A}_{11}}{\partial \bar{y}}. \quad (\text{H.25c})$$

Thus, to ensure $\mathcal{D} = \mathcal{A}_{11}\mathcal{A}_{22} \neq 0$, this condition leads to

$$\frac{\partial \mathcal{A}_{11}}{\partial \bar{y}} = 0 \quad \text{at } \bar{y} = 0. \quad (\text{H.26})$$

2. Condition (H.24f) for $\bar{y} = 0$: Analogously, we find

$$\frac{\partial \mathcal{A}_{22}}{\partial \bar{y}} = 0 \quad \text{at } \bar{y} = 0. \quad (\text{H.27})$$

3. Condition (H.24e) for $\bar{y} = 1$: With Eq. (H.24b) and $\mathcal{D} = \mathcal{A}_{11}\mathcal{A}_{22}(1 + r'^2)$ we obtain

$$0 = \frac{2(1 + r'^2)\mathcal{A}_{22}^3}{\mathcal{D}} \left(\frac{\partial \mathcal{A}_{11}}{\partial \bar{y}} + r' \frac{\partial \mathcal{A}_{12}}{\partial \bar{y}} \right), \quad (\text{H.28})$$

which for $\mathcal{D} = \mathcal{A}_{11}\mathcal{A}_{22}(1 + r'^2) \neq 0$ requires

$$\frac{\partial \mathcal{A}_{11}}{\partial \bar{y}} + r' \frac{\partial \mathcal{A}_{12}}{\partial \bar{y}} = 0 \quad \text{at } \bar{y} = 1. \quad (\text{H.29})$$

4. Condition (H.24f) for $\bar{y} = 1$: Analogously, we find

$$\frac{\partial \mathcal{A}_{22}}{\partial \bar{y}} - r' \frac{\partial \mathcal{A}_{21}}{\partial \bar{y}} = 0 \quad \text{at } \bar{y} = 1. \quad (\text{H.30})$$

In total, we obtain a reduced system of conditions given by

$$\mathcal{A}_{12} = \mathcal{A}_{21} = 0 \quad \text{at } \bar{y} = 0, \quad (\text{H.31a})$$

$$\mathcal{A}_{12} - r' \mathcal{A}_{11} = \mathcal{A}_{21} + r' \mathcal{A}_{22} = 0 \quad \text{at } \bar{y} = 1, \quad (\text{H.31b})$$

$$\frac{\partial \mathcal{A}_{11}}{\partial \bar{y}} = \frac{\partial \mathcal{A}_{22}}{\partial \bar{y}} = 0 \quad \text{at } \bar{y} = 0, \quad (\text{H.31c})$$

$$\frac{\partial \mathcal{A}_{11}}{\partial \bar{y}} + r' \frac{\partial \mathcal{A}_{12}}{\partial \bar{y}} = \frac{\partial \mathcal{A}_{22}}{\partial \bar{y}} - r' \frac{\partial \mathcal{A}_{21}}{\partial \bar{y}} = 0 \quad \text{at } \bar{y} = 1. \quad (\text{H.31d})$$

This system of conditions ensures the reflection behavior (H.6). It is a boundary value problem for the partial derivatives $\mathcal{A}_{ij}(\bar{x}, \bar{y})$ of the point transformation (H.1) at the boundaries $\bar{y} = 0$ and $\bar{y} = 1$.

H.2. Nonexistence of a solution

We now prove, that the boundary value problem (H.31) is overdetermined, by showing that any solution is not invertible and thus no valid transformation. Any transformation (H.1) connects the billiard domain Ω to a unit square $[-\frac{1}{2}, \frac{1}{2}] \times [0, 1]$. As these sets are technically “manifolds with corners”, the local invertibility conditions for the transformation are stated as follows: (i) the boundaries and corners of both manifolds must be mapped onto each other and (ii) the Jacobian determinant $\mathcal{D} \neq 0$ everywhere, including the boundary [60]. While (i) is fulfilled, we show in the following, that (ii) is violated on the upper boundary $\bar{y} = 1$. First, we differentiate the right hand condition (H.31b) with respect to \bar{x} ,

$$0 = \frac{\partial}{\partial \bar{x}} [\mathcal{A}_{21}(\bar{x}, 1) + r' [x(\bar{x}, 1)] \mathcal{A}_{22}(\bar{x}, 1)], \quad (\text{H.32a})$$

$$= \frac{\partial \mathcal{A}_{21}}{\partial \bar{x}}(\bar{x}, 1) + r' [x(\bar{x}, 1)] \frac{\partial \mathcal{A}_{22}}{\partial \bar{x}}(\bar{x}, 1) + r'' [x(\bar{x}, 1)] \mathcal{A}_{11}(\bar{x}, 1) \mathcal{A}_{22}(\bar{x}, 1). \quad (\text{H.32b})$$

By symmetry of the second derivatives, we can replace $\frac{\partial \mathcal{A}_{2j}}{\partial \bar{x}} = \frac{\partial \mathcal{A}_{1j}}{\partial \bar{y}}$ and get

$$0 = \frac{\partial \mathcal{A}_{11}}{\partial \bar{y}}(\bar{x}, 1) + r' [x(\bar{x}, 1)] \frac{\partial \mathcal{A}_{12}}{\partial \bar{y}}(\bar{x}, 1) + r'' [x(\bar{x}, 1)] \mathcal{A}_{11}(\bar{x}, 1) \mathcal{A}_{22}(\bar{x}, 1). \quad (\text{H.32c})$$

Here, $\frac{\partial \mathcal{A}_{11}}{\partial \bar{y}} + r' \frac{\partial \mathcal{A}_{12}}{\partial \bar{y}}$ must vanish too because of condition (H.31d), and we conclude

$$0 = r'' [x(\bar{x}, 1)] \mathcal{A}_{11}(\bar{x}, 1) \mathcal{A}_{22}(\bar{x}, 1). \quad (\text{H.32d})$$

This, however, contradicts the requirement of invertibility $\mathcal{D} = \mathcal{A}_{11} \mathcal{A}_{22} (1 + r'^2) \neq 0$. Consequently, there exists no invertible transformation which solves the problem (H.31) in general. An exception is the trivial case of an overall straight billiard boundary $r'' = 0$.

H.3. Solution for the relaxed problem

We now slightly relax the problem (H.31) by removing condition (H.31d), i. e., going without the reflection $\dot{\bar{p}}_y \mapsto -\dot{\bar{p}}_y$ on the upper boundary $\bar{y} = 1$. We solve this relaxed problem using the ansatz (5.6) which involves the function $f(\bar{x}, y)$. We justify the conditions (5.11) on $f(\bar{x}, y)$ and solve them.

With the ansatz (5.6) and (5.7), the Jacobian (H.3) becomes

$$\mathcal{A}_{11}(\bar{x}, \bar{y}) = \frac{\partial f}{\partial \bar{x}}(\bar{x})[\bar{x}, r(\bar{x})\bar{y}] + \frac{\partial f}{\partial y}[\bar{x}, r(\bar{x})\bar{y}]\mathcal{A}_{12}(\bar{x}, \bar{y}), \quad (\text{H.33a})$$

$$\mathcal{A}_{12}(\bar{x}, \bar{y}) = r'(\bar{x})\bar{y}, \quad (\text{H.33b})$$

$$\mathcal{A}_{21}(\bar{x}, \bar{y}) = \frac{\partial f}{\partial y}[\bar{x}, r(\bar{x})\bar{y}]\mathcal{A}_{22}(\bar{x}, \bar{y}), \quad (\text{H.33c})$$

$$\mathcal{A}_{22}(\bar{x}, \bar{y}) = r(\bar{x}). \quad (\text{H.33d})$$

Inserting this into the relaxed boundary value problem (H.31) (without (H.31d)), yields

$$\frac{\partial f}{\partial \bar{x}}[\bar{x}, r(\bar{x})] = 1 + r'(\bar{x})^2, \quad (\text{H.34a})$$

$$\frac{\partial f}{\partial y}[\bar{x}, r(\bar{x})] = -r'(\bar{x}), \quad (\text{H.34b})$$

$$\frac{\partial f}{\partial y}(\bar{x}, 0) = 0, \quad (\text{H.34c})$$

$$\frac{\partial^2 f}{\partial \bar{x} \partial y}(\bar{x}, 0) = -\frac{r'(\bar{x})}{r(\bar{x})} \frac{\partial f}{\partial y}(\bar{x}, 0). \quad (\text{H.34d})$$

We solve these equations while also accounting for the connection condition (5.7). Choosing $f(\bar{x}, y)$ as a polynomial in y , the lowest order solution is the quadratic function

$$f(\bar{x}, y) = \bar{x} + \frac{1}{2}r(\bar{x})r'(\bar{x}) - \frac{r'(\bar{x})y^2}{2r(\bar{x})}. \quad (\text{H.35})$$

H.4. Invertibility for the cosine billiard

Finally, we discuss the invertibility of the derived point transformation for the cosine billiard (5.2). As the coordinate \bar{y} grows monotonously with y , Eq. (5.6b), the contour lines of \bar{y} never intersect. Thus, noninvertibility can only occur due to an intersection of the contour lines of \bar{x} . One such contour line in the (x, y) -plane is shown by the red curve in Fig. 5.4. By construction, it meets the upper boundary at $x = \bar{x}$. Let $(x_0(\bar{x}), 0)$ denote the point where this line meets the lower boundary, i. e.,

$$x_0(\bar{x}) = x(\bar{x}, 0) = \bar{x} + \frac{1}{2}r(\bar{x})r'(\bar{x}). \quad (\text{H.36})$$

Now we consider the whole family of these lines, which is parametrized by \bar{x} . As these lines are parabolas, the only possibility to get an intersection of two contours is, when the lower point $x_0(\bar{x})$ moves contrary to the upper point. This is the case where

$$\frac{dx_0}{d\bar{x}}(\bar{x}) = 0. \quad (\text{H.37})$$

With Eq. (H.36) and the specific boundary curve (5.2) of the cosine billiard, this condition is

$$1 + \frac{(\pi w)^2}{2} \sin(2\pi\bar{x})^2 - \pi^2 w \left[h + \frac{w}{2} + \frac{w}{2} \cos(2\pi\bar{x}) \right] \cos(2\pi\bar{x}) = 0. \quad (\text{H.38})$$

Substituting $c = \cos(2\pi\bar{x})$, this is rearranged to a quadratic equation

$$c^2 + \frac{2h+w}{2w}c - \frac{2+(\pi w)^2}{2(\pi w)^2} = 0, \quad (\text{H.39})$$

with the solutions

$$c_{\pm} = -\frac{2h+w}{4w} \pm \sqrt{\left(\frac{2h+w}{4w}\right)^2 + \frac{2+(\pi w)^2}{2(\pi w)^2}}. \quad (\text{H.40})$$

For $c_{\pm} = \cos(2\pi\bar{x})$ only solutions $-1 \leq c_{\pm} \leq 1$ are valid. As the solutions c_{\pm} are located symmetrically around the negative center $(c_+ + c_-)/2 < 0$, c_+ is the first of both solutions which enters the interval $[-1, 1]$. To ensure global invertibility, we set $c_+ > 1$ which implies the sufficient condition

$$\pi^2 w(h+w) < 1, \quad (\text{H.41})$$

as claimed in Sec. 5.2.

H.5. Boundary transformation for smooth billiards

In the previous Apps. H.1 to H.3, we developed the boundary transformation \mathcal{T}_1 for a general class of 2D billiards with $\mathcal{C} = 4$ corners. Here, we demonstrate the generality of this approach by deriving an analogous boundary transformation for a large class of smooth 2D billiards without corners, $\mathcal{C} = 0$. Specifically, we consider all billiards, whose boundary can be expressed in polar coordinates (ϕ, r) as

$$r = R(\phi), \quad (\text{H.42})$$

where the boundary curve $R(\phi)$ is an arbitrary smooth, positive, 2π -periodic function.

To this end, we decompose the boundary transformation \mathcal{T}_1 into

$$\mathcal{T}_1 = \mathcal{T}_{\text{pol}} \circ \mathcal{T}'_1 \circ \mathcal{T}_{\text{pol}}^{-1}, \quad (\text{H.43})$$

as shown in Fig. H.1. Here, \mathcal{T}_{pol} is the transformation to polar coordinates

$$\mathcal{T}_{\text{pol}} : \quad \begin{pmatrix} \phi \\ r \end{pmatrix} \mapsto \begin{pmatrix} x \\ y \end{pmatrix} = \begin{pmatrix} r \cos \phi \\ r \sin \phi \end{pmatrix}. \quad (\text{H.44})$$

For the transformation \mathcal{T}'_1 , we choose an ansatz analogous to Eqs. (5.6),

$$\phi(\bar{\phi}, \bar{r}) = \mathcal{F}[\bar{\phi}, r(\bar{\phi}, \bar{r})], \quad (\text{H.45a})$$

$$r(\bar{\phi}, \bar{r}) = \bar{r}R(\bar{\phi}), \quad (\text{H.45b})$$

leading to a straight boundary $\bar{r} = 1$, see Fig. H.1(d). In this analogy, $\mathcal{F}(\bar{\phi}, r)$ corresponds to $f(\bar{x}, \bar{y})$, however, as different conditions will be derived for $\mathcal{F}(\bar{\phi}, r)$, its solution will also differ from $f(\bar{x}, \bar{y})$. In correspondence to Eq. (5.7), we require

$$\mathcal{F}[\bar{\phi}, R(\bar{\phi})] = \bar{\phi}. \quad (\text{H.46})$$

The remaining task is to find $\mathcal{F}(\bar{\phi}, r)$ by ensuring elastic reflections in (\bar{x}, \bar{y}) . The conditions for these reflection are given by Eqs. (H.6a) and (H.6b) when all \bar{x} - and \bar{y} -components are replaced by the corresponding components that are parallel and perpendicular to the boundary, respectively. In

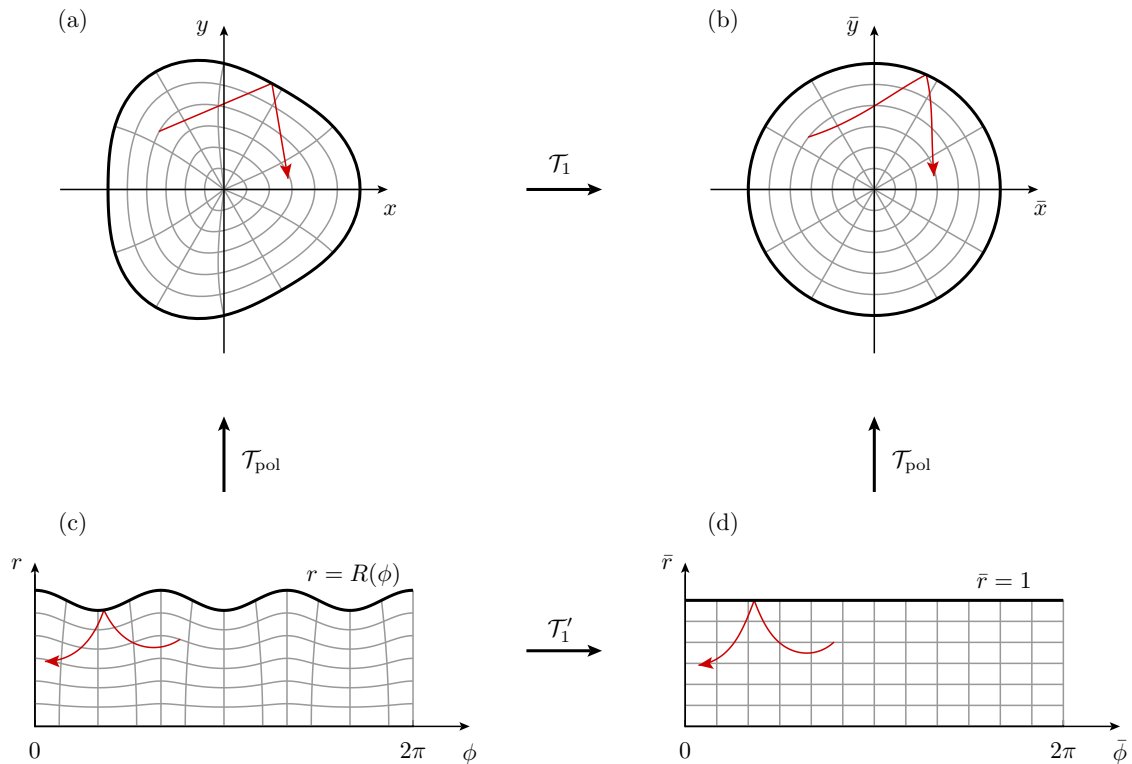


Figure H.1.: Visualization of the boundary transformation \mathcal{T}_1 for a smooth billiard and its decomposition (H.43). We show the billiard boundary (black lines), an orbit (red) and lines of $\bar{r} = \text{const.}$ and $\bar{\phi} = \text{const.}$ (gray) in the coordinates (x, y) (a), (\bar{x}, \bar{y}) (b), (ϕ, r) (c), and $(\bar{\phi}, \bar{r})$ (d).

polar coordinates $(\bar{\phi}, \bar{r})$, these reflections have a notably simple representation, given by

$$\frac{1}{2} \begin{pmatrix} \dot{\phi}' + \dot{\phi} \\ \dot{r}' + \dot{r} \end{pmatrix} = \begin{pmatrix} \dot{\phi} \\ 0 \end{pmatrix}, \quad (\text{H.47a})$$

$$\frac{1}{2} \begin{pmatrix} \dot{p}'_{\phi} + \dot{p}_{\phi} \\ \dot{p}'_r + \dot{p}_r \end{pmatrix} = \begin{pmatrix} \dot{p}_{\phi} \\ 0 \end{pmatrix}. \quad (\text{H.47b})$$

The previous derivation for the cornered billiard has shown, that requiring elastic reflections in the momentum velocities $\dot{\mathbf{p}}$ cannot be accomplished. As this impossibility occurred as a local property on the boundary, independently of the corners, we also expect this to be impossible in the present case.

We now formulate the reflections in the untransformed polar coordinates (ϕ, r) that are implied by the boundary curve $R(\phi)$. We start in the original coordinates $\mathbf{r} = (x, y)$. Here, the velocity reflections are given by

$$\dot{\mathbf{r}}' + \dot{\mathbf{r}} = 2(\dot{\mathbf{r}} \cdot \mathbf{e}_{\parallel}) \cdot \mathbf{e}_{\parallel}, \quad \mathbf{e}_{\parallel} = \frac{\rho(\phi)\mathbf{e}_{\phi} + \mathbf{e}_r}{\sqrt{1 + \rho(\phi)^2}}, \quad (\text{H.48})$$

where \mathbf{e}_{ϕ} and \mathbf{e}_r denote the unit vectors in ϕ - and r -direction, respectively, and

$$\rho(\phi) := \frac{R'(\phi)}{R(\phi)}. \quad (\text{H.49})$$

Translated into polar velocities $(\dot{\phi}, \dot{r})$, these reflections are

$$\frac{1}{2} \begin{pmatrix} \dot{\phi}' + \dot{\phi} \\ \dot{r}' + \dot{r} \end{pmatrix} = \frac{\dot{\phi} + R(\phi)^{-1}\rho(\phi)\dot{r}}{1 + \rho(\phi)^2} \begin{pmatrix} R'(\phi) \\ 1 \end{pmatrix}. \quad (\text{H.50a})$$

In analogy to App. H.1, we derive the reflections of the polar momentum (p_{ϕ}, p_r) as

$$\frac{1}{2} \begin{pmatrix} p'_{\phi} + p_{\phi} \\ p'_r + p_r \end{pmatrix} = \frac{r^{-1}p_{\phi} + \rho(\phi)p_r}{1 + \rho(\phi)^2} \begin{pmatrix} r \\ \rho(\phi) \end{pmatrix}. \quad (\text{H.50b})$$

The condition for $\mathcal{F}(\bar{\phi}, r)$ is, that the reflections (H.47) should be transformed to the reflections (H.50). To formulate this condition, we express the velocities $(\dot{\phi}, \dot{r})$ in terms of $(\dot{\bar{\phi}}, \dot{\bar{r}})$ using Eqs. (H.45), which gives

$$\dot{r} = \frac{d}{dt} \bar{r} R(\bar{\phi}) = \dot{\bar{r}} R(\bar{\phi}) + \bar{r} R'(\bar{\phi}) \dot{\bar{\phi}}, \quad (\text{H.51a})$$

$$\dot{\phi} = \frac{d}{dt} \mathcal{F}[\bar{\phi}, r(\bar{\phi}, \bar{r})] = \frac{\partial \mathcal{F}}{\partial \bar{\phi}} [\bar{\phi}, \bar{r} R(\bar{\phi})] \dot{\bar{\phi}} + \frac{\partial \mathcal{F}}{\partial r} [\bar{\phi}, \bar{r} R(\bar{\phi})] \cdot [\dot{\bar{r}} R(\bar{\phi}) + \bar{r} R'(\bar{\phi}) \dot{\bar{\phi}}]. \quad (\text{H.51b})$$

With this relation between $(\dot{\phi}, \dot{r})$ and $(\dot{\bar{\phi}}, \dot{\bar{r}})$, we connect the reflections (H.47a) and (H.50a), leading

to the conditions

$$\frac{\partial \mathcal{F}}{\partial r} [\bar{\phi}, \bar{r}R(\bar{\phi})] = -\frac{R'(\bar{\phi})}{R(\bar{\phi})^2}, \quad (\text{H.52a})$$

$$\frac{\partial \mathcal{F}}{\partial \bar{\phi}} [\bar{\phi}, \bar{r}R(\bar{\phi})] = R(\bar{\phi})^2 + R'(\bar{\phi})^2. \quad (\text{H.52b})$$

By solving Eqs. (H.46) and (H.52) for $\mathcal{F}(\bar{\phi}, r)$ using a second order polynomial in $\bar{\phi}$, we obtain

$$\mathcal{F}(\bar{\phi}, r) = \bar{\phi} + \frac{R'(\bar{\phi})}{2R(\bar{\phi})} \left[1 - \left(\frac{r}{R(\bar{\phi})} \right)^2 \right]. \quad (\text{H.53})$$

We remark, that an analogous treatment would be necessary to connect the momentum reflections (H.47b) and (H.50b). Here, we skipped this treatment, as it implies no additional conditions when the ansatz for \mathcal{F} is quadratic in $\bar{\phi}$. The resulting transformation has been visualized already in Fig. H.1 for the boundary function

$$R(\phi) = 1 + \epsilon \cos(k\phi), \quad (\text{H.54})$$

with $\epsilon = 0.08$ and $k = 3$.

I. Generalized quantizations \mathcal{Q}

In this appendix, we perform certain derivations concerning the generalized quantization \mathcal{Q} , Eq. (6.10). We first derive a general monomial formula, which will be helpful (App. I.1), deduce the conditions (6.15) for the integral kernel (App. I.2), and finally derive matrix element formulae for the practical evaluation of the quantization (App. I.3).

I.1. Monomial formulae

Apart from the integral representation (6.10) of a quantization rule \mathcal{Q} it is also convenient, to characterize \mathcal{Q} by its application to a monomial $\mathcal{Q}(q^n p^m)$. Due to linearity, this completely defines the action of \mathcal{Q} on arbitrary analytic functions. We now connect the integral representation to the monomial representation by expressing $\mathcal{Q}(q^n p^m)$ in terms of the integral kernel $w(\theta, \tau)$. Starting with Eq. (6.10), we have

$$\mathcal{Q}(q^n p^m) = \frac{1}{(2\pi)^2} \int dq \int dp \int d\theta \int d\tau w(\theta, \tau) e^{-i\theta q} e^{-i\tau p} e^{i\theta \hat{q}} e^{i\tau \hat{p}} q^n p^m. \quad (\text{I.1})$$

By rewriting

$$e^{-i\theta q} e^{-i\tau p} q^n p^m = i^{n+m} \left(\frac{\partial}{\partial \theta} \right)^n \left(\frac{\partial}{\partial \tau} \right)^m e^{-i\theta q} e^{-i\tau p}, \quad (\text{I.2})$$

this can be rearranged to

$$= \frac{i^{n+m}}{(2\pi)^2} \int d\theta \int d\tau w(\theta, \tau) e^{i\theta\hat{q}} e^{i\tau\hat{p}} \left(\frac{\partial}{\partial\theta}\right)^n \left(\frac{\partial}{\partial\tau}\right)^m \underbrace{\int dq e^{-i\theta q}}_{= 2\pi\delta(\theta)} \underbrace{\int dp e^{-i\tau p}}_{= 2\pi\delta(\tau)}, \quad (\text{I.3a})$$

$$= i^{n+m} \int d\theta \int d\tau w(\theta, \tau) e^{i\theta\hat{q}} e^{i\tau\hat{p}} \left(\frac{\partial}{\partial\theta}\right)^n \left(\frac{\partial}{\partial\tau}\right)^m \delta(\theta)\delta(\tau). \quad (\text{I.3b})$$

To detach the differentiation operators from the δ -functions, we use integration by parts, applied n times in θ and m times in τ . Here, all intermediate terms vanish due to the fast asymptotic decay of the δ -function and its derivatives [87]. As each application of integration by parts changes the sign of the integral, we collect a total factor of $(-1)^{n+m}$, leading to

$$= (-i)^{n+m} \int d\theta \int d\tau \delta(\theta)\delta(\tau) \left(\frac{\partial}{\partial\theta}\right)^n \left(\frac{\partial}{\partial\tau}\right)^m w(\theta, \tau) e^{i\theta\hat{q}} e^{i\tau\hat{p}}. \quad (\text{I.4})$$

Finally, we obtain the monomial formula

$$\mathcal{Q}(q^n p^m) = (-i)^{n+m} \left[\left(\frac{\partial}{\partial\theta}\right)^n \left(\frac{\partial}{\partial\tau}\right)^m w(\theta, \tau) e^{i\theta\hat{q}} e^{i\tau\hat{p}} \right]_{\theta=\tau=0}. \quad (\text{I.5})$$

As a side result, we find that Rivier's rule, Eq. (6.16) with $\alpha = \frac{1}{2}$, has the monomial representation

$$\mathcal{Q}(q^n p^m) = \frac{\hat{q}^n \hat{p}^m + \hat{p}^m \hat{q}^n}{2}. \quad (\text{I.6})$$

I.2. Conditions for the integral kernel $w(\theta, \tau)$

We now translate the properties (6.13) of a quantization rule \mathcal{Q} to the conditions (6.15) of its integral kernel $w(\theta, \tau)$. Considering condition (6.13a), Eq. (6.10) becomes

$$\mathcal{Q}(1) = \frac{1}{(2\pi)^2} \int d\theta \int d\tau w(\theta, \tau) \underbrace{\left(\int dq e^{-i\theta q}\right)}_{= 2\pi\delta(\theta)} \underbrace{\left(\int dp e^{-i\tau p}\right)}_{= 2\pi\delta(\tau)} e^{i\theta\hat{q}} e^{i\tau\hat{p}} \quad (\text{I.7a})$$

$$= w(0, 0), \quad (\text{I.7b})$$

leading to condition (6.15a).

For condition (6.13b), we first consider the right hand side, which is

$$\mathcal{Q}(A)^\dagger = \frac{1}{(2\pi)^2} \int dq \int dp \int d\theta \int d\tau \left[w(\theta, \tau) e^{-i\theta q} e^{-i\tau p} e^{i\theta\hat{q}} e^{i\tau\hat{p}} A(q, p) \right]^\dagger. \quad (\text{I.8})$$

Using the Baker-Campbell-Hausdorff formula and the self-adjointness of \hat{q} and \hat{p} we have

$$\left[e^{i\theta\hat{q}} e^{i\tau\hat{p}} \right]^\dagger = e^{-i\tau\hat{p}} e^{-i\theta\hat{q}} = e^{i\theta\tau\hbar} e^{-i\theta\hat{q}} e^{-i\tau\hat{p}}, \quad (\text{I.9})$$

and Eq. (I.8) becomes

$$= \frac{1}{(2\pi)^2} \int dq \int dp \int d\theta \int d\tau w(\theta, \tau)^* e^{i\theta\tau\hbar} e^{i\theta q} e^{i\tau p} e^{-i\theta\hat{q}} e^{-i\tau\hat{p}} A(q, p)^*. \quad (\text{I.10})$$

By substituting the integration parameters $(\theta, \tau) \mapsto (-\theta, -\tau)$, we obtain

$$= \frac{1}{(2\pi)^2} \int dq \int dp \int d\theta \int d\tau w(-\theta, -\tau)^* e^{i\theta\tau\hbar} e^{-i\theta q} e^{-i\tau p} e^{i\theta\hat{q}} e^{i\tau\hat{p}} A(q, p)^*. \quad (\text{I.11})$$

Identifying this with $\mathcal{Q}(A^*)$ leads to the condition (6.15b) for the kernel $w(\theta, \tau)$.

To evaluate condition (6.13c), we consider the classical limit $\hbar \rightarrow 0$, where $\hat{q} \rightarrow q$ and $\hat{p} \rightarrow p$. Here, condition (6.13c) becomes

$$A(q', p') = \frac{1}{(2\pi)^2} \int dq \int dp \int d\theta \int d\tau w_0(\theta, \tau) e^{-i\theta q} e^{-i\tau p} e^{i\theta q'} e^{i\tau p'} A(q, p) \quad (\text{I.12})$$

where we substituted

$$w_0(\theta, \tau) = \lim_{\hbar \rightarrow 0} w(\theta, \tau). \quad (\text{I.13})$$

Thus, it is required that any function $A(q, p)$ must be invariant under the integral operator (I.12). Clearly this is true for $w_0(\theta, \tau) = 1$, where Eq. (I.12) is just the identity transformation in Fourier integral representation. Consequently, Eq. (I.12) is necessary for condition (6.15c). To be sufficient, the solution $w_0(\theta, \tau) = 1$ must be unique. We prove this by showing that

$$u(\theta, \tau) := w_0(\theta, \tau) - 1 = 0. \quad (\text{I.14})$$

Substituting $w_0(\theta, \tau)$ by $u(\theta, \tau)$ in Eq. (I.12) we have

$$0 = \frac{1}{(2\pi)^2} \int dq \int dp \int d\theta \int d\tau u(\theta, \tau) e^{-i\theta q} e^{-i\tau p} e^{i\theta q'} e^{i\tau p'} A(q, p). \quad (\text{I.15})$$

Using the test function $A(q, p) = \delta(q - q_0)\delta(p - p_0)$ with arbitrary (q_0, p_0) and substituting $(\bar{q}, \bar{p}) = (q' - q_0, p' - p_0)$ leads to

$$0 = \frac{1}{(2\pi)^2} \int d\theta \int d\tau u(\theta, \tau) e^{i\theta\bar{q}} e^{i\tau\bar{p}}. \quad (\text{I.16})$$

Thus the Fourier transform of $u(\theta, \tau)$ vanishes. As (\bar{q}, \bar{p}) is arbitrary, the whole function must vanish, leading to Eq. (I.14).

Finally, to evaluate condition (6.13d), we consider the power series expansion of $A(q)$. Here, due to linearity, the condition becomes $\mathcal{Q}(q^n) = \hat{q}^n$ which can be expressed recursively as

$$\mathcal{Q}(q^n) = \hat{q}\mathcal{Q}(\hat{q}^{n-1}), \quad \forall n \in \mathbb{N}. \quad (\text{I.17})$$

Using the monomial formula (I.5), we have

$$\mathcal{Q}(q^n) = (-i)^n \left[\left(\frac{\partial}{\partial \theta} \right)^n w(\theta, 0) e^{i\theta \hat{q}} \right]_{\theta=0}. \quad (\text{I.18})$$

With the product rule of differentiation we get

$$= (-i)^n \left[\left(\frac{\partial}{\partial \theta} \right)^{n-1} \left(w(\theta, 0) i \hat{q} e^{i\theta \hat{q}} + \frac{\partial w}{\partial \theta}(\theta, \tau) e^{i\theta \hat{q}} \right) \right]_{\theta=0}, \quad (\text{I.19a})$$

$$= \underbrace{\hat{q} (-i)^{n-1} \left[\left(\frac{\partial}{\partial \theta} \right)^{n-1} w(\theta, 0) e^{i\theta \hat{q}} \right]_{\theta=0}}_{= \mathcal{Q}(q^{n-1})} + (-i)^n \left[\left(\frac{\partial}{\partial \theta} \right)^{n-1} \frac{\partial w}{\partial \theta}(\theta, 0) e^{i\theta \hat{q}} \right]_{\theta=0}. \quad (\text{I.19b})$$

To fulfill Eq. (I.17), the second term in Eq. (I.19b) must vanish. This second terms evaluates to

$$(-i)^n \left[\left(\frac{\partial}{\partial \theta} \right)^{n-1} \frac{\partial w}{\partial \theta}(\theta, 0) e^{i\theta \hat{q}} \right]_{\theta=0} = (-i)^n \sum_{k=0}^{n-1} \binom{n-1}{k} (i \hat{q})^k \frac{\partial^{n-k} w}{\partial \theta^{n-k}}(0, 0). \quad (\text{I.20})$$

Consequently, all derivatives of the kernel need to be zero in the origin,

$$\frac{\partial^k w}{\partial \theta^k}(0, 0) = 0, \quad (\text{I.21})$$

with $k \leq n$. To hold for all powers n , Eq. (I.21) is required for any $k \in \mathbb{N}$, leading to condition (6.15d). The conjugate condition (6.15e) is derived analogously.

I.3. Matrix element formulae

Evaluating a quantization rule via the monomial formula becomes impractical for functions $A(q, p)$ which are not given in polynomial form. For this case, integral formulae can be derived, which we do in the following for the parametrized quantization rule \mathcal{Q}_α given by Eq. (6.16).

Considering the matrix elements in position representation, we obtain

$$\langle q_1 | \mathcal{Q}_\alpha(A) | q_2 \rangle = \frac{1}{(2\pi)^2} \int dq \int dp \int d\theta \int d\tau w_\alpha(\theta, \tau) e^{-i\theta q} e^{-i\tau p} e^{i\theta q_1} \langle q_1 | e^{i\tau \hat{p}} | q_2 \rangle A(q, p). \quad (\text{I.22})$$

Evaluating the translation operator $e^{i\tau \hat{p}}$ gives

$$\langle q_1 | e^{i\tau \hat{p}} | q_2 \rangle = \langle q_1 | q_2 - \tau \hbar \rangle = \delta(q_1 - q_2 + \tau \hbar) = \frac{1}{\hbar} \delta\left(\tau - \frac{q_2 - q_1}{\hbar}\right). \quad (\text{I.23})$$

Applying this delta function and inserting w_α via Eq. (6.16), Eq. (I.22) becomes

$$= \frac{1}{4\pi\hbar} \int dq \int dp e^{-i(q_2-q_1)p/\hbar} A(q, p) \sum_{s=\pm 1} \underbrace{\frac{1}{2\pi} \int d\theta e^{i\theta[(q_2-q_1)(\frac{1}{2}+s\alpha)+q_1-q]}}_{= \delta[q - q_1(\frac{1}{2} - s\alpha) - q_2(\frac{1}{2} + s\alpha)]}, \quad (\text{I.24})$$

$$= \frac{1}{4\pi\hbar} \int dp e^{i(q_1-q_2)p/\hbar} \sum_{s=\pm 1} A[q_1(\frac{1}{2} - s\alpha) + q_2(\frac{1}{2} + s\alpha), p]. \quad (\text{I.25})$$

For the Weyl rule, $\alpha = 0$, this becomes

$$\langle q_1 | \mathcal{Q}_0(A) | q_2 \rangle = \frac{1}{2\pi\hbar} \int dp e^{i(q_1-q_2)p/\hbar} A\left(\frac{q_1+q_2}{2}, p\right). \quad (\text{I.26})$$

The corresponding matrix elements in momentum representation are derived analogously, leading to

$$\langle p_1 | \mathcal{Q}_0(A) | p_2 \rangle = \frac{1}{2\pi\hbar} \int dq e^{-iq(p_1-p_2)/\hbar} A\left(q, \frac{p_1+p_2}{2}\right). \quad (\text{I.27})$$

J. Optimized algorithm for the Weyl matrix elements $A_{\mathbf{nm}}$

In this appendix, we design an optimized algorithm to compute the matrix elements

$$A_{\mathbf{nm}} = \left(\frac{\pi\hbar}{4}\right)^2 \sum_{s_1, s_2, s'_1, s'_2}^{\pm} s_1 s_2 s'_1 s'_2 \int_{\mathcal{S}} d^2\mathbf{q} A\left[\mathbf{q}, \begin{pmatrix} s_1 n_1 + s'_1 m_1 \\ s_2 n_2 + s'_2 m_2 \end{pmatrix}\right] \exp\left[-i\pi\mathbf{q} \begin{pmatrix} s_1 n_1 - s'_1 m_1 \\ s_2 n_2 - s'_2 m_2 \end{pmatrix}\right], \quad (\text{J.1})$$

see Eq. (6.50). When evaluating this equation, many different combinations of the signs $\{s_1, s_2, s'_1, s'_2\}$ and the indices $\{n_1, n_2, m_1, m_2\}$ lead to the same momentum argument in the function $A(\mathbf{q}, \mathbf{p})$. This makes a straightforward computation of the matrix elements (J.1) inefficient, especially when A refers to an integrable approximation H_{reg}^n , Eq. (3.15), which is evaluated rather slowly for large orders n . To compute the matrix elements while calling the function $A(\mathbf{q}, \mathbf{p})$ as rarely as possible, we define the integral

$$\mathcal{A}_{\ell_1^-, \ell_2^-}^{\ell_1^+, \ell_2^+} := \left(\frac{\pi\hbar}{4}\right)^2 \int_{\mathcal{S}} d^2\mathbf{q} A(\mathbf{q}, \ell_1^+, \ell_2^+) \exp[-i\pi(\ell_1^- q_1 + \ell_2^- q_2)], \quad (\text{J.2a})$$

and rewrite Eq. (J.1) as

$$A_{\mathbf{nm}} = \sum_{s_1, s_2, s'_1, s'_2}^{\pm} s_1 s_2 s'_1 s'_2 \mathcal{A}_{s_1 n_1 - s'_1 m_1, s_2 n_2 - s'_2 m_2}^{s_1 n_1 + s'_1 m_1, s_2 n_2 + s'_2 m_2}. \quad (\text{J.2b})$$

Here the new indices

$$\ell_i^\pm = s_i n_i \pm s'_i m_i, \quad (\text{J.3})$$

have been introduced, which for $n_i = 1, 2, \dots, N_i$ take the values

$$\ell_i^+ = -2N_i, -2N_i + 1, \dots, 2N_i, \tag{J.4a}$$

$$\ell_i^- = |\ell_i^+| - 2N_i, |\ell_i^+| - 2N_i + 2, \dots, 2N_i - |\ell_i^+|, \tag{J.4b}$$

see Fig. J.1 Now, the following scheme is applied:

1. For each index pair (ℓ_1^+, ℓ_2^+) , compute the values $A(\mathbf{q}, \ell_1^+, \ell_2^+)$ at the positions \mathbf{q} that are required for the integration.
 - 1.1. For each index pair (ℓ_1^-, ℓ_2^-) , compute the integral $\mathcal{A}_{\ell_1^-, \ell_2^-}^{\ell_1^+, \ell_2^+}$ from these values via Eq. (J.2a) and store it.
2. For each (\mathbf{n}, \mathbf{m}) , compute $A_{\mathbf{nm}}$ by summing over $\mathcal{A}_{\ell_1^-, \ell_2^-}^{\ell_1^+, \ell_2^+}$ via Eq. (J.2b).

Compared to a straightforward evaluation of Eq. (J.1), where $A(\mathbf{q}, \mathbf{p})$ would be called $(4N_1N_2)^2$ times on each position \mathbf{q} , this optimized scheme only needs $(4N_1 + 1)(4N_2 + 1)$ calls, as the momentum argument of $A(\mathbf{q}, \mathbf{p})$ in Eq. (J.2a) depends on two indices (ℓ_1^+, ℓ_2^+) only. This improves the complexity by two orders from $\mathcal{O}(N_1^2N_2^2)$ to $\mathcal{O}(N_1N_2)$, thus the algorithm grows linear in matrix size N_1N_2 . Moreover, if the observable $A(\mathbf{q}, \mathbf{p})$ fulfills the scaling property (5.16), the number of function calls can be reduced further on. Here, for each index pair (ℓ_1^+, ℓ_2^+) with a common integer factor $\lambda > 1$, we have $\mathcal{A}_{\ell_1^-, \ell_2^-}^{\ell_1^+, \ell_2^+} = \lambda^2 \mathcal{A}_{\ell_1^-/\lambda, \ell_2^-/\lambda}^{\ell_1^+/\lambda, \ell_2^+/\lambda}$. However, as the asymptotic rate of coprime integer pairs is $6/\pi^2$ [88, theorem 332] this only enhances the computation speed by a factor of order 1.

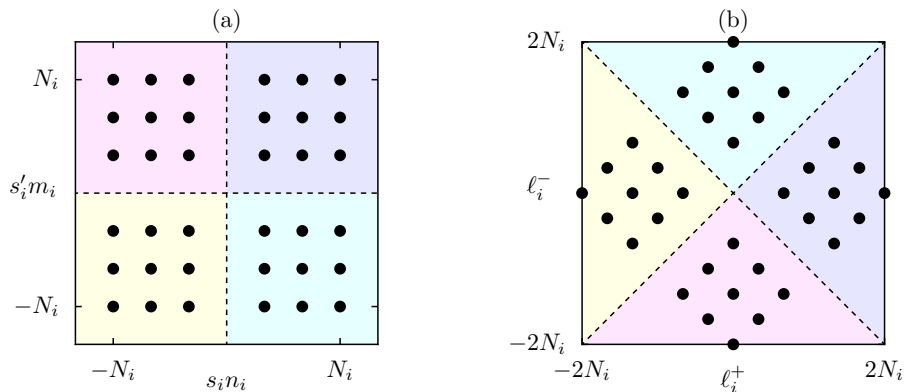


Figure J.1.: Visualisation of the index transformation (J.3) from the integer grid $-N_i \leq s_i n_i, s'_i m_i \leq N_i$ (a) to the grid of (ℓ_i^+, ℓ_i^-) (b), shown for $N_i = 3$. Colors indicate different sign combinations of s_i and s'_i .

List of Figures

1.1. Phase space of the standard map at $\kappa = 1.25$ and of an integrable approximation H_{reg}	1
2.1. Illustration of canonically conjugated phase flows and area preservation	5
2.2. Illustration of Poincaré sections	7
2.3. Action–angle coordinates for the harmonic oscillator	9
2.4. Integrability in one degree of freedom: the role of the frequency function $\omega(J)$ and the canonical transformation T	10
2.5. Integrability in two degrees of freedom: angular parametrization of the 2-torus.	11
2.6. Integrability in two degrees of freedom: periodic and quasiperiodic motion	12
2.7. Integrability in two degrees of freedom: fundamental loops on the 2-torus	13
2.8. Phase space of the standard map for the near-integrable and mixed case	15
2.9. Nonlinear resonance chains and corresponding gaps in the frequency function	16
4.1. Application to the standard map at $\kappa = 1.25$: frequency approximation	29
4.2. Application to the standard map at $\kappa = 1.25$: shape approximation	31
4.3. Application to the standard map at $\kappa = 1.25$: cost function	32
4.4. Globally non-invertible canonical transformation	36
4.5. Achieving global invertibility via the damping mechanism	37
4.6. Illustration of the adapted damping mechanism	39
4.7. Asymptotics of the iterative canonical transformation method with \mathcal{N}	41
4.8. Asymptotics of the iterative canonical transformation method with \mathcal{N} for an integrable target system	42
4.9. Comparison to the normal-form method for the standard map at $\kappa = 0.5$	46
4.10. Comparison to the normal-form method for the standard map at $\kappa = 1.25$	47
4.11. Comparison to the normal-form method for the standard map at $\kappa = 2.9$	47
4.12. Comparison to the Lie method for the standard map at $\kappa = 0.5$	50
4.13. Comparison to the Lie method for the standard map at $\kappa = 1.25$	50
4.14. Comparison to the Lie method for the standard map at $\kappa = 2.9$	51
4.15. Comparison of computation times for different methods	52
4.16. Iterative canonical transformation method with separatrix: basic idea	53
4.17. Iterative canonical transformation method with separatrix: shape approximation	55
4.18. Iterative canonical transformation method with resonance: basic idea	56
4.19. Iterative canonical transformation method with resonance: frequency approximation	59

4.20. Iterative canonical transformation method with resonance: shape approximation	60
5.1. Cosine billiard: examples	62
5.2. Cosine billiard: Poincaré sections	62
5.3. Boundary simplification: basic idea	64
5.4. Boundary simplification: family of curves	65
5.5. Boundary simplification: cosine billiard with trajectories	67
5.6. Application to the cosine billiard at $(h, w) = (0.2, 0.066)$: frequency approximation	71
5.7. Application to the cosine billiard at $(h, w) = (0.2, 0.066)$: shape approximation	74
5.8. Application to the cosine billiard at $(h, w) = (0.2, 0.066)$: cost function	74
6.1. Classical phase space, integrable approximation, eigenstates, and quasimodes for the standard map at $\kappa = 2.9$	78
6.2. Tunneling rates for the standard map at $\kappa = 2.9$	79
6.3. Tunneling rates for the standard map at $\kappa = 2.9$ from random quantizations	82
6.4. Eigenstates of the square billiard	86
6.5. Test of the numerical computation scheme for eigenstates of a toy Hamiltonian	91
6.6. Eigenstates and quasimodes for the cosine billiard at $(h, w) = (0.2, 0.066)$	92
6.7. Quantizing actions for the cosine billiard at $(h, w) = (0.2, 0.066)$	93
6.8. Tunneling rates for the cosine billiard at $(h, w) = (0.2, 0.066)$ from H_{reg}^1	94
6.9. Tunneling rates for the cosine billiard at $(h, w) = (0.2, 0.066)$ from H_{reg}^0	95
6.10. Tunneling rates for the cosine billiard at $(h, w) = (0.115, 0.06)$ from H_{reg}^0	96
E.1. Illustration of the normal-form transformation T^*	107
H.1. Construction of the boundary transformation \mathcal{T}_1 for smooth billiards	120
J.1. Illustration of the integer transformation $(s_i n_i, s'_i m_i) \mapsto (\ell_i^+, \ell_i^-)$ used in the optimized algorithm for the Weyl matrix elements	127

Bibliography

- [1] L. Markus and K. R. Meyer: *Generic Hamiltonian Dynamical Systems are neither Integrable nor Ergodic*, no. 144 in Mem. Amer. Math. Soc., (American Mathematical Society, Providence, Rhode Island), (1974). Cited on pages 1 and 14.
- [2] S. Hudson and R. Dewar: *Construction of an integrable field close to any non-integrable toroidal magnetic field*, Phys. Lett. A **247** (1998), 246–251. Cited on page 1.
- [3] A. Bazzani, S. Siboni, and G. Turchetti: *Action diffusion for symplectic maps with a noisy linear frequency*, J. Phys. A **30** (1997), 27–36. Cited on pages 1 and 101.
- [4] M. Kaasalainen and J. Binney: *Construction of Invariant Tori and Integrable Hamiltonians*, Phys. Rev. Lett. **73** (1994), 2377–2381. Cited on pages 1 and 2.
- [5] M. J. Davis and E. J. Heller: *Quantum dynamical tunnelling in bound states*, J. Chem. Phys. **75** (1981), 246–254. Cited on pages 2 and 75.
- [6] S. Keshavamurthy and P. Schlagheck: *Dynamical Tunneling: Theory and Experiment*, (Taylor & Francis, Boca Raton), (2011). Cited on pages 2 and 75.
- [7] O. Brodier, P. Schlagheck, and D. Ullmo: *Resonance-Assisted Tunneling in Near-Integrable Systems*, Phys. Rev. Lett. **87** (2001), 064101. Cited on pages 2, 56, 58, 75, and 100.
- [8] O. Brodier, P. Schlagheck, and D. Ullmo: *Resonance-Assisted Tunneling*, Ann. Phys. (N.Y.) **300** (2002), 88–136. Cited on pages 2, 43, 48, 49, 56, 58, 75, 99, and 100.
- [9] C. Eltschka and P. Schlagheck: *Resonance- and Chaos-Assisted Tunneling in Mixed Regular-Chaotic Systems*, Phys. Rev. Lett. **94** (2005), 014101. Cited on pages 2, 58, 75, and 100.
- [10] A. Mouchet, C. Eltschka, and P. Schlagheck: *Influence of classical resonances on chaotic tunneling*, Phys. Rev. E **74** (2006), 026211. Cited on pages 2, 75, and 100.
- [11] J. Le Deunff and A. Mouchet: *Instantons re-examined: Dynamical tunneling and resonant tunneling*, Phys. Rev. E **81** (2010), 046205. Cited on pages 2, 75, and 100.
- [12] A. Bäcker, R. Ketzmerick, S. Löck, and L. Schilling: *Regular-to-Chaotic Tunneling Rates Using a Fictitious Integrable System*, Phys. Rev. Lett. **100** (2008), 104101. Cited on pages 2, 76, 79, and 99.

- [13] A. Bäcker, R. Ketzmerick, and S. Löck: *Direct regular-to-chaotic tunneling rates using the fictitious-integrable-system approach*, Phys. Rev. E **82** (2010), 056208. Cited on pages 2, 76, 79, and 99.
- [14] S. Löck, A. Bäcker, R. Ketzmerick, and P. Schlagheck: *Regular-to-Chaotic Tunneling Rates: From the Quantum to the Semiclassical Regime*, Phys. Rev. Lett. **104** (2010), 114101. Cited on pages 2, 56, 58, 76, 77, 99, and 100.
- [15] A. Bäcker, R. Ketzmerick, S. Löck, M. Robnik, G. Vidmar, R. Höhmann, U. Kuhl, and H.-J. Stöckmann: *Dynamical Tunneling in Mushroom Billiards*, Phys. Rev. Lett. **100** (2008), 174103. Cited on pages 2, 83, and 100.
- [16] A. Bäcker, R. Ketzmerick, S. Löck, J. Wiersig, and M. Hentschel: *Quality factors and dynamical tunneling in annular microcavities*, Phys. Rev. A **79** (2009), 063804. Cited on pages 2 and 100.
- [17] S. Chapman, B. C. Garrett, and W. H. Miller: *Semiclassical eigenvalues for nonseparable systems: Nonperturbative solution of the Hamilton–Jacobi equation in action-angle variables*, J. Chem. Phys. **64** (1976), 502–509. Cited on page 2.
- [18] A. Bazzani, M. Giovannozzi, G. Servizi, E. Todesco, and G. Turchetti: *Resonant normal forms, interpolating Hamiltonians and stability analysis of area preserving maps*, Physica D **64** (1993), 66–97. Cited on pages 2, 43, and 99.
- [19] A. Bazzani, E. Todesco, G. Turchetti, and G. Servizi: *A normal form approach to the theory of nonlinear betatronic motion*, CERN Yellow Report **94-02** (1994), 1–225. Cited on pages 2, 43, and 99.
- [20] A. Deprit: *Canonical transformations depending on a small parameter*, Celest. Mech. Dyn. Astr. **1** (1969), 12–30. Cited on pages 2, 43, 48, and 99.
- [21] J. R. Cary: *Lie transform perturbation theory for Hamiltonian systems*, Phys. Rep. **79** (1981), 129–159. Cited on pages 2, 43, 48, and 99.
- [22] A. J. Lichtenberg and M. A. Leiberman: *Regular and Chaotic Dynamics*, (Springer, New York), 2nd edn., (1992). Cited on pages 2, 3, 30, 43, 48, 53, 54, 57, and 99.
- [23] R. Eichhorn, S. J. Linz, and P. Hänggi: *Transformation invariance of Lyapunov exponents*, Chaos, Solitons and Fractals **12** (2001), 1377–1383. Cited on page 5.
- [24] V. I. Arnold: *Mathematical Methods of Classical Mechanics*, no. 60 in Graduate Texts in Mathematics, (Springer New York), (1989). Cited on pages 5, 6, and 7.
- [25] J. M. Lee: *Introduction to Smooth Manifolds*, (Springer, New York), 2nd edn., (2003). Cited on page 5.

- [26] H. Goldstein, C. P. Poole, and J. L. Safko: *Classical Mechanics*, (Addison–Wesley, San Francisco), 3rd edn., (2002). Cited on page 5.
- [27] H. Hopf: *Vektorfelder in n -dimensionalen Mannigfaltigkeiten* (in German), *Math. Ann.* **96** (1926), 225–250. Cited on page 8.
- [28] A. N. Kolmogorov: *Preservation of conditionally periodic movements with small change in the Hamilton function* (in Russian), *Dokl. Akad. Nauk. SSSR* **98** (1954), 527–530, English translation in G. Casati and J. Ford, *Stochastic Behavior in Classical and Quantum Hamiltonian Systems*, vol. 93 of *Lect. Notes Phys.* (Springer-Verlag, Berlin, 1979), 51–56. Cited on page 14.
- [29] V. I. Arnold: *Proof of a theorem of A. N. Kolmogorov on the invariance of quasi-periodic motions under small perturbations of the Hamiltonian*, *Russ. Math. Surv.* **18** (1963), 9–36. Cited on page 14.
- [30] V. I. Arnold: *Small denominators and problems of stability of motion in classical and celestial mechanics*, *Russ. Math. Surv.* **18** (1963), 85–191. Cited on page 14.
- [31] J. Moser: *On invariant curves of area-preserving mappings of an annulus*, *Nachr. Akad. Wiss. Göttingen* **1** (1962), 1–20. Cited on page 14.
- [32] H. Poincaré: *Sur un théorème de géométrie* (in French), *Rend. del. Cir. Mat. di Palermo* **33** (1912), 375–407. Cited on page 14.
- [33] G. D. Birkhoff: *Proof of Poincaré’s geometric theorem*, *Trans. Amer. Math. Soc.* **14** (1913), 14–22. Cited on page 14.
- [34] J. Moser: *Proof of a generalized form of a fixed point theorem due to G. D. Birkhoff*, in: *Geometry and Topology*, *Lecture Notes in Mathematics*, 464–494, (Springer), (1977). Cited on page 14.
- [35] A. Kruscha, R. Ketzmerick, and H. Kantz: *Biased diffusion inside regular islands under random symplectic perturbations*, *Phys. Rev. E* **85** (2012), 066210. Cited on pages 14 and 101.
- [36] S. Tomsovic and D. Ullmo: *Chaos-assisted tunneling*, *Phys. Rev. E* **50** (1994), 145–162. Cited on page 14.
- [37] A. Shudo and K. S. Ikeda: *Complex Classical Trajectories and Chaotic Tunneling*, *Phys. Rev. Lett.* **74** (1995), 682–685. Cited on pages 14, 77, and 100.
- [38] A. Shudo and K. S. Ikeda: *Chaotic tunneling: A remarkable manifestation of complex classical dynamics in non-integrable quantum phenomena*, *Physica D* **115** (1998), 234–292. Cited on page 14.
- [39] M. V. Berry and M. Robnik: *Semiclassical level spacings when regular and chaotic orbits coexist*, *J. Phys. A* **17** (1984), 2413–2421. Cited on page 14.

- [40] A. Bäcker, R. Ketzmerick, S. Löck, and N. Mertig: *Fractional-Power-Law Level Statistics Due to Dynamical Tunneling*, Phys. Rev. Lett. **106** (2011), 024101. Cited on page 14.
- [41] C. Löbner, S. Löck, A. Bäcker, and R. Ketzmerick: *Integrable approximation of regular islands: The iterative canonical transformation method*, Phys. Rev. E **88** (2013), 062901. Cited on pages 19 and 61.
- [42] J. Laskar, C. Froeschlé, and A. Celletti: *The measure of chaos by the numerical analysis of the fundamental frequencies. Application to the standard mapping*, Physica D **56** (1992), 253–269. Cited on page 28.
- [43] R. Bartolini, A. Bazzani, M. Giovannozzi, W. Scandale, and E. Todesco: *Tune evaluation in simulations and experiments*, Part. Accel. **52** (1996), 147–177. Cited on page 28.
- [44] S. G. Krantz and H. R. Parks: *The Implicit Function Theorem: History, Theory, and Applications*, (Birkhäuser, Boston), (2002). Cited on pages 33, 34, and 105.
- [45] J. M. Ortega and W. C. Rheinboldt: *Iterative Solution of Nonlinear Equations in Several Variables*, (Academic Press, New York), (1970). Cited on pages 34 and 106.
- [46] V. V. Sokolov: *Quasienergy integral for canonical maps*, Theor. Math. Phys. **67** (1986), 464–473. Cited on page 43.
- [47] R. Scharf: *The Campbell-Baker-Hausdorff expansion for classical and quantum kicked dynamics*, J. Phys. A **21** (1988), 2007–2021. Cited on page 43.
- [48] B. McNamara: *Super-convergent adiabatic invariants with resonant denominators by Lie transforms*, J. Math. Phys. **19** (1978), 2154–2164. Cited on page 49.
- [49] M. Abramowitz and I. A. Stegun: *Handbook of Mathematical Functions with Formulas, Graphs, and Mathematical Tables*, (Dover, New York), ninth dover printing, tenth gpo printing edn., (1964). Cited on page 54.
- [50] J. Kullig: *Resonanzunterstütztes Tunneln und integrable Näherungen* (in German), Diploma thesis, Technische Universität Dresden, Fachrichtung Physik, (2013). Cited on pages 55, 77, 96, and 100.
- [51] J. Kullig, C. Löbner, N. Mertig, A. Bäcker, and R. Ketzmerick: *Integrable approximation of regular regions with a nonlinear resonance chain*, Phys. Rev. E **90** (2014), 052906. Cited on page 55.
- [52] B. V. Chirikov: *A universal instability of many-dimensional oscillator systems*, Phys. Rep. **52** (1979), 263–379. Cited on page 56.
- [53] A. M. Ozorio de Almeida: *Hamiltonian Systems: Chaos and Quantization*, (Cambridge University Press, Cambridge), (1988). Cited on pages 56 and 58.

- [54] P. Leboeuf and A. Mouchet: *Normal Forms and Complex Periodic Orbits in Semiclassical Expansions of Hamiltonian Systems*, Ann. Phys. (N.Y.) **275** (1999), 54–112. Cited on pages 56 and 58.
- [55] J. Le Deunff, A. Mouchet, and P. Schlagheck: *Semiclassical description of resonance-assisted tunneling in one-dimensional integrable models*, Phys. Rev. E **88** (2013), 042927. Cited on pages 56, 58, and 77.
- [56] H.-J. Stöckmann: *Quantum Chaos*, (Cambridge University Press, Cambridge), (1999). Cited on page 61.
- [57] M. V. Berry: *Regularity and chaos in classical mechanics, illustrated by three deformations of a circular ‘billiard’*, Eur. J. Phys **2** (1981), 91–102. Cited on page 61.
- [58] H.-J. Stöckmann and J. Stein: *“Quantum” chaos in billiards studied by microwave absorption*, Phys. Rev. Lett. **64** (1990), 2215–2218. Cited on page 61.
- [59] R. Luneburg and M. Herzberger: *Mathematical Theory of Optics*, (University of California, Berkeley), (1964). Cited on page 61.
- [60] J. Margalef-Roig and E. Outerelo Dominguez: *Differential Topology*, no. 173 in North-Holland Mathematics Studies, (North Holland, Amsterdam), (1992). Cited on pages 64 and 117.
- [61] F. Hund: *Zur Deutung der Molekelspektren. I* (in German), Z. Physik **40** (1927), 742–764. Cited on page 75.
- [62] G. Gamow: *Zur Quantentheorie des Atomkernes* (in German), Z. Physik **51** (1928), 204–212. Cited on page 75.
- [63] J. D. Hanson, E. Ott, and T. M. Antonsen: *Influence of finite wavelength on the quantum kicked rotator in the semiclassical regime*, Phys. Rev. A **29** (1984), 819–825. Cited on page 75.
- [64] J. Feist, A. Bäcker, R. Ketzmerick, S. Rotter, B. Huckestein, and J. Burgdörfer: *Nanowires with Surface Disorder: Giant Localization Lengths and Quantum-to-Classical Crossover*, Phys. Rev. Lett. **97** (2006), 116804. Cited on page 75.
- [65] N. Mertig: *Complex Paths for Regular-to-Chaotic Tunneling Rates*, Ph.D. thesis, Technische Universität Dresden, Fachrichtung Physik, (2013). Cited on pages 76, 77, and 81.
- [66] J. Kullig, N. Mertig, C. Löbner, A. Bäcker, and R. Ketzmerick: to be published, (2015 + ϵ). Cited on pages 77 and 100.
- [67] S. C. Creagh: *Directional Emission from Weakly Eccentric Resonators*, Phys. Rev. Lett. **98** (2007), 153901. Cited on pages 77 and 100.
- [68] S. C. Creagh and M. M. White: *Differences between emission patterns and internal modes of optical resonators*, Phys. Rev. E **85** (2012), 015201. Cited on pages 77 and 100.

- [69] N. Mertig, S. Löck, A. Bäcker, R. Ketzmerick, and A. Shudo: *Complex paths for regular-to-chaotic tunnelling rates*, Europhys. Lett. **102** (2013), 10005. Cited on pages 77 and 100.
- [70] F. Fritzsche: *Semiklassische Vorhersage des resonanzassistierten Tunnelns im gemischten Phasenraum* (in German), Master's thesis, Technische Universität Dresden, Fachrichtung Physik, (2014). Cited on pages 77 and 100.
- [71] S.-J. Chang and K.-J. Shi: *Evolution and exact eigenstates of a resonant quantum system*, Phys. Rev. A **34** (1986), 7–22. Cited on page 77.
- [72] M. Zworski: *Semiclassical Analysis*, no. 138 in Graduate Studies in Mathematics, (American Mathematical Society, Providence, Rhode Island), (2012). Cited on page 81.
- [73] H. Weyl: *Quantenmechanik und Gruppentheorie* (in German), Z. Physik **46** (1927), 1–46. Cited on page 81.
- [74] D. C. Rivier: *On a One-to-One Correspondence between Infinitesimal Canonical Transformations and Infinitesimal Unitary Transformations*, Phys. Rev. **83** (1951), 862–863. Cited on page 81.
- [75] S. Löck: *Dynamical Tunneling in Systems with a Mixed Phase Space*, Ph.D. thesis, Technische Universität Dresden, Fachrichtung Physik, (2010). Cited on page 81.
- [76] M. Moshinsky: *Linear Canonical Transformations and Their Unitary Representations*, J. Math. Phys. **12** (1971), 1772–1780. Cited on page 82.
- [77] M. Eger and E. P. Gross: *Point transformations and the many body problem*, Ann. Phys. (N.Y.) **24** (1963), 63–88. Cited on page 90.
- [78] M. Brack and R. K. Bhaduri: *Semiclassical Physics*, no. 96 in Frontiers in Physics, (Addison-Wesley, Reading), (1997). Cited on page 93.
- [79] M. Moshinsky: *Canonical Transformations and Quantum Mechanics*, SIAM J. Appl. Math. **25** (1973), 193–212. Cited on page 100.
- [80] P. A. Mello and M. Moshinsky: *Nonlinear canonical transformations and their representations in quantum mechanics*, J. Math. Phys. **16** (1975), 2017–2028. Cited on page 100.
- [81] K. B. Wolf: *The Heisenberg-Weyl ring in quantum mechanics*, in: *Group theory and its applications Vol. 3* (Ed. E. M. Loebl), 189–247, (Academic Press, New York), (1975). Cited on page 100.
- [82] J. Lacki: *The puzzle of canonical transformations in early quantum mechanics*, Stud. Hist. Phil. Mod. Phys. **35** (2004), 317–344. Cited on page 100.
- [83] A. Shudo and K. S. Ikeda: *Tunneling Effect and the Natural Boundary of Invariant Tori*, Phys. Rev. Lett. **109** (2012), 154102. Cited on page 100.

-
- [84] E. Doron and S. D. Frischat: *Semiclassical Description of Tunneling in Mixed Systems: Case of the Annular Billiard*, Phys. Rev. Lett. **75** (1995), 3661–3664. Cited on page 101.
- [85] W. H. Press, S. A. Teukolsky, W. T. Vetterling, and B. P. Flannery: *Numerical Recipes in C. The Art of Scientific Computing*, (Cambridge University Press, Cambridge), 2nd edn., (1992). Cited on page 106.
- [86] M. Sieber and F. Steiner: *Classical and quantum mechanics of a strongly chaotic billiard system*, Physica D **44** (1990), 248–266. Cited on page 109.
- [87] G. B. Arfken, H. J. Weber, and F. E. Harris: *Mathematical Methods for Physicists*, (Academic Press, San Diego), 6th edn., (2005). Cited on page 123.
- [88] G. H. Hardy and E. M. Wright: *An Introduction to the Theory of Numbers*, (Clarendon Press, Oxford), 4th edn., (1975). Cited on page 127.

Danksagung / Acknowledgements

Wie jede Arbeit ist auch diese nicht nur das Ergebnis eigener Anstrengungen, sondern eines sozialen Prozesses. An dieser Stelle möchte ich allen Menschen danken, die mich auf diesem Weg unterstützt haben.

Zunächst danke ich Prof. Roland Ketzmerick für die Aufnahme in seine Arbeitsgruppe “Computational Physics” und die Vergabe dieses interessanten Themas, für die durchgängig vertrauensvolle und konstruktive Zusammenarbeit sowie für seine zahlreichen Anregungen. Ich danke auch Prof. Peter Schlagheck für viele aufschlussreiche Gespräche und für die Übernahme des Zweitgutachtens.

Für die Begleitung meiner Arbeit danke ich auch Dr. Steffen Löck und PD Dr. Arnd Bäcker. Letzterem gilt besonderer Dank für die Koordination der Entwicklung unserer Gruppensoftware, die in entscheidendem Maße zur vorliegenden Arbeit beigetragen hat.

Des Weiteren danke ich unserer Sekretärin Gundula Schädlich und meinen Kolleg*innen Alexander Köhler, Alexander Schnell, Daniel Vorberg, Felix Fritzsich, Franziska Onken, Jérémy Le Deunff, Julius Kullig, Konstantin Clauß, Dr. Lars Bittrich, Martin Körber, Dr. Martin Richter, Martin Weigert, Dr. Matthias Michler, Dr. Normann Mertig, Dr. Shashi Srivastava, Stefan Majewski, Steffen Lange, Torsten Rudolf und Dr. Waltraut Wustmann. Ich verdanke Euch eine freundschaftliche und angenehme Arbeitsatmosphäre, die nie langweilig war. Besonders dankbar bin ich Lars Bittrich, Martin Richter und Normann Mertig für bereichernde Gespräche, die oft über ihren bloßen Zweck hinausgingen. Auch Felix Fritzsich und Julius Kullig möchte ich für die angenehme und produktive Zusammenarbeit danken. Für ihre Hilfe beim Korrekturlesen dieser Arbeit danke ich Martin Gerlach, Martin Körber, Normann Mertig und Robert Biele.

I want to thank the following people for inspiring discussions which came along during my work on this thesis: Dr. Eduardo Altmann, Prof. Steven Creagh, Dr. Arseni Goussev, Prof. Kensuke Ikeda, Prof. Srihari Keshavamurthy, and Prof. Akira Shudo. I thank the software developers behind `numpy`, `scipy` and `sympy`. The plots of this thesis have been produced with the `pyxgraph` python module. I thank the communities of `projecteuler` and `stackexchange`, which enriched me with both useful knowledge and the joy in purposeless thinking.

Ein besonders großer Dank für ihre Unterstützung gilt meiner Partnerin Antje und meiner Tochter Ruth.

Versicherung

Diese Arbeit wurde am Institut für Theoretische Physik der Technischen Universität Dresden unter der wissenschaftlichen Betreuung durch Prof. Roland Ketzmericks durchgeführt.

Hiermit versichere ich, dass ich die vorliegende Arbeit ohne unzulässige Hilfe Dritter und ohne Benutzung anderer als der angegebenen Hilfsmittel angefertigt habe; die aus fremden Quellen direkt oder indirekt übernommenen Gedanken sind als solche kenntlich gemacht. Die Arbeit wurde bisher weder im Inland noch im Ausland in gleicher oder ähnlicher Form einer anderen Prüfungsbehörde vorgelegt.

Darüber hinaus erkenne ich die Promotionsordnung der Fakultät Mathematik und Naturwissenschaften der Technischen Universität Dresden vom 23. Februar 2011 an. Ich versichere, dass ich in der Vergangenheit keine anderen Promotionsverfahren beantragt habe.

Clemens Löbner

Dresden, 22. 05. 2015